Morphodynamic Response of Estuaries to Climate Change

Yin, Yunzhu

Swansea University
Prifysgol Abertawe

Morphodynamic Response of Estuaries to Climate Change

Yunzhu Yin

Submitted to Swansea University in fulfilment of the requirements for the degree of Doctor of Philosophy in the College of Engineering

SWANSEA UNIVERSITY

2017

Abstract

Estuaries are one of the most important aspects of coastal systems globally. They are often hubs for human civilisation due to the socioeconomic advantages they offer. As they are highly vulnerable to natural forces, including tides, waves, surges and river discharges, it is essential to study the relationship between estuarine morphologies and these natural variables, which is crucial in order to assess estuarine evolution.

The Deben Estuary (UK) has been selected as the case study in this study as its morphology has been significantly changed over time. It can be expected that the estuary will undergo significant morphodynamic changes under future climate change. The objective of this study is to investigate the morphodynamic responses of the estuary to the climate change in order to better understand the relationship between morphological change and climate change.

A regional scale depth-averaged hydrodynamic and morphodynamic model Delft 3D was set up to the Deben Estuary, which incorporates wave propagation. The model was validated against measurements of water levels and waves before using it to simulate detailed scenarios. Then, the future climate projection data was used as the boundary conditions for the model scenarios. First, the calm weather conditions were considered since the model was run in long-term time scale. Then the episodic events were accounted for to investigate the impact of waves in future storms on the estuarine morphodynamics.

The results show that future climate change will enforce different responses of morphodynamics at the estuary. Responses vary depending on whether natural forces are episodic or long term, and also according to different climate change scenarios, such as different emission scenarios. The comparison between the responses under the present and future conditions indicates that the estuary may undergo different evolution to what is historically observed.

Declaration and Statements

I, Yunzhu Yin, declare that this thesis titled, 'Morphodynamic responses of estuaries to climate change' and the work presented in it are my own, I confirmed that

This work has not previously been accepted in substance for any degree and is not being concurrently submitted in candidature for any degree.

Singed……..(Yunzhu Yin)

Date……..

This thesis is the result of my own investigations, except where otherwise stated. Where correction services have been used, the extent and nature of the correction is clearly marked in a footnote(s).

Other sources are acknowledged by footnotes giving explicit references. A bibliography is appended.

Signed…….. (Yunzhu Yin)

Date……..

I hereby give consent for my thesis, if accepted, to be available for photocopying and for inter-library loan, and for the title and summary to be made available to outside organisations.

Signed……..(Yunzhu Yin)

Date……..

Contents

Acknowledgements

First of all, I would like to thank my first supervisor, Professor Harshinie Karunarathna for providing this PhD opportunity and supporting me throughout the entire study. I thank her patience, guidance and continuous encouragement all the time period. Her immense knowledge, valuable comments and inspired ideas have helped me to complete my PhD research and finish this thesis.

I would like also to express my sincere gratitude to my second supervisor, Professor Dominic Reeve, for his kindly suggestions and continuous guidance for my study. Also, great thanks should go to all my colleagues in the office. Dr Pushpa Dissanayake helped me to get knowledge and build the numerical models, and Dr Jose Horrillo-Caraballo's data supporting is greatly appreciated. Thanks also go to all my PhD office friends for their support, discussion, and for making my time working on this PhD such an enjoyable experience.

I am grateful to the Swansea University College of Engineering and China Scholarship Council for providing me with the scholarship and living funds for pursuing my research. Similarly, iCOASST and EFRaCC also provided me with invaluable data, and helped me pay for conference expenses. I am also grateful to the organisations of British Oceanographic Data Centre (BODC) and Centre for Environment, Fisheries and Aquaculture Science (Cefas) for providing the measured tide and wave data.

Finally, I would like to thank my family and friends in the UK and China for their unwavering support. Many thanks are also due to my wife, Shaoni Sun, for moving with me to UK to support me. The dissertation is dedicated to my daughter, Willow Yin, who is the best gift I have ever received. I wish she will have a heathy and happy life in the future.

List of figures

List of tables

List of symbols

Symbols	Units	Meaning
$\bar{c}$	kg/m^2	Depth-averaged mass concentration of sediment
C	$m^{1/2}/s$	Chèzy coefficient
C_d	-	The wind drag coefficient
D_{50}	m	Median grain size diamter of non-cohesive sediment fraction
D_{90}	m	90-percentile sediment diameter
E	J/m^2	Wave energy
f	$1/s$	Coriolis parameter
g	m/s^2	Gravitational acceleration
h	m	Water depth
h_w	m	Wave height
k_w	$1/m$	Wave number
M_x	-	External sources and sinks of momentum in -x direction
M_y	-	External sources and sinks of momentum in -y direction
n	$m^{-1/3}s$	Manning coefficient
P_x, P_y	Pa	Hydrostatic pressure in -x direction and -y direction
P_{atm}	Pa	Atmospheric pressure
q_{in}	$1/s$	Local sources of water per unit of volume
q_{out}	$1/s$	Local sinks of water per unit of volume
r_c	m	Roughness height for currents
S	-	Sediment source and sink terms per unit
T	s	Wave period
T_p	s	Peak wave period
U_{10}	m/s	Wind speed 10 meters above the free surface
U	m/s	The depth-averaged velocity in -x direction
U_{cr}	m/s	Critical bed shear velocity
U_{orb}	m/s	Wave orbital velocity
V	m/s	The depth-averaged velocity in -y direction
w	m/s	Sediment fall velocity
x, y, z	-	Cartesian coordinates
$A^{(m,n)}$	m^2	Area of computational cell at location (m, n)
$\Delta^{(m,n)}_{SED}$	kg/m^2	Change in quantity of bottom sediment at location (m, n)
Δt	s	Computational time-step
$\Delta x^{(m,n)}$	m	Cell width in -x direction at the v point of cell (m, n)
$\Delta y^{(m,n)}$	m	Cell width in -y direction at the u point of cell (m, n)

$\varepsilon_{s,x}$	m^2/s	Eddy diffusivities of sediment in -*x* direction
$\varepsilon_{s,y}$	m^2/s	Eddy diffusivities of sediment in -*y* direction
$\varepsilon_{s,x}$	m^2/s	Vertical eddy diffusivity
ζ	*m*	Water level
θ	*deg.*	Wave direction
θ_{cr}	/	Critical Shield parameter
θ_m	/	Mean Shield parameter
κ	/	Von Karman constant
ν_h	m^2/s	Horizontal eddy viscosity coefficient
ν_V	m^2/s	Vertical eddy viscosity coefficient
ρ_a	kg/m^3	The density of air
ρ_s	kg/m^3	The density of sediment
ρ_0	kg/m^3	Reference density of water
σ	-	Vertical coordinate in *Sigma* coordinate system
τ_{bx}, τ_{by}	N/m^2	Components of bed stress in -*x* and -*y* direction
τ_s	N/m^2	The magnitude of the wind shear-stress
φ	*deg*	The angle between wave and current
ω	*m/s*	Vertical velocity in -σ direction

Chapter 1: Introduction

1.1. Estuary research

Estuaries, defined as the area connecting the fresh water river and sea, are important residential areas and due to the socio-economic potential, are often sites of cities with large populations. For instance, London is located at the mouth of the river Thames, New York City is situated at the mouth of the Hudson River and Shanghai is at the mouth of the Yangtze River. Therefore, understanding the evolution of estuaries is essential for sustaining the environment and socio-economics associated with these systems.

There is numerous research concerning the estuarine environment, both in terms of geophysical processes and biological aspects. These extremely complicated areas are acutely affected by natural forces (such as tide, wave and wind), human activities and the activities of oceanic creatures like shallow water animals; they are also affected by seabed materials such as fossils and sediments. It is impossible to consider all these factors systematically as most of them contain uncertainties and interact with each other non-linearly. Most studies only refer to some of elements for specific purposes. For example, when considering the process of morphological changes of an estuary, the natural forces and human activities are mostly included. These two factors control most physical process of the estuary. But for the biological aspect, the species, the salinity or the sediment should also be considered.

Researchers have investigated the morphological responses of the estuary to the hydrodynamic effects from the process aspects and were able to determine the relationship between hydrodynamic conditions and morphodynamic conditions. Similarly, the investigations working from measured data to find the empirical relations between the estuarine elements have also been considered. However, these researches are mostly dependent on the specific estuaries in which the behaviours can be accurately explained but the relationship between hydrodynamics and morphodynamics is poorly understood.

As the rapidly changing climate has become increasingly concerning, the investigation into its effects on the estuarine morphodynamics has become more urgent these days. The impacts of Sea Level Rise (SLR) on the morphology of estuaries have been investigated by previous studies either from the aspect of long-term numerical simulations (Dissanayake, 2011) or data analysis based on historical measured data. The future climate conditions not only affect the hydrodynamics (Nicholls, et al., 2007; Brown et al., 2008; Chini et al., 2009) but also influence the morphodynamics of coastal areas (Gornitz, et al., 2002; Dissanayake, 2011). Therefore, it is necessary to understand both the hydrodynamic and morphodynamic responses to the climate change and the relationship between them.

Most researches about the impact of climate change on the estuarine morphology are carried out through numerical modelling studies by reducing hydrodynamic boundaries significantly for the sake of reducing computational intensity. However, due to uncertainties involved in the boundary conditions, the reliability of these models is in doubt because the realistic conditions are more complex and the cumulative effects will be significant even if a very small change occurs at the beginning of a long-term simulation that is carried out over a number of years or decades.

Estuary management personnel often do not want to predict the future morphological changes. Sometimes, they only want to know what will change under future climate conditions. As they already know the morphodynamic responses to the current hydrodynamic conditions, they only need to know whether these responses will change or not in the future rather than the exact final morphology of the future. This study will determine the different responses of the morphodynamics between present and future climate conditions to investigate the morphodynamic responses to the future climate conditions. Additionally, in this case, there is no need to run a very long simulation: it is feasible to use a process-based model without reducing the boundary conditions dramatically. This will also allow the exploration of the specific relation between morphodynamics and hydrodynamics.

1.2. Motivations and objectives of this study

As discussed above, estuaries are complex morphodynamic systems which are continuously changed by natural factors, such as waves, tides, and river flow. The morphodynamic environment of an estuary depends on the interactions and feedbacks between the driving forces and the morphology of the estuary. As a result, any changes to hydrodynamic force due to climate change will have significant consequences on how the estuary will behave in future. In this study, the implications of global climate change on estuary morphology will be investigated using a process-base computational modelling approach.

Objectives

The overarching aim of this study is to investigate the response of estuarine morphodynamics to climate change and their sensitivity to the hydrodynamic changes due to climate change. The following questions will be answered to efficiently achieve the main aim:

- Will estuary morphology change significantly in future climates?
- How will different morphodynamic elements of the estuary, such as the main channel and the ebb deltas, respond to the climate change?
- How sensitive is the estuary system to SLR and extreme wave condition changes?

The research will take a case study approach and the research objectives are:

- To develop a process-based computational model to simulate estuarine hydrodynamics, waves and morphodynamics.
- To investigate the impacts of climate change on waves and water levels in the case study area.
- To investigate the impacts of hydrodynamic and wave changes induced by climate change to medium-term estuary morphodynamic evolution.

- To explore the morphodynamic behaviour of the estuary when responding to extreme episodic events in present and future.

In order to achieve the study's aims, the research strategy has been designed as follows:

1. The process-based Delft 3D model is set up for the Deben Estuary (UK) by using the global model tidal conditions. Three different resolution models have been developed utilising nesting in order to provide the hydrodynamic conditions.
2. The calibration and validation of the model is carried out against the measured data in both hydrodynamic and morphodynamic aspects, to ensure that the model is able to capture the most features of the real estuary.
3. The projected future global wave data is analysed statistically to investigate future climate conditions so that they can be used in the regional model.
4. A range of scenario simulations based on the current climate conditions and future climate conditions is carried out by using the validated models to investigate the hydrodynamic and morphodynamic responses.

1.3. Structure of the thesis

This thesis consists of nine chapters including the introduction in Chapter 1 and conclusion in Chapter 9.

Chapter 2 is a review of the previous literature on estuarine hydrodynamics and morphodynamics. The classifications of the estuaries have been discussed and numerical methods are also summarised.

Chapter 3 introduces the study site with a discussion on the historical hydrodynamic and morphodynamic conditions and presents the historical hydrodynamic and bathymetrical data available around the estuary.

Chapter 4 describes the numerical model used in this study and model domains, set up and boundary conditions. The detailed discussion of model set up is followed by a summary of the limitations.

Chapter 5 calibrates and validates the numerical models, in which the tide, wave and morphology modules are analysed against the measured data and hindcast data with the help of evaluation methods.

Chapter 6 statistically analyses the forecasted future wave data from global models in order to provide the future climate conditions for the regional models. The results can be used by regional management as a reference for future climate change.

Chapter 7 investigates the estuary's response to SLR during calm weather conditions. The estuary's morphodynamic response under different SLR scenarios will be modelled and discussed.

Chapter 8 investigates the estuary's morphodynamic response to the present and future storm wave conditions. The sensitivity of the selected bathymetry will be analysed.

Chapter 9 concludes the results and identifies the recommendations for future work.

Chapter 2: Literature review

Due to the complex flow and morphodynamic environment in estuaries, the evolution of estuaries is affected by number of natural and human forces. For example, the delta of the Yellow River estuary in China, had expanded dramatically over the last centuries due to the high concentration of sediment in the upstream river. In contrast, some estuaries, such as the Seven Estuary in UK, have significantly retreated due to the combination of changing hydrodynamic forces such as wave swash, sea level changes and coastal flooding which is associated with the less sediment discharge from rivers. Thus, focus on estuaries has increased in the last few decades in order to create a balance between human activities and natural impacts by exploring the morphological behaviours.

Morphodynamic behaviours of estuaries are closely related to estuarine hydrodynamics such as tides and waves (Boothroyd, 1985; Burningham and French, 2006). Other factors such as storm surges and river flows can also contribute to the changes of estuary systems and can determine their stability and integrity. Over longer period, global climate change will have a significant impact on the hydrodynamic regime of estuaries and, thus, on the morphological change. Hence, both the short-term morphological changes and long-term topographical changes should be known and understood before undertaking sustainable management of estuaries in the future.

However, estuaries may contain different features in terms of geometrical variations and aspects of various hydrodynamics and morphodynamics conditions. The interactions between waves, wave and tide-induced currents, river discharge and the seabed all induce complex morphological changes that are characteristic to any specific estuary. Thus, before exploring the interactions, some specific types of estuaries need to be understood.

2.1. Classification of estuaries

Different methods of estuary classification can be found in literatures, in which the most notable and commonly used methods are the classifications due to tidal prism or

salinity structure (Hansen and Rattray, 1966; Valle-Levinson, 2010), tidal range (Davies, 1964; Hayes, 1979) and geomorphology (Hume and Herdendorf, 1988; Davidson, 1991; DEFRA, 2008).

In the classification based on the tidal prism or salinity vertical structure, estuaries can be divided into: salt wedge, partially mixed and fully mixed (Valle-Levinson, 2010). In the vertical stratification of the estuary, the river flow occurs above the tide prism. This classification is based on the competition between river flow and mixture from tidal forcing, which is proportional to the tidal prism. When the river discharge is large compared to tidal flow, a salt wedge is created at the bottom layers of the estuary thus creating large salinity gradients across the water column (Figure 2.1).

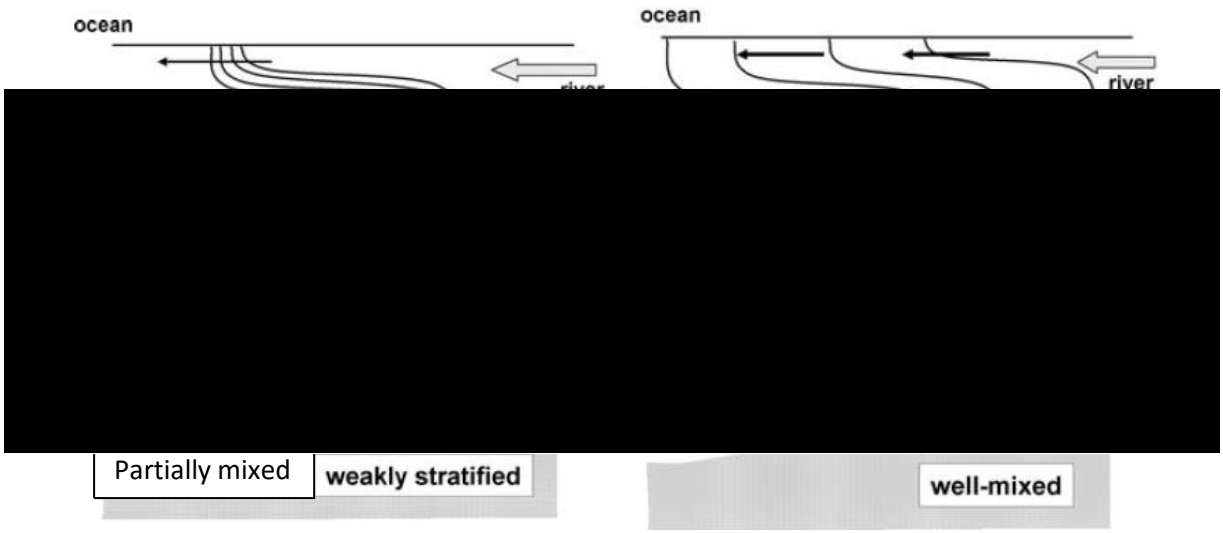

Figure 2.1 – Classification based on the vertical salinity structure (Valle-Levinson, 2010)

On the other hand, when ocean tide is large compared to river discharge, the estuary becomes partially mixed and contains weak salinity gradients across the water column. Vertical salinity gradients in partially mixed estuaries can vary from large to small, depending on the relative magnitudes of tidal flow and river discharge (Figure 2.1). When the tidal flow is significantly larger than the river discharge, the estuary will become well-mixed, resulting in no significant variation in vertical salinity profile. It is essential to note that the systems may change from one type to anther depending on

tidal periods and river discharges because the tidal prism and river discharge can vary monthly and seasonally.

According to the tidal range, the estuaries can be divided into: micro-tidal estuary, meso-tidal estuary and macro-tidal estuary (Davies, 1964). In micro-tidal estuaries, the tidal range is usually less than 2 meters in which the physical processes are not significantly altered by tides. In meso-tidal estuaries, where tidal range is from 2 meters to 4 meters, estuarine processes are strongly but not predominantly affected by tides. In macro-tidal estuaries, the tidal range is larger than 4 meters and the estuarine processes are predominantly influenced by the tidal activities. When considering the interaction between the tides and wave energy, Hayes (1979) refined this classification under the medium wave energy conditions (Table 2.1), in which more categories had been developed.

Table 2.1 – The classification based on tidal range (Davies, 1964; Hayes, 1979).

Classification by Davies (1964)		Refined classification by Hayes (1979) *Medium wave energy*	
Micro-tidal Meso-tidal Macro-tidal	0-2m 2-4m >4m	Micro-tidal	0-1m
		Low meso-tidal	1-2m
		High meso-tidal	2-3.5m
		Low macro-tidal	3.5-5m
		Macro-tidal	>5m

However, the above two classifications are based on hydrodynamics and do not consider the morphology of an estuary. Therefore, in terms of investigating and understanding morphodynamics, the classification based on the geomorphology of an estuary is most useful.

According to the presence of constituent geomorphological elements and behaviours, estuaries have been classified into the following seven types: Fjord; Fjard; Ria; Spit-enclosed estuary; Funnel-shaped estuary; Embayment; Tidal inlet (DEFRA, 2008). Since there is no exact criteria for this classification, they may vary slightly in different

researches. The following descriptions are based on the classification of DEFRA report (DEFRA, 2008).

Fjords & Fjards

Fjords are generally long, deep and narrow features that are bound by relatively erosion-resistant, steeply rising slopes. Examples are Loch Etive and the Ruel Estuary in Western Scotland (DEFRA, 2008). Fjards are indented, drowned features fringing rocky, glaciated lowlands with extensive intertidal sand and mud deposits. Pwllheli Harbour in Wales is an example of a small fjard with spits.

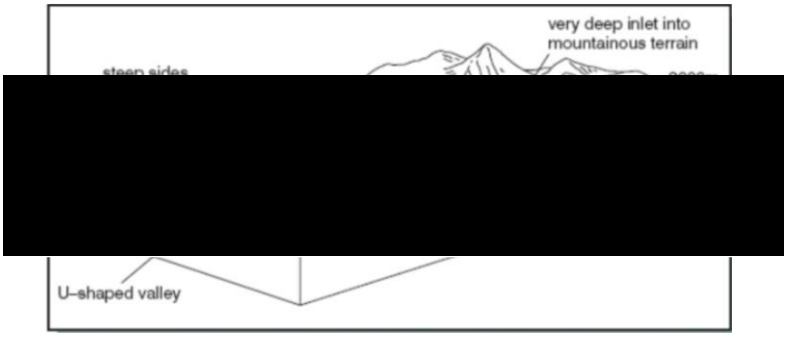

Figure 2.2 – The example of fjord
(https://www.slideshare.net/6thformmatt/submergent-and-emergent-coastlines).

Both fjords and fjards originated in glacial valleys, where the general rule is that fjords have exposed to rock platforms set within steep-sided relief with no significant mud or sand flats while fjards contain low lying relief with significant sand or mud flats. Fjords are usually formed due to the over deepened trough submerging resulting from the rising of sea level from the Pleistocene ice sheets and often exhibit a shallower sill near the mouth (Figure 2.2); but fjards usually contain more extensive intertidal deposits, including inner estuary saltmarsh without deep glaciated troughs (Figure 2.3).

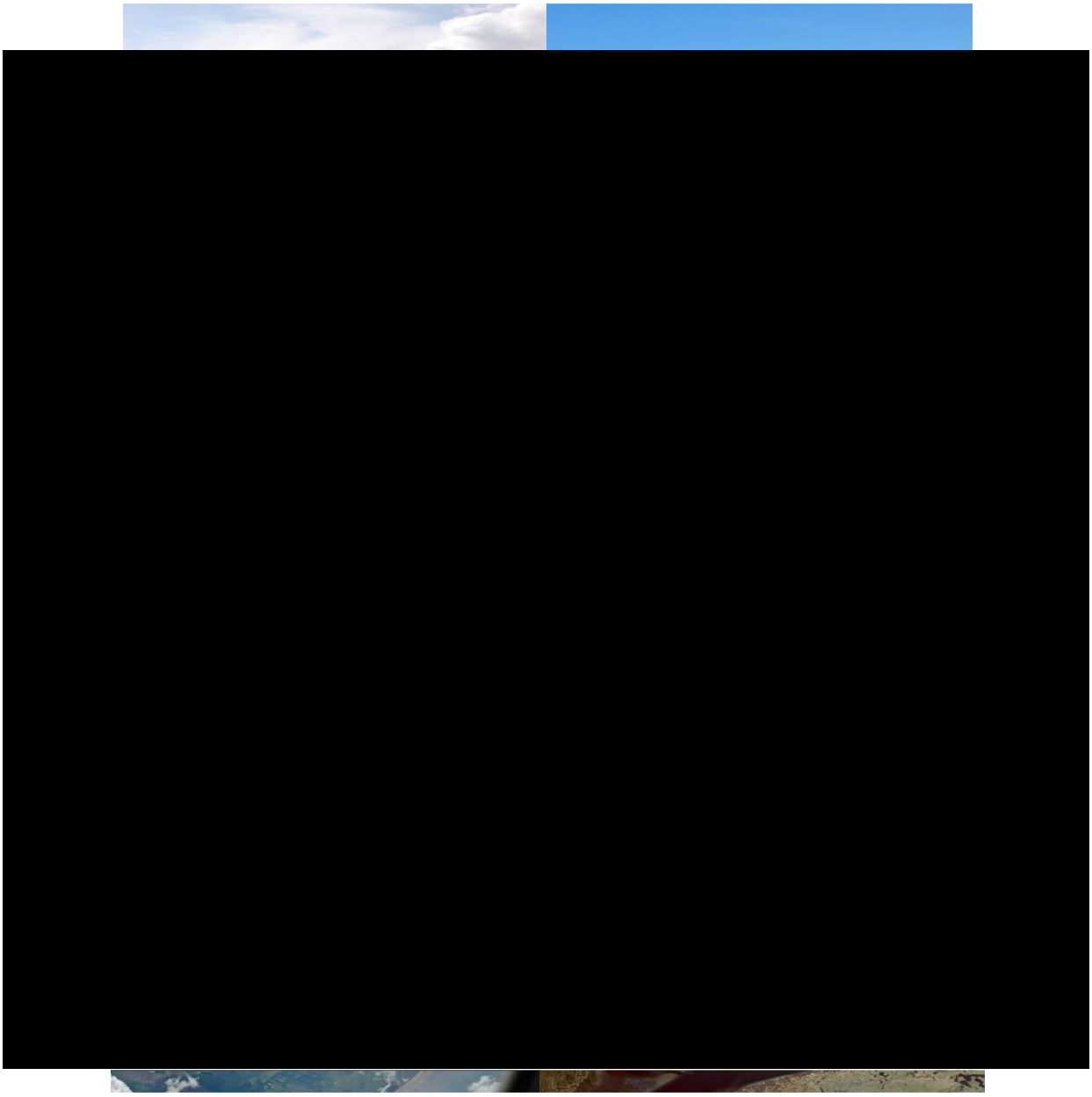

Embayment (The Wash, UK) Essex inlet (Massachusetts, USA)

Figure 2.3 – The samples of different types of estuaries in the world (British Geographer).

Since the banks and bed materials of fjords and fjards are usually glacial rocks which are not easily moved or eroded by hydrodynamic forces, morphological changes in these estuaries are not very significant. Research about fjords mostly concerns the hydrodynamic aspects such as stratified flows, the interaction between sea water and fresh water and water renewal by ocean dynamics (Edwards, 1977). Most fjords usually contain strongly stratified flows that described by the layer theories. The

circulation of these estuaries is complicated, which usually relates to the density variation between salt water and fresh water. Stigebrandt (1981) argued that a two-layer description of the flow field can be used as the mechanism that governs the estuarine circulation in deep, strongly stratified fjords.

Rias

Rias are drowned valleys located in periglacial areas, with the original valley being created by fluvial process. Typically, rias are 'v-shaped' in cross-section, with relatively steep valley sides and composed of hard rock (Figure 2.3; Figure 2.4). Examples of rias in the UK are Wear (with spits), Tweed and Tyne (without spits) and Mersey; the coast of Iberian Peninsula in Europe also contains numerous rias (Perillo, 1995).

Figure 2.4 – The example of ria
(https://www.slideshare.net/6thformmatt/submergent-and-emergent-coastlines)

The morphological changes in rias are usually not the same from the mouth to points further upstream. For example, over the last 150 years, the outer estuary of Mersey has experienced a far greater morphological change than the inner estuary (Blott et al., 2006). Also, the sediment in the adjacent beaches, which can be a source of sediment, is imported into the estuary not only by the tidal current but also by the salinity-induced gravitational circulation flow (Thomas et al, 2002; Blott et al., 2006).

Spit-enclosed estuary

Spit-enclosed river valleys are drowned river valleys that have single or double spits at their mouths, which tends to restrict the exchange of flow and sediment between the sea and the river (Figure 2.3). These estuaries often contain flood and ebb tidal deltas and are mostly found in the east, south and south-west England. Some examples are Humber Estuary, which has a single spit, Deben Estuary and the connected mouth between Orwell Estuary and Stour Estuary in UK.

Many spit-enclosed estuaries experience large tidal velocities through the mouth and limited wave penetration due to the spit sheltering at their mouths. Although most of these estuaries are tide-dominated, wave impact on the adjacent shores and the spits should not be ignored because the adjacent shore areas may become the primary source of sediment to the estuaries in a long time-scale (Al-Bakri, 1986; Burningham and French, 2006). However, in situations where the estuary contains large spits with a small inlet, such as is seen in the Medway Estuary in the UK, the tides and waves play a minor role on the changes of mudflats in the estuary while the fine particles inside the estuary are reworking because there is no significant external sediment supply (Deloffre et al., 2007). In these estuaries, the hydrodynamic regime is not the only decisive factor when morphodynamic change is concerned. Sediment availability and sediment bypassing through the estuary mouth also play a major role in the estuary's long-term changes (HR Wallingford, 2002; Townend, 2007).

Funnel-shaped estuary

Funnel-shaped estuaries often possess elongated linear sand banks within the area of the estuarine mouth instead of spits. The rivers Thames and Ribble in the UK are examples of this kind of estuary. These estuaries usually have wide open mouths, which means that they are very sensitive to tide regime but are hardly affected by the littoral drift from adjacent coasts; this results in a tide-dominated inner estuary and a wave-dominated outer estuary (DEFRA, 2008). The channels, mudflats and saltmarshes that usually coexist within these estuaries make it difficult to quantify the interactions and mechanisms particularly when topographical variations happen on the

channels and mudflats (Figure 2.5). However, one of the advantages for investigating these estuaries is that they can be schematized to be a simple system so that it is easy to establish the relationship between hydrodynamic and morphodynamic due to relative simplified geometries (Lanzoni, 2002; Hibma, 2003; Prandle, 2003).

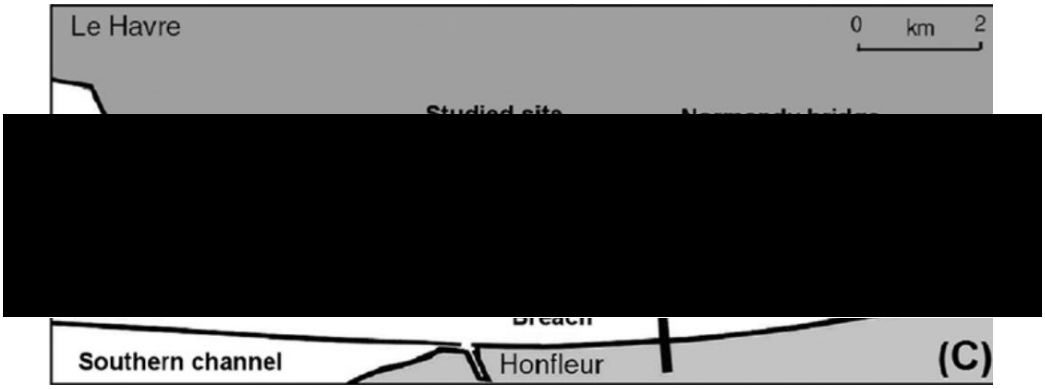

Figure 2.5 – The example of funnel-shaped estuary (Seine Estuary in France, Deloffre et al., 2007)

Embayment

Embayments are formed where several rivers converge, and their joint valleys create a wide mouth which is sensitive to large wave and weather effects (Figure 2.3). The Wash in the UK is a classic example of an embayment. Compared to a funnel-shaped estuary, embayments usually cover a larger area (Figure 2.6), so the tidal forces at the seaward boundary, which may generate tidal resonance or over-tides among the bay area, will provide the most significant impact on morphological changes. An additional difference to the preceding funnel-shaped estuary, is the increase of the local wind-induced wave will have impacts on the embayment's morphological changes due to large wind fetch impacts. The embayment also can be simplified in order to investigate the relationship between hydrodynamics, geometry and morphodynamics (Schuttelaars, 2000).

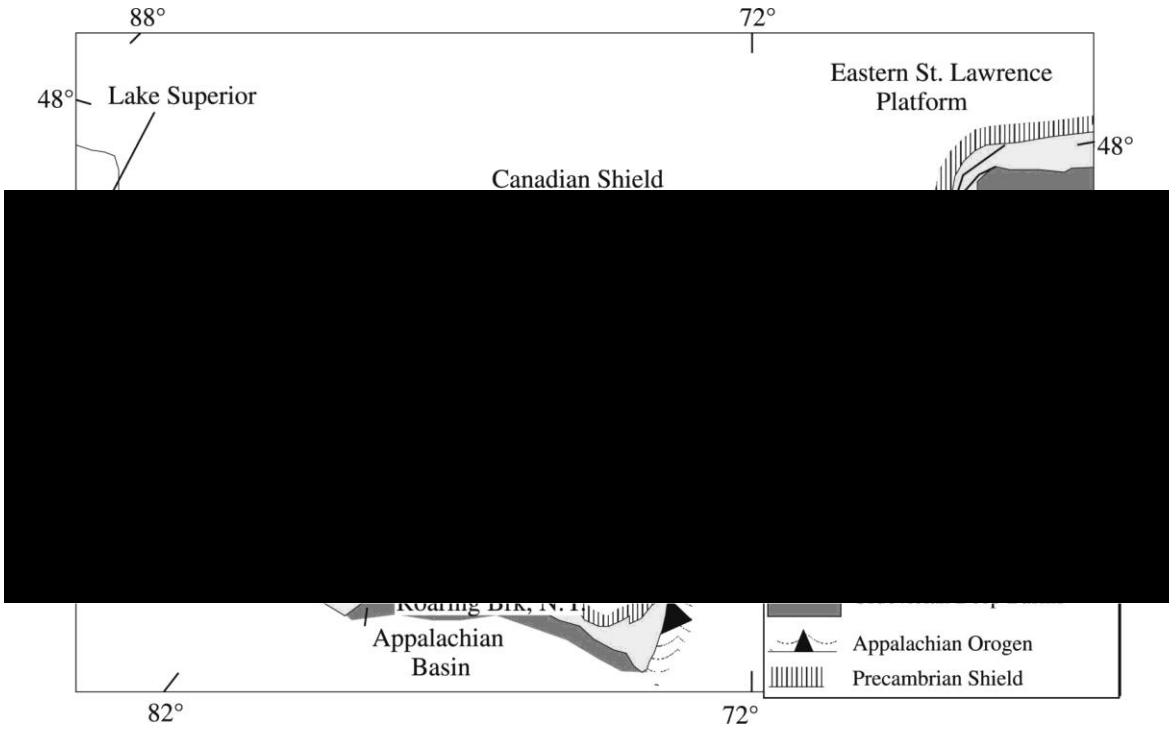

Figure 2.6 – The example of embayment (Ottawa Embayment in USA, Hersi, et al., 2000).

Tidal inlet

Tidal inlets are produced where the relative sea-level rise has occurred over an extremely low relief coastal plain. There are characterised by narrow channels through fronting barrier beaches and backed by extensive tidal lagoons (e.g. Essex inlet in Figure 2.3). The south coast of England contains several of these estuaries, including Portsmouth, Langstone, Chichester and Pagham Harbours. The inlet acts as the throat of river mouth; its morphology is easily changed by the sediment transport.

The morphological changes of tidal inlets are not only related to the sediment in the inlet but also essentially depend on the adjacent sediment supply. Finley (1978) examined the close relationship between wave energy, longshore sediment supply, and the ebb-tidal delta morphology of North Inlet in South Carolina. He discovered that 82% of the ebb-tidal delta accretion rate was contributed by the inlet-directed longshore sediment transport while some northeast storms may also have an

accretionary effect on the delta. Dissanayake (2011) has found that erosion/accretion of the inlet is positively correlated to sea level rise by using an idealised inlet.

Although every described type of estuary has its own feature, the exact distinctions between them are uncertain, such as the difference between fjords and fjards. Additionally, some morphological features can exist in more than one type of estuary. For example, it is easy to find the ebb-deltas or channels in both spit-enclosed and tidal inlet estuaries. Therefore, it is reasonable to treat every specific estuary as unique, even if some general features are the same.

2.2. Estuary hydrodynamics

It is well known that the primary natural drivers of morphological changes are hydrodynamics such as tides, waves, storm surges and river discharges. These factors play important roles in the development and evolution of morphological characteristics of estuaries.

2.2.1. Tides

Tides in the coastal areas often originate from the ocean tides which result from the gravitational relationship between the Earth, Moon and the Sun. There are two main tidal theories: one is the equilibrium tidal theory, developed from the Newton's gravitational theory. It is based on Euler's equations of fluid motion, which explains the diurnal inequality, spring-neap cycles and observed semidiurnal nature tides. Another tidal theory is based on Laplace's mathematical theory of the tides, which indicates the wave nature of tidal range explicitly and determines the tide-generating forces (Reeve, 2012).

The equilibrium tidal theory is derived from the attractive forces between Earth, Moon and Sun by applying Newton's law of universal gravitation resulting in astronomical tides whose feature is periodic. This periodic change in water level always has a cycle associated with high water level (flood tide) and low water level (ebb tide). If there are

two high waters and two low waters per day, it is called semi-diurnal tide, while if there is only one high water and one low water per day, it is called a diurnal tide. However, these water level variations are not constant globally because of the positions of three bodies and the relationship with the declination and latitude of Earth. The well-known phenomenon of semi-diurnal inequality has been formed which is able to be changed by latitude. When the inequality is pronounced enough in higher latitude, it even becomes diurnal (Figure 2.7). So, the predominant frequency of periodic tide wave is various in different place.

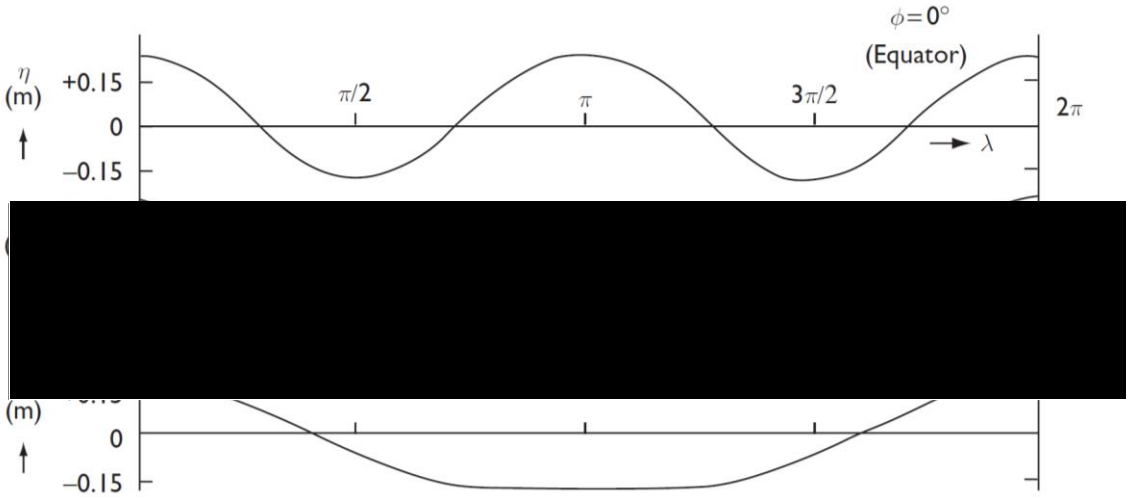

Figure 2.7 – Tides at three latitudes (0°, 30° and 60°N) for Moon declination of 28°30′. Longitude, λ, is shown in radians (Reeve, 2012).

Due to the various gravitational forces derived by relative positions of three bodies in Earth-Moon-Sun system, an additional variation in tidal heights can be observed, which known as 'Spring-Neap cycle', occurring approximately bimonthly. The increased equilibrium tidal height due to the enhanced gravitational force when the Moon, Earth and Sun act along a single axis (full moon and new moon) makes the tide become 'spring' tide, whereas the decreased equilibrium tidal height due to the reduced gravitational force when the Earth, Moon and Sun are in quadrature, in the first and last quarter, makes the tide become 'neap'. This means the tidal range in 'spring' is much larger than the tidal range in 'neap' and the highest water level and the lowest water level usual occur in the 'spring' tide periods (Figure 2.8).

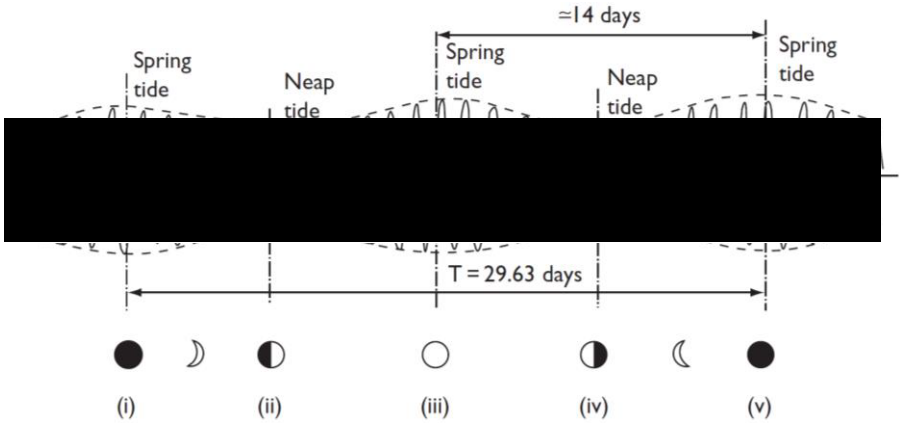

Figure 2.8 – The spring-neap tide variation in tidal range with phases of the Moon (Reeve, 2012).

Theoretically, the real tide data can be divided into several groups (tide species) and in every group, it is considered as the superposition of many tidal harmonics (cosine curves) with different frequencies by using mathematical transformation. The process of this division is called harmonic analysis and every tidal harmonic has its own frequency, amplitude and phase. However, in real cases, only the predominant harmonics are considered as some of them are not important. For example, the amplitude of semi-diurnal tidal constituent M_2 with frequency 28.99 deg/hr has occupies the amplitude of real tide data about 56% while the diurnal tide K_1 with frequency 15.04 deg/hr has only occupied approximately 5% of the amplitude of real tide data in Norfolk (UK) (Table 2.2).

In coastal areas, minor tide harmonic components are often ignored for the sake of simplification. However, under shallow-water conditions, the harmonic tidal constituent will sometimes change its propagation speed (frequency) partly due to topographical variations. When the speed of one tidal constituent is an exact multiple of the speed of one of the fundamental constituents, this tidal constituent is the over-tide of the fundamental tidal constituent (i.e. the M_4 tidal constituent is the over-tide of the fundamental tidal constituent M_2). If the parent tidal constituent contains two different tidal components, the new tidal constituent is the compound tide of these two parent fundamental tides (i.e. the MS_4 is the compound tide of M_2 and S_2 fundamental tides). However, the differing importance of role played by tidal components at outer

and inner estuaries results in tidal distortion (or tidal asymmetry) within the estuarine system with the help of non-linear tidal propagation (Speer and Aubrey, 1984).

Table 2.2 – The example of harmonic tide constituents in Norfolk (UK) (Reeve, 2012)

Name	*Frequency* (Cycles/h)	*Amplitude* (m)	*Phase* (Degrees)
[redacted]			
K_1	0.042	0.15	285

Tides distortion in estuary system

When the tides propagate to the estuarine areas, the spectral energy will transform from one constituent to another (Aubrey and Speer, 1985). The tidal constituent that plays a minor impact outside of the estuary may become dominant in the inner estuary due to changes in tidal characteristics as a result of local geometrical characteristics of the estuary. This is known as tidal distortion, which can lead to the asymmetric ebb and tidal characteristics that can be represented by the non-linear growth of harmonics of the astronomical tidal constituents (Speer and Aubrey, 1984). The low frequent harmonic energy growth which is extracted from the fundamental frequency by non-linear friction, advection and continuity and the energy lost to dissipation sometimes becomes much stronger than the harmonic energy at the outside of the estuary (Speer and Aubrey, 1985). This asymmetry may lead higher flood velocities and weaker tidal currents resulted from the shorter, intense flood tide and longer, weaker ebb tides (Figure 2.9). The phase-locked property (which means the phase does not change between over-tides and tidal compounds) makes the tidal constituents persistent along the total estuary (Aubrey and Speer, 1985).

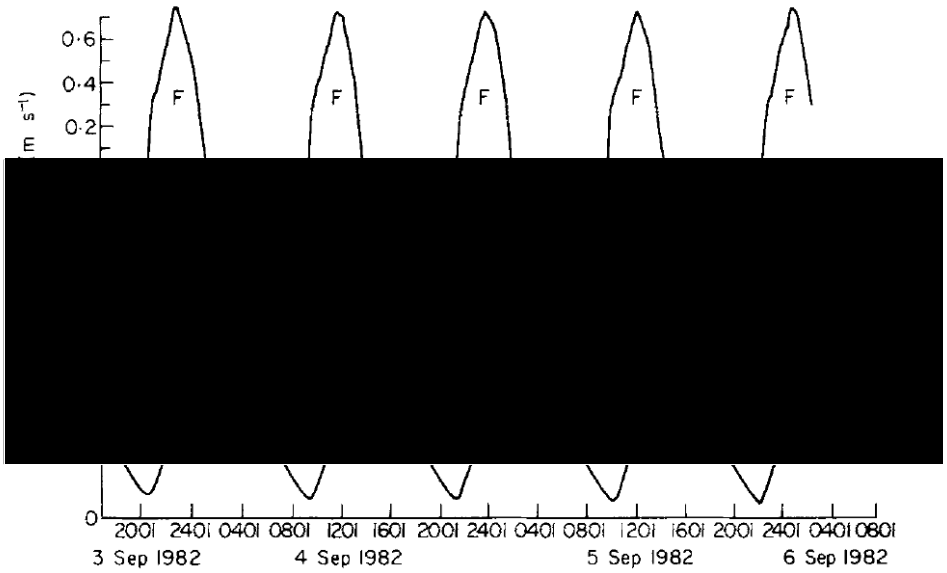

Figure 2.9 – The characteristic distortion of the tide inside the Nauset Inlet (U.S.) upper: velocity; bottom: sea surface; F: Flood; E: Ebb (Aubrey and Speer, 1985).

The most important factor for determining the tidal asymmetry is the geometry and topography of estuaries. Aubrey and Speer (1985) concluded that the shallowest estuaries are generally characterized by longer falling tides and stronger flood currents, so are flood-dominant, unless extensive tidal flats are present; however, deeper systems with tidal flats likely to have longer rising tides and stronger ebb currents: they are ebb-dominant. The flood-dominant estuaries will be directed up-estuary with consequent channel shoaling if sediment supply is sufficient while ebb-dominant estuaries may represent more stable configuration with stronger ebb currents which are able to flush coarse sediments entering the estuary through the inlet (Speer and Aubrey, 1985).

In contrast, the tidal asymmetry can have a great impact on the topography in return such as the formulation of flood or ebb delta (Aubrey and Speer, 1985; Friedrichs and Aubrey, 1988). The imported or exported sediment will change the estuary's bathymetry and depth. The new depth will have non-linear influence on the tidal response as the tidal distortion is closely related to the parameter *a/h* (tidal amplitude/water depth). The non-linearity of the estuary to tidal response complicates the estuarine system.

Tidal properties related to morphodynamics

Numerous research has investigated the relationship between certain tidal properties (tidal ranges, tidal volumes, tidal prisms, vertical tidal excursion) and morphological changes (Capo et al, 2006; Walkden, 2009). Deloffre et al. (2007) found that tide range has a linear relationship with the resulting deposit thickness of the Authie mudflat in Pas-de-Calais in Franc. Walton and Adams (1976) explored the 44 inlets around the United States coastline and found a relationship between tidal prisms and the inlet entrance area; this was the major governing parameter on the bar system.

In the physical aspect, the most important and direct tidal effect on the morphology is the tide-induced current; this is the main force on the sediment transport as the bed shear stress is related to the current. However, the current is not only related to the bed stress: it also can generate turbulence, contributing to the inception of sediment. Research into the role of turbulence in estuary sediment transport is currently limited, although several turbulence closure models have been developed (Rodi, 1984; Uittenbogaard et al., 1992). Among these models, the k-ε turbulence closure model (second order) is most frequently used. It is based on the so-called eddy viscosity concept which can be used in tidal simulations (Baumert and Radach, 1992; Davies and Gerritsen, 1994).

In terms of the mechanism of the sediment movement, the critical tidal velocity plays a great important role in sediment inception. Sediment movement is dependent on a shear force, τ_0, which is closely related to the bottom velocity. When this shear force is gradually increased from zero due to the increased bottom velocity, the moment that the particles moved can be identified. When there is widespread sediment movement associated with critical shear stress, τ_{CR}, it is clear that the motion threshold has been reached. After further velocity increase, the finer particles begin to be swept up to the flow, an inception of suspended load has occurred (Reeve, 2012). Therefore, as the velocity threshold can determine the sediment transport and the consequent morphological changes, it is essential in the morphological change investigation.

2.2.2. Waves

In many estuaries, the wave effect is the major driving force of estuarine morphology. Waves induce complex flow patterns as result of oscillatory wave-induced particle motions and wave-current interactions, and can trigger sediment transport. The mechanism that turbulence or oscillatory flow affects the sediment movement is still uncertain, although it has been explored by many researchers (Fredsoe, 1992; Van Rijn, 1993).

Due to the existence of wind forcing, propagating waves can be divided into two types: wind waves and swell waves. Wind waves are formed by the interaction between wind and water surface, whereas swell waves are only affected by gravity and inertia when the wave is outside the generation area. When the waves are formed by the wind shearing action, they can travel vast distances and spread with high-frequency wave energy. In the process of spreading, both waves are dissipated and transferred to lower frequencies so that the sea state is modified. Then the swell sea state will be formed when the low-frequency waves travel more quickly than the high-frequency waves, which is also known as ‘dispersion’ (Reeve, 2012). Thus, wind waves can be characterised as irregular, short-crested and steep with a large range of frequencies and directions. Swell waves can be characterised as regular, long crested, and gentle with a small range of low frequencies and directions.

When waves approach a shoreline, their height and wavelength are altered by the processes of refraction and shoaling before breaking in the surf zone. When they are in the surf zone, their transformation becomes more complex, which includes the generation of cross and longshore currents, a set-up of water level and wave breaking.

Because of the complication of random waves, describing them becomes much more difficult. The observed wave data at a particular point consists of component waves of various heights and periods and comes from different directions. The most popular explanation is the wave spectrum, which is used to describe the wave statistically. It is assumed that the wave energy is separated by a range of frequencies, which divides the random waves into different frequency and direction bins; the wave energy then

spreads into these bins. The widely-used forms of spectra are Bretschneider (Bretschneider, 1959), Pierson-Moskowitz (Pierson and Moskowitz, 1964) and JONSWAP spectra (Hasselmann et al., 1973). The detailed description of these spectra can be found in these references.

The complication of wave description is not only due to the complex wave itself but also due to the wave-current interactions when the waves propagate into the coastal area and the wave-wave interactions (Hasselmann et al., 1973; Komen, 1984; Beji and Battjes, 1993; Eldeberky, 1994). In the shallow coastal area, the specific features will occur such as wave breaking, wave run-up or whitecapping (Eldeberky and Battjes, 1995; Komen, 1984). This will drive the sediment transport at the coastal area dramatically and is associated with other hydrodynamic factors such as tides (Stive, 1987). The estuary will be much more dynamic, particularly with the extreme wave inputs.

Extreme waves

Extreme waves occur during storm conditions and may considerably impact estuarine morphology. When combined with high tides and surges, the consequences of sea-bed bathymetry change would be significant. Although these intensive hydrodynamic conditions usually happen over several hours or even days, the estuarine and coastal morphology will still experience significant changes (Roelvink, 2009; Dissanayake, 2014). However, in terms of long term morphological changes, the morphodynamic changes due to extreme wave conditions are not comparable.

2.2.3. Storm surges

The Storm surge is the rise of sea water level due to low pressures developed during storm conditions. Local wind stresses during storms can also generate local wind set-up, which can add to water level rise due to surge. If this extreme meteorologically-induced high water level coincides with high tide and storm waves, it may have devastating consequences on coastal and estuarine morphology. Storm surge impacts are not only linearly related to maximum water level but also rely on more complex

non-linear tide-surge interactions and wind wave field since the wave propagation will affect the surface drag coefficient and radiation stress (Smith and Banke, 1975; Janssen, 1991; Mastenbroek et al., 1993). Thus, with these severe hydrodynamic influences, the landscapes of the coastline can be dramatically changed with effects such as the cliffs notching, coastal dunes erosions, barrier island reacting to wash-over deposits or the bank breaching (Gornitz, et al., 2002; Spencer et al., 2015).

2.2.4. Current

Tide or wave induced currents are the most direct driving forces of sediment transport. The sediment particles are dragged by the near-bed current and after this, the particles will be carried by the flow to other places. The direction and speed that the particles travel with are determined by the current's direction and speed. Normally, the coastal current is divided into two parts.

Tidal-induced currents are important to the long-term estuarine morphology. According to derived forces, tidal-induced currents contain two types of currents: flood and ebb currents. Flood currents are induced by the flooding tide and the ebb currents are induced by ebb tide. Most morphodynamic elements are closely related to both two currents. Although both coexist within the flood and ebb delta, the flood delta is mostly formed by flood current, while the generation of ebb delta is mostly contributed by ebb tidal current. Therefore, according to the relative intensity between flood and ebb currents, estuaries can also be categorised as flood-dominated or ebb-dominated by tidal currents.

When investigating the long-term sediment pathway, the residual tidal current, which is defined as the average tidal current over a time period, such as tidal cycle, plays a significant role in the morphological changes. As aforementioned, the flood and ebb tides are sometimes unequal during the tidal cycle, which means the sediment flood flux and ebb flux are not equal. The net sediment transport can be indicated by the net tidal current. Therefore, by exploring the residual tidal current, one can understand the hydrodynamic trend of the estuary and consequently, enabling further investigation of the morphodynamic responses.

Wave-induced currents are usually generated by the waves that approach the coastline. As the existence of two dimensions at the coastline, two types of currents usually happen, one is longshore currents and the other is cross-shore currents. When a wave reaches a beach or coastline obliquely with breaking process, it releases a burst of energy to generate a longshore current running parallel to the shorelines. For the other direction that is normal to coastline, the undertow is introduced as a longshore homogeneous current flowing offshore near the seabed. Since the wave-induced current is usually much lower than the tidal current, the morphodynamic changes due to wave-induced currents are smaller than that caused by tidal-induced currents, but are more important in the long-term formation of the estuary.

2.2.5. River discharges

River discharge is one of the major driving hydrodynamic forces in some estuaries. In tropical and subtropical areas where rainfall and runoff can be extremely high, the river flow in an estuary can be significantly higher than the tidal prism, thus significantly driving estuary morphology change. However, around the UK and Europe, rivers carry less amount of water when compared to tidal flows generated by significantly large tidal variations. Furthermore, river flows can be highly seasonal: wet winters may lead to higher river flows than those during dry summers.

Other than flow velocities, some rivers that carry a very large proportion of sediment such as Yellow River in China, can also significantly contribute to morphological changes in estuaries. Accumulation of river-born sediment over very long periods of time may alter tidal deltas, infill inter-tidal channels and change the entire course of a river (Ren and Shi, 1986). This is seen with the expansion of delta at Yellow River mouth in recent decades and centuries

2.3. Estuary morphology

Estuarine systems inherently consist of numerous morphodynamic features. Most estuaries primarily consist of intertidal channels and intertidal flats. Some estuaries are characterised by salt marshes located at the fringes of intertidal flats while others

contain prominent sediment spits that interact with the littoral transport regime. Sand or mud banks are found in some estuaries. Therefore, different morphodynamic features will response differently to the hydrodynamics.

2.3.1. Inlet

The inlet is the most important part of the estuary where the most flow movement happens. It is the throat of the estuary, and is the connection point between fresh water and sea water. Due to the narrow width, it is the place where the most significant morphological changes usually happen. The inlet system is associated with extensive tidal flats inside or outside the estuary, thus, the morphological behaviour of an inlet is largely dependent on the tides and waves which are also influenced by the flood and ebb deltas.

Numerous studies have explored the relationship between cross-sectional area of inlet and tidal prism in order to offer a simple alternative to costly and complex physical or numerical models (O'Brien, 1969; Roelvink, 2012). For instance, the tidal direction and asymmetry strongly define the inlet morphology. In terms of wave impact, it will break the equilibrium of tide-driven sediment transport by eroding the ebb delta or driving sediment alongshore to down wave direction.

2.3.2. Channel

Some small shallow channels may also appear on the ebb delta as result of the asymmetrical tide propagation (Sha and Van den Ber, 1993). Channel is usually the deepest place in the estuarine system and the position of channel can be changed in a long-term period. For example, the Deben Estuary's channel has shifted considerably further to the south coastline during the last decades (Burningham and French, 2006). For the channels in a tidal basin, the relationship is also derived simplistically between the tidal prism and the total volume of channels below mean sea level (MSL). Most estuary system channels not only determine the water storage capacity but also affect the tidal and wave propagations which results to strong import of fine sediment or

strong export of fine sediment (Dronkers, 1986; Townend, 2007). Thus, the channel may change the sediment transport patterns under different hydrodynamic conditions.

2.3.3. Flood and ebb delta

The flood and ebb deltas are formed by flood tide and ebb tide separately. It seems that the tidal propagation determines the area and the wave changes the shape of respective deltas (Walton and Adams, 1976). The areas are usually shallow, where the sediment can be very sensitive to flow conditions. Sediment stirring due to wave action mostly occurs in the ebb delta. As a result, there can be an imbalance between sediment export and import from and to the ebb delta even if the tide-drive sediment transport remains the same. The flood and ebb delta also determine the distortion of the estuary tides (Friedrichs and Aubrey, 1988).

2.3.4. Intertidal mud flats

Intertidal mud flats can be defined as coastal wetlands when mud is deposited by tides; this usually occurs in estuaries and other sheltered areas such as bays and lagoons. These shallow-sloped flats mostly consist of silts and clays with organic content and the proportion of sand increases towards mouth of estuaries, where salinity and wave energy are strong. They are mostly dependent on coastal habits, such as soft cliffs and saltmarshes, where a high abundance of species settled for feeding and resting. In large estuaries, intertidal mudflats are often several kilometres wide. This may reduce the risk of eroding saltmarshes and destroying coastal defences significantly because the wave energy is dissipated within large area. Thus, this is a very important place that may affect the estuary system.

2.3.5. Salt marshes

Salt marshes are coastal ecosystems in the upper coastal intertidal zone between land and open salt water that is regularly flooded by tides. It is filled with numerous salt-tolerant plants which are vital to the stability of the salt marshes because they trap and bind sediments. They usually coexist with mudflats on low-energy environment barrier

coasts or in estuaries and embayment. The marshes are usually controlled externally by water elevations and sediment supply regimes (Allen, 2000).

Since the marsh species provide surface for the sediments to adhere to, the sediment within saltmarsh is much easier to deposit upwards. Thus, marshes usually expand upwards under the condition of sea-level movements. Because of the highly porous and permeable sediment, saltmarshes experience minimal tidal inundation. In terms of sediment supply, there are four natural sources: river catchment discharge, retreated coastal cliffs, sedimentary rocks exposed on the nearby sea floor and the hard parts of organisms (Allen, 2000). However, the human interference can also contribute to the total changes on marshes such as land claim, which increases the tidal prism and reduces the tidal damping as result of the tidal mudflats and marshes decreased storage capacity (Allen, 2000).

2.3.6. Estuary morphology change

Morphological changes of estuaries can take place over a range of time and space scales. In terms of time scales, morphology evolution may vary from hours to days (short term), months to few years (medium term), decades to few hundred years (long-term) and several millennia (geological scale). In terms of spatial scales, the smallest morphological phenomena are ripples and dunes formed on the bed, and these are categorised as micro-scale features. Alternating and interacting ebb and flood channels and shoals are categorised as meso-scale elements. Features such as ebb tidal deltas, tidal flats and inlet channel belong to the macro-scale. The entire estuary and the adjacent coastal areas are classified as mega-scale (De Vriend, 1993; Hibma et al., 2003).

When the estuary is taken as a morphodynamic system, short term changes may not be obvious under normal circumstances. However, extreme waves or storm surges can drive significant morphological changes over a very short period of time (Anthony, 2004; Dissanayake, 2014). On the other hand, wave and tidal forces over a long period can drive notable medium to long term morphological changes in the estuary system.

2.4. Overview of estuary modelling methods

To investigate the complex processes involved in morphodynamic change of estuaries, numerous modelling approaches have been used to simulate these morphological changes.

2.4.1. Data analysis

Data analysis, which is based on large historical datasets, is used to compare topographical changes at different periods and then find morphological trends. This is known as Historical Trend Analysis (HTA). This method has also been extended to develop top-down conceptual models for the use of predicting future changes. In some applications, the hydrodynamic data has been used to set up correlation between hydrodynamics and morphodynamics (van der Wal, 2002; Thomas, 2002; Burningham and French, 2006, Blott et al., 2006).

Although this method is more accurate as it is based on real historical datasets, its reliability depends on the availability and quality of the datasets. If long term data is available, methods such as Expert Geomorphological Analysis (EGA) can also be used to explore the long-term future morphological changes (DEFRA, 2008). This method involves setting up a conceptual model based on the site data and will vary according to the specific purpose of the model.

In estuaries which have large amount of historical data, data reduction can be applied for the analysis of long-term morphology change (de Vriend et al., 1993). Several methods have been previously used include: statistical analysis, empirical orthogonal functions and contour analysis. However, almost all data analysis methods are site-specific.

2.4.2. Computational models

Computational modelling of morphological change of estuaries generally follows two approaches. The first is the use of geological and geomorphological evolution models, designed to simulate morphological evolution over very long periods of time. They are defined as top-down models (Di Silvio, 1989; Stive et al., 1998; Dennis et al., 2000). Most of these models are based on empirical rules or expert analysis, and the use of long-term morphology data. They are sometimes also known as behaviour-oriented models. The majority of these models are designed to predict an estuary's long-term physical response to natural changes, such as the morphological changes due to sea level rise and human interference.

On the other hand, two- or three-dimensional hydrodynamic models combined with sediment transport and morphodynamic modules are used to simulate short term morphological change (de Vriend and Ribberink, 1996; Friedrichs and Aubrey, 1996; Dronkers, 1998). These models are known as bottom-up models and give detailed information of physical processes. In recent years, estuary morphology models that combine aspects of both top-down models and bottom-up models have been developed in order to simulate medium term morphology change of estuaries (Stive et al., 1998; Karunarathna et al. 2009, 2016). These models are sometimes known as hybrid models or reduced physics models.

2.4.2.1.Bottom up models

These modelling approaches have a good logical consequence of causes, processes, behaviours. They are therefore also known as 'process-based' models that have a significant physical robustness represented by partial different equations mathematically. In terms of solving the hydrodynamics and morphodynamics in the coastal area models, two physical approaches can be used: Lagrangian models and Eulerian models. The Lagrangian models treat the water or sediment as discrete particles which can be tracked numerically. The Eulerian models treat the water as a continuum by satisfied the conservation law and treat the sediment in suspension as a concentration with a continuum aspect (Amoudry and Souza, 2011). The latter models

are widely used in the coastal and estuarine modelling while the Lagrangian models require expensive computations even in small spatial scale such as bottom boundary layer processes.

The Eulerian models are extensively used in the coastal areas which are usually based on the shallow water equations. The hydrodynamics elements such as flow velocities are solved by the continuity and momentum equations while the sediment transports are explained by the advection-diffusion equations. Even though these models are mostly based on similar equations, the solutions are various due to different discretization schemes and numerical methods associated with different inclusions of sub models such as turbulence models. Some models are based on the Finite Difference (FD) numerical methods such as Regional Ocean Model System (ROMS) model (Warner et al., 2008) and Estuarine Coastal Ocean Model with Sediment Transport (ECOMSED) model (Blumberg, 2002) while other may use the Finite Element (FE) and Finite Volume (FV) methods such as Finite Volume Coastal Ocean Model (FVCOM) model (Chen et al., 2003a), TELEMAC finite element model (Villaret, 2004) and MIKE 21 (DHI, 2009).

In FD method, the explicit difference method and implicit difference method are usually used. The former method is more efficient but is numerically stable and convergent under certain conditions. This means the time step or space step should be selected carefully. The latter method may require more computation time but it is numerically stable and convergent. But in terms of accuracy, some model may terminate the implicit calculation by considering the accuracy of the model.

For the FE and FV models, which are more conservative, they may not be as efficient as FD method. But the flexibility of the discretization enables the models to be used in more complicated geometry areas. Both methods can increase the local accuracy by refining the mesh of interested area. But the FE method would be able to increase the order of the elements by approximating the variables with higher polynomials while the functions that approximate the solution by using FV method cannot be easily made of higher order. The number of examples that use these two methods is increased. The Finite Volume Coastal Ocean Model (FVCOM) is recently used to investigate the

coastal area associated with complex coastal geometry and steep bottom slope (Chen, et al., 2003; Chen, et al., 2007). It can reproduce the tide correctly in the coastal ocean. However, in terms of sediment transport, even though the suspended sediment can be solved by advection-diffusion transport equation the same as others, the selection of bedload sediment transport formulae is limited. This model is much more suitable for the investigation on the salinity, heat and buoyancy of estuaries. It is not efficient to solve the non-cohesive sediment transport issues.

The TELECMAC finite element model is also used to investigate the hydrodynamics and morphodynamics of the coastal area (Galland, J.C., 1991). This 3D and 2D hydrodynamic module can be coupled to the 2D sediment transport and morphodynamic model (SISYPHE) (Villaret, C., 2004). The bedload is calculated by using classical sediment transport formulae and the suspended load is solved by suspended sediment concentration. MIKE 21 (DHI, 2009) is also an example of finite volume model to solve the depth-average Saint-Venant equations. It contains the mud transport module and sand transport module. Therefore, the ability to deal with sediment multi-fractions is not strong enough.

When considering the sediment transport associated with water movement, one numerical scheme may be used to solve the water equation and another scheme is used to solve the transport equation. For example, in Delft 3D model (Lesser, et al., 2004), the hydrodynamic solver is the finite difference method, but the transport equations are solved by a finite volume approach, which ensures mass conservation (Delft 3D User Manual, 2014).

In these models, a 2D or 3D flow model and a suitable wave model are usually coupled to determine the flow field resulting from tidal variations, river discharge and wave propagation. Hydrodynamics are then combined with a sediment transport model and a morphological bed updating model to determine morphological change. The flow model is usually based on the shallow water equations solved by certain numerical methods (FD, FE or FV methods) with different numerical scheme implementations. For example, the Alternative Direction Implicit (ADI) method was used in the Delft 3D. It splits the time step into two stages. Each stage consists of half a time step. In

both stages, all the terms of the model equations are solved in a consistent way with at least second order accuracy in space (Delft 3D Flow User Manual, 2014).

Most wave models are based on action balance equations with the assumption of hydrostatic conditions. The wave models are designed to simulate the evolution of waves which described by the energy transfer equation (Willebrand, 1975) in which the various physical processes are represented by a source term that relating to the spectral evolution (Komen, 1984). The most used wave model in recent is the third-generation wave model SWAN model (Booij et al., 1999) with a high frequent usage of JONSWAP spectrum as the source spectrum term. In the solution on action density, because the fact that the phase information of the individual waves is not retained, this modelling approach allows for relatively large spatial computational steps and as such is suitable to compute the wave conditions in a large domain.

In terms of the morphodynamic models, they are based on the sediment exchange between the bed and suspended load. The updated morphology is usually derived from suspended sediment transport and bedload transport. The suspended sediment transport is based on the advection-diffusion equations in which the sediment concentration is treated as a conservative constituent or tracer and they were solved by the numerical schemes. For the bedload transport, the empirical equations are introduced such as formulae of Meyer-Peter-Muller (1948), Engelund and Hansen (1967), Bijker (1971), Van Rijn (1993), Soulsby (1997) and so on. However, all these bedload formulae are either based on the field or laboratory data, which contains limitations.

Some numerical models that are used for simulation of estuary change, input conditions are usually reduced as using representative tides or waves instead of the realistic input conditions. One way of tidal schematization is to multiply the bed evolution due to a single tidal cycle by a factor so that the yearly bed evolution was reproduced. For the wave input filter, two approaches can be used: multiple and single representative wave approach. Following these approaches, computational efficiency and cost can be significantly reduced at the expense of some reduction in the accuracy of the results.

However, these models have various limitations when applied to timescales longer than a few months as result of inadequate physical process descriptions, uncertainties in initial and boundary conditions and excessive computational intensity. Therefore, the optimization between efficiency, accuracy and capability is essential for selecting the best model to achieve the objectives.

2.4.2.2.Top down models

Top down models are simple forms of models which capture estuary behaviour. By exploring the system behaviour using historical estuary morphological change data, a conceptual model can be generated with certain empirical theories. These models then can be used to predict how these systems behave in the future. So, the accuracy of this method depends to some extent on the available historical data. These models are mostly suitable for simulating long-term and larger-scale morphological change; they are usually used for forms of analysis such as historical trends analysis and expert geomorphological analysis.

Karunarathna and Reeve (2008) and Reeve and Karunarathna (2009) developed a top down estuary morphology model by using Boolean Network approach to investigate the long-term morphodynamic response of estuarine systems to sea level rise and human interference. In this model, the variables' morphodynamic response to a given change can be deduced from its corresponding Boolean function, which describes the feedbacks between the particular variable and the others in the network. This approach provides qualitative insights into the behaviour of estuarine systems without knowing the quantitative linkages between the various components of the system.

By defining the morphological equilibrium state of coastal inlets and tidal basins as a function of hydrodynamic conditions such as tidal range and tidal prism, Van Goor et al. (2001) developed a model based on the systems methods (Aggregated Scale Morphological Interaction between a Tidal basin and the Adjacent coast [ASMITA]). For the estuary modelling, the ASMITA characterised the morphological elements such as channel and tidal flat, and their interactions by using mathematical expressions to derive equilibrium volumes and areas based on a schematised representation of an

estuary system (Stive, et al., 1998; Huthnance, et al., 2008). As a linear relationship between tidal prism and equilibrium volumes and areas for these elements is assumed, the changes of tidal prism due to accretion or reclamation will alter the equilibrium volumes and areas and cause the sediment exchange towards a new equilibrium. But this model focuses on the inlet system interacting with adjacent beaches so that it only can be used in some specific estuaries which contain inlets and deltas. For the embayment and funnel-shaped estuary, since the characteristic process is not easily got and the exchange of sediment between adjacent beaches is limited, this model is not suitable.

Niedorora et al. (2001) developed a Coastal Systems Tract (CST) model, which is based on the concept of coastal tracts expresses first-order relationship between sediment sharing components of coastal systems, to simulate the large-scale morphodynamics of complex coastal systems.

2.4.2.3.Hybrid models

As the name implies, hybrid models combine some aspects of top-down models and bottom up models. Hybrid approaches combine the explanatory power and physical robustness of bottom up models with the conceptual insights into whole system behaviour afforded by a top down model. Usually, it is suggested to use an insight into long-term behaviour (from top down models) to provide a conceptual framework for the prediction from bottom up models.

Karunarathna et al (2008) divided the estuary morphological evolution into diffusive and non-diffusive processes in which the non-diffusive was contributed by a source function incorporating into the governing equation. This source function is derived by solving an inverse problem using long term historic survey data of the estuary. The key concept of the inverse method is the use of available data to determine unknown parameters or functions in the governing equation. If the source function derived from historical data can capture the trends at longer term scales, then it could be used to predict the estuary's morphology.

In summary, all these three types of models can be used for investigating the estuarine morphology. However, the selection of models not only depends on the available datasets but is also related to the requirements of time and space scale, estuarine activities and budget of the project. Thus, it should take careful consideration when using numerical model to investigate specific estuaries.

2.5. Climate change impacts on estuaries

It has been well-documented and observed that numerous changes to land and ocean based on natural processes have taken place as a result of global climate change. Sea Level Rise (SLR) increased storminess and storm intensity, and altered river flows due to changes on precipitation patterns are the most important climate change results that affect estuarine processes.

Sea Level Rise (SLR)

It is well reported that the SLR due to global warming has taken place over the last one hundred years. The Intergovernmental Panel for Climate Change (IPCC) assessment reported that the average rate of sea level rise was about 1.8±0.5mm/yr during the period 1961 to 2003 and was 1.7±0.5mm/yr during the 20th century (Houghton, 2001). Also, there has been evidence that the wave climate, storm climate in particular, around the world is also changing as a result of global climate change.

In the coastal area, the wave propagation is closely influenced by the water depth variations. If SLR occurs in the future, the increased water depth will change the wave climate, the impact to some extreme conditions will be significant. Chini et al. (2009) found that climate change has led to a significant increase of extreme wave heights on the East Anglia coast (UK); they found the increased Mean Sea Level (MSL) would alter the extreme wave height and the frequency of occurrence of extreme wave conditions. Brown et al. (2008) investigated the future extreme coastal flooding due to climate change in eastern Irish Sea (UK) and found that the SLR has greater potential to increase peak surge levels, which means there is a greater potential of flood risk.

Future climate change does not only affect the hydrodynamic conditions, such as the significant increase of the tidal prism for the estuaries; it can also enforce different wave conditions resulting in different morphodynamic responses. Therefore, since there are many investigations on the coastal processes by using the top down and hybrid models, the hydrodynamic responses to climate change and its relation to the morphodynamics are still not investigated. The lack of explanations on physical processes from top down and hybrid models should be solved by introducing the bottom up models in the climate change issues. This study is going to investigate a way to use bottom up (process-based) models to investigate the estuarine hydrodynamics and morphodynamics responses to climate change.

Chapter 3: The introduction of study site: Deben Estuary

3.1. General description

To investigate climate change impacts on estuary morphodynamic change, the Deben Estuary is studied. The Deben Estuary, which is located on the east coast of the United Kingdom (UK), is one of the most morphodynamically active estuaries in the UK. The estuary is an integral part of the Suffolk coastline and contributes to the hydrodynamics and morphodynamics of the Suffolk coastal system (Figure 2.1). The Deben Estuary is categorised as a tide-dominated spit-enclosed estuary by DEFRA/EA estuary classification (DEFRA, 2008). However, the mouth of the estuary is subjected to significant wave activities and a complex littoral sediment transport regime. The estuary has undergone significant morphodynamic changes in the recent decades (Burningham and French, 2006) and provides a challenging case study site to investigate climate change impacts on estuary morphology change. The characteristics of the estuary and its dynamism make it a perfect study site to investigate long term climate change impacts on estuary morphodynamics.

3.1.1. River Deben

The source of River Deben is approximately 3 km to the north of the village of Debenham, 17km north-west of Woodbridge (Figure 3.1). The meandering river between Debenham and Woodbridge is non-tidal (around 34km) and it is not considered in this study.

The tidal river (estuary) starts from Bromeswell to the mouth of the river. The upper estuary, which starts from Bromeswell to Martlesham Creek, runs in a south-westerly direction for approximately 3.5 kilometres widening the river significantly (not shown in Figure 3.1). The river makes small gentle meanders between relatively narrow mudflats and fringing saltmarsh in this distance. Then, from Martlesham Creek down to Ramsholt, the main low water channel tends to meander within the limits of the wide inter tidal area (Figure 3.1). From Ramsholt south-eastwards to its mouth, the river follows a meandering path over this length, gradually becoming wider towards to the coast. Before entering the sea, the river mouth narrows significantly due to the

constriction between the ridge of higher land at east bank Bawdsey and the low ridge of shingle and clay at west bank Felixstowe Ferry (Posford Duvivier , 1999).

The narrowest cross section of the inlet channel is 180m wide (Burningham and French, 2006), which reduces the impact of waves on the inner estuary's morphology. In further offshore areas, interaction between tidal estuary processes and open coast wave and littoral processes has led to the development of a series of shifting shingle shoals at the mouth of estuary known as 'The Knolls' (Figure 3.4).

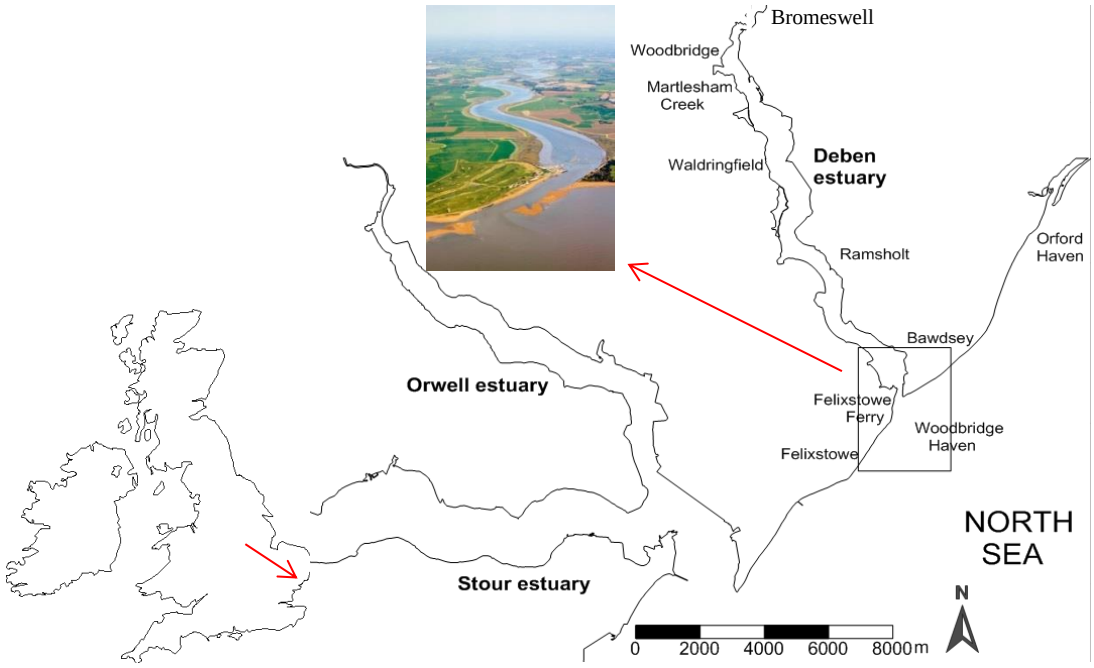

(a) (b)

Figure 3.1 – Deben Estuary. a): the position of the Deben Estuary in UK; b): the detailed Deben river area with the interested place in the rectangular.

3.1.2. Geological and anthropogenic context

The south-west Suffolk coast is formed by the Plio-Pleistocene sands and clays, as seen with the Coralline and Red Crags (Funnell, 1996; Kendall and Clegg, 2000). The London Clay is thought to be underneath the softer clays in the catchment area of the Deben River (Brew, 1990). The Deben Valley used to be merged at the time of Holocene with the Stour and Orwell to the southeast of Felixstowe (Figure 3.1). When the water level rose, the river then has been formed due to the higher terrain of

Felixstowe and Bawdsey nearby. Within the middle and upper reaches of the estuary, the bottom sediment is predominantly muddy with some accumulation of shelly sand and gravel from the outcrop of the Coralline and Red Crag (Posford Duvivier , 1999).

Presently, the offshore seabed contains a mixture of mud, fine sand and broken shell. The outcrops of London Clay and sub-marine river channels are buried and filled with fine materials, which influence the offshore bathymetry. A sandbank has been formed with shell materials likely derived from Red Crag deposits (HR Wallingford, 2002).

3.1.3. Human interference

During the 19th century, more than 2000 ha of high intertidal mudflat and saltmarsh were reclaimed (Beardall et al., 1991). In the upper and middle areas of the estuary, numerous flood banks were built to protect nearby areas from tidal inundation. It has been suggested that many of old defences should be repaired and aligned with the flood defence management strategy (Posford Duvivier, 1999). The river frontage in Woodbridge, at the head of estuary, is almost entirely devoted to boating activities; there are thousands of swinging moorings on the river and sailing clubs and boatyards are spread along the Deben river.

At the mouth of the river, some coastal defences have been built up before the Felixstowe Ferry in order to protect from frequent flooding. However, these defences need urgent repairs due to the destruction from flood and wave attacks. Also, there are some groynes that spread along the updrift Bawdsey beaches and downdrift Felixstowe beaches to protect adjacent eroding coastlines.

3.2. Physical characteristics

A large amount of historic hydrodynamic data on the Deben Estuary is available. Some explanations on river flow, tides and waves of River Deben have also been reported (Posford Duvivier, 1999; Hydrographic Office, 2002; HR Wallingford, 2002; Burningham and French, 2006).

3.2.1. River flow

Compared to the tide discharges, the river flow in Deben is found to be small. Mean river flow is only around 0.6m^3/sec and the highest flows are in the range of 12m^3/sec, which is still far lower than tidal flow of the mouth: approximately 1700m^3/sec (Posford Duvivier, 1999). Therefore, the river flow's contribution to the morphological changes is negligible when compared to the tidal flow's contribution.

3.2.2. Tides

The mean spring and neap ranges are 3.2m and 1.9m respectively at Woodbridge Haven while the tide ranges have been increasing by 0.3m to 0.4m beyond Woodbridge 12km up from the estuary (Hydrographic Office, 2002). As for the estuary, the tidal length is about 18km and the mean spring tidal prism is approximately $17\times10^3m^3$ while the peak spring tidal discharges through the narrow inlet exceed 2000m^3/s.

Tide volume

At the end of 20th century, the volume of water moving into and out of the estuary during each tide has been estimated to be 8.95 million cubic meters. The tidal volume will increase in the future due to the SLR. It is predicted that, impacted solely by the sea level rise of 0.5m, the intertidal area of the estuary would result in an increase tidal volume from 8.95 million cubic meters to 11.77 million cubic meters in fifty-year's time. The worst SLR scenario would increase the present volume by 298%, reaching 26.6 million cubic meters if defences are removed (Posford Duvivier, 1999). Therefore, the tide volume is very sensitive to the sea level rise.

3.2.3. Wave

The average offshore wave height along the Suffolk coastline around the Deben Estuary is approximately 0.96m with the two main approach directions: one is from the northeast and the other is from southwest with the percentage of 50% and 32% respectively (HR Wallingford, 2002). However due to reduction of the sea waves that propagate through the narrow estuary inlet, the inner estuary only experiences locally

generated fetch-limited wind waves (Burningham and French, 2006). Although strong tidal stream controls the alignment of a series of offshore sandbanks, the large scale of littoral drift patterns was mostly implicated by the northeaster waves and some southwest extreme wave conditions. Both wave directions should contribute the morphodynamics of the estuary historically (HR Wallingford, 2002).

However, for changes on future wave conditions due to wave climate change, the simulated data from a global wave simulation indicated that the extreme wave condition at the offshore boundary will increase slightly in the future while the average wave climate will not change much by the end of this century (see the detailed discussions in Chapter 6). The significant wave height (H_s) at 'West Gabbard' wave rider, which is approximately 60km northeast from Deben Estuary, will increase by 0.4m in terms of one in one hundred-year return period H_s event at the end of this century. This will be discussed in detail in Chapter 6.

3.2.4. Extreme water levels

Extreme water levels occur as a result of superposition of high tide with sea surge during storm conditions (the sum of high tide level and surge). One of the extrapolated results from a scant one-year data set gives the value of the one in one hundred-year level as being 3.1m OD (above Ordnance Datum, generated by surge conditions) at Woodbridge Haven (Posford Duvivier, 1999). The results are listed in Table 3.1.

Table 3.1-- Best Estimate of extreme water levels with Various Return Period (years) (Posford Duvivier, 1999)

	Water level (m OD)			
	MHWS	Return Period (years)		
		1	10	100
Woodbridge		2.7	3.15	3.62
Waldringfield		2.6	3.03	3.47
Ramsholt		2.4	2.8	3.32
Woodbridge Haven	1.77	2.55	2.95	3.35

However, in terms of long-term morphological change, there is no evidence of a direct dependency between inlet behaviours and storm occurrence, although the North Sea storm surge of 1953 is reported to have caused considerable flooding within the Deben Estuary and onshore sediment transport in the vicinity of inlet (Guthrie and Cottle, 2002). Calm weather can recover these changes over a long time-scale.

3.2.5. Wind

It has been found that two-thirds of winds approach from the direction between 135^{o} and 315^{o} (nautical), of which the north to north-easterly wind climate is linked to the total ebb-tidal delta volume (Burningham and French, 2004). An increase in the frequency of easterlies has been reported between 1973 and 1997; before the mid of 1970s, the frequency of gale force winds has been increased at Essex which is 65 km to the south (van der Wal and Pye, 2004).

3.3. Relative Sea Level Rise (RSLR)

Mean Sea Level (MSL) has been rising for hundreds of centuries (Louters and Gerritsen, 1994). During the last Ice Age, around 10,000 years ago, most of the North Sea was dry; as the North European ice-cap thawed the MSL has risen dramatically as a result of the warmer climate. The MSL has been increasing gradually during the last few thousand years, although the rate is decreasing. The MSL increased at a moderate rate during the 20th century: the rate in the second half of the 20th century was greater than that of the first half, although it is not significant. In terms of the North Sea, the change rate of the Newlyn (1.46±0.30mm/yr) was lower than the global mean rate of sea level rise (1.74±0.16mm/yr) in the 20th century (Holgate, 2007).

Recent studies by IPCC (Intergovernmental Panel of Climate Change) predict that global warming will accelerate the mean sea level rise as a result of increased emission of greenhouse gases (i.e. CO_2, CH_4 and NO_2) (IPCC, 2001). The estimated eustatic sea level rise in the next century ranges between 20cm to 90cm (Figure 3.2).

The highest global-mean scenario is a 0.88 m rise from 1990 to 2100 (Church et al., 2001). In the Great Britain, by considering the land subsidence, which uplifts for land in northwest and subsides land for southeast (Shennan and Woodworth, 1992), the

relative sea level rise may be able to reach one metre in the southern Britain by assuming that a global rate rises in the twentieth century based on the highest global-mean scenarios (Church et al., 2001; Vega-Leinert and Nicholls, 2008). However, SLR research does contain large uncertainties.

For the eastern coast of England, the SLR at the end of the 21st century is estimated to be 22cm with the lowest emission scenario and by 82cm with the high emission scenario according to UKCP09 (Jenkins, et al., 2008).

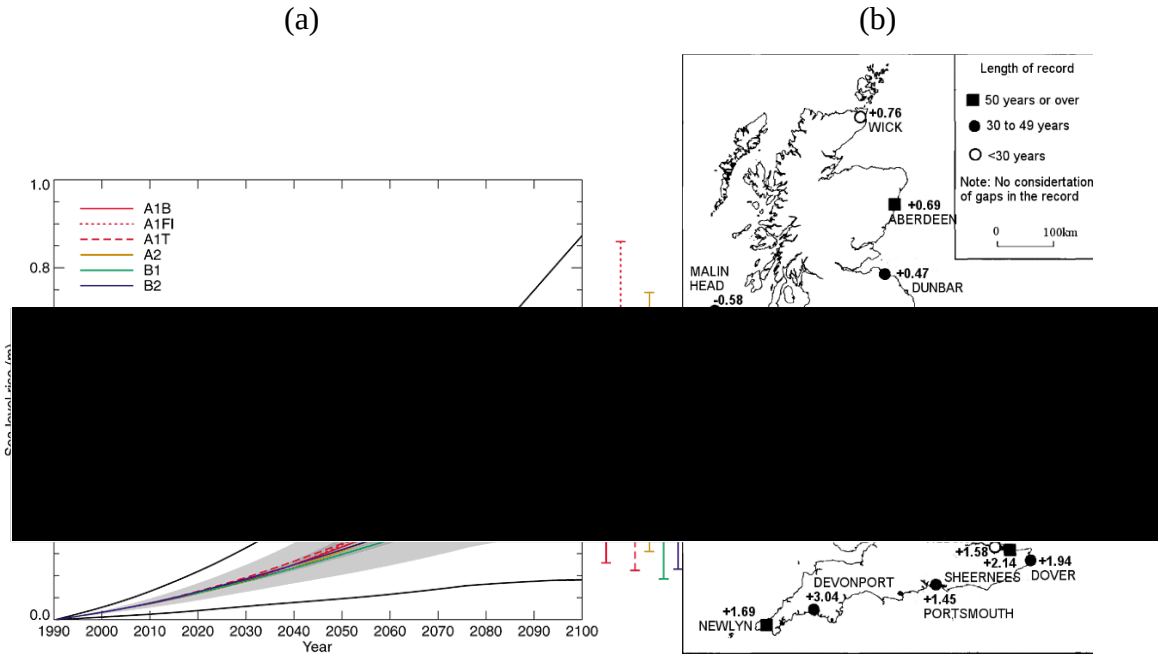

Figure 3.2 – Predicted global average eustatic sea level rise from 1990 to 2100 (a) and relative trends in mean sea level for Great Britain during the twentieth century (b). (IPCC, 2001; Vega-Leinert and Nicholls, 2008).

3.4. Sedimentology

The sediment distribution is mixed at the mouth of the Deben Estuary. Sandy gravel (D_{50}=5.5mm; 25% sand, 75% gravel by weight) is found throughout the ebb-tidal delta and adjacent coastal beaches of the Deben, whilst gravel-sized material floors the channels (D_{50}=-5.4φ, 42.4mm). The flood-tidal delta 'Horse Sand' (Figure 3.3) is largely composed of shelly medium sand (D_{50}=1.3φ, 0.4mm). Ebb delta sediments are frequently sorted, which often appear as significant patches of 'pure' gravel or sand,

Exploratory trenches (to depths of 0.5-1m) showed coarser (D_{50}=6.7mm) fractions dominated the upper foreshore and supratidal crests (to depths of 20-40cm), while sand (D_{50}=1mm) fractions often occur as thin surfaces on the mid-foreshore. At the depth greater than 0.5m below the surface, and throughout most of the lower foreshore, the dominant well-mixed and bimodal character was consistent: pure sand was found only as discrete, thin surficial patches (Burningham and French, 2006).

Sedimentologically, the ebb-tidal delta can be defined as mixed sand-gravel due to the strongly bimodal medium sand and gravel composition. The coarse-grained feature of the system is thought to exert an important control on the ebb delta volume and transport capabilities of waves and tidal currents, resulting in a smaller coarse ebb-tidal delta that moves slower than would be predicted by previously published models (Hume and Herdendorf, 1992; Hick and Hume, 1996).

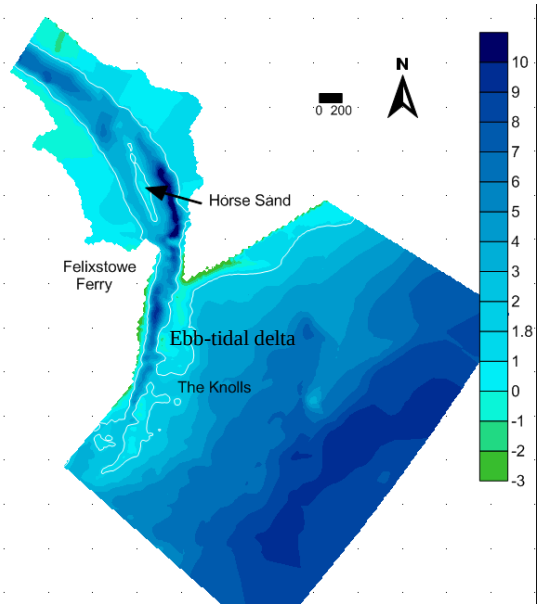

Figure 3.3 – The interpolated bathymetry at Deben river mouth (depth in meters in the year of 2002) of digitised Trinity House surveys and UKHO chart data, supported by information from aerial photography, maps and lidar data.

3.5. Morphology

Burningham and French (2006) provide historic bathymetry maps of the Deben Estuary over a period of 180 years from 1819 to 2003 (refer to section 3.6.3). These

maps indicated that the morphodynamic elements have experienced significant historic variation.

3.5.1. The channel

The historical bathymetries show that the ebb channel position has varied significantly during the measurement period. However, when a standardized 15-20yr time-scale is used (based on the frequency of pre-1950 surveys), variability is much reduced: ebb-jet orientation shift angle has been reduced from 120^{o} to 90^{o}. This was considered to be the characteristic time scale for the natural ebb-tidal delta dynamics (Burningham and French, 2006). From the 1990s the ebb-jet variability has widened largely to the south extension area, following progressive recession of the downdrift shoreline.

3.5.2. The Knolls

The Knolls, shown in Figure 3.3, play an important role in the estuary's behaviour. They provide shelter for the estuary mouth by absorbing wave energy approaching the coast. The direct benefit of this shelter is the protection provided along the Felixstowe Ferry frontage. The Knolls at the mouth of the estuary not only limit available sediment supply but also influence the pattern of sediment drift along the shore to the south (Wallingfor HR, 2002). However, due to the repetition of flooding and the frequently changing position of the Knolls, modern flood and coastal defences at Felixstowe Ferry have been constructed since the 1953 flood, to protect the area from future flooding during storms. As a result, the alignment of the frontage is now fixed to prevent erosion or flooding of valuable assets on the coastal flood plain behind the beach.

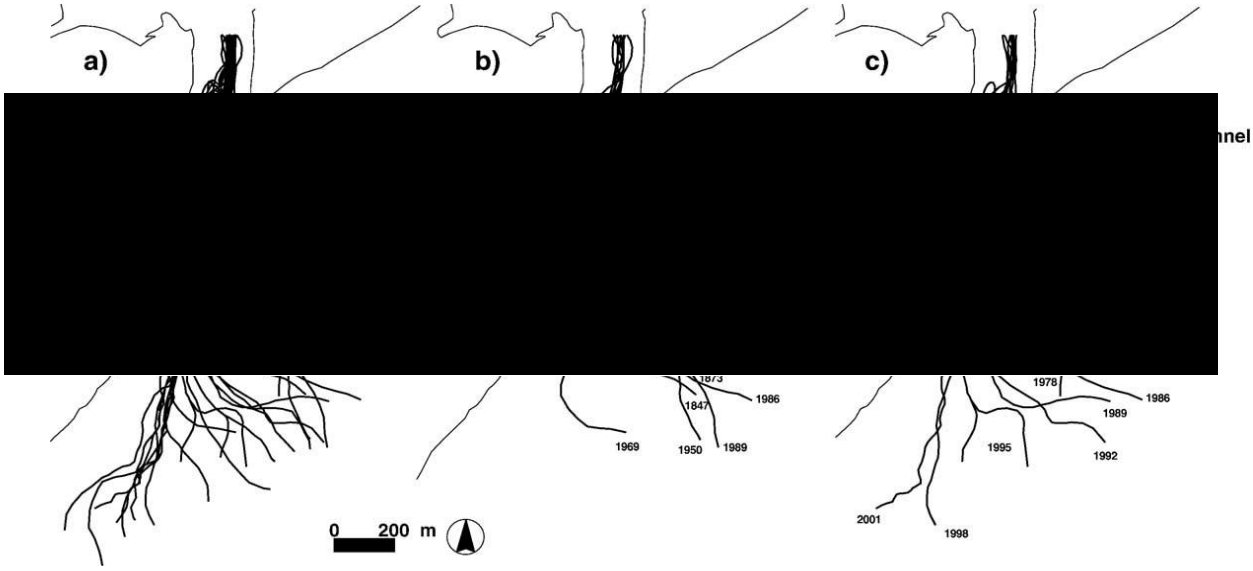

Figure 3.4 – Channel variability within the ebb delta region (source: Burningham and French, 2006)

Nevertheless, since the channels change positions frequently (Figure 3.4), it has been recognized that the protected coastal defences at Felixstowe Ferry will face more difficulties when new channels open up through the Knolls, which has been considered by the Environment Agency (Posford Duvivier, 1999).

3.5.3. The nearshore and ebb delta shoals

The predominant long sediment transport around the estuary is to the south of Orford Ness spit where the coarse sediment is sinking (HR Wallingford, 2002). Different drift rates and directions have happened in the areas south of the Deben Estuary.

It has been found that the shoreline recession and steepening of the nearshore zone happened both at the north and south of the inlet (Burningham and French, 2006). Between 1819 to 2003, the inlet deepened by up to 2m (Taylor et al., 2004) while the ebb-tidal delta volume has increased in the last 30 years. In terms of longshore sediment transport, the accretion that occurred in updrift component and erosion in downdrift component of the delta implied that the longshore sediment transported from north of the inlet to the south of the inlet with the rate of approximately $30\text{-}40\times10^3$ m^3/yr. Due to the characteristic of mixed gravel and sand, the sediment bypassing processes are less efficacious than in other inlets presented by Gaudiano and Kana

(2001), which makes the inlet maintain a dynamic equilibrium with a longer cycle interval (Burningham and French, 2006).

3.5.4. Throat and inner estuary

Historically, the throat position of the inlet has remained stable. Although the wave propagation through the inlet is negligible, the tidal impact is of importance on the inner estuary. A landward flood-tidal delta (Horse Sand) divides the inner channel into flood dominant channel (northeast of Horse Sand) and ebb dominant channel (southwest of Horse Sand). This intertidal delta, which is composed of shelly medium sand (D_{50}=0.4mm), has been found to be stable as a result of decreased tidal velocities in this area (Figure 3.3).

3.6. Available measured data at and around Deben Estuary

Since Deben is a very dynamic estuary which has been determined by complicated hydrodynamics, the hydrodynamic data is very important when considering estuarine morphodynamic evolution. The estuary has a significant amount of historic hydrodynamic and bathymetry measurements carried out over a period longer than a century.

3.6.1. Tide

There are two available tidal gauges operating in this area: Felixstowe and Bawdsey (this will be discussed in detail in Chapter 4). Felixstowe Tidal Gauge is located about 4.5km south of the Deben inlet at the seaward end of Felixstowe Pier (51^{o}57’24.3”N, 01^{o}20’54.2”E). This is one of the tide gauges that are operated by the British Oceanographic Data Centre (BODC) with the observational periods of 1982, 1984, 1986-1988 and 1990-2011. So, this site has a large amount of data available for the research. The data that are collected from BODC refer to Admiralty Chart Datum (ACD) which has the following relationship between Ordnance Datumn Newlyn (ODN): ACD=ODN-1.95m (based on the local low astronomic tide levels). In this study, all the data refer to ODN with 15-minute interval from 1993 to 2011. The tide

range at this site is between 3m to 4m at spring tides and around 2.3m at neap tides with the average tide range approximately 2.5m (Figure 3.5).

Bawdsey IHO tidal station, which is another available tide data resource, is located about 500 meters away from the coastline of Bawdsey and approximately 3.5km northeast from the Deben inlet (52º00'0.32"N, 01º25'58.8"E). Water level measurements at this site are available from the International Hydrographic Organization (IHO) Tidal Constituent Bank. The water depth of this tidal station is around 4.5m with tidal range varying between 1.4m to 3.8m.

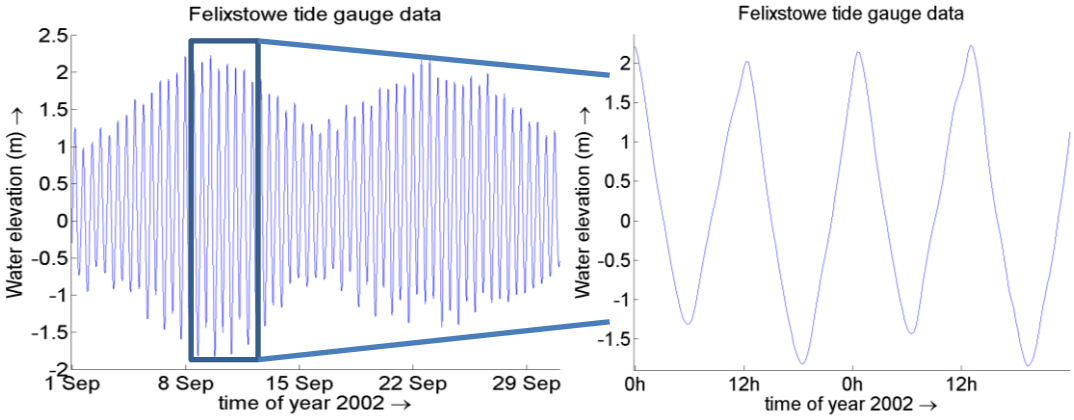

Figure 3.5 – The data sample of Felixstowe tide gauge

3.6.2. Wave

According to the Centre for Environment, Fisheries and Aquaculture Science (Cefas), there are several wave measurements that are either currently or historically available. One is from offshore wave rider at 'West Gabbard WaveNet Site' (WG) and the other is onshore wave rider 'Felixstowe Waverider' (FW) which is much closer to the shore line.

West Gabbard Wave Net wave buoy is located at (51º58'46.8"N, 01º26'47.4"E). The wave data at WG are available from 28th of August 2002 until to date. WG is located approximately 60 km northeast from the Deben inlet at a water depth of around 34m. Wave measurements have been taken at 2 hourly intervals.

Long term wave measurement analysis at this site reveals that the averaged significant wave height at this site is around 1.5m with the predominant wave direction from the

northeast (Figure 3.6). The largest wave height occurred on the 27th of October during 2002 to 2003, which was about 4.89m and approached from south southwest direction, as demonstrated by the red arrow in Figure 3.6 (nautical 214°).

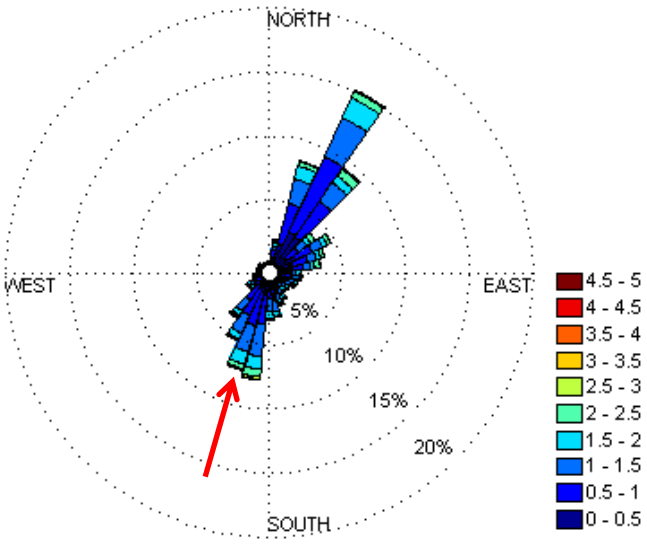

Figure 3.6 – Wave rose at West Gabbard wave rider based on 1-year data samples (data from September of 2002 to September of 2003 in Cefas) and maximum wave directions (red arrow).

Felixstowe Wave rider buoy is around 6km southeast from Deben inlet at the depth of 8m (51°56'18"N, 01°23'37.8"E). Wave data from FW wave rider is available from September 2012 to date. The mean significant wave height at this site for the period of measurements is found to be 0.6m and the predominant wave direction was from east northeast (see Figure 3.7). The maximum significant wave height which occurred in the year 2012 is 1.7m with an approach direction of 79° (nautical).

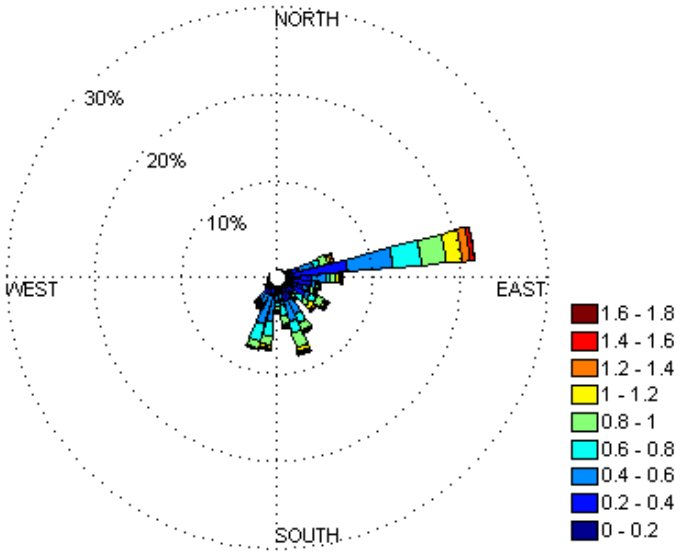

Figure 3.7 – Wave rose of FW site based on 1-year wave data of 2012 (data from Cefas).

In addition to the above wave measurements, hindcast wave data are available closer to Felixstowe wave gauge at (51°53'1.68"N, 01°26'18.96"E) (FW_H). This wave hindcast data is derived from the WaveWatch III 8km dataset hosted by CEFAS on behalf of the Environment Agency[1]. This data covers 1980 to 2012, however it accuracy is unverified.

3.6.3. Bathymetry

There is abundant historical bathymetry data available due to the long navigation history here. These detailed bathymetries from 1991 to 2013 are derived through interpolation of digitised Trinity House surveys and UKHO chart data, supported by information from aerial photography, maps and Lidar data file format (Burningham and French, 2006). These bathymetries are combined with the bathymetry outside the local Deben area provided by Admiral Chart to generate a series of available regional bathymetry maps (Figure 3.8). It is acceptable to use these bathymetries in this study since they cover the most morphodynamically active estuary mouths, including ebb delta and the surrounding coastline. The inner estuary is fairly stable.

[1] WaveWatch III dataset: http://polar.ncep.noaa.gov/waves/wavewatch/

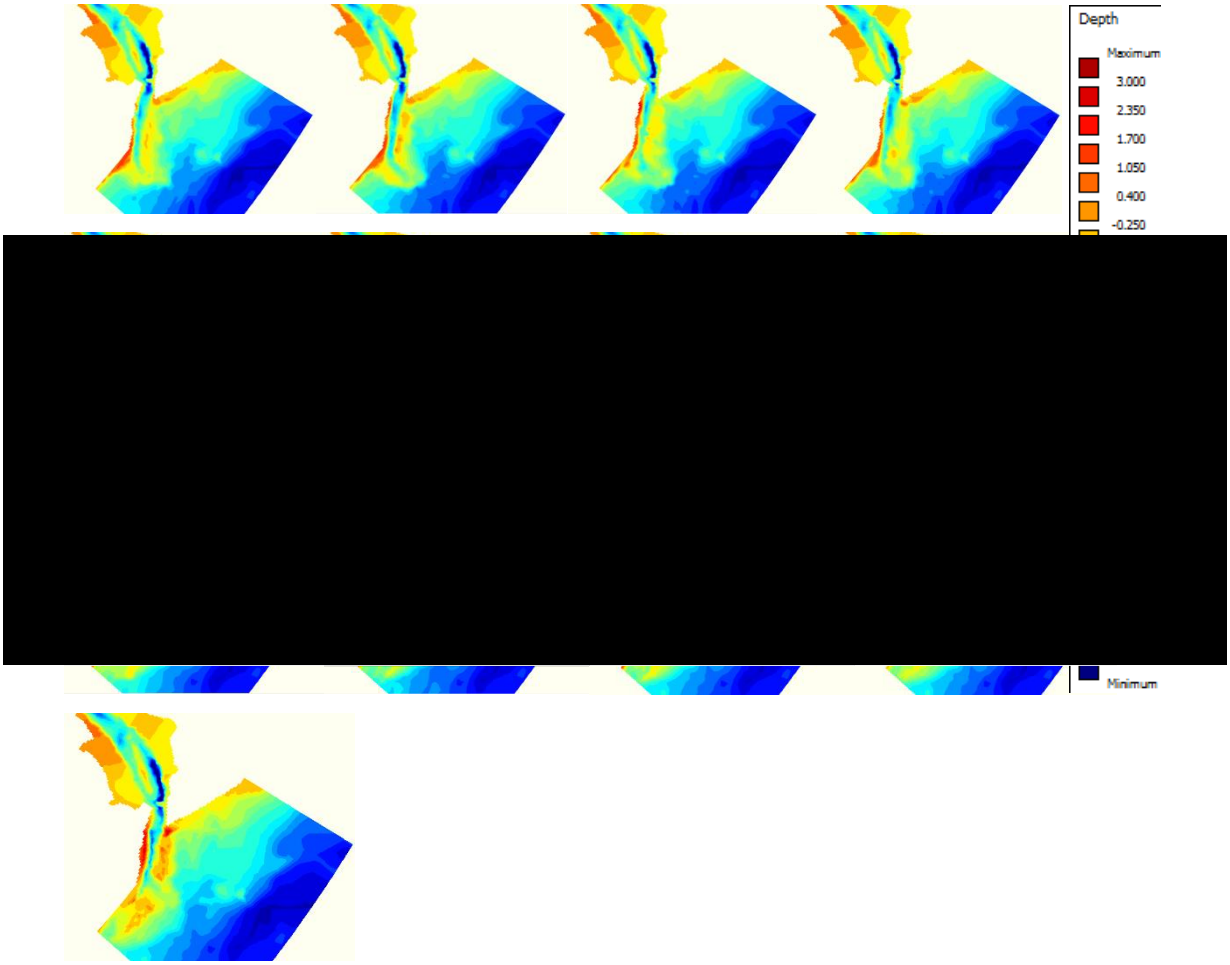

Figure 3.8 – The historical bathymetries in the Deben Estuary (from 1991 to 2003, Burningham and French, 2006).

In addition to this historical bathymetry data, the admiral chart that covers larger areas is also available and can be used in the numerical modelling (Figure 3.9). However, this chart is comprised of the combined datasets sourced from different data surveys (such as Harwich Haven Authority Surveys and Trinity House Lighthouse Surveys). In order to obtain the required bathymetries in numerical domains, the detailed area of the Deben mouth in this chart can be replaced by the bathymetries in Figure 3.8 to generate different years' bathymetries for the model. It is assumed that the morphology of the deep area outside the Deben mouth in the chart did not change annually. So, this replacement and interpolation is acceptable.

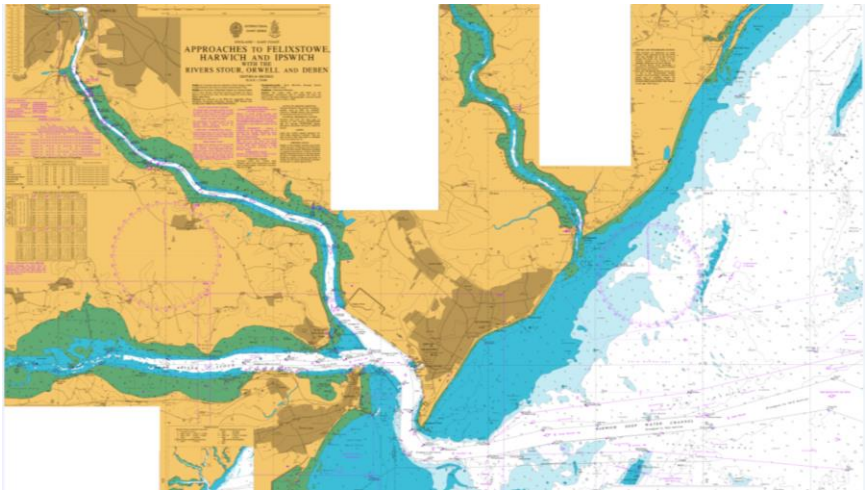

Figure 3.9 – The Admiralty Chart covering bigger areas around Deben Estuary (From United Kingdom Hydrographic Office).

3.7. Summary

Deben Estuary, which is located at the south-east coastline of the UK is taken as the study site to investigate climate change impacts on estuary morphodynamics. There is a great deal of historic hydrodynamic and morphodynamic data available on the Deben Estuary. The analysis of these data has shown that in history the Deben Estuary experienced a very dynamic regime in terms of both hydrodynamics and morphodynamics. Therefore, it is expected that future changes to global climate and hence to increasing sea levels and storm climates may have significant impacts on the future morphology of the estuary, which will be investigated through a numerical modelling approach as presented and discussed in proceeding chapters in this thesis.

Chapter 4: Deben Estuary Model and Computational Domain Set Up

In this study, the process-based computational model Delft3D (developed by the Deltares, Netherland) was used (Lesser et al., 2004; Booij et al., 1999). Delft3D is a fully integrated computer software suite for modelling coastal, river and estuary dynamics. It is composed of several modules including hydrodynamic and morphodynamic modules, wave module, water quality module and ecology module. Present study uses the hydrodynamic module which includes morphology (Delft3D-FLOW) and the wave module (Delft3D-WAVE).

4.1. Delft3D-FLOW

Delft3D-FLOW is a multi-dimensional (2D or 3D) hydrodynamic-morphodynamic simulation model which calculates non-steady flow (based on the shallow water assumption) and transport phenomena that resulted from water and meteorological forces, including the effect of density differences due to a non-uniform temperature and salinity distribution (density-driven flow). It can be used to simulate the physical processes of flow in shallow coastal areas, estuaries, lagoons, rivers and lakes, with the aim to reproduce flow phenomena in which the horizontal spatial scales are significantly larger than the vertical scales.

In this study, the 2DH (depth-averaged model) model has been employed where vertical density stratification and curvature induced flow are not considered. The interested site is a shallow area and the chosen domain will be far larger than the water depth in which the vertical velocity can be simplified into depth-averaged velocity. In addition, there is no sharp angle change along the Deben Estuary, which means the secondary flows need not be considered in this study.

In the model setup developed for the Deben Estuary, morphodynamic changes in the estuary take place as a result of the hydrodynamics driven by tidal and wave forcing. The main structure of the model is shown in Figure 4.1.

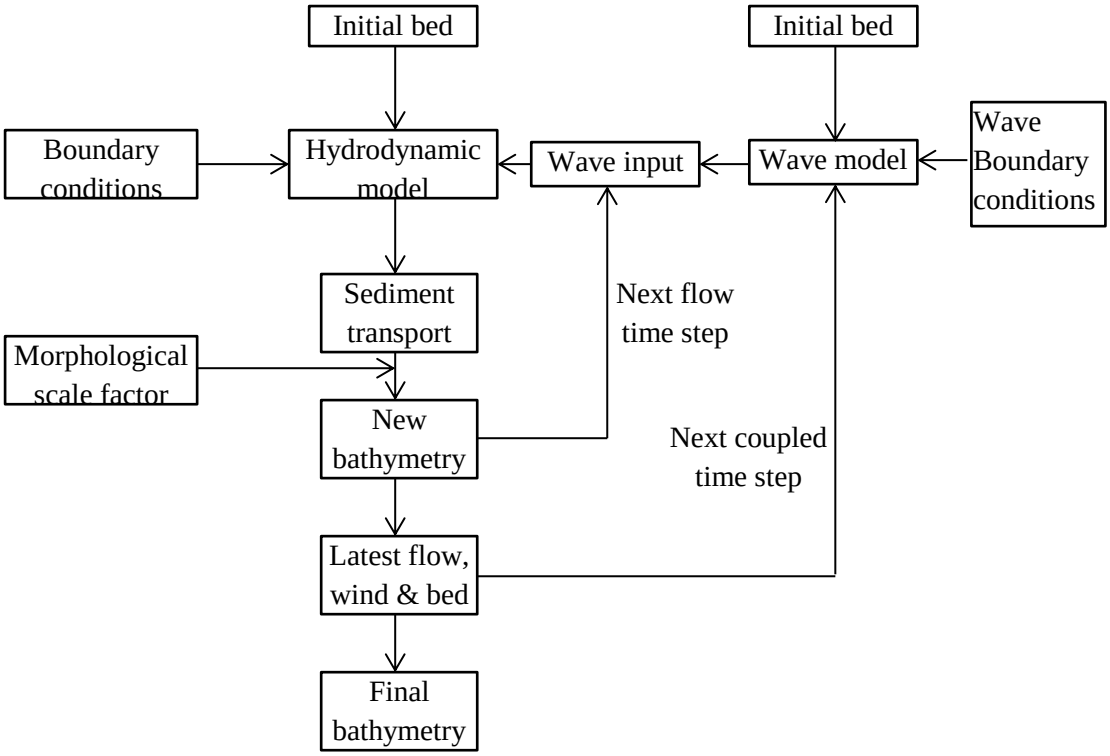

Figure 4.1 – Structure of the Delft 3D online coupled FLOW and WAVE modules with updated morphological changes.

4.1.1. Hydrodynamics

The Delft3D-FLOW module solves the unsteady shallow-water equations in two (depth-averaged) or three dimensions. The system of equations consists of the horizontal momentum equations, the continuity equations, the transport equation and a chosen turbulence closure model (Lesser et al., 2004). The vertical momentum equation is reduced to the hydrodynamic pressure relation (vertical hydrostatic) because the vertical accelerations are assumed to be small compared to gravitational acceleration. In this study, the depth-average are model (2DH) is used in which the vertical velocity profile is simplified into a constant long the water depth. The unsteady shallow-water equations in two dimensions are described following.

4.1.1.1. Continuity equation

The depth-averaged continuity equation is given by (Lesser et al., 2004):

$$\frac{\partial \zeta}{\partial t} + \frac{\partial [hU]}{\partial x} + \frac{\partial [hV]}{\partial y} = S \tag{4-1}$$

in which ζ stands for the water level (m); U and V express the depth-averaged velocity in x and y directions (m/s); h denotes the water depth (m); and S represents the contributions per unit area due to the discharge or withdrawal of water, evaporation and precipitation. The S can be expressed as:

$$S = \int_{-1}^{0} (q_{in} - q_{out}) d\sigma + P - E \tag{4-2}$$

in which the q_{in} and q_{out} are the local sources and sinks of water per unit of volume (1/s), respectively, σ means the σ co-ordinate vertical system, P is the non-local source term of precipitation and E is the non-local sink term due to evaporation. In this study, neither the water evaporation nor precipitation, so P and E will be zero in this case. Since no local sources and sinks of water are considered and the vertical coordinate is ignored in 2DH model, the S should be zero.

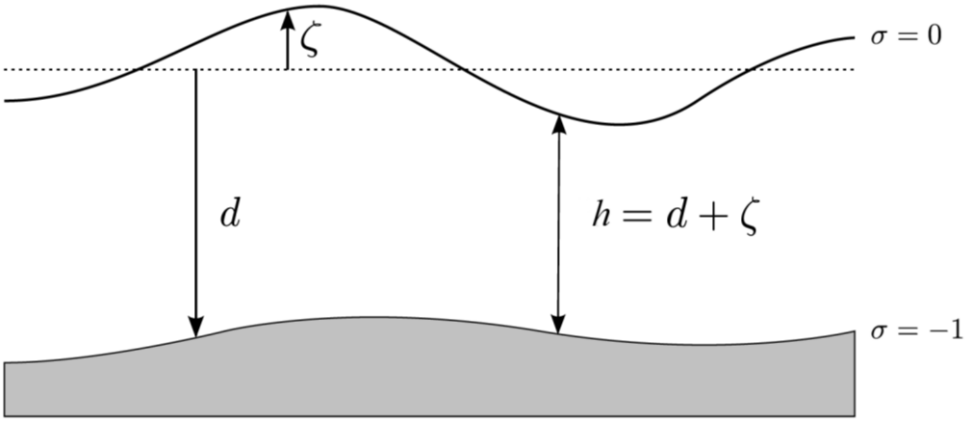

Figure 4.2 – Definition of water level (ζ), depth (h) and vertical coordinates.

4.1.1.2. Horizontal momentum equation

The original 3D horizontal momentum equations are given by (Lesser et al., 2004):

$$\frac{\partial U}{\partial t}+U\frac{\partial U}{\partial x}+v\frac{\partial U}{\partial y}+\frac{\omega}{h}\frac{\partial U}{\partial \sigma}-fV=-\frac{1}{\rho_0}P_x+F_x+M_x+\frac{1}{h^2}\frac{\partial}{\partial \sigma}\left(\nu_V\frac{\partial U}{\partial \sigma}\right) \quad (4\text{-}3)$$

$$\frac{\partial V}{\partial t}+U\frac{\partial V}{\partial x}+V\frac{\partial V}{\partial y}+\frac{\omega}{h}\frac{\partial V}{\partial \sigma}-fU=-\frac{1}{\rho_0}P_y+F_y+M_y+\frac{1}{h^2}\frac{\partial}{\partial \sigma}\left(\nu_V\frac{\partial V}{\partial \sigma}\right) \quad (4\text{-}4)$$

in which f is the Coriolis parameter (1/s) which is not considered here; σ stands for the vertical coordinate system and is scaled as $\sigma=(z-\zeta)/h$; ρ_0 is the reference density of water; M_x and M_y represent the contributions due to external sources or sinks of momentum (i.e. the effects from hydraulic structures, discharges or withdrawal of water, wave stresses, etc) which are also ignored in this study; the horizontal pressure terms, P_x and P_y, with the assumption of hydrostatic pressure derived from vertical momentum equation, are given by (with a non-uniform density):

$$\frac{1}{\rho_0}P_x=g\frac{\partial \zeta}{\partial x}+g\frac{h}{\rho_0}\int_\sigma^0\left(\frac{\partial \rho}{\partial x}+\frac{\partial \sigma'}{\partial x}\frac{\partial \rho}{\partial \sigma'}\right)d\sigma' \quad (4\text{-}5)$$

$$\frac{1}{\rho_0}P_y=g\frac{\partial \zeta}{\partial y}+g\frac{h}{\rho_0}\int_\sigma^0\left(\frac{\partial \rho}{\partial y}+\frac{\partial \sigma'}{\partial y}\frac{\partial \rho}{\partial \sigma'}\right)d\sigma' \quad (4\text{-}6)$$

With the constant water density conditions, these two equations can be simplified into (by accounting for the atmospheric pressure P_{atm}):

$$\frac{1}{\rho_0}P_x=g\frac{\partial \zeta}{\partial x}+\frac{1}{\rho_0}\frac{\partial P_{atm}}{\partial x} \quad (4\text{-}7)$$

$$\frac{1}{\rho_0}P_y=g\frac{\partial \zeta}{\partial y}+\frac{1}{\rho_0}\frac{\partial P_{atm}}{\partial y} \quad (4\text{-}8)$$

In this study, the gradients of atmospheric pressure on the free surface are assumed to be zero because the storm surge simulation are not included. This means the second

term at the right side of the equation (4-7) and (4-8) can be neglected since we do not consider the storm surges.

The horizontal Reynold's stresses, F_x and F_y, are determined by the eddy viscosity concept in which the shear stresses along the closed boundaries are ignored (Rodi, 1984):

$$F_x = \nu_h \left(\frac{\partial^2 U}{\partial x^2} + \frac{\partial^2 U}{\partial y^2} \right) \qquad F_y = \nu_h \left(\frac{\partial^2 V}{\partial x^2} + \frac{\partial^2 V}{\partial y^2} \right) \tag{4-9}$$

ν_h represents the horizontal eddy viscosity which consists of three parts (Delft 3D Flow User Manual, 2014) in which the vertical eddy viscosity coefficient ν_V is also included if a 3D simulation is carried out. However, in this study, the vertical eddy viscosity is not considered.

Since we consider the depth-averaged situation by neglecting the density differences, the momentum equation (4-3) and (4-4) can be simplified into 2D equation which eliminates the vertical coordinate system.

$$\frac{\partial U}{\partial t} + U\frac{\partial U}{\partial x} + V\frac{\partial U}{\partial y} + g\frac{\partial \zeta}{\partial x} + \frac{g}{C^2}\frac{U\left(\sqrt{U^2+V^2}\right)}{h} - \nu_h\left(\frac{\partial^2 U}{\partial x^2} + \frac{\partial^2 U}{\partial y^2} \right) - fV = 0 \tag{4-10}$$

$$\frac{\partial V}{\partial t} + V\frac{\partial V}{\partial x} + U\frac{\partial V}{\partial y} + g\frac{\partial \zeta}{\partial x} + \frac{g}{C^2}\frac{V\left(\sqrt{U^2+V^2}\right)}{h} - \nu_h\left(\frac{\partial^2 V}{\partial x^2} + \frac{\partial^2 V}{\partial y^2} \right) - fU = 0 \tag{4-11}$$

In which C is Chèzy coefficient ($m^{1/2}/s$); the other variables in these two equations are the same with that in equation (4-3) and (4-4).

4.1.2. Morphological module

The Delft3D-FLOW sediment transport and morphology module supports both the bedload and suspended load transport of non-cohesive sediments and suspended load of cohesive sediments. For the suspended load on both non-cohesive and cohesive sediment, the suspended load advection-diffusion equation is solved. For the bedload transport of non-cohesive sediment, different transport empirical formulas can be chosen. They are briefly discussed below.

4.1.2.1. Suspended sediment concentration

Two-dimension transport of suspended sediment concentration is calculated by solving the 2D depth-integrated advection-diffusion (mass-equation) equation for the suspended sediment (Lesser et al., 2004):

$$\frac{\partial h\bar{c}}{\partial t} + U\frac{\partial h\bar{c}}{\partial x} + V\frac{\partial h\bar{c}}{\partial y} - \varepsilon_{s,x}\frac{\partial^2 h\bar{c}}{\partial x^2} - \varepsilon_{s,y}\frac{\partial^2 h\bar{c}}{\partial y^2} = hS \qquad (4\text{-}12)$$

in which:

$\bar{c}$: depth-averaged mass concentration of sediment fraction (kg/m3);

U, V: depth-averaged velocity components (m/s);

$\varepsilon_{s,x}$, $\varepsilon_{s,y}$: eddy diffusivities of sediment fraction (m^2/s);

h: water depth (m);

S: sediment source and sink terms per unit.

Although the Delft 3D can deal with multiple sediment fractions and the interaction of sediment fractions can also be implemented, the lack of sediment fraction data in the estuary and limited understanding of multi-fraction sediment dynamics requires that this model uses single fractions for the sake of simplification.

4.1.2.2. Bedload transport

In the Delft3D-FLOW modelling suite, several transport formulae are available to select to compute sediment transport (Table 4.1). The bedload transport is only calculated for non-cohesive sediment by two steps: first, the magnitude and direction of the bedload transport at the cell centre is computed by using the chosen transport formula; then, the transport rate at the cell interfaces are determined, corrected for bed-slope effect and upwind bed composition and sediment availability.

Table 4.1 – The available sediment transport formulae in Delft 3D (Delft 3D Flow User Manual, 2014).

Formula	Bedload	Waves
[redacted]		
calibration	Bedload	No

However not all the transport formulas are considering wave impacts (Table 4.1) and some formulae use bedload transport as total transport. The formulae that include wave impacts are: Van Rijn (1993), Bijker (1971), Soulsby/Van Rijn and Soulsby (1997). The Soulsby/Van Rijn formula is intended for rippled bed conditions. According to Van Rijn (Soulsby, 1997):

$$U_{cr} = \begin{cases} 0.19 D_{50}^{0.1} \log_{10}\left(4h / D_{90}\right) if D_{50} \le 0.5mm \\ 8.5 D_{50}^{0.6} \log_{10}\left(4h / D_{90}\right) if\ 0.5mm < D_{50} \le 2mm \end{cases} \quad (4\text{-}13)$$

where U_{cr} is the critical bed shear velocity, h is the water depth.

This means the method was designed for those medium sediment diameters smaller than 2mm. But in the Deben Estuary, most of medium sediment diameters are larger than 5mm except the 'Horse Sand' which is around 0.4 mm (Burningham and French, 2006). In Delft 3D suite, it will be treated as if $0.5mm<D_{50}\leq 2mm$ for those $D_{50}>2mm$, which has not been validated by the developers. Thus, it will be high risk to use this formula in this study. It is ignored here. The following three formulae have been chosen for validation: Van Rijn (1993), Bijker (1971) and Soulsby (1997).

Van Rijn (1993)

In this formula, a reference height, which is a function of water depth and a user defined reference factor, is used to sperate the bedload and suspended. The sediment transport below this reference height was treated as bedload and that above the height is treated as suspended load. The reference concentration at this height imposes the sediment entrainment into the water column. The magnitude of the bedload transport, which includes both current and wave effects, reads as:

$$\left|S_b\right| = \eta 0.006 \rho_s w D_{50} M^{0.5} M_e^{0.7} \tag{4-14}$$

$\left|S_b\right|$ =magnitude of bedload transport (kg/m/s); η= the relative availability of the sediment fraction in the mixing layer; ρ_s=sediment density; w=sediment settling velocity; M=sediment mobility number due to waves and currents; Me=excess sediment mobility number; they are computed as:

$$M = \frac{v_{eff}^2}{(s-1) g D_{50}} \tag{4-15}$$

$$M_e = \frac{\left(v_{eff} - v_{cr}\right)^2}{(s-1) g D_{50}} \tag{4-16}$$

where

$$v_{eff} = \sqrt{v_R^2 + U_{on}^2} \tag{4-17}$$

in which s=relative sediment density (=ρ_s/ρ), v_{cr}=critical depth-averaged velocity for initiation of motion, v_R=magnitude of an equivalent depth-averaged velocity computed from the (Eulerian) velocity in the bottom computational layer, U_{on}=near-bed peak orbital velocity in onshore direction (in the direction on wave propagation) base on the significant wave height.

Bijker (1971)

The Bijker (1971) formula sediment transport treated bedload and suspended load separately with the combination force of currents and waves. It is possible to include sediment transport in the wave direction due to wave asymmetry and bed slope following the Bailard approach (Bailard, 1981; Stive, 1986). The original expressions that include wave asymmetry and bed slope components are given as (both extra bedload and suspended load are added to the bedload transport):

$$\vec{S}_b = \vec{S}_{b0} + \vec{S}_{b,asymm} + \vec{S}_{s,asymm} + \vec{S}_{b,slope} + \vec{S}_{s,slope} \tag{4-18}$$

$$\vec{S}_s = \vec{S}_{s0} \tag{4-19}$$

In this study, the wave asymmetry impacts are ignored so that the sediment transport in the wave direction is not included and the bed slope components are neglected. Thus, the sediment transport equations can be simplified to basic formula only in flow directions which are expressed as:

$$S_b = bD_{50}\frac{q}{C}\sqrt{g}\left(1-\phi\right)\exp\left(Ar\right) \tag{4-20}$$

$$S_s = 1.83 S_b \left(I_1 \ln\left(\frac{33.0h}{r_c} \right) + I_2 \right) \tag{4-21}$$

in which:

C – Chèzy coefficient; h – water depth; q – flow velocity magnitude (it equals $|U|$ for x direction and $|V|$ for y direction); ϕ – porosity and

$$Ar = \max(-50, \min(100, Ara)) \tag{4-22}$$

$$b = BD + \max(0, \min(1, \frac{h_w / h - C_d}{C_s - C_d}))\left(BS - BD\right) \tag{4-23}$$

$$I_1 = 0.216 \frac{\left(\frac{r_c}{h}\right)^{z_*-1}}{\left(1-\frac{r_c}{h}\right)^{z_*}} \int_{r_c/h}^{1} \left(\frac{1-y}{y}\right)^{z_*} dy \tag{4-24}$$

$$I_2 = 0.216 \frac{\left(\frac{r_c}{h}\right)^{z_*-1}}{\left(1-\frac{r_c}{h}\right)^{z_*}} \int_{r_c/h}^{1} \ln y \left(\frac{1-y}{y}\right)^{z_*} dy \tag{4-25}$$

where

BS – Coefficient b for shallow water;

BD – Coefficient b for deep water;

C_s – Shallow water criterion (H_s/h) (default value 0.4);

C_d – Deep water criterion (default value 0.05);

r_c – Roughness height for currents;

h_w – wave height;

and

$$Ara = \frac{-0.27 \Delta D_{50} C^2}{\mu q^2 \left(1 + 0.5\left(\psi \frac{U_b}{q}\right)^2\right)} \tag{4-26}$$

$$\mu = \left(\frac{C}{18\log_{10}\left(12h/D90\right)} \right)^{1.5} \tag{4-27}$$

$$z_* = \frac{w}{\frac{\kappa q\sqrt{g}}{C}\sqrt{1+0.5\left(\psi\frac{U_b}{q}\right)^2}} \tag{4-28}$$

$$U_b = \frac{\frac{2\pi}{T}h_w}{2\sinh\left(k_w h\right)} \tag{4-29}$$

$$\psi = \begin{cases} C\sqrt{\frac{f_w}{2g}} & ;T > 0 \\ 0 & ;otherwise \end{cases} \tag{4-30}$$

$$f_w = \exp\left(-5.977 + \frac{5.123}{a_0^{0.194}}\right) \tag{4-31}$$

$$a_0 = \max\left(2, \frac{U_b}{\omega r_c}\right) \tag{4-32}$$

where k_w – wave number; T – wave period computed by the wave model; U_b – wave velocity; w – sediment fall velocity; Δ – relative density $(\rho_s - \rho)/\rho$; κ – Von Karman constant (0.41).

Soulsby(1997)

The interaction of the currents and waves is taken into account by introducing a factor Y in the formula of mean bed shear stress.

$$\tau_m = Y\left(\tau_w + \tau_c\right) \tag{4-33}$$

in which shear stress due to waves (τ_w) is expressed as:

$$\tau_w = 0.5\rho f_w U_{orb}^2 \tag{4-34}$$

where orbital velocity U_{orb} is computed as:

$$U_{orb} = \frac{\pi h_w}{T_p \sinh(k_w h)} \tag{4-35}$$

T_p is peak wave period; h is water depth.

The friction factor of the rough bed (fw) is determined by (Swart, 1974):

$$f_w = \begin{cases} 0.3 & if \quad a_* \le 30\pi^2 \\ 0.00251\exp(14.1 a_*^{-0.19}) & if \quad a_* > 30\pi^2 \end{cases} \tag{4-36}$$

where a_* is expressed by roughness length (z_0): $a_* = \frac{U_{orb} T_p}{z_0}$.

The shear stress due to currents (τ_c) is expressed as:

$$\tau_c = \rho C_D U^2 \tag{4-37}$$

in which

$$C_D = \left(\frac{\kappa}{1 + \ln(z_0 / h)} \right)^2 \tag{4-38}$$

The factor Y in equation (4-33) can be obtained by regarding coefficients with various regression models (Soulsby, 1997).

The two Shields parameters are computed by using the shear stresses given above:

$$\theta_m = \frac{\tau_m}{\rho g \Delta D_{50}} \text{ and } \theta_w = \frac{\tau_w}{\rho g \Delta D_{50}} \tag{4.39}$$

The critical Shields parameter in this transport formula is computed as:

$$\theta_{cr} = \frac{0.30}{1+1.2D_*} + 0.055(1-\exp(-0.02D_*)) \tag{4.40}$$

in which D* is expressed as: $D_* = \left(\frac{g\Delta}{\nu^2}\right)^{1/3} D_{50}$

Then the expressions of the actual bedload transport rates are given as:

$$S_{b,x} = \frac{\sqrt{g\Delta D_{50}^3}}{U}\left(\Phi_x U - \Phi_y V\right) \tag{4-41}$$

$$S_{b,x} = \frac{\sqrt{g\Delta D_{50}^3}}{U}\left(\Phi_x V - \Phi_y U\right) \tag{4-42}$$

In which the Φ is related to the Shields parameters given above:

$$\Phi_{x1} = 12\left(\theta_m - \theta_{cr}\right)\sqrt{\theta_m} \tag{4-43}$$

$$\Phi_{x2} = 12\left(0.95 + 0.19\cos(2\varphi)\right)\theta_m\sqrt{\theta_w} \tag{4-44}$$

$$\Phi_x = \max\left(\Phi_{x1}, \Phi_{x2}\right) \tag{4-45}$$

$$\Phi_y = \frac{12\left(0.19\theta_m\theta_w^2\sin(2\varphi)\right)}{\theta^{1.5} + 1.5\theta^{1.5}} \tag{4-46}$$

in which φ is the angle between the wave and current directions.

4.1.2.3.Morphology

The bed level changes are determined by sediment reworking due to hydrodynamics and the changes of sediment mass due to sources and sinks. The elevation of the bed is dynamically updated at each computational time-step which means every hydrodynamic flow calculation is always carried out using the updated bathymetry. The implementation of the updating is based on the change in the mass of bed material that was transported. The multiplication between transport rate and the sediment dry bed densities (user defined) is used to get this mass. This change in mass is then translated into a bed level change based on the dry bed densities of the various sediment fractions (Delft 3D FLOW User Manual, 2014).

The change in the quantity of bottom sediments caused by the bedload transport is calculated using the expression:

$$\Delta_{SED}^{(m,n)} = \frac{\Delta t f_{MORFAC}}{A^{(m,n)}} \left(S_{b,uu}^{(m-1,n)} \Delta y^{(m-1,n)} - S_{b,uu}^{(m,n)} \Delta y^{(m,n)} + S_{b,vv}^{(m,n-1)} \Delta x^{(m,n-1)} - S_{b,vv}^{(m,n)} \Delta x^{(m,n)} \right) \quad (4\text{-}47)$$

where:

$\Delta_{SED}^{(m,n)}$ – change in quantity of bottom sediment at location (m,n)

Δt – computational time-step

f_{MORFAC} – user-defined morphological acceleration factor

$A^{(m,n)}$ – area of computational cell at location (m,n)

$S_{b,uu}^{(m,n)}$ – computed bedload sediment transport vector in u direction at the u velocity point of the computational cell at location (m,n) (Figure 4.2)

$\Delta x^{(m,n)}$ – cell width in the x direction at the V point of cell (m,n)

$\Delta y^{(m,n)}$ – cell width in the y direction at the U point of cell (m,n)

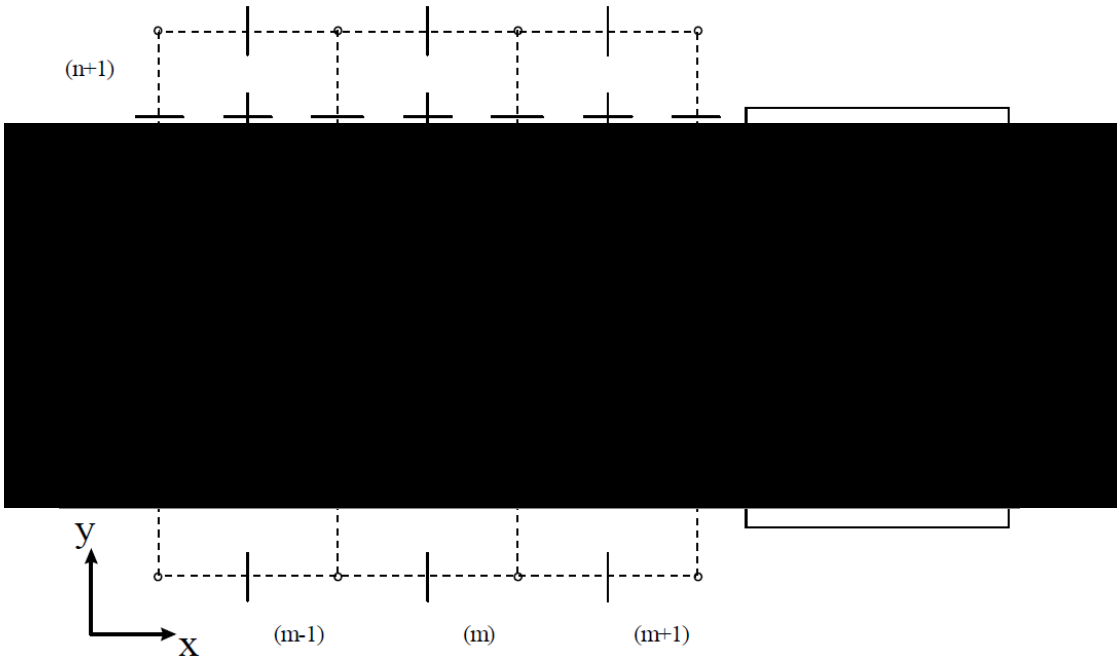

Figure 4.2 – Morphology control volume and bedload transport components in the computational grids (Delft 3D FLOW User Manual, 2014).

In this equation, it is noted that f_{MORFAC} is the morphological acceleration factor which is a technique scaling up the morphological changes to a rate so that it begins to have a significant impact on the hydrodynamic flows. Usually, the morphological changes need a time scale several times longer than typical flow changes. So, the morphological factor can accelerate the morphological changes if f_{MORFAC} is not equal to 1, so that it can be incorporated dynamically into the hydrodynamic flow calculations to reduce the real computational time. Also, if f_{MORFAC} equals 0, there would not be a change on the bathymetry which prevents the flow depth and quantity of sediment from updating. A sample layout of the computational cells is shown in Figure 4.2.

4.2. Delft3D-WAVE

In Delft-3D WAVE, waves are described with the two-dimensional wave action density spectrum instead of the energy density spectrum since in the presence of currents, action density is conserved whereas energy density is not (Whitham, 1974).

The evolution of the wave spectrum is expressed by the spectral action balance equation in Cartesian co-ordinates as (Hasselmann et al., 1973):

$$\frac{\partial}{\partial t}N+\frac{\partial}{\partial x}c_x N+\frac{\partial}{\partial y}c_y N+\frac{\partial}{\partial \sigma}c_\sigma N+\frac{\partial}{\partial \theta}c_\theta N=\frac{S}{\sigma} \tag{4-48}$$

The first term on the left-hand side represents the local rate of change on action density on time, the second and third term are propagation of action in geographical space, the fourth term is shifting of the relative frequency due to variations in depths and currents, and the fifth term represents depth-induced and current-induced refraction, the term S [$=S(\sigma,\theta)$] at the right-hand side is the source term including effects of generation, dissipation and non-liner wave-wave interactions. In equation 4-48, the terms c_x, c_y, c_σ and c_θ are the propagation velocities in x, y, σ, and θ spaces, respectively.

Wave action density N reads as:

$$N(\sigma,\theta)=\frac{E(\sigma,\theta)}{\sigma} \tag{4-49}$$

where E is wave energy (J/m^2); σ is wave frequency (1/s); θ is wave direction (deg).

Wave simulations can be done by using the second-generation HISWA wave model (Holthuijsen et al., 1989) or the third-generation SWAN model (Holthuijsen et al., 1993; Booij et al., 1999). The latter model was selected in this study because it can run on the same curvilinear grids as that are used for the Delf3D-FLOW calculations so that it will reduce the effort of preparation on combined WAVE and FLOW simulations (Lesser et al., 2004). In addition, the wave forces in SWAN can be calculated on the gradient of the radiation stress tensor rather than on the dissipation rate in the HISWA model and also, the fully implicit schemes in SWAN have been implemented which can make computations unconditionally stable. (Delft 3D WAVE User Manual, 2014). A brief introduction of various source terms in SWAN model is given next.

4.2.1. The SWAN source terms

The term S [$=S(\sigma,\theta)$] at the right-hand side of the action balance equation (4-48) is the source term in terms of energy density representing the effects of generation by wind, non-linear wave-wave interaction and dissipation caused by white-capping, bottom friction and depth-induced breaking.

Wave input

The SWAN model considers wave growth by wind which is expressed by:

$$S(\sigma,\theta) = A + BE(\sigma,\theta) \tag{4-50}$$

A denotes the linear wave growth and $BE(\sigma, \theta)$ accommodates the exponential wave growth. It is noted that the SWAN model is driven by the wind speed at 10 m elevation above the sea surface U_{10} while the computation uses the friction velocity U_*.

Dissipation of energy

The SWAN model includes the dissipation of wave energy as a result of white-capping (which is related to the mean frequency and the mean wave number), bottom friction (which is expressed by a bottom friction coefficient that depends on the bottom orbital motion) and depth-induced wave breaking (which is based on the Battjes and Janssen model, 1978). Detailed information on wave dissipation can be found in Delft3D-WAVE user manual[2].

Nonlinear wave-wave interactions

There are two kinds of wave-wave interactions considered in SWAN model: quadruplet wave-wave interactions and triad wave-wave interactions. The former is

[2] http://oss.deltares.nl/web/delft3d/manuals

computed with the Discrete Interaction Approximation (DIA) (Hasselmann et al., 1985) and the latter is computed using the Lumped Triad Approximation (LTA) (Eldeberky and Battjes, 1996). Both interactions can be computed simultaneously (Delft3D-WAVE user manual, 2014).

Apart from the processes mentioned above, the Delft3D-WAVE model also accounts for the wave-induced set-up and diffraction since this model is used in the coastal shallow water area with possible consideration of adding obstacles to wave propagation. Because the calculation of wave-induced set-up is based on the vertical momentum balance equation which has been used in the Delft3D-FLOW model, the wave model will not use it again when it is coupled with the flow model. The diffraction is not considered in this study.

4.2.2. Wave effects on coupled WAVE and FLOW model

Wave forcing due to breaking is modelled as a shear stress at the water surface in FLOW model while the enhanced wave-induced bed shear stress which results from the wave-current interaction model of Fredsoe (1984) (selected in this study) is coupled into the Flow model. Apart from these effects, additional turbulence generation due to wave dissipation at bottom and wave white-capping and breaking at the surface, the wave-induced mass flux and wave-induced streaming are also important for the 3D sediment transport simulation in a nearshore coastal zone (Lesser et al., 2004). However, for the depth-averaged simulation, these effects are not particularly important for the vertical averaged model.

4.3. Numerical scheme

The following sections will describe the numerical schemes used in different modules in Delft 3D.

4.3.1. Hydrodynamics

The solution of equations in Delft3D-FLOW model is based on the finite difference method. There are three possible grid systems which are Cartesian rectangular, orthogonal curvilinear or spherical respectively. It is assumed that the grid is orthogonal and well structured. The variables are arranged in a pattern called the Arakawa C-grid (a staggered grid) where the water level points (pressure points) are defined in the centre of the cell and the velocity components are perpendicular to the cell faces (see Figure 4.3).

Since the depth points are defined at the corners of the cell, the bottom depths at water level points (centres of grids) are determined by using three algorithms (maximum, mean and minimum) of the four surrounding depth points. And for the depth values at the cell interface, they are got from the mean of the adjacent two depth points. The total water depth in a cell face is from the sum of the depth value of this cell face and the average water level at the cell centre. For the water level at the cell interface, the mean value of water level at both sides was used.

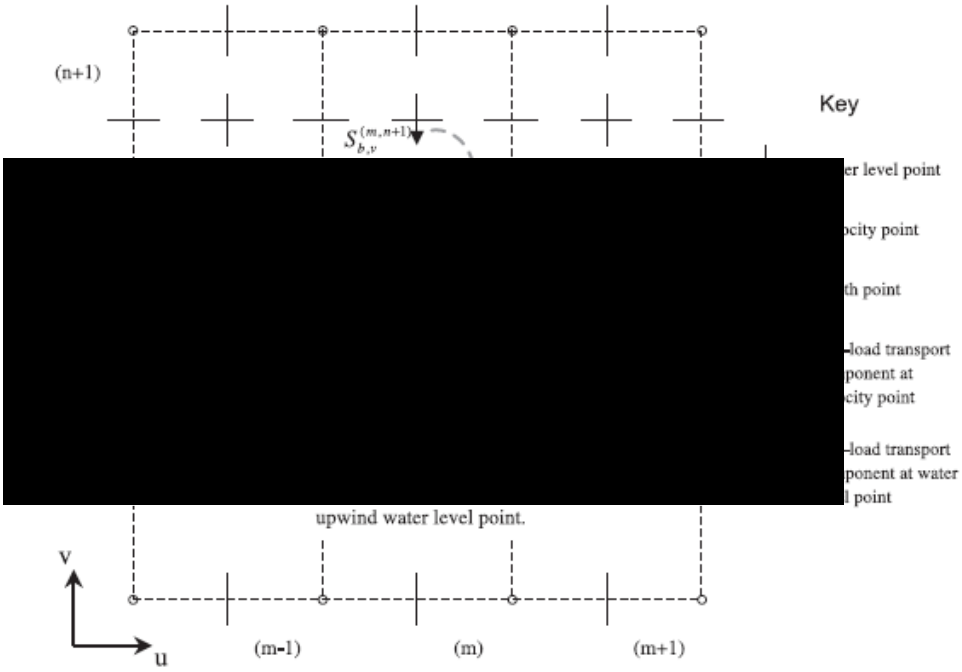

Figure 4.3 – Delft3D-FLOW computational staggered grids (Lesser et al., 2004)

In terms of time integration, the unsteady shallow equations are solved by an Alternating Direction Implicit (ADI) method which splits one time step into two stages (Leendertse, 1973). In both stages, all the terms of the model equations are solved in a consistent way with at least second order accuracy in space. For the spatial discretisation of the horizontal advection terms, three options (Waqua, Cyclic and Flooding) are available in Delft3D-FLOW (Stelling, 1984). Herein, the 'Cyclic method' was selected which leads to a method that is computationally efficient and well-converged.

4.3.2. Sediment Transport

The advection-diffusion transport equation is formulated in a conservative form (finite-volume approximation) to make sure that the total mass is conserved for the equation (4-12). There are two options for the spatial discretization of the horizontal advection terms: Cyclic and Van Leer-2 schemes (Van Leer, 1974; Stelling and Leendertse, 1992). The Cyclic method is based on an implicit time integration (ADI) method of both advection and diffusion and does not impose a time step restriction.

The second scheme is an explicit scheme that contains two numerical schemes: a first order upwind scheme and the second order upwind scheme. The explicit time integration requires small time steps but produces a more diffusive numerical solution because a first order upwind discretization is applied. However, the Van Leer-2 scheme is slightly less accurate than the Cyclic method. In this study, the Cyclic method is used.

Delft3D-FLOW also includes an algorithm to approximate the horizontal diffusion along z-planes in a σ-coordinate framework (Stelling and van Kester, 1994). Also, a horizontal Forester filter (Forester, 1979) based on diffusion along σ-planes is applied to remove any negative concentration values that may occur.

4.3.3. Wave

The integration of the wave action balance equation has been implemented in SWAN with finite difference schemes in all five dimensions (time, geographic space and spectral space). In this study, the stationary wave model is used for simplification, which means that the time dimension in equation (4-48) is omitted. This is the most efficient way to simulate the waves in a large scale and long-term model.

The geographic space is discretised with the same grid as the Delft3D-FLOW model while the spectrum in the model is discretised with a constant directional resolution $\Delta\theta$ and a constant relative frequency resolution $\Delta\sigma/\sigma$ (logarithmic frequency distribution).

The numerical scheme in SWAN is an implicit upwind scheme (in both geographic and spectral space), supplemented with a central approximation in spectral space. It can switch between the upwind scheme and central scheme in the spectral space. This scheme is unconditionally stable which permits relatively large time steps in the computations and also the second-order central approximation is sufficiently accurate. In geographic space, the state of a grid point is determined by the state in the up-wave grid points. It permits a decomposition of the spectral space into four quadrants. In each quadrant, simulation can be carried out independently from the other quadrants except for the interactions between them due to refraction and non-linear wave-wave interactions. And for the boundaries (including closed boundaries), the wave energy is assumed to be fully absorbed both in geographic and spectral spaces.

4.4. Deben Estuary model domains and set-up

The Delft3D FLOW and WAVE models were setup for the Deben Estuary inlet in order to simulate the estuary's morphological change as a result of tidal flows and waves and to investigate the impacts of climate change.

The model domain which covers the estuary and the surrounding seas is shown in Figure 4.4. There are two main parts of the procedure when considering both the

resolution of interested areas and hydrodynamic data available: nested process and domain decomposition.

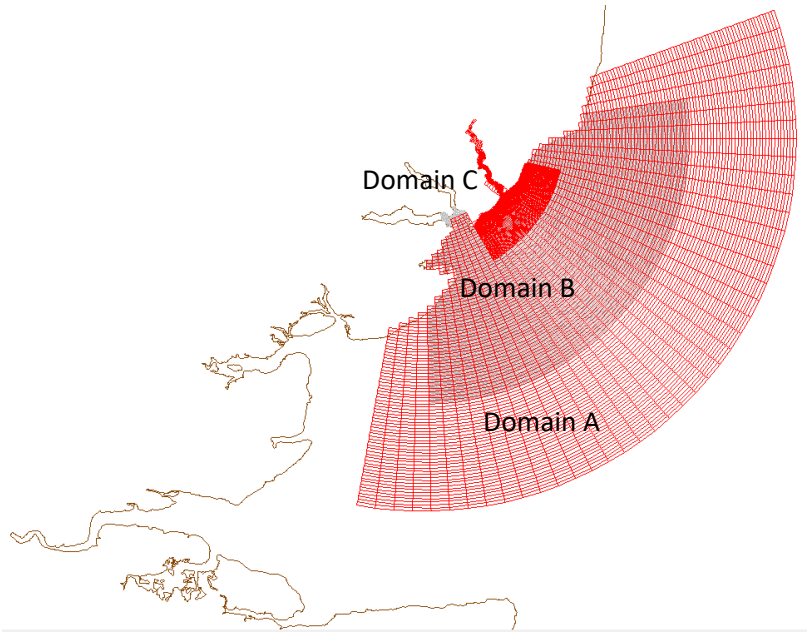

Figure 4.4 – Nested model domains at the study site in the Flow models. The biggest domain is named ‘Domain A’, the medium domain is named ‘Domain B’ and the smallest domain is called ‘Domain C’.

4.4.1. Flow models

Since the available data is in deep ocean which is far away from the interested area, the nested process is the best choice in order to introduce the offshore hydrodynamic conditions to coastal area. The hydrodynamic model is using the implicit numerical scheme which means it is the unconditional convergent in the simulation. However, in terms of the accuracy, the model will check whether it is tolerant or not. Therefore, for the very large-scale model which requires less accuracy, the simulation is efficient and convergent. For the local model, resolution should be high enough to investigate the morphological changes with maximum efficiency. Before setting up the final grid sizes, several different grid sizes have been selected by considering the interested areas to test whether the resolution is high enough to carry out investigations. For the local

model, the model with grid size 100×100m (test a), 50×50m (test b) and gradually from 100×100m offshore to 50×50m onshore (test c) has been tested (Figure 4.5).

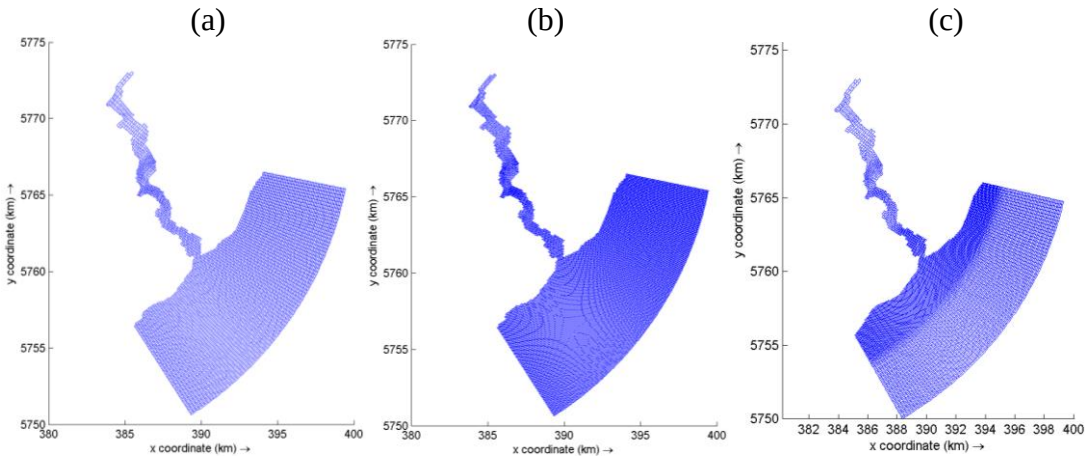

Figure 4.5 – The testes grid size of local model. (a) 100×100m, (b) 50×50m, (c) gradually from 100×100m offshore to 50×50m onshore.

The model is running for one month on the ACPI ×64 – based PC with 8 Intel Core i7-3770 CPU processors. The calculation of test (a) is taken about 15 minutes based on the default setting without wave and morphological modules. The test (c) uses around half an hour to finish the running while the test (b) needs more than one and a half hour to finished simulation because the time step should be reduced significantly in test (b) in order to grantee the accuracy. By comparing with these tests, the test (c) would be the best choice. However, none of these grids is able to represent morphological features clearly (Figure 4.6). It is difficult to distinguish the channel and ebb tidal delta areas which are the most important characteristics in the estuary. Therefore, the local refinement is required so that the grid structure of Figure 4.7 is introduced by Domain Decomposition. Then the detailed model set-up process is provided following.

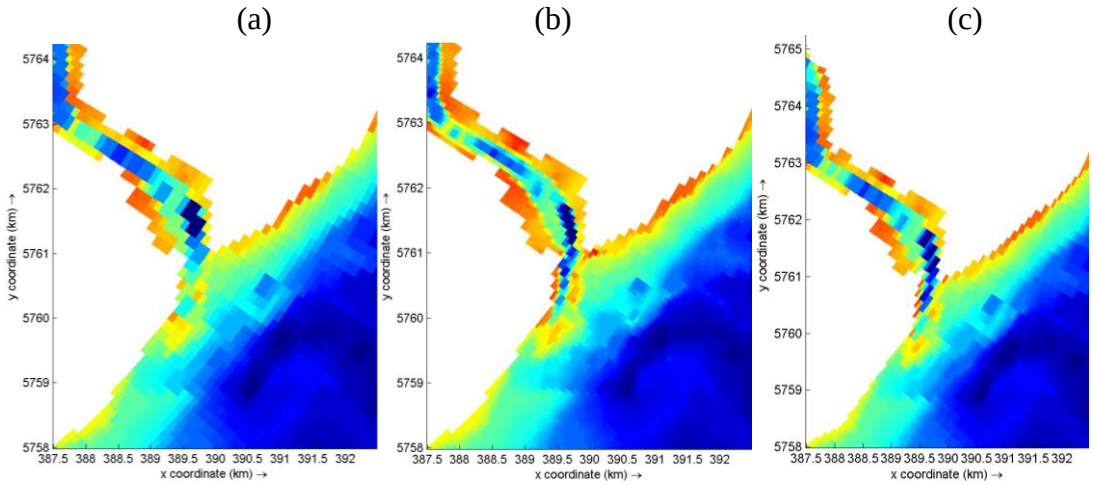

Figure 4.6 – The initial bed level of interested area in the tested models by using different grid sizes. (a) 100×100m, (b) 50×50m, (c) gradually from 100×100m offshore to 50×50m onshore.

Nested models

The model setup consists of three nested models in order to achieve the required fine resolution for morphodynamic simulations (Figure 4.4). The extent of the largest model (Domain A) was determined by the availability of wave boundary conditions since the model needs to capture offshore waves from both predominant directions of Northeast (50%) and Southeast (32%) (CEFAS, 2004). Therefore, a curvilinear grid, that covers both north and south offshore areas of the estuary, was developed (Figure 4.4). For simplicity, the same grid was used for both flow and wave modelling.

The grid size of the large domain (Domain A) is approximately 800m×500m (long-shore×cross-shore) at the onshore boundary and 3km×500m at the offshore boundary. The whole longshore length at land boundary is around 50km while the longshore length at offshore bosundary is around 120km. The length of lateral boundaries is approximately 30km. The total area covered by large model is about $3.46\times10^{3}km^{2}$.

A medium grid (Domain B) was introduced to achieve a smooth transition from a course resolution Domain A to the fine resolution Domain C, as Domain C should receive offshore flow and wave boundary conditions from the larger domains. The grid

sizes of Domain B are 720m×160m and 270m×160m at the offshore boundary and onshore boundary, respectively. Domain C has grid resolution of approximately 220m×100m (offshore boundary) and 160m×50m (onshore area). This domain covers a coastline length of 18km and has a lateral boundary length of 6km.

Domain Decomposition

The extent of Domain C is determined by the availability of tide gauges measurements for model validation. The tidal measurements available within the Deben model setup (refer to Chapter 3 for details about the tide gauge locations and data) are used for flow validation, which are all in Domain C. Therefore, in order to avoid artificial impact around the boundary area by covering all the validated points, the lateral boundary is defined further away from the flow validation points (south lateral boundary is around 2.3km away from the 'Felixstowe' and north lateral boundary is approximate 4.0km away from the 'Bawdsey') (Figure 4.7).

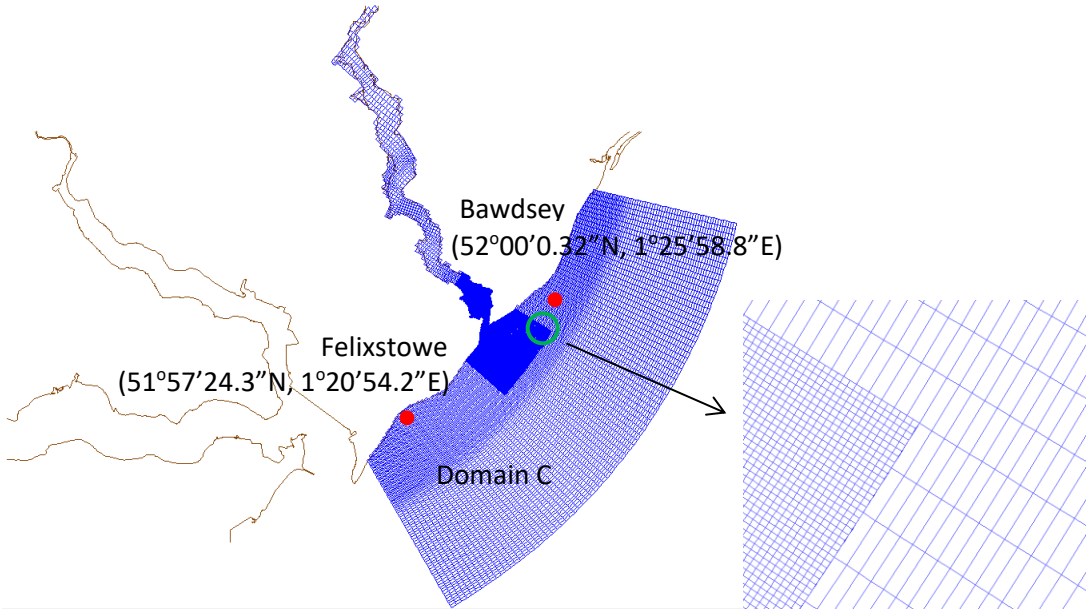

Figure 4.7 – The detail of Domain C with the local interested area, validated points (red) (see the text) and grid refinement in horizontal direction (Note: right figure is the detailed domain decomposition boundary).

However, since Domain C is still very large and needs much more computational time, the local refinement on grid resolution is required in order to investigate the morphodynamic changes clearly by not increasing the computational time. So the 'Domain Decomposition' (DD) process is used to solve the difficulty that two different grid resolutions coexist within one domain (Figure 4.7).

Following the principle of grid refinement in Delft3D-FLOW that the local grid refinement along domain interfaces have to be based on a 1-to-N refinement with N is an integer number, the grid cell near the interface in the coarser domain corresponds to N grid cells in the refined domain. In this DD procedure, the coarse grid size is 2 times larger than the detailed small grid size in the cross-shore direction and 8 times larger than that in the long shore direction (Figure 4.7). Although it is suggested that it is better to use an odd number to refine grids in DD boundary (Delft 3D FLOW User Manual, 2014), it is tested by the author that the even number can generate the same results without any disturbances.

For better accuracy, the coupled area of these two domains is made non-overlapping, which allows for a nearly optimal distribution of grid points. However, due to the overlap of only one grid cell, the spatial discretisation at or near the interface may be of lower order than the discretisation in the interior, which will lead to less accuracy compared to the single domain simulation. But this is acceptable when the DD process is used one or twice and the DD boundaries are away from the interested area.

4.4.2. Wave models

Unlike those flow model domains, whose accuracy is essential to the tidal-dominated estuary, there are only two domains used for wave modelling, which are Domain A and Domain C, for the purpose of reducing computational time (Figure 4.8). It is suggested that the wave model domain should be larger than the area of interest (Delft-WAVE user manual, 2014) because the existence of disturbed area when wave propagating into the domain with direction spreading towards shore can cause computational errors. This means the lateral boundaries should be sufficiently far away

from the area of interest to avoid this disturbed area. In this study, the area of interest is the Deben estuary inlet which is far away from the boundaries of Domains A and C.

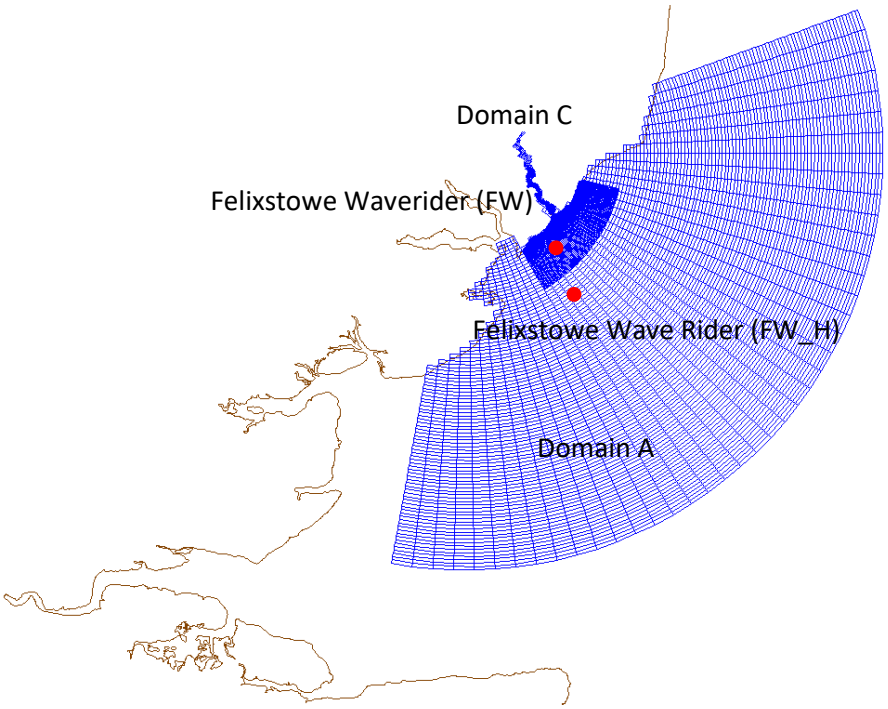

Figure 4.8 – Wave nested domains (only two domains are used: Domain A and Domain C) and the validated points (red) (see the text).

4.5. Boundary conditions for Flow and Wave models

Boundary conditions for flow and wave models should be defined before the simulation. The required boundaries for model calibration and validation are discussed below.

4.5.1. Boundary conditions of the flow model

In order to solve the equation system, the following boundary conditions are required.

Seabed boundary condition

The vertical velocities at bed and free surface boundaries are set to be:

$$\omega|_{\sigma=-1}=0 \text{ and } \omega|_{\sigma=0}=0 \tag{4-51}$$

In depth-average flow, the bed shear-stress at the bed is assumed to be given by a quadratic friction law:

$$\vec{\tau}_b = \frac{\rho_0 g \vec{U} \left|\vec{U}\right|}{C^2} \tag{4-52}$$

where: $\left|\vec{U}\right|$ is the magnitude of the depth-averaged horizontal velocity which corresponds to the logarithm vertical velocity profile with the relationship:

$$\int_z^{z+h} u dz = Uh \tag{4-53}$$

where u is the flow velocity, h is the water depth; C is the Chèzy coefficient ($m^{1/2}/s$) which is given by:

$$C = \frac{\sqrt[6]{h}}{n} \tag{4-54}$$

where: n is Manning coefficient ($m^{-1/3}s$). In this study, according to the calibrated results, the Chèzy coefficient is simplified into a constant in both U and V directions.

Free surface boundary condition

Similar with the seabed boundary conditions, the vertical flux at the free surface boundary is zero. The magnitude of the wind horizontal shear-stress that widely used is defined as quadratic expression:

$$\left|\overrightarrow{\tau_s}\right| = \rho_a C_d U_{10}^2 \tag{4-55}$$

where:

ρ_a: the density of air;

U_{10}: the wind speed 10 meters above the free surface (time and space dependent);

C_d: the wind drag coefficient dependent on the wind speed U_{10}.

$$C_d = \begin{cases} C_d^A & U_{10} \le U_{10}^A \\ C_d^A + \left(C_d^B - C_d^A\right)\dfrac{U_{10} - U_{10}^A}{U_{10}^B - U_{10}^A}, & U_{10}^A \le U_{10} \le U_{10}^B \\ C_d^B + \left(C_d^C - C_d^B\right)\dfrac{U_{10} - U_{10}^B}{U_{10}^C - U_{10}^B} & U_{10}^B \le U_{10} \le U_{10}^C \\ C_d^C & U_{10}^C \le U_{10} \end{cases} \tag{4-56}$$

U_{10}^i : user-defined wind speeds (i=A,B,C).

Lateral boundary conditions

Along the closed boundaries, the velocity component perpendicular to the closed boundary is set to zero which is free-slip condition. At the open boundary, there are several options for depth-averaged simulation: water level, velocity (normal to the boundary), discharge, Riemann invariant (weakly reflective boundary condition; Verboom and Slob, 1984) and Neumann boundary conditions (Roelvink and Walstra, 2004).

The Riemann type of boundary is used to simulate a weakly reflective boundary. The main characteristic is that the boundary up to a certain level is transparent for outgoing waves (normal to the boundary) which can cross the open boundary without being reflected back into the computational domain as happens for the other types of boundaries. This boundary condition can be expressed as: $f(t) = U \pm 2\sqrt{gH}$.

However, availability of both water level and velocity information at the boundary makes it difficult to determine the Riemann invariant.

The Neumann boundary conditions define the alongshore water level gradient instead of a fixed water level or velocity, which can be expressed as: $f(t) = \frac{\partial \zeta}{\partial n}$. This can make the boundary condition match up to the certain flow level or velocity distribution in the cross-shore direction to avoid boundary disturbances. In many cases, such as those with steady flow, the gradient can be assumed to be zero; however, in tidal or storm surge modelling, the alongshore gradient varies in time but does not vary much along lateral boundaries when the model domain is not large.

Open boundary conditions for flow model

In Delft 3D FLOW model, the flow boundary conditions at the offshore boundary are specified in a limited number of boundary points and linear interpolation is adopted to generate the boundary conditions at the intermediate points along the boundary. Interpolations can generate physically unrealistic flows in the region close to the open boundary particularly when the bathymetry is complex at boundaries (e.g. big slope along the boundary). So, in order to avoid any disturbances arising from flow interpolations along the offshore boundary and the errors of interpolation, the specified points can be defined intensively which will be discussed later.

The flow model is forced by the tides derived from the TPXO7.2 Global Inverse Tidal model[3] at the offshore boundary of the computation Domain A. In this study, 13 tidal components were used. All three open boundaries (one offshore boundary and two lateral boundaries) use astronomical tides (including limited tidal constituents) in which the amplitudes and phases are fixed at the specific places. Tidal amplitudes were defined at three nodes spreading along the boundaries where they were interpolated to all offshore grid points by interpolating linearly.

[3] http://volkov.oce.orst.edu/tides/global.html

The boundary conditions for Domain B were determined by weighted averaged water levels from Domain A. In this domain, three open boundaries (one offshore boundary and two lateral boundaries) use the time series water levels (every 10 minutes). It is acceptable for the model with a large area by using both water level conditions at offshore boundary and lateral boundary although it is suggested that using different types of boundary conditions at different boundaries is more accurate and stable (Delft 3D FLOW User Manual, 2014).

Figure 4.9 – Defined boundaries of Domain C and the process of dealing with the dredged channel (Note: right figure is the enlarged west boundary with crossed channel)

For higher accuracy and the model stability, the open boundaries of small Domain C were carefully chosen from Domain B. The offshore boundary uses time series water levels while the lateral boundaries are using the time series current conditions. For the boundary conditions of nested domain (Domain C), there is no need to take water levels and velocities at all grid points by nested process since this is time consuming. In order to get water levels and velocities along all the grid of the boundary, the interpolation can be carried out.

At the north of lateral boundary, three segments with twice linear interpolation are used whereas eight segments are used at the south lateral boundary due to the existence

of a dredged channel crossing through this boundary (Figure 4.9). In order to eliminate linear errors along the large bed slope, it is better to reduce the length of interpolation segments.

A sample water level time series at a selected point on the offshore boundary of Domain C, which covers two spring-neap cycles, is shown in Figure 4.10.

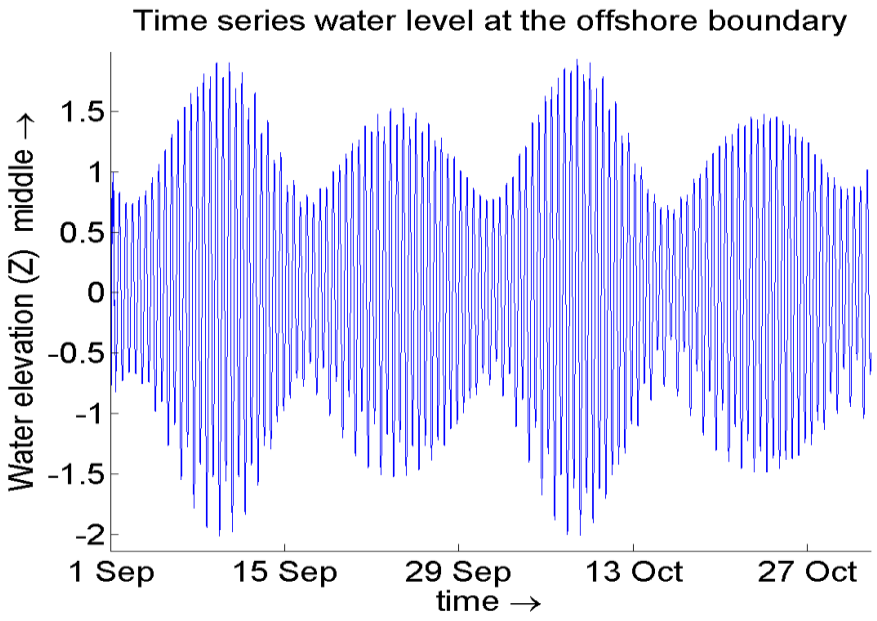

Figure 4.10 – The sample of time series water level boundary conditions

4.5.2. Morphological module

In order to avoid the model instabilities at the beginning of simulation due to the transition from initial conditions to the dynamic boundary conditions, the morphological updating process began 12 hours after hydrodynamic and wave simulations.

Morphological module boundary conditions

Morphological model requires the definition of a set of boundary conditions at the seabed, on the water surface and at the open inflow boundaries.

1) Water surface boundary

The vertical diffusive fluxes through the free surface are set to zero:

$$-wc - \varepsilon_{s,z} \frac{\partial c}{\partial z} = 0, \quad \text{at } z=\zeta \tag{4-57}$$

where $\varepsilon_{s,x}$ is the vertical eddy diffusivity of sediment fraction (m^2/s).

2) Bed boundary condition

The exchange of material in suspension and the bed is indicated by the sediment fluxes from the bottom computational layer to the bed, and vice versa. The fluxes are also applied to the bed in order to update the bed level. The boundary condition at the bed is given by:

$$-wc - \varepsilon_{s,z} \frac{\partial c}{\partial z} = D - E, \quad \text{at } z=z_b \tag{4-58}$$

where: D—sediment deposition rate; E – sediment erosion rate; $\varepsilon_{S,z}$ – Eddy diffusivity of sediment.

3) Open sediment inflow boundaries

Since the transport equation is advection dominated at coastal area, the boundary conditions at an open inflow (flood) boundary is needed while at the outflow (ebb) boundary the concentration must be zero (Lesser et al., 2004). For sand sediment fractions, the local equilibrium sediment concentration profile may be used which means the flow should enter carrying all ‘sand’ sediment fractions at their ‘equilibrium’ concentration profiles at all open inflow boundaries. This is implemented by setting zero sediment concentration gradient at the boundary (a Neumann boundary condition).

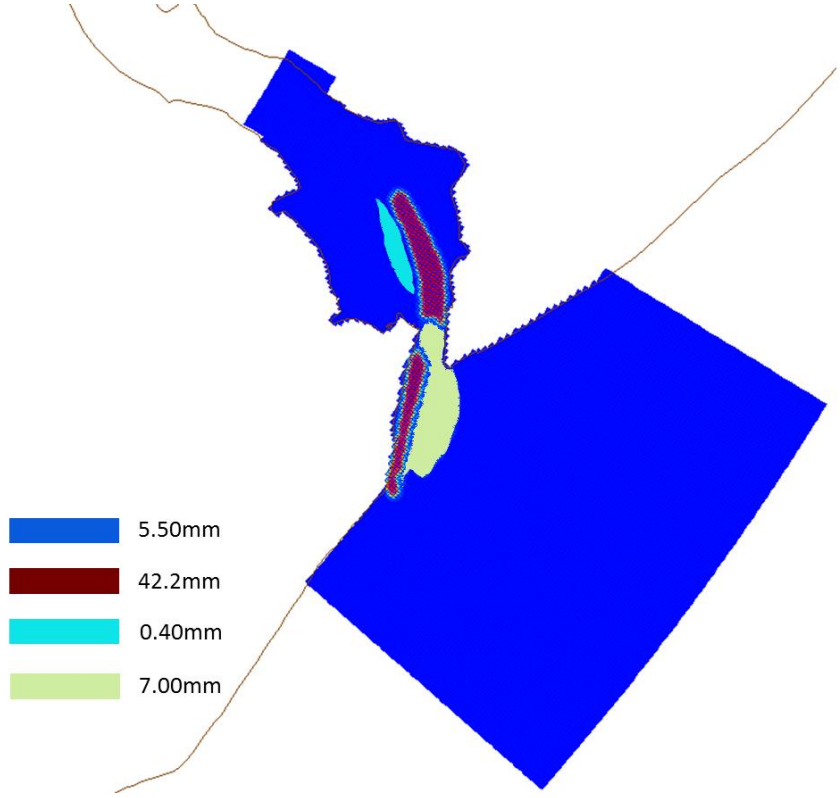

Figure 4.11 – The special distribution of sediment medium diameter D_{50} within the Domain C.

Sediment fraction

In the sediment transport and morphology module of Delf3D-FLOW, a mixture of up to 99 suspended fractions and unlimited amount of bedload fractions are allowed to be used. But in this study, one sediment fraction in every single cell is considered mainly due to scarcity of detailed sediment information in and around the Deben Estuary and also for the sake of simplicity, as described in detail earlier.

However, the sediment diameters vary spatially in the model domain. Figure 4.11 shows the spatial distribution on the medium sediment diameter (D_{50}) in which the D_{50} at the channel equals to 42.2mm, D_{50} at the flood tidal delta (Horse Sand) equals to 0.4mm, D_{50} at the spit of the domain was assumed to be 7mm and that of the other places defined to be 5.5mm (Burningham and French, 2006).

In this study, the several transport formulae that account for wave impacts were tested (mentioned above) and different bottom roughness coefficients were used to calibrate the model in which both the bedload and suspended load are considered under the impacts of flow and wave.

Morfac (Morphological Acceleration factor)

One of the issues in simulating morphological change based on the hydrodynamic flows is that the morphological developments take place in a time scale much longer than typical flow change timescales (Delft 3D-FLOW User Manual, 2014). For instance, the morphology of a coastline usually takes months or years to change significantly while the tidal flows change over a period of hours. So, one technique for solving this problem is to introduce a 'Morphological time scale Factor' (Morfac) whereby the speed of the changes in the morphology is accelerated up to a rate that it begins to be incorporated dynamically into the hydrodynamic flow calculation. The implementation of the Morfac is achieved by simply multiplying the erosion and deposition fluxes from the bed to the flow and vice-verse by the Morfac at each computational time step.

However, care should be taken when using Morfac as the choice of this value affects the accuracy of model results (Ranasinghe et al., 2011). It is necessary to determine a suitable value in the particular situations so that it will not affect the accuracy of the model results. An extensive sensitivity analysis was carried out at the beginning of this study using a range of Morfac values which confirmed that Morfac values great than 12 will have notable impacts on model performance.

4.5.3. Open boundary conditions for wave models

The wave boundary conditions for the computation domain were determined from the Wave Net wave rider 'West Gabbard' (Cefas). Detail of wave measurements at WG are given in Chapter 3. Validation of the wave model is carried out using wave hindcast data from the 'Felixstowe Wave Rider', as described in next section, which has a depth

of 9.5m, and is shown in Figure 4.8 (51°53’1.68”N, 01°26’18.96”E). This site can be used to validate the wave model.

The boundary conditions in Delft 3D Wave model, both in geographic space and spectral space are taken as fully energy absorbing. The incident wave conditions are defined as time series spectra along the boundary. The specification of spectra has two options: one is parametric within which wave parameters (i.e. significant wave height, wave period and directional spreading) can be specified manually; another is specified from file in which the conditions are defined in advance. The spectral space shape in both options can be defined in different ways: JONSWAP type spectrum, Pierson-Moskowitz type spectrum and Gauss-shaped spectrum. In this study, wave time series generated by JONSWAP (Hasselmann et al., 1973) spectrum is used. The time interval of the time series of wave heights is 12 hours when it is communicated to the FLOW model. The offshore wave boundary coincides with the offshore flow boundary described in previous sections.

In terms of discretisation on the spectral space, the directional space was divided into 36 bins and the frequency space was divided into 24 portions from 0.05Hz to 1Hz with logarithmic distribution. So, the spectral directional resolution is 10 however, the spectral frequency resolution is not constant since the frequencies are distributed logarithmically.

4.6. Flow model and Wave model validation points

Within the flow model domains, there are two tide gauges that can be used to validate the hydrodynamic model (Figure 4.7). One is the ‘Felixstowe’ Tidal Gauge, located about 4.5km to the south of the Deben inlet at the seaward end of Felixstowe Pier (51°57’24.3”N, 01°20’54.2”E). Another one is the Bawdsey IHO tidal station, at a water depth of 4.5m shown in Figure 4.7 (52°00’0.32”N, 01°25’58.8”E). This data is detailed in Chapter 3.

In the wave model, the only available point is hindcast wave data at ‘Felixstowe Wave Rider’ (FW_H; position: 51°53’1.68”N, 01°26’18.96”E) which is located within

Domain A but outside the Domain C (Figure 4.8). In addition to hindcast wave data at Felixstowe, another set of measured wave data are available around Felixstowe ('Felixstowe Waverider' (FW)) (position: 51°56'18"N, 01°23'37.8"E) which is located inside Domain A at an approximate water depth of 8m. However, the measurement period at FW was outside the modelling time frame selected in this study. Therefore, in order to strengthen model validation, an additional validation process was carried out using the FW measured wave data for the period from September 2012 to September 2013.

4.7. Time frame and bathymetry

The bathymetry of the Domain A was digitized from the Admiralty Charts and the bathymetry of the detailed domain (Domain C) around the estuary (Figure 3.9) was derived by interpolating digitised Trinity House surveys and UKHO chart data, supported by the information from aerial photography, maps and Lidar data (iCCOAST). This detailed bathymetry data used in Domain C has 10m resolution. In terms of the bathymetry used in Domain A (Suffolk cost), a single Admiralty Chart was available while for the detailed model domain (Deben mouth area), 23 annual interpolated bathymetries were available. It should be noted that the incompatibility of data resolution and accuracy between the two available datasets have some impacts on the hydrodynamic results when the single Admiralty Chart data was combined to 23 annual bathymetry data. However, in the absence of more detailed bathymetries in the outer domain, there is not any alternative way.

Simulation time for calibration and validation process

In this study, the morphological simulation period is 12 months from September 2002 with the appropriate Morfac value which will be used for model validation and calibration. Due to the complicated bathymetry and high resolution in the detailed domain, the time step in hydrodynamic module should be set up carefully. Although the model is using implicit numerical scheme, which means it should be unconditional stable, the model would also terminate when the accuracy is not satisfied. For example, the method to approximate the horizontal advective fluxes for suspended sediment

transport is required to meet the Courant-(Friedrichs-Lewy) CFL condition giving a stability condition: $CFL = \max(\frac{U\Delta t}{\Delta x}, \frac{V\Delta t}{\Delta y}) \leq 1$. For the accuracy ADI for barotropic mode, the Courant number for surface waves should be less than $4\sqrt{2}$ ($CFL = 2\Delta t\sqrt{gh\left(\frac{1}{\Delta x^2} + \frac{1}{\Delta y^2}\right)} \leq 4\sqrt{2}$). *Δt*, *Δx*, *Δy* is the time step (s) and spatial step (m) in two horizontal coordinates respectively. *U*, *V* are depth averaged velocities (m/s) and *h* is the water depth (m). By considering both the accuracy and the efficiency of the model used here, it is optimal to select the time step as 15s in the hydrodynamic module (including the morphological module) according to the minimum grid size.

As the wave module is using the stationary method, there is no need to set up the time step for wave model. But the online communication between wave and flow models is carried out, the time interval of communication will determine the wave simulation running frequency. Time interval of 720 minutes was used to communicate between wave and flow models during the validation process. For the simulation scenarios in Chapter 8, the communication time will reduce to 60 minutes while the simulation is carried out in a short term.

Simulation time for future climate scenarios simulations

Since the purpose of this study is to investigate the impact of climate change on estuarine morphology, it is essential that morphological simulations to be carried out are at over several decades. However, morphodynamic simulations of this large time scale will be highly computationally intense and due to the uncertainties of boundary conditions, they may not be accurate and useful (proved from the tested cases). Therefore, a different approach is used where morphological change under ‘current’ and ‘future’ hydrodynamic and wave conditions were carried out over a period of one year and cross comparisons of results were made for a range of climate scenarios.

4.8. Summary

The Delft 3D modelling suite was used to develop a computational wave/flow/morphology model of the Deben Estuary to investigate the estuary' morphodynamic responses to climate change. The computational model domains and initial and boundary conditions of the flow and waves used are described in detail in this chapter.

Although the process-based model cannot be run for decades or centuries, morphology change resulting from current and future climate conditions can be effectively modelled and compared in order to investigate the impact of global climate change on morphodynamic responses of the estuary. As the historic morphodynamic evolution of the estuary is well-documented, the results can be compared to investigate climate-induced morphodynamic changes that may take place in the estuary in future.

Chapter 5: Model Calibration and Validation

The Delft3D FLOW and WAVE models contain a large number of parameters that needs to be calibrated and validated before using the model for a specific estuary, which will be discussed in this chapter.

5.1. Evaluation methods

To evaluate the numerical model performance, three main indices were considered: bias, accuracy and skill (Sutherland, 2004).

5.1.1. Bias

Bias is a measure of the difference in the central tendencies of the predictions and the observations within which the most common use is the mean of bias or median of bias. It reveals the tendency toward under- or over-prediction; a positive bias indicates that the model consistently overpredicts the observations. The mean of bias can be expressed as:

$$Bias_a = \left\langle Z_{predicted} \right\rangle - \left\langle Z_{measured} \right\rangle \tag{5-1}$$

where: $Z_{measured}$ is measured samples; $Z_{predicted}$ is predicted samples; The <> denotes the mean of the values.

And the median of bias can be expressed as:

$$Bias_m = Z^m_{predicted} - Z^m_{measured} \tag{5-2}$$

in which $Z^m_{measured}$ and $Z^m_{measured}$ are the median values of all $Z_{measured}$ and $Z_{predicted}$, respectively. In this study, the variable sample Z can be replaced by water depths or bed elevations according to the purpose of usage.

5.1.2. Accuracy

The most common measures of accuracy are the Mean Absolute Error (MAE), Mean Square Error (MSE) and the Root Mean Square Error (RMSE), defined as:

$$MAE = \frac{\left| Z_{measured} - Z_{predicted} \right|}{N} \tag{5-3}$$

$$MSE = \frac{\left\langle (Z_{measured} - Z_{predicted})^2 \right\rangle}{N} \tag{5-4}$$

$$RMSE = \sqrt{\frac{\sum \left(Z_{measured} - Z_{predicted} \right)^2}{N}} \tag{5-5}$$

The lower the MAE, MSE and RMSE are the higher the agreement between measured and predicted values is.

5.1.3. Skill

Skill score is one of the most popular evaluation methods to investigate the performance of morphodynamic models (Ruessink et al., 2003; Pedrozo-Acuna et al., 2006; Roelvink et al., 2009; Ruggiero et al., 2009) which can be defined as (Sutherland et al., 2004):

$$SS = \frac{A\left(Z_{base}, Z_{measured} \right) - A\left(Z_{predicted}, Z_{measured} \right)}{A\left(Z_{base}, Z_{measured} \right) - A\left(Z_{perfect}, Z_{measured} \right)} \tag{5-6}$$

where $A(Z_{base}, Z_{measured})$= the accuracy of the baseline prediction, $A(Z_{predicted}, Z_{measured})$= is the accuracy of predictions and $A(Z_{perfect}, Z_{measured})$=accuracy of a perfect set of predictions. Therefore, this skill score can be based on Mean Absolute Error, Mean Square Error or Root Mean Square Error in which the accuracy of perfect modelling,

represented by *MAE* ($Z_{perfect}$, $Z_{measured}$), *MSE* ($Z_{perfect}$, $Z_{measured}$) or *RMSE* ($Z_{perfect}$, $Z_{measured}$), is taken to be zero (Murphy and Epstein, 1989). The simplified expression of skill derived from probabilistic models based on MSE is given by Brier Skill Score (BSS):

$$BSS = 1 - \frac{\left\langle \left(z_{predicted} - z_{measured} \right)^2 \right\rangle}{\left\langle \left(z_{base} - z_{measured} \right)^2 \right\rangle} \tag{5-7}$$

The BSS includes contributions due to errors in predicting amplitudes, phase and mean of a variable. So, in order to know which type of errors contributes the most to lowering the skill score, it is useful to use the decomposition of the BSS proposed by Murphy and Epstein (1989). This shows that the BSS can be decomposed in terms of the anomalies in the prediction, $Y'=Z_{predicted}-Z_{base}$, and the measurements, $X'=Z_{measured}-Z_{base}$. So the Murphy-Epstein decomposition can be written as:

$$BSS = \frac{\alpha - \beta - \gamma + \varepsilon}{1 + \varepsilon} \tag{5-8}$$

where, $\alpha = r_{Y'X'}^2$ is a measure of phase error—when the sand is moved to the wrong position; the correlation coefficient $r_{Y'X'} = \frac{\langle Y'X' \rangle}{\sigma_{Y'}\sigma_{X'}}$ in which: $Y' = Z_{predicted} - Z_{base}$, $X' = Z_{measured} - Z_{base}$; $\sigma_{Y'}$ and $\sigma_{X'}$ stand for standard deviations in the predicted and observed anomalies, respectively.

$\beta = \left(r_{Y'X'} - \frac{\sigma_{Y'}}{\sigma_{X'}} \right)^2$ is a measure of amplitude error—when the wrong volume of sand is moved;

$\gamma = \left(\frac{\langle Y' \rangle - \langle X' \rangle}{\sigma_{X'}} \right)^2$ is a measure of the map mean error—when the predicted averaged bed level is different from the measured.

$\varepsilon = \left(\frac{\langle X' \rangle}{\sigma_{X'}} \right)^2$ is a normalization term, and is only affected by measured changes from the baseline predictions.

According to Van Rijn (Van Rijn et al., 2003), the base line bathymetry can be replaced by the initial bed level so the BSS is given as:

$$BSS = 1 - \frac{\left\langle \left(Z_{predicted} - Z_{measured} \right)^2 \right\rangle}{\left\langle \left(Z_1 - Z_{measured} \right)^2 \right\rangle} \tag{5-9}$$

where z_1=initial bed level. This BSS can be used either for validation or for sensitivity analysis (just changing the measured bathymetry into the assumed basic bathymetry).

In order to minimise excessive computation time, the calibration process was divided into three different parts according to the importance of the role that parameters play: hydrodynamics, morphodynamics and waves. This reduced the number of simulation cases significantly.

5.2. Validation points

The tidal data from the two tidal stations situated within the computational Domain C (Figure 4.7) are used to validate the hydrodynamic model. In the 'Felixstowe' tide gauge, located at 2.12m water depth (51°57'24.3"N, 01°20'54.2"E), the data was collected from British Oceanographic Data Centre (BODC) which was available from 1986 to 2012. The other tidal station 'Bawdsey', is operated by the International Hydrographic Organization (IHO) and is located at a water depth of 4.2m

(52º00’0.32”N, 01º25’58.8”E). These two sites are used to validate the simulated water level (the detailed data has been discussed in Chapter 3).

5.3. Sensitivity analysis (calibration process) and validation

In order to select the optimum values of the model parameters for the study area, a sensitivity analysis was undertaken by using the model evaluation methods mentioned above. For the sake of computational time limitation, the hydrodynamic modules are separated from the morphodynamic module and the hydrodynamic validation was carried out first. In this case, some parameters need to be calibrated again for morphodynamic simulation after the sensitivity discussion in hydrodynamic module. It is assumed that if any of these parameters varying in a certain range will not have great impacts on the hydrodynamics, such as the water level, it is acceptable to change it freely within this range during the morphodynamic module validation so that it does not need to turn back to validate hydrodynamic again.

The sensitivity analysis process is that the selected parameters are systematically changed with reference to a selected baseline case which represents the default setting of every module in Delft 3D. Therefore, a series of models that run with a range of different model parameters were carried out.

5.3.1. Hydrodynamics

Three most important parameters that impact the hydrodynamic results are bed roughness (described by Chèzy coefficient: *C*), horizontal viscosity coefficient (ν_h) and the threshold depth for drying and flooding (*Dryflc*) which are shown in Table 5.1 with the tested values. These three parameters were selected because they are the most important parameters in determining the hydrodynamic results. When one parameter changed, the others will be kept as default (i.e. when three values of C were tested, the other two parameters were kept as default shown in bold in Table 5.1). So, there are 7 cases for sensitivity analysis. All the test cases are compared with the basic case.

Table 5.1 – Values of parameters used for the sensitivity analysis of the hydrodynamic model

hydrodynamic-related input parameters				
model parameters	basic case	test series 1	test series 2	description
C	**65**	25	95	Chèzy coefficient ($m^{1/2}/s$)
ν_h	**1**	0.5	5	horizontal viscosity coefficient (m^2/s)
Dryflc	**0.1**	0.01	0.5	Threshold depth for drying/flooding (m)

Due to the lack of velocity data in this study, the sensitivity analysis is only based on the deviation of the water elevation in the hydrodynamic module since only the tidal elevation data are available. The time series water elevation at 'Felixstowe' tide gauge (FT) and 'Bawdsey' tide gauge (BT) positions (Figure 4.7) were chosen to carry out the sensitivity analysis. All test simulations lasted for one month.

Table 5.2 – MAE & RMSE of water elevations of FT tidal gauge between test series and baseline model (basic case) regarding to three parameters (*C*, ν_h and *Dryflc*).

	Bed roughness		Horizontal viscosity		Threshold depth	
	C=25	C=95	ν_h=0.5	ν_h=5	Dryflc=0.01	Dryflc=0.5
MAE	0.0401	0.0094	0.0004	0.0006	0.0011	0.0069
RMSE	0.0491	0.0124	0.0008	0.0009	0.0034	0.027

The MAE and RMSE values of simulated and measured tidal water levels at FT tide gauge are shown in Table 5.2. The bed roughness shows the highest impact on the water elevation among these parameters which means the water elevation is more sensitive to the bed roughness than the horizontal viscosity coefficient or minimum wet threshold depth. This is because, for the large-scale flow simulation, the horizontal viscosity terms are reduced to the Laplace operator (second order differential operator) (Delft 3D FLOW User Manual, 2014) along the grid lines in which the impact of the coefficient has been reduced. In addition, for the depth-averaged simulation, the horizontal turbulent motions contributed by horizontal eddy viscosity are not

significant. So, the horizontal viscosity would have insignificant impact on 2D simulation.

Table 5.3 — MAE & RMSE of water elevation on BT tidal gauge between the test cases and baseline case (basic case) regarding to three parameters (*C*, ν_h and *Dryflc*).

	Bed roughness		Horizontal viscosity		Threshold depth	
	C=25	C=95	ν_h=0.5	ν_h=5	Dryflc=0.01	Dryflc=0.5
MAE	0.0133	0.0049	0.0003	0.0004	0.0007	0.0035
RMSE	0.0154	0.0057	0.0006	0.0006	0.0010	0.0059

For the wet threshold depth value, since it is the judgment of wet or dry cell, it is sensitive to the location. For instance, the MAE and RMSE at FT point (shallow area) are much larger than the ones at BT point (deeper than FT) (see Table 5.3). However, for the intertidal area, this parameter should not to be too large for the accuracy reason and not to be too small for the computational time limitation (the smaller the *Dryflc* is, the longer the computational time needs) in the coastal simulation. So, in this study, the two coefficients (ν_h and *Dryflc*) are kept as default.

Although the changes of roughness have greatest impact on the water elevation, the MAE and RMSE is still very small (0.04 and 0.05 at FT and 0.013 and 0.015 at BT respectively) which means the changes on water elevation can be negligible between basic case and test cases. The default Chèzy coefficient, which is $65 m^{1/2}/s$ shown in Table 5.1, is sufficient for the simulations. However, it is necessary to calibrate the roughness coefficient further in the morphodynamic module. Since this parameter will not significantly change the hydrodynamics, there is no need to recalibrate when doing the morphodynamic validation.

Validation of base model

Due to the available data at both tidal measurement sites, the validation of the hydrodynamic model can be carried out by comparing the time series water elevations of base case with the real data at the sites (see Table 5.4).

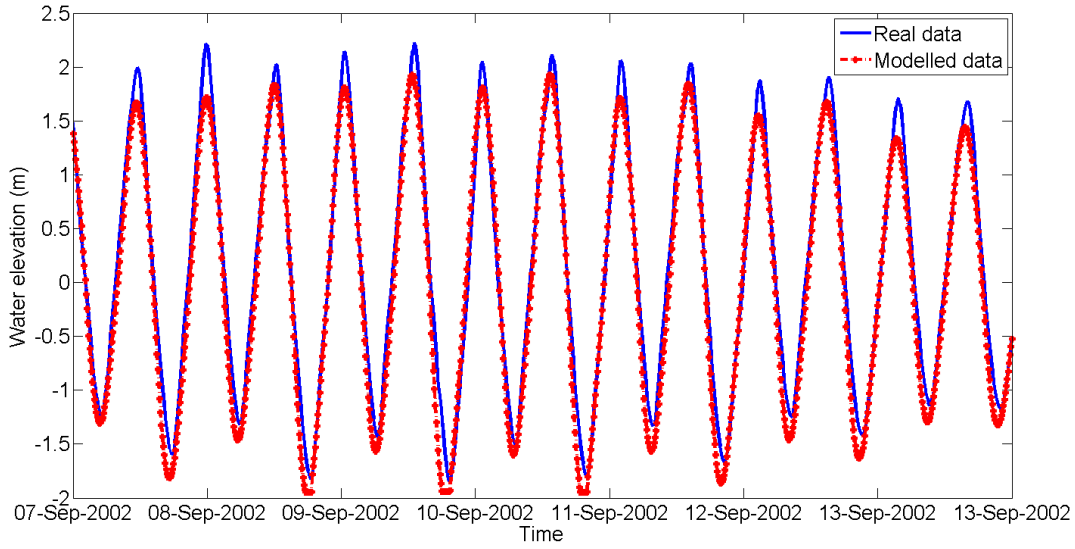

Figure 5.1 – The time series water elevation comparison at FT between real data and base simulation

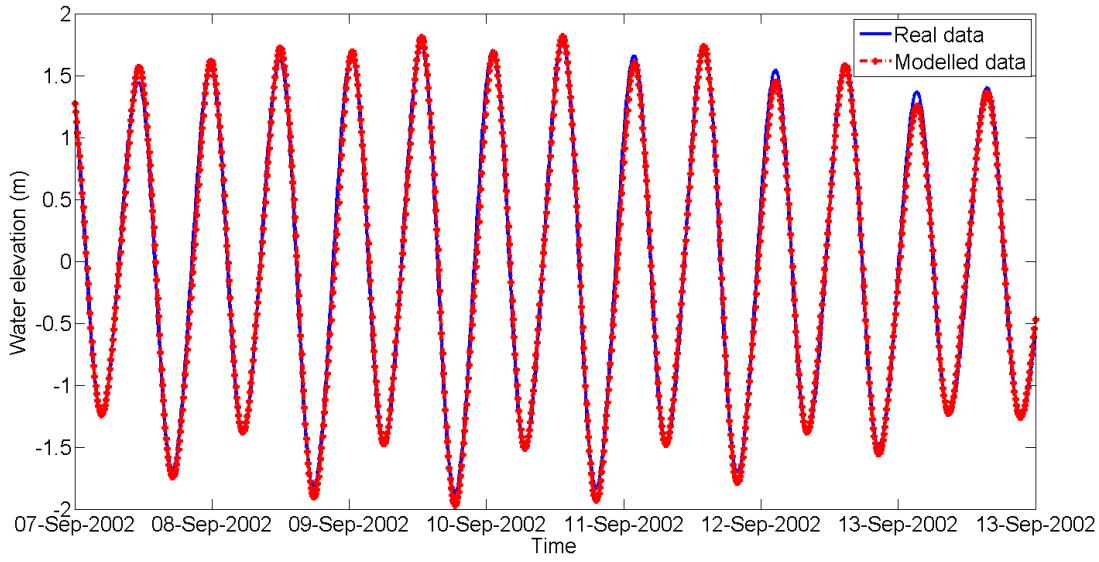

Figure 5.2 – The time series water elevation comparison at BT between real data and base simulation

It can be seen in Figure 5.1 and 5.2 that at FT site, the model captured tidal peaks and troughs less accurately than at BT site. For the bias, the same trend can be seen at the FT site where the negative bias values indicate that the model under predicts the observations (Table 5.4). In term of the bias magnitude, the values at FT is much larger

than that at BT. The reason is that the FT tide gauge is in the shallow area where the wave effects cannot be ignored, which is not considered in the present hydrodynamic module. Furthermore, the measured values in the shallow area may have more measured errors. Additionally, the boundary conditions that the hydrodynamic model used was introduced from the model Domain A in which several tidal components were chosen, whereas the tide gauge at 'Felixstowe' has measured the real water elevations which includes all the tidal elevations. Therefore, differences between measured and modelled water levels are tolerable.

As Figures 5.1 and 5.2 show the modelled tides have no phase error compared to the measured data in both FT and BT tide gauges. Therefore, the results reveal that the baseline model can reproduce the water elevation well in the study area with the calibrated parameters.

Table 5.4 —The bias parameters on water elevations at the two sites between observation and simulation of baseline model.

	MAE	RMSE	$Bias_a$	$Bias_m$
FT	0.2408	0.3054	-0.1957	-0.1658
BT	0.0634	0.0792	0.0085	0.0187

Note: FT—stands for Felixstowe Tide gauges; BT—stands for Bawdsey Tide gauge.

5.3.2. Wave module calibration and validation

In order to reproduce wave conditions in the model domain, the third-generation SWAN wave model was used which has been explained in detail in Chapter 4. In SWAN model, the stationary mode was used based on the assumption that wave propagation from the boundary to the coast takes place instantaneously. In this case the time has been omitted from the action balance equation which makes model computation timesaving and unconditionally stable.

In wave propagation, the wind impact on wave is not negligible due to significantly large wind velocities exist and the wind direction sometimes being opposite to the

wave direction. In all cases used in the following sensitivity analysis, a space uniform and time varying wind condition was used in the model. This wind data from the hindcast wave model at the site of FW_H (from WAVEWATCH III based on global simulations) was used. This means the whole area of domain is assumed to use the same wind data as that at FW_H.

5.3.2.1. The simulations in the year of 2002

a. Sensitivity analysis

The SWAN model contains numerous parameter input options for wave simulation in which some of them have more significant impact on the results than others. In this section, the results of sensitivity tests that use the selected parameters given in Table 5.5 are presented and discussed.

Table 5.5 – Wave related input options

online wave-related input parameters				
model parameters	base simulation	test series 1	test series 2	description
wave forces	**dissipation**	radiation stresses	/	wave forces at surface
bottom friction	**Jonswap (0.067)***	Collins (0.015)	Madsen et al. (0.05)	dissipation due to bottom friction
spectral shape	**Jonswap**	Pierson-moskowitz	Gauss	boundary spectral input

*: default value of coefficient

All simulations cover the same time frame with the pure hydrodynamic simulation above. The hindcast data at Felixstowe wave rider location (FW_H in Figure 4.8) was selected to calibrate the results of the sensitivity tests. It should be noted that the site of FW_H is located in Domain A but outside the regional Domain C. The simulations started on September 1st, 2002 and lasted for one month.

Table 5.6 – MAE & RMSE on significant wave height (H_s) at FW_H between tested series and baseline simulation.

	Wave forces		Bottom friction		Spectral shape	
	Radiation stresses	/	Collins (0.015)	Madsen et al. (0.05)	Pierson-moskowitz	Gauss
MAE	0	/	0.0669	0.0730	0.0100	0.0294
RMSE	0	/	0.0759	0.0956	0.0126	0.0417

As shown in Table 5.6, the calculated wave forces either based on the energy dissipation rate or the radiation stresses will have no impact on the significant wave height at the point FW_H however, in terms of dissipation due to bottom friction, three methods generate different significant wave heights. Although different types of spectral shape inputs can produce differences on significant wave height, the differences between them are small (within 0.05 in MAE and RMSE, not list here) which means it is acceptable to use the default wave spectrum (JONSWAP). So, both wave forces and spectral shape input were set to be default values (the same with that used in basic simulation).

Bottom friction

The bottom friction has an important contribution on wave energy dissipation which plays a significant role in wave-current interaction. The SWAN model provides three options: empirical model of JONSWAP (Hasselmann et al., 1973), the drag law model of Collins (1972) and the eddy-viscosity model of Madsen et al. (1988). In this sensitivity analysis, the JONSWAP model with coefficient 0.0067 and 0.0038, the 'Collins' model with coefficient 0.015 and 'Madsen et al.' model with coefficient 0.05 were tested. The modelled significant wave heights at FW_H are shown in Figure 5.3.

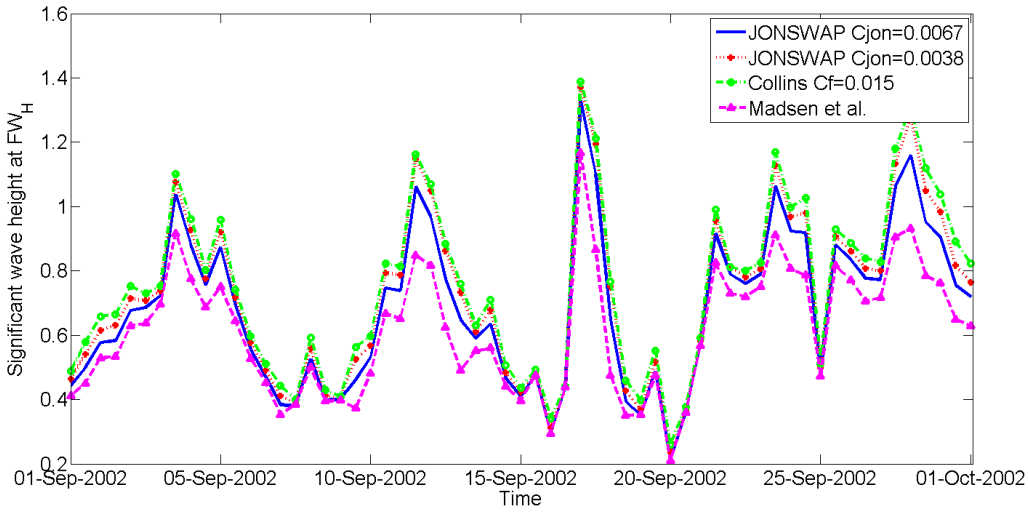

Figure 5.3 – Comparison of the significant wave height at FW_H between different bottom friction methods.

It is seen that the 'Collins' and the JONSWAP (Cjon=0.0038) models produce higher significant wave heights than the default option (JONNSWAP with Cjon=0.0067) while 'Madsen et al.' method produces a smaller significant wave height. This is because 'Collins' method may underestimate the energy loss (Collins, 1972) while 'Madsen et al' method makes bottom turbulent flow as a dissipative process (Madsen et al., 1988).

Table 5.7 – Accuracy and bias between tested cases and the default method (JONSWAP with Cjon=0.0067)

	Cjon0038	Collins	Madsen et al.
MAE	0.0389	0.0669	0.073
RMSE	0.0475	0.0759	0.0956
$Bias_a$	0.0389	0.0669	-0.0727
$Bias_m$	0.0468	0.067	-0.0565

Although, as Table 5.7 shows, discrimination exists between these methods, the impacts on the significant wave height between them is not significant even if the simulated results do not reproduce the measured wave height, switching between these options will not make a significant difference to the results. Thus, for convenience, the

default bottom friction method which is JONSWAP with the coefficient of 0.0067 is used in this study. Apart from the comparison at this deep site (FW_H), the difference on the significant wave height at the shallow water is also minimal.

b. Validation of the wave model

For validation of the wave model, the results from the base case simulation and 'Madsen et al.' simulation were selected to compare with the hindcast wave data at the site FW_H since these two methods are the most sensitive to significant wave height. The comparison is shown in Figure 5.4.

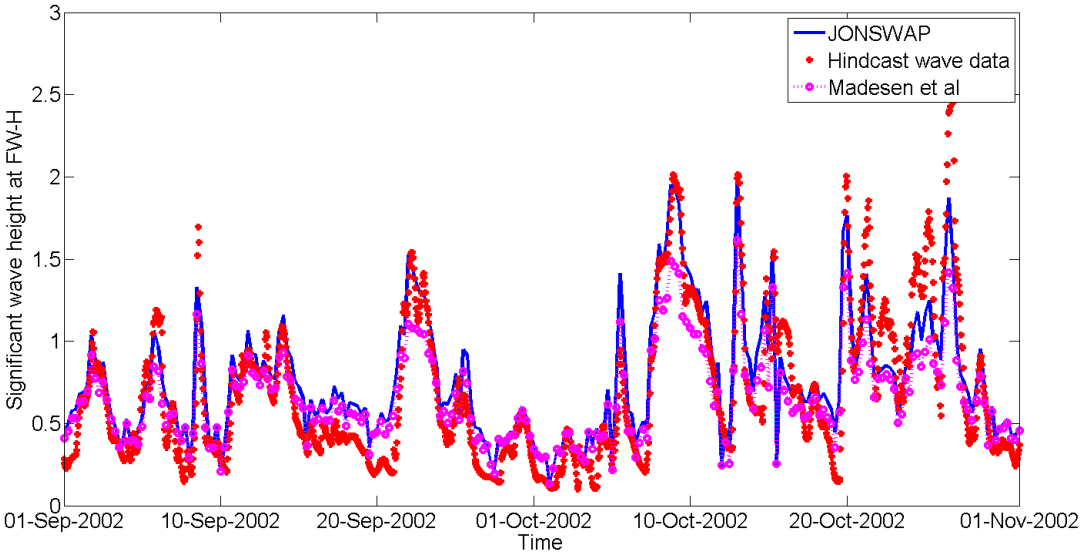

Figure 5.4 – the comparison on significant wave height at FW_H between simulated results and hindcast wave data.

It can be seen that the model used JONSWAP bottom friction method can reproduce the hindcast wave data accurately while 'Madsen et al.' method underestimated the significant wave height particularly at high wave heights shown in Figure 5.4. For the accuracy and bias between simulated results and hindcast data, the JONSWAP bed friction plays better (Table 5.8). So it is acceptable to use the JONSWAP method as a calculation of bottom friction in this study.

Table 5.8 – The accuracy and bias between the two simulated results (JONSWAP and Madsen et al.) and hindcast wave data at FW_H.

	Accuracy		Bias	
	MAE	RMSE	Biasa	Biasm
JONSWAP	0.1704	0.2176	0.0721	0.1298
Madsen et al	0.1724	0.2383	-0.0325	0.0459

5.3.2.2. Extra validation in the year of 2012

Since the wave site FW_H is in the Domain A but outside the Domain C, it will be credible if the results at model Domain C can be validated. Although there is a tidal gauge (FW in Figure 4.8) in the Domain C, data collection only commenced in 2012, which is outside of the present simulation period. So, an additional model simulation of 2012 took place in order to validate the regional model (Domain C).

While the most important parameters of model are set up previously, it is possible to use a more time-consuming coupled online model (FLOW model + SWAN model) in order to generate more realistic results. In this process, the hydrodynamic model without sediment module is coupled with the calibrated SWAN model above, which means the various water elevations have been included. This simulation ran from October 2012 to December 2012 with online coupled wave-flow process. In this case, the wave data both at FW and FW_H are used to compare the simulated results.

a. Site FW validation

A comparison between the modelled significant wave heights and measured data at FW is shown in Figure 5.5. Since the communication interval between these Wave and Flow models is 12 hours, the simulated wave properties are stored in every 12 hours which means that during this 12-hour time period the flow model is using the same wave properties. The comparison is shown in Figure 5.5.

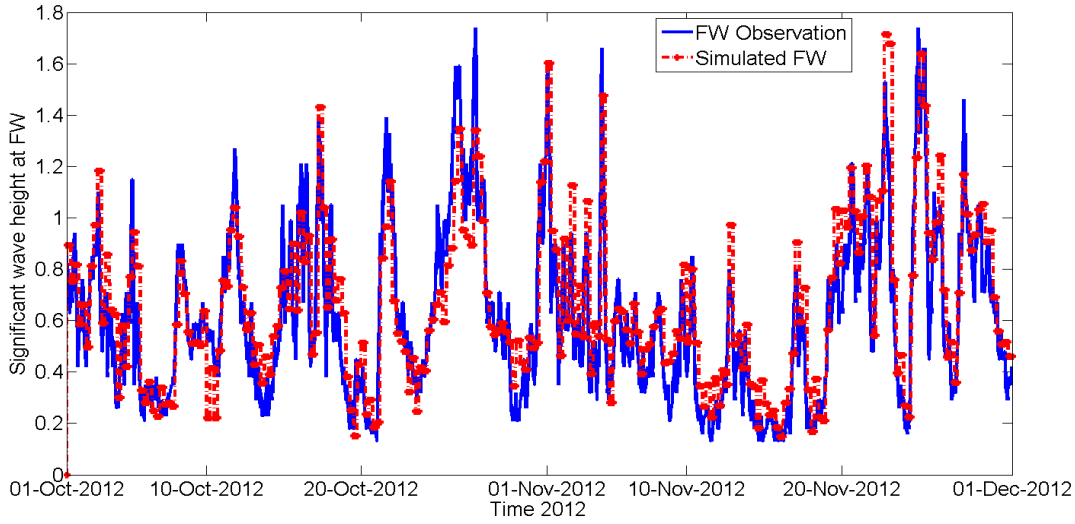

Figure 5.5 – Comparison of significant wave height at FW between measured data and simulated results from October of 2012 to December of 2012.

Figure 5.5 shows that the model can reproduce wave conditions very well. The MAE and RMSE between them are 0.1436m and 0.196m separately while the mean bias is 0.0475m and median bias is 0.0194m (Table 5.9). So, in terms of significant wave height, the regional model (Domain C) can produce the measured results very well.

In terms of modelled wave directions, Figure 5.6 provides a comparison of measured and simulated wave directions at FW wave rider. The model is mostly able to reproduce wave direction at FW, however, some exceptions can be seen. This is partly because the wave module was using the selected time series wave data with larger time interval (every 12 hours) from the boundary wave condition, which means they may miss some wave directions from the boundary condition in the 12-hour interval.

The errors are mostly caused by the simplification on the wave boundary conditions rather than by the module itself. Therefore, the model is confirmed to be able to reproduce the wave direction with good accuracy (Figure 5.6), in addition to its ability to correctly reproduce wave heights.

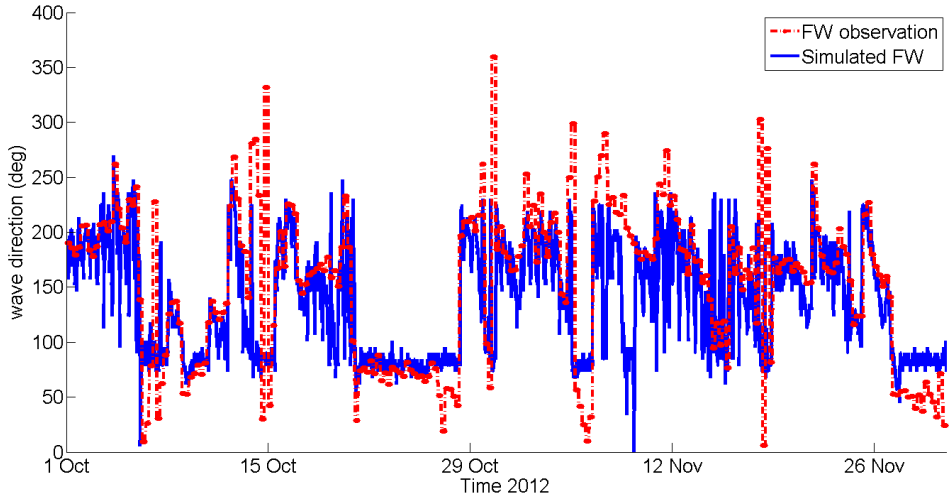

Figure 5.6 – The comparison on wave directions at the site of FW between measured data and simulated results from October of 2012 to December of 2012.

b. Site FW_H validation

In addition to the aforementioned comparisons in 2002, the validation of the regional model in 2012 was carried out using hindcast wave data at FW_H. Figure 5.7 shows the differences between hindcast and modelled significant wave height at FW_H from October of 2012 to December of 2012 period.

The Figure 5.7 shows that the significant wave heights are under-estimated for a few peaks. The MAE and RMSE at FW_H is 0.269m and 0.370m respectively while the mean bias is -0.016m and the median bias is 0.044m (Table 5.9). The differences between the modelled and hindcast results can be attributed to three aspects. Firstly, the numerical techniques and formulations for wind input and the whitecapping in SWAN model is different with WAVEWATCH III so that it will generate slightly different results (SWAN user manual, 2017). Secondly, the time window of SWAN model is every 12-hour. This means some values within two successive time windows would be missed which probably results in that some peaks are unable to predict. Finally, this extra model is using a totally different time frame from the model that is validated in the flow model section. Even though the boundary conditions and initial bathymetry have switched to the year of 2012, the parameters used in the previous flow model did not change. For example, the roughness and sediment distributions in

this new bathymetry is the same with that in the year of 2002. Thus, the lack of revalidated flow model may affect the wave results when using the online coupled flow-wave model. Apart from a few peaks, the entire trend of significant wave height variation can be predicted by the model.

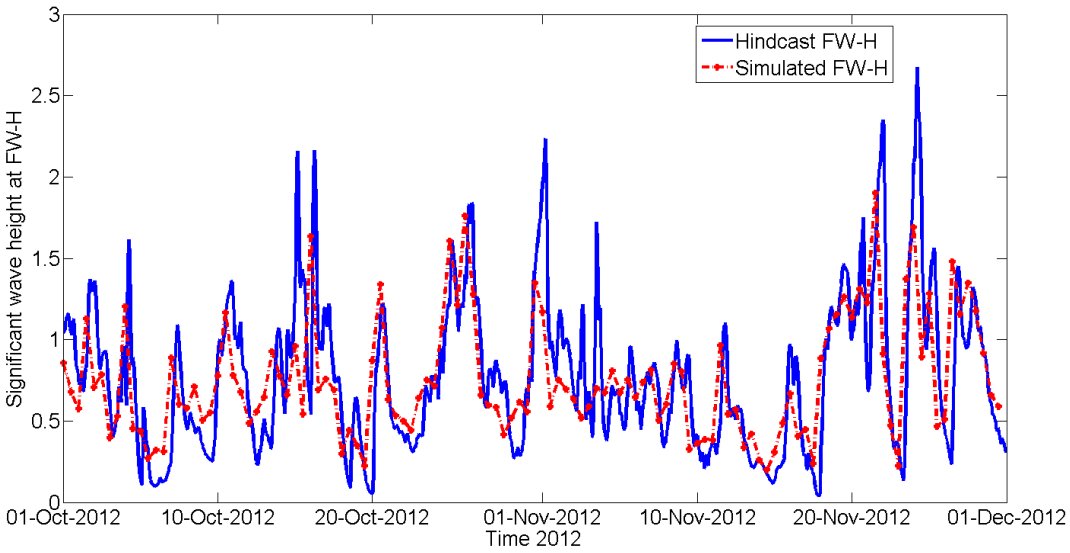

Figure 5.7 – The comparison on significant wave height at FW_H between the simulated model and hindcast wave results in the year of 2012.

By considering the errors from the model itself and the process of boundary reduction, the results generated from the calibrated models can be said to be reliable for an appropriate reproduction of the wave properties.

Table 5.9 – The accuracy and bias of the modelled significant wave height during the simulation of 2012

	Accuracy		Bias	
	MAE	RMSE	$Bias_a$	$Bias_m$
FW	0.1436	0.1961	0.0475	0.0194
FW_H	0.2692	0.3698	-0.0159	-0.0438

5.3.3. Morphodynamic calibration and validation

It is essential to validate the model for morphodynamics simulations before applying for the specific estuary. The available data of annual bathymetries of the Deben Estuary inlet allows morphodynamic validations to be taken in detail. However, morphodynamic simulations of long time periods take significant computer resources and time. To overcome this, the 'Morphological acceleration factor (Morfac)' available in the Delft 3D modelling suite will be used. But a calibration of Morfac values is necessary.

1) Model sensitivity to Morfac

Before morphodynamic simulations are carried out, a suitable Morfac value should be selected so that the model does not distort the final bathymetry or take up excess time. Since the annual bathymetry data is available at the detailed Deben inlet, the basic morphodynamic model should simulate at least one year of bathymetry change with no morphological acceleration (from 1st of September 2002 to 1st of September 2003 with Morfac=1). The other tested models with different Morfac values are carried out for comparison.

All the above simulations use the optimised hydrodynamic conditions discussed previously but are not included the wave module to save the modelling time as the coupled process is time-consuming. However, the morphodynamic related parameters, such as sediment transport formula, are defined as default before the morphodynamic model was validated to simplify the process.

Since the modelled area is morphodynamically complex it is assumed that Morfac values should not be overly large. Based on that, in this study several test values were chosen (Morfac=10, Morfac=12, Morfac=20, Morfac=24). The resulted final bathymetries are shown in Figure 5.8, together with the baseline simulation (Morfac=1).

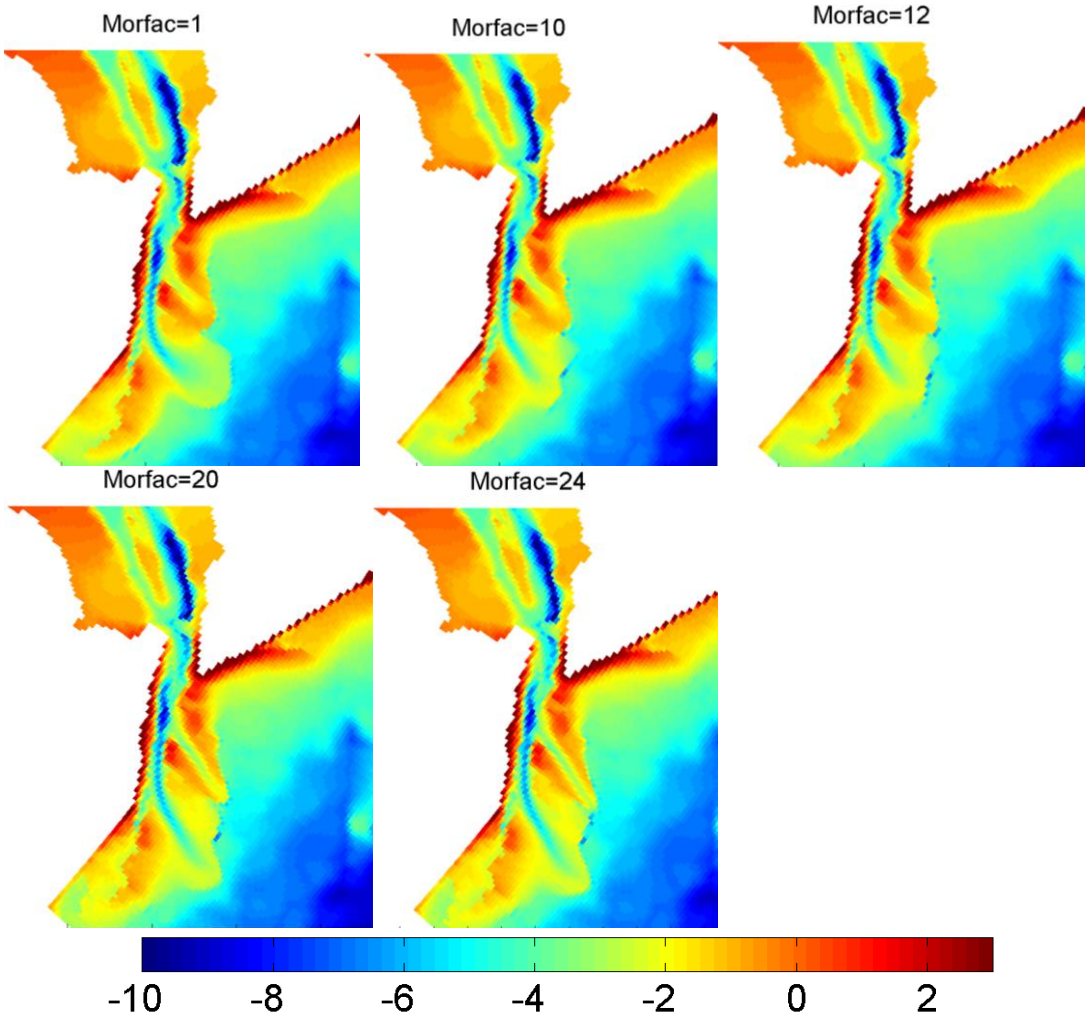

Figure 5.8 – The final bathymetries from the cases using different Morfac values after one morphodynamic year simulation; the base model is Morfac=1 (the first one)

The models are running on the ACPI ×64 – based PC with 8 Intel Core i7-3770 CPU processors. The baseline simulation lasts for approximate three weeks while the model with Morfac=10 only lasts for around two and half days. The model using Morfac=12 makes the model running time within two days while the model of Morfac=24 has reduced the simulation time into two hours. Therefore, with the increase of Morfac values, the CPU time has reduced significantly so that the model become more efficient. However, in terms of the accuracy, the assessments of the performances between them should be carried out.

Skill performance

In this case, the simulated bathymetries resulted from the selected Morfac values were compared with the baseline simulation with Morfac=1. Therefore, BSS for this application can be translated into:

$$BSS = 1 - \frac{\left\langle \left(Z_{MorfacN} - Z_{Morfac1} \right)^2 \right\rangle}{\left\langle \left(Z_1 - Z_{Morfac1} \right)^2 \right\rangle} \tag{5-10}$$

Where $Z_{MorfacN}$ stands for the final bathymetry of model with Morfac=N ($N \neq 1$); $Z_{Morfac1}$ is the final bathymetry of model with Morfac=1; Z_1 stands for the initial bathymetry.

According to this equation, a BSS value of 1 indicates a perfect match between baseline simulation and simulations with Morfac higher than 1.

Area BSS skill

For 2D model, the BSS is calculated using the entire model domain instead of cross-sections. So, the averaged process is carried out in both directions (longshore and cross-shore) (Table 5.10). According to the skill performance criteria shown in Table 5.11, the models with Morfac values under 12 gave 'good' performances when compared with base model. Morfac values of 20 or above gave 'fair' performance.

Table 5.10 – The BSS skills of the whole modelled area with different Morfac values (based on the base simulation Morfac=1)

	Morfac=10	Morfac=12	Morfac=20	Morfac=24
BSS	0.75	0.72	0.55	0.46

It is possible to consider the target morphological time and the available time period of hydrodynamic data before choosing the reasonable Morfac value. In this study, the Morfac values below 12 are all available to produce good performance.

Table 5.11 – Qualification of error ranges of process parameter(L.C. van Rijn, 2003).

Qualification	Morphology BSS
Excellent	1.0-0.8
Good	0.8-0.6
Reasonable/fair	0.6-0.3
Poor	0.3-0
Bad	<0

In addition, the nonlinear relationship (which is not considered in previous Morfac test cases) between the bed bathymetry and wave impact is also important in determining the Morfac values. Two series of test models were carried out (not listed here): in one case, the wave models use the bed updating from flow models, in the other, the wave models do not use the updating bed from flow models. For the same Morfac, the former models performed better than the latter done. However, in terms of realistic physical processes, the updating bathymetry from flow model cannot be ignored when considering the wave impact. This comparison highlighted that the Morfac value can be increased greatly when the impact of wave is not considered.

Cross-sections performance

In order to investigate the model performance in detail, several cross-sections were selected for further analysis (Figure 5.9). The most dynamic profiles of the estuary are the middle section of the ebb delta areas: Profile 3 and Profile 4 (Figure 5.9). The cross-section profile performance BSS skills are shown in Table 5.12. Almost all the results, except for Profile 5, are in the ‘fair’ category, for Morfac values of 12. This part of the estuary is extremely dynamic and show complex morphodynamic behaviour, which makes it difficult to model accurately. Accounting for that, it is reasonable to use Morfac=12 in this model.

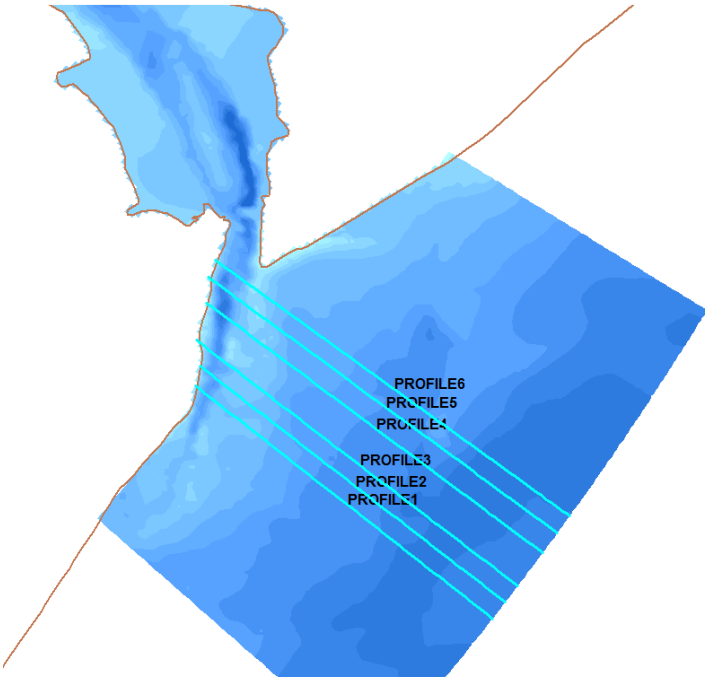

Figure 5.9 – The selected cross sections for the BSS analysis in the validation process

Profile 5 performs better while the Morfac value increased. However, this profile shows no significant difference during the baseline model simulation (Figure 5.9) which indicates that this skill is not always validating the model performance very well. For those profile with no great changes (in the case of $(z_1\text{-}z_{morfac1})\approx 0$), the BSS will probably be very small even if the difference between the tested models and base model is minimal.

Table 5.12 – The BSS of the different Morfac values based on the basic model (Morfac=1).

	Morfac=6	Morfac=10	Morfac=12	Morfac=20	Morfac=24
P1	0.71	0.53	0.52	0.53	0.52
P2	1.00	0.47	0.45	0.40	0.42
P3	0.61	0.55	0.39	-0.16	0.13
P4	0.14	0.64	0.43	0.47	0.44
P5	-0.07	0.36	0.45	0.41	0.53
P6	1.00	1.00	0.98	0.30	-0.03
Averaged	0.57	0.59	0.54	0.33	0.34

2) Sediment and morphology calibration and validation

To investigate the model's ability to capture the morphodynamic change of the estuary, first, the initial bathymetry of the estuary was set to the measured bathymetry in 2002, as aforementioned. Then the model was used to reproduce the measured bathymetry in 2003. All model parameters were set to be determined values from sensitivity and validation analysis of flow and wave modules before. The primary reason to select the 2002-2003 period was that measured wave data to be used as the offshore boundary condition is available at West Gabbard from May 2002. The morphodynamic-related parameters will be calibrated and validated in this section.

In this validation process, the Morfac value of 12 is used. The comparison between modelled final bathymetry (2003) and real bathymetry (bathymetry in 2003) will be carried out.

Bottom roughness

The most important parameter for sediment transport is the bottom roughness which is indicated by Chèzy coefficient. Sedimentologically, the Deben ebb-tidal delta is defined as mixed sand-gravel which is strongly bimodal medium sand and gravel composition. So the bottom roughness should be larger than that for pure sand bed (default in the model) which means the Chèzy coefficient that used in this study should be smaller than the default value (which is $65 m^{1/2}/s$). In the validation process the Chèzy coefficient values (spatial uniform) are chosen as ($m^{1/2}/s$): 15, 25, 45, 65, as shown in Table 5.13.

Sediment transport formulae

In Delft 3D, several sediment transport formulae options are available. Since the wave impact cannot be ignored in this study, only formulae that can calculate the wave impacts were selected: Van Rijn (1993), Bijker (1971) and Soulsby (1997).

In order to select the best sediment transport formula in the morphodynamic model, the above three formulae were tested as shown in Table 5.13. All the abbreviations in Table 5.13 are explained in 'Description' column in the table. The process is to pick

up the most reliable Chèzy coefficient in VR simulations (here is 45$m^{1/2}$/s), then use it to conduct proceeding simulations, which will be discussed in the next section.

Table 5.13 – Tested sediment transport formulae and calibrated cases for morphodynamic model.

Calibration coefficient				Chèzy coefficient $m^{1/2}$/s				Description
VR	/			15	25	45	65	VR--Van Rijn (1993)
B	0.05, 0.02*	0.1, 0.04	0.5, 0.2	45				B--Bijker (1971)
S	0.2	0.6	1					S—Soulsby (1997)

*The numbers stand for calibration coefficient for shallow water (BS) and deep water (BD) (Delft 3D User Manual, 2014).

Van Rijn (1993)

The final simulated bathymetries from the models using VR model with Chèzy coefficients given in Table 5.13 are shown in Figure 5.10 with their comparisons between the measured bathymetry of 2003. It shows that the VR models with Chèzy coefficient 45$m^{1/2}$/s were best reproduced the final 2003 bathymetry.

In terms of VR method with Chèzy coefficient of 65$m^{1/2}$/s (default option in Delft 3D), the model overestimated the sediment transport volumes at the ebb jet region and the north part of ebb shoal although it can reproduce the ebb jet direction well (Figure 5.10). This formula generates a new small channel at the middle of the delta bar which does not exist in the real bathymetry. But for VR models with Chèzy number below 45$m^{1/2}$/s, the bathymetries were not able to change a lot, which means the rougher the bed is, the less sediment was transported.

Since the Chèzy coefficient 45$m^{1/2}$/s has been selected, other two formulae can also use the same Chèzy number (45$m^{1/2}$/s) since they have their own calibration coefficients available for calibrating accordingly. This will significantly decrease the number of simulation cases necessary for calibrating Bijker (1971) and Soulsby (1997)

formulae. So, for the simulations using Bijker (1971) and Soulsby (1997) formulae, the constant Chèzy number ($45m^{1/2}/s$) is used with different calibration coefficients (Table 5.10).

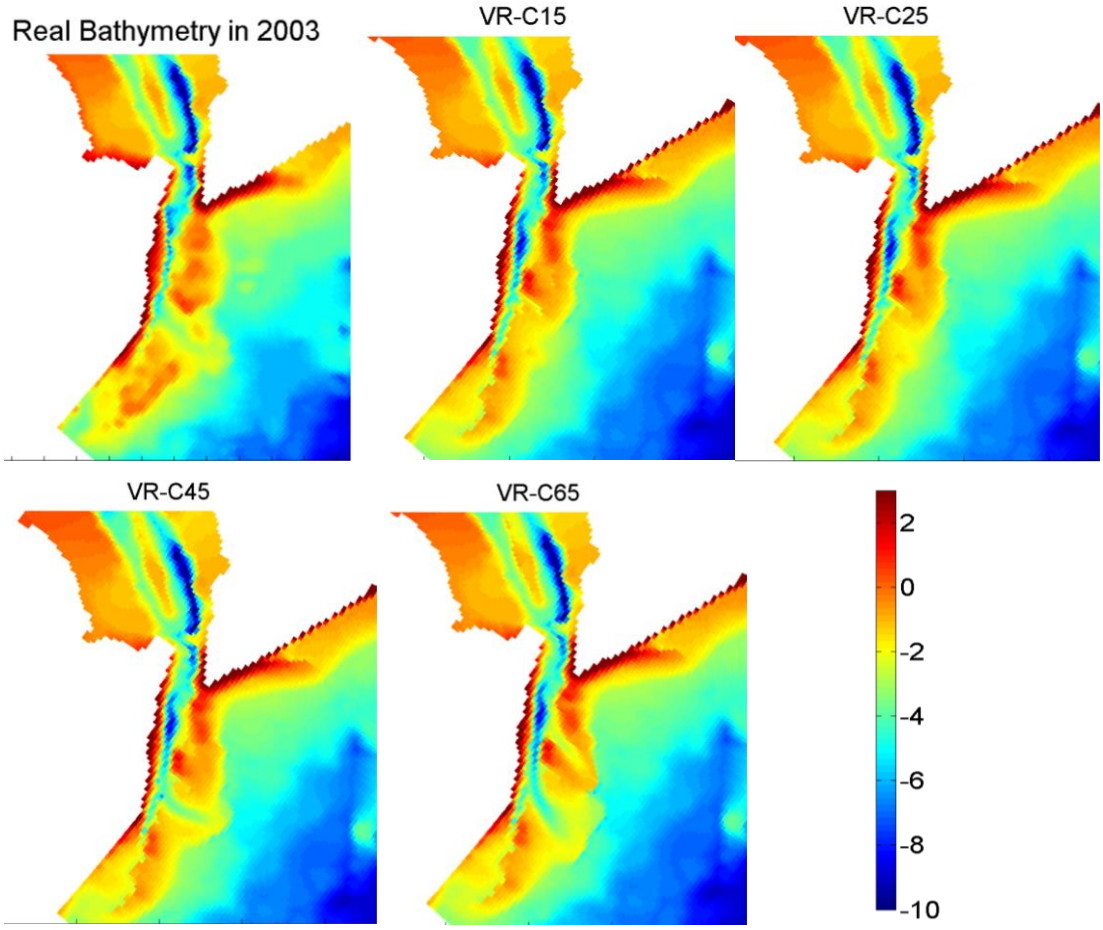

Figure 5.10 – Final bathymetry of VR models with different Chèzy coefficients and the real bathymetry.

Bijker (1971)

For the Bijker (1971) model series, the large calibration coefficient (e.g. BS=0.5, BD=0.2) seems to overestimate sediment transport since the Figure 5.11 shows that in the middle of ebb shoal a new channel was appeared, which is not developed in the real situation (Figure 5.11). Additionally, the sediment on the ebb delta region in the Knolls is eroded more severely than that in real 2003 bathymetry. Both the northern

part of ebb shoal and the ebb jet have experienced more erosion than that can be seen in the real 2003 bathymetry.

When the calibration coefficient values are reduced (BS=0.05 and BD=0.02), the model reproduced 2003 bathymetry very well except for underestimating the accretion on the frontage of downdrift delta slightly (south). But this is the most reliable coefficients among these cases. It is therefore considered that Bijker (1971) formula with coefficient BS=0.05 and BD=0.02 gives the best results.

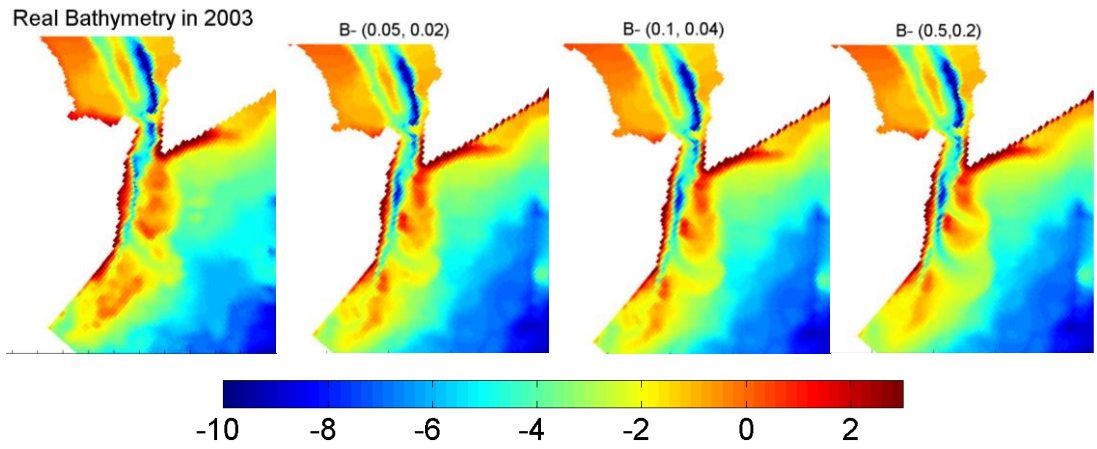

Figure 5.11 – Final bathymetries with different calibration coefficient of Bijker (1971) formula

Soulsby (1997)

In terms of Soulsby equations, the most accurate model is the one using calibration coefficient of 0.2 (Figure 5.12). However, all the models in this group were not able to accurately reproduce the ebb jet as deep as that in the real 2003 bathymetry (Figure 5.12). In addition, the eroded area at the ebb jet is expanded greatly in these cases and sediment here deposited towards to the offshore. Therefore, it can be concluded that the Soulsby formula is unsuitable for this application.

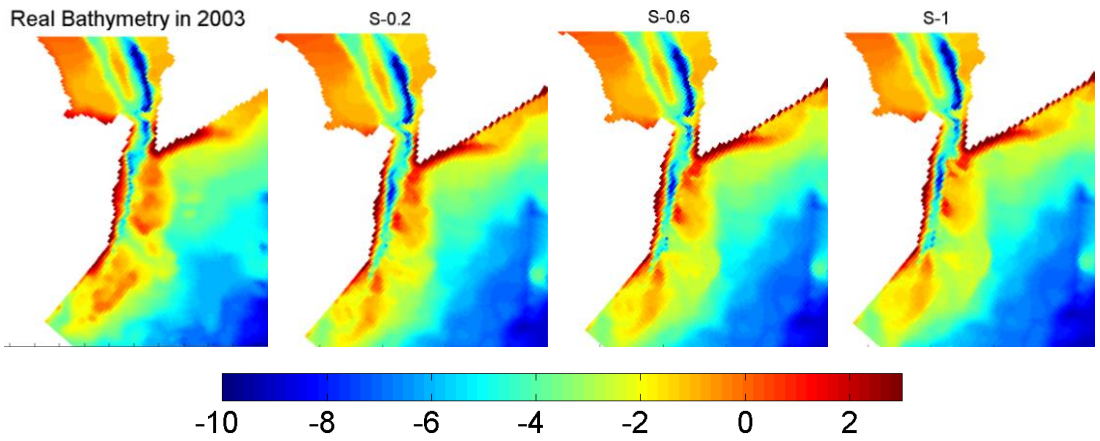

Figure 5.12 – Final bathymetry with different calibration coefficient of Soulsby (1997) model

However, it is not sufficient to validate the model just in the aspect of quality. In order to verify the model more accurately, it is necessary to validate the model in a quantitative way. The following discussion will focus on both the whole area and several chosen profiles. Some cases that have a higher BSS values do not generate a similar bathymetry in eye fit aspect: this can be found when the BSS value of VR_C25 is larger than the value of VR_C45, but the VR_C25 model has not captured the main feature of the real bathymetry. In order to reduce the comparison work and avoid the misleading of BSS, only the best model in every group has been chosen: VR_C45, B_(0.05,0.02) and S_0.2.

Area skill performance

Even though the numerical model cannot reproduce the real bathymetry change exactly, the morphological model that used in this study satisfactorily reproduced the morphological change of the Deben Estuary. It should be noted that, there is no exact sediment transport formula available in Delft 3D that can simulate the mixed sand-gravel sediment that exist in the Deben Estuary. Considering this and the complexity of the morphodynamic characteristics of the estuary, it is satisfactory to develop a model that can accurately simulate most important morphodynamic trends of the estuary as the interest is on investigating climate change impacts on the estuary morphology process.

As discussed in the last section, only quantitative comparisons are done so far to determine best sediment transport model parameters: VR_C45, B_(0.05, 0.02) and S_0.2. The area BSS of these models are -0.13, 0.012 and -0.05 respectively. It shows that all the BSS values in these three models are very low, even though they have provided the best estimation among these models. The best performance is B_(0.05,0.02) in these cases. However, this is not surprising in dealing with complex morphodynamic simulations. In order to judge the model performance further, it is necessary to explore the performance of the model in recreating some important profiles in the ebb delta region of the estuary.

BSS of longshore and cross shore profiles

In order to investigate the model performance further, a set of measured and simulated profiles across the ebb delta region was chosen (Figure 5.13).

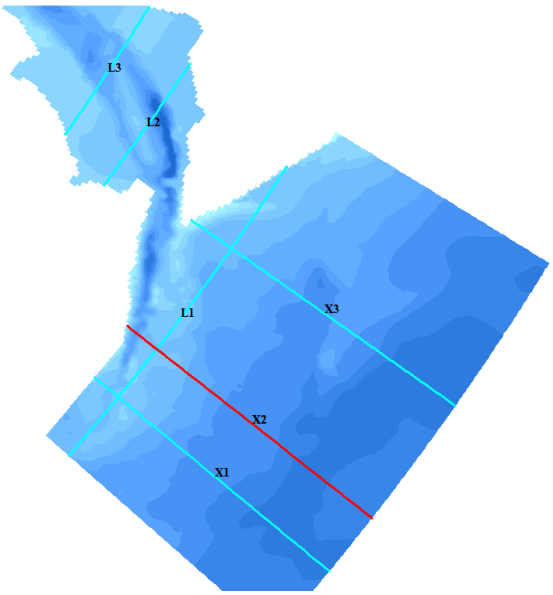

Figure 5.13 – The cross sections that are chosen to be validated

The initial and final cross-section of the selected profiles in three modelled cases are shown in Figure 5.14 associated with the real bathymetry. It can be seen that the B_(0.05,0.02) model reproduced the profile most accurately.

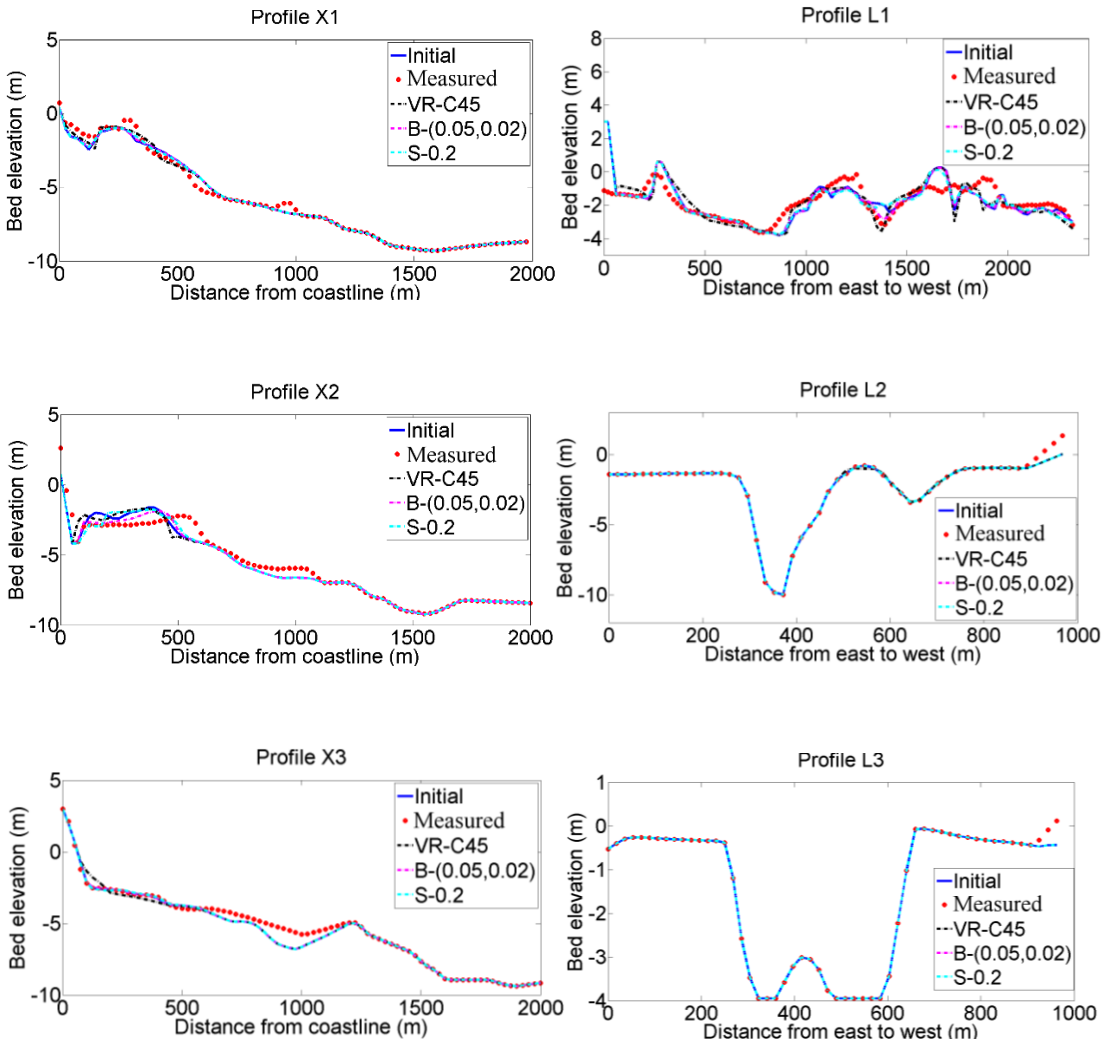

Figure 5.14 – The comparison on bathymetry of selected profiles between different models and the initial/real bathymetry

Taking Profile X2 as an example (Figure 5.15), only the B_(0.05,0.02) can reproduce the same trend as the real bathymetry: erosion within the first 500m and accretion after 500m, even though it cannot predict the exact erosion/accretion values.

According to the analysis of the most dynamic profile, the best model is B_(0.05, 0.02). There are numerous reasons to be noted for discrepancies between modelled and measured bathymetry change: (i) simplified wave boundary condition; (ii) use of single sediment fraction in morphodynamic model; (iii) simplified spatial variation of sediment used in the model; (iv) model not being able to capture some complex

morphodynamic processes; (v) limitation of sediment transport formulations used for sand-gravel mixed sediment environment.

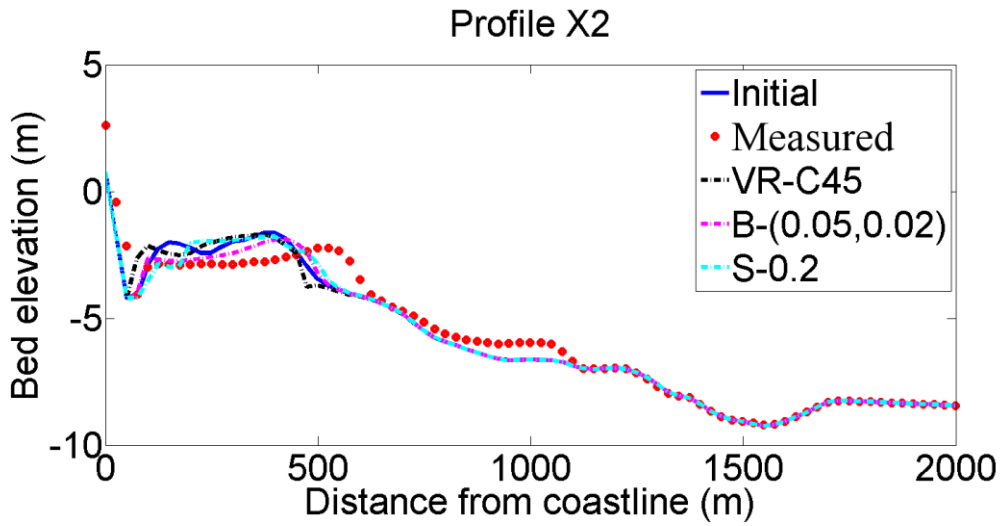

Figure 5.15 – The detail bed elevation of profile X2

In summary, although none of the model can reproduce the real morphological changes exactly, the closest is the model using Bijker (1971) sediment transport formula with the coefficient B_(0.05, 0.02) as it can capture the trend of the morphological change in Deben Estuary. Therefore, Bijker (1971) formula will be used in morphodynamic simulation presented and discussed in the following chapters.

5.4. Summary

The flow, wave and morphology models of the Deben Estuary were calibrated and validated in aspects of hydrodynamic, wave and morphodynamics based on the available data.

The validated hydrodynamic model is able to reproduce tidal water levels in the model domain accurately. Unfortunately flow velocity measurements are not available within the model domain for model calibration and validation.

For the wave validation, the time series of measured and hindcast significant wave heights at two locations within the model domains are used. The model is successfully validated to reproduce wave heights and directions.

Morphodynamically, Bijker (1971) equation proved to be the best choice to capture sediment transport and morphology change of the Deben Estuary, in the absence of an appropriate sediment transport formula for sand-gravel mixed sediment that dominated the outer Deben Estuary.

Chapter 6: Climate changes around Deben Estuary

Since this study is focused on investigating the impacts of global climate change on the Deben Estuary morphology, it is necessary to discuss the climate change conditions around the Deben Estuary. The most significant aspects of global climate change are Seal Level Rise (SLR) and changes in storm climate (IPCC, 2000).

6.1. Sea Level Rise (SLR)

Sea levels have risen globally for the last few hundred years due to global warming. The global average rate of SLR over the last 6,000 years is about 0.5mm/yr, and over the last 3,000 years, is 0.1 to 0.2 mm/yr on average. This value has increased to 1.0 to 2.0 mm/yr during the 20^{th} century with a central value of 1.5mm/yr (IPCC, 2000). The most important factors that affect present-day sea level change are ocean thermal expansion, which leads to an increase in ocean volume at constant mass, the melt of glaciers and ice caps and Greenland and Antarctica adjustment to past climate change. But after the 21st century, SLR will be heavily influenced by green-house gas emissions. Thermal expansion is expected to be the largest contributor to absolute SLR over the next 100 years (IPCC, 2000).

In terms of regional sea level changes, the changes in the geographical pattern that reflect ocean circulation and the regional density changes should also be considered. The sea level change situations for the UK with three emission scenarios (Low emissions, Medium emissions and High emissions) have been carried out by considering the combination of thermal expression of oceans, land ice melt components and both isostatic and tectonic vertical land movement in UKCP09 report (Jenkins, et al., 2008).

By combining the UK's absolute time mean sea level change with the land movement estimates taken from Bradley et al. (2009), the Relative Sea Level Rise (RSLR) at four UK sites: London, Cardiff, Edinburgh and Belfast, have been reported in UKCP09 with the uncertainty of eustatic SLR (Figure 6.1). Figure 6.1, which ignore land movement uncertainty which is smaller than that in the absolute SLR estimates, shows variations among these sites due to vertical land movement. It has been reported that

the northern part of UK has uplift movement of the land while the southern part experiences downlift movement (Jenkins, et al., 2008, Bradley et al., 2009).

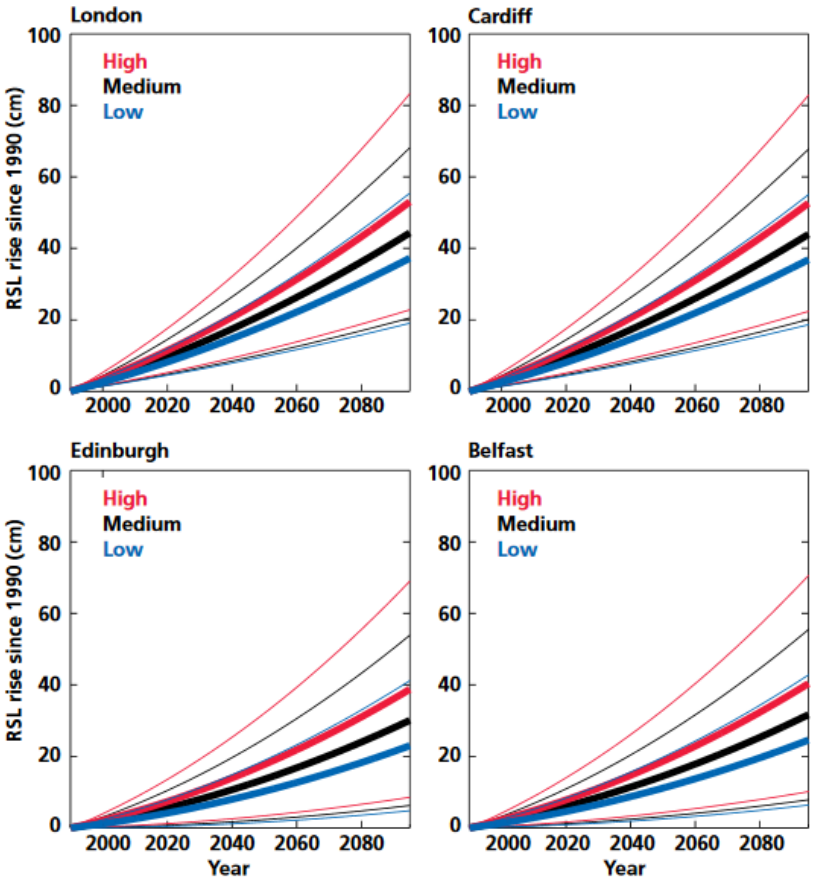

Figure 6.1 – The RSLR over the 21st century with central estimate values (thick lines) and 5th and 95th percentile limits of the range of uncertainty (thin line) for four sample locations around the UK based on three emission scenarios in which the 'London' site is the nearest to the Deben Estuary. (UKCP09 report)

For the morphodynamic modelling of the Deben Estuary, located in the southeast UK, sea level data of 'London' from UKCP09 was selected (Figure 6.1). In the 'London' site, the lower percentile limits of RSLR (5th percentile) of all the three emissions are around 20cm by the end of this century while the largest upper percentile limits of RSLR (95th percentile), which belongs to the high emission scenario, is around 80cm by the end of this century.

In order to consider the most possible sea levels in the future, one should consider the variation of the RSLR curve at 'London' site in Figure 6.1. So, three values are

considered here: 0.2m, 0.5m, and 0.8m. This is implemented by increasing the Mean Sea Level (MSL) by 0.2m, 0.5m and 0.8m at the end of the century respectively in the modelled scenarios. It did not use the central estimate values in every emission scenario because the difference between them is within 20cm which will not induce much difference on morphological changes in the region models.

6.2. Wave climate change

Increasing storminess is one of the observations of global climate change. This study investigated both the impacts from SLR and the implications of increasing storminess on the estuary's morphology.

Although there are several future projections of global wave climate, a new version of the Atmospheric General Circulation Model of the Meteorological Research Institute in Japan (MRI-AGCM3.2H) was used to obtain the sea surface wind data for wave simulation WAVEWATCH Ⅲ in this study (Mizuta et al., 2012; Shimura et al., 2015). The global domain of this wave simulation was set for the latitudinal range of 90^{o}S-67^{o}N over all longitudes with 1^{o}×1^{o} spatial grids. By considering the forcing of Sea Surface Temperature (SST), sea ice at the bottom boundary and greenhouse gases in the atmosphere, modelling has been conducted to simulate wave climate between 1979-2009 for the present scenario and between 2075-2099 for the future climate scenarios.

In this original projection, there are four future statistically-analysed SSTs (Murakami et al., 2012) defined as boundary conditions for MRI-AGCM3.2H (Shimura et al., 2015). However, this study only considers the first SST condition: the ensemble-mean SST projected by 18 models from phase 3 of the Coupled Model Intercomparison Project (CMIP3) (Meehl et al., 2007) under the A1B scenario of the Special Report on Emission Scenarios. Wave prediction points around the UK are shown in Figure 6.2.

The resolution of GCM model grid (1^{o}×1^{o} spatial grids) is still coarse for the regional coastal model of the Deben Estuary developed in this study. It is assumed that the selected data from the appropriate node of this model represent all the values of the area covered by this node. Then, the measured data at position of West Gabbard

WaveNet Site (WGW located at 51°58.96'N, 2°4.91'E), can be used to validate this global model by comparing it with the wave data at node 19 (Figure 6.2).

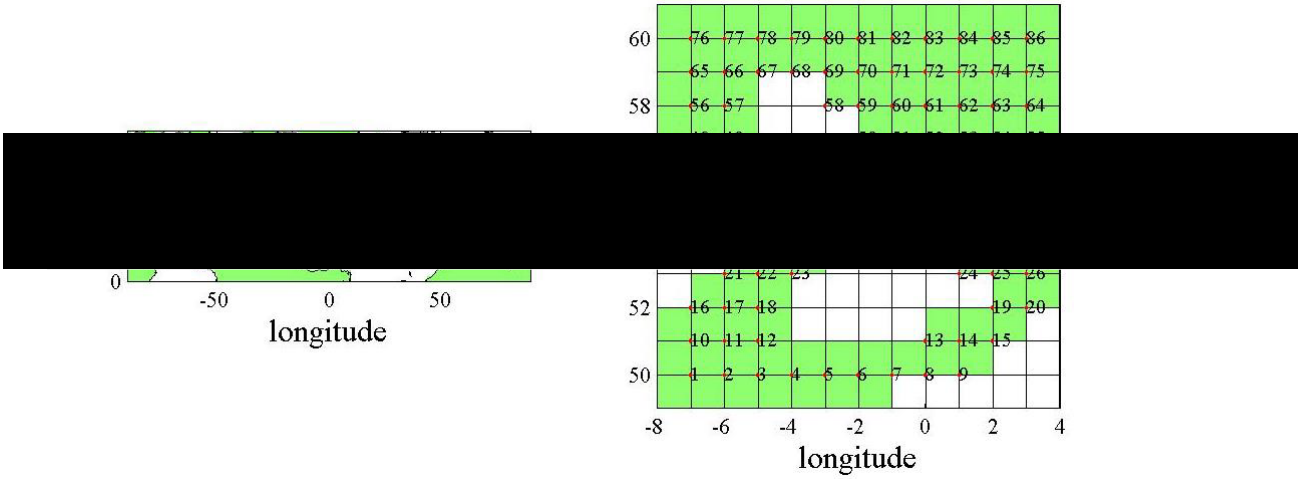

Figure 6.2 – The global WAVEWATCH III model (left) and the nodes around UK area (right) (Murakami et al., 2012; Shimura et al., 2015)

Both the data from 'present' and 'future' time slices at point 19 are selected. The data contains three wave properties: significant wave height (H_s), peak wave period (T) and wave direction (D). Firstly, the 'present' data of WAVEWATCH III model at point 19 is validated using the measured historical data at WGW which is provided by Cefas, Then the differences between present data and future data will be analysed for both calm and extreme wave conditions.

6.2.1. Global WAVEWATCH III model validation

The present wave data that covers the period of 1979 to 2009 contains 271750 time points with 1 hour interval. However, the observation data from West Gabbard Wavenet (WGW) wave rider is only available from 2002 to 2009. So, the overlapped period, which is from 2002 to 2009, in both global wave model data and measured data is used for model validation.

6.1.1.1. Statistical comparison

In order to investigate the reliability of the modelled data, statistic comparisons between 'present' modelled wave data and measured wave data were carried out. Both datasets' empirical Probability Distribution Functions (PDF) and Cumulative Distribution Functions (CDF) of significant wave heights (H_s) were compared and contrasted (Figure 6.3).

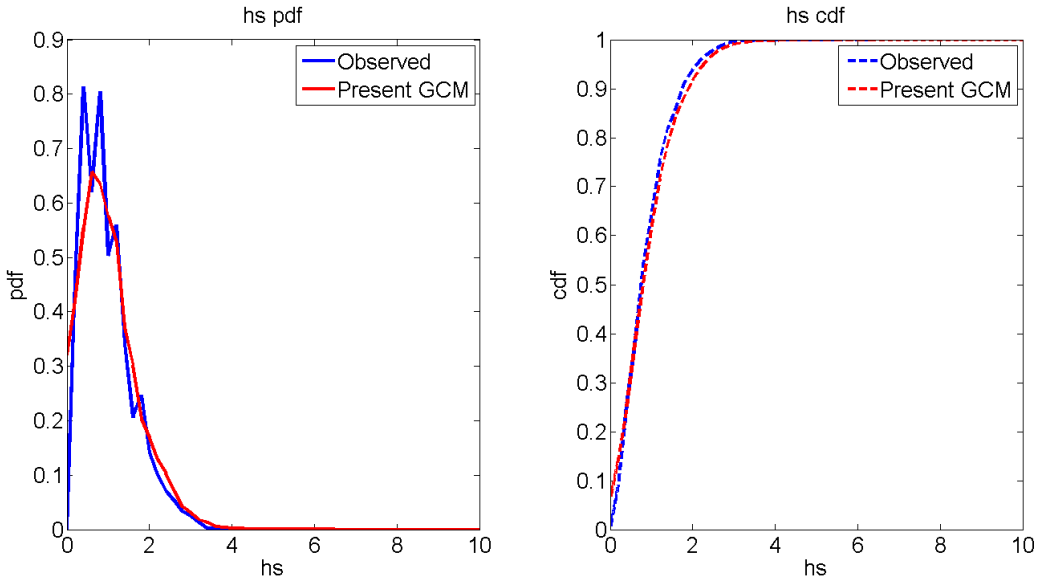

Figure 6.3 – The PDF of H_s (left) and the CDF distribution of H_s (right) between the 'present' modelled results from global wave model and observed data at WSW.

The agreement between both PDF and CDF of modelled and measured wave heights is good, although there is a lower PDF peak from the GCM model, indicating that the statistical properties of modelled H_s agree with measured wave heights.

In more detail, when specific distribution, such as Gumbel distribution (Gumbel, 1941) or the Weibull distribution (Weibull, 1951) is used, the distributions can be expressed with some parameters which can be used to make comparisons.

The CDF of Gumbel distribution can be expressed as:

$$F(x) = e^{-e^{\left(-\frac{x-b}{a}\right)}} \tag{6-1}$$

and the CDF of Weibull distribution is defined as:

$$F(x) = 1 - e^{-e^{\left(-\left(\frac{x}{a}\right)^b\right)}}, x \geq 0, a, b > 0 \qquad (6\text{-}2)$$

In both formulae, *x* is the sample, *a* and *b* are the scale parameter and shape parameter, respectively.

Figure 6.4 shows that the empirically estimated probability of both observed and modelled datasets equally fit well to Gumbel Distribution with no significant difference between the parameters.

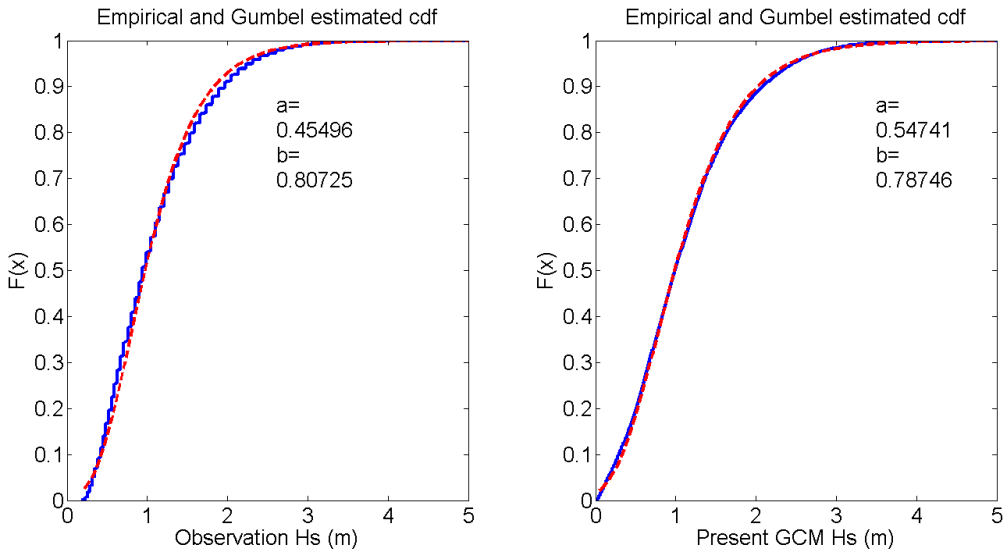

Figure 6.4 – The Gumbel distribution fits of H_s of observed model (left) and modelled data (right) with fitting parameters (parameters a, b is in equation (6-1)).

In order to investigate further the modelled and observed data, the quantile-quantile plot can be drawn based the two data sets with 1-99% quantiles for H_s (Figure 6.5). Both the observed data and 'present' global model data have the same distribution while the quantile-quantile relationship is linear.

In more detail, the global wave model underestimated the smaller measured H_s in history but overestimated those bigger measured values of H_s slightly. But in general, the H_s in the modelled results can represent the measured H_s in average. So, the global wave model is reliable statistically in the Deben Estuary area.

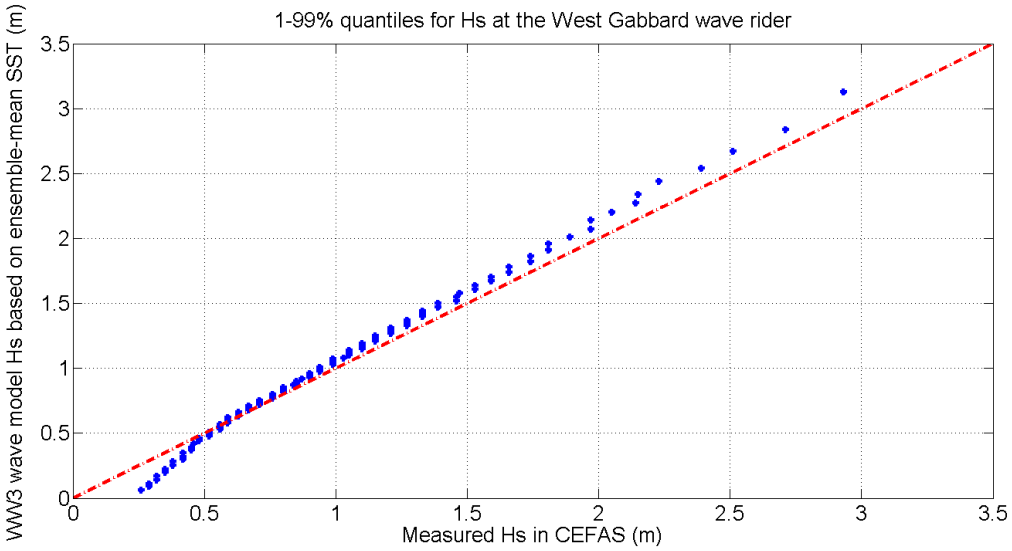

Figure 6.5 – Quantile-quantile plot on the Hs between observation data and present global wave model

However, when considering the wave directions of these two data sets, the 'present' modelled wave direction differs from the direction of the measured wave data (Figure 6.6). The model was unable to accurately reproduce the second predominant wave direction of the observed southwest data. But for the northeast direction in the observed data can be reproduced by the 'present' global model.

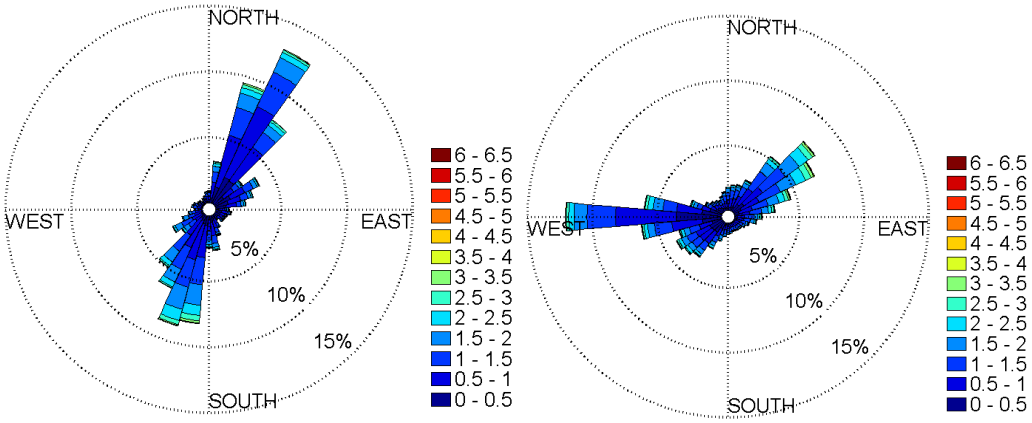

Figure 6.6 – The wave roses of observed data (left) and 'present' modelled data (right). The colour bar indicates the magnitude of H_s.

6.1.1.2. Accuracy analysis

The statistical comparison shown in the previous section does not sufficiently assess the accuracy of the model outputs. In order to make a direct comparison between 'present' modelled wave data and the measured wave data, the time interval difference is solved by interpolating linearly (so that both data sets have a 1 hour interval), thus enabling comparison.

The Mean Errors (ME), defined as the difference of averaged values between two samples, on significant wave height and peak wave period between two datasets is 0.0277m and -0.2586s with respective standard deviations of 0.8814m and 1.8502s. The Mean Absolute Error (MAE) between them is 0.6757m and 1.4908s while the Root Mean Square Errors (RMSE) is 0.8818m and 1.8682s respectively. The interpolation errors are all included in these values.

One of the main reasons for the differences between 'present' modelled and measured data may be that the modelled wave data output point is significantly far away from wave buoy location of WGW, which has been assumed to be the same in this study. Some differences may also be attributed to local conditions that may not have been captured by the global model.

However, by considering the interpolation errors and modelled errors, the accuracy of the H_s that global wave model generated can be tolerated, but it should be noted that there is a big difference between their peak wave periods. In this study, the H_s is the most important wave parameter in morphodynamic simulation. Therefore, it is acceptable to use this modelled wave data to represent the future projections of the Deben Estuary's wave conditions.

6.2.2. The average changes of future wave properties

The 'future' wave data predicted by the model covered the period from the start of year 2075 to the end of year 2099 (25 years) with a one-hour interval and 219142 time points. In order to investigate the wave climate changes as a result of global climate change, the 'future' modelled data can be compared with the 'present' modelled data in aspects of both statistical ways and straight comparison so that the changes between

them can be investigated. This includes the comparison between 'present' and 'future' data in aspect of mean (calm) wave condition and extreme wave condition.

Current and future mean (calm) wave conditions

The average of the significant wave height for the 'present' data is 1.1079m (based on the entire data set) while that of the 'future' data is 1.1068m, in which there is no significant difference between them. The average peak wave period of 'present' modelled data is 5.27s while that of 'future' is 5.24s, once again is not significantly different. Similarly, there was no significant difference between 'present' and 'future' predominant wave directions (Figure 6.7), both of which are from northeast.

The time averaged wave properties based on the entire dataset cannot capture the variability of wave climate seasonally. For instance, winter-summer variability of wave climate may be important as winter months may have significant number of storm wave conditions. It has been reported globally that one of the most noticeable impact of global climate change on ocean waves is that winter storm conditions get stronger and frequent (Lowe, et al., 2001; Woth, et al., 2006). Therefore, in this section, monthly and seasonally changes in the 'present' and 'future' wave conditions are investigated.

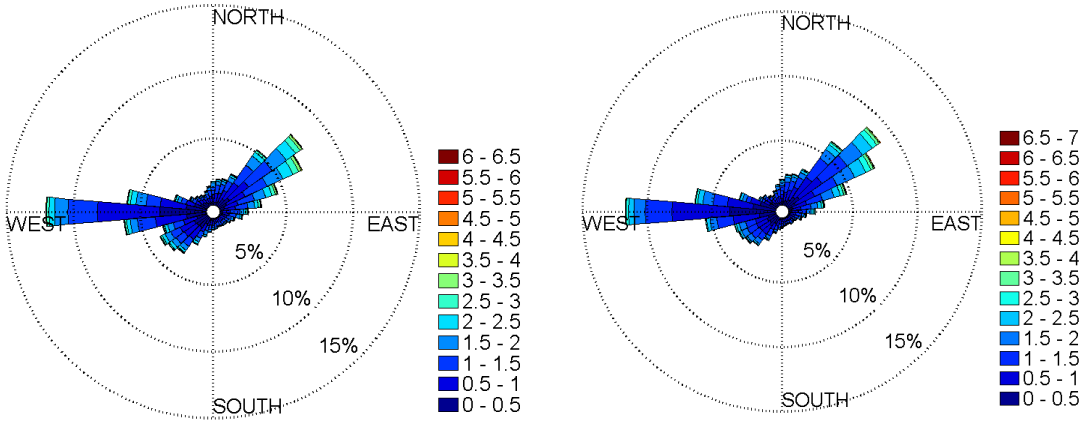

Figure 6.7 – The wave roses based on the total data sets: 'present' model (left); 'future' model (right)

a) Monthly averaged wave properties of 'present' and 'future' conditions

The variations of monthly-averaged significant wave heights and peak wave periods of both 'present' and 'future' modelled data are shown in Figure 6.8. The averages were calculated, with all 'present' and 'future' time slices accounted for.

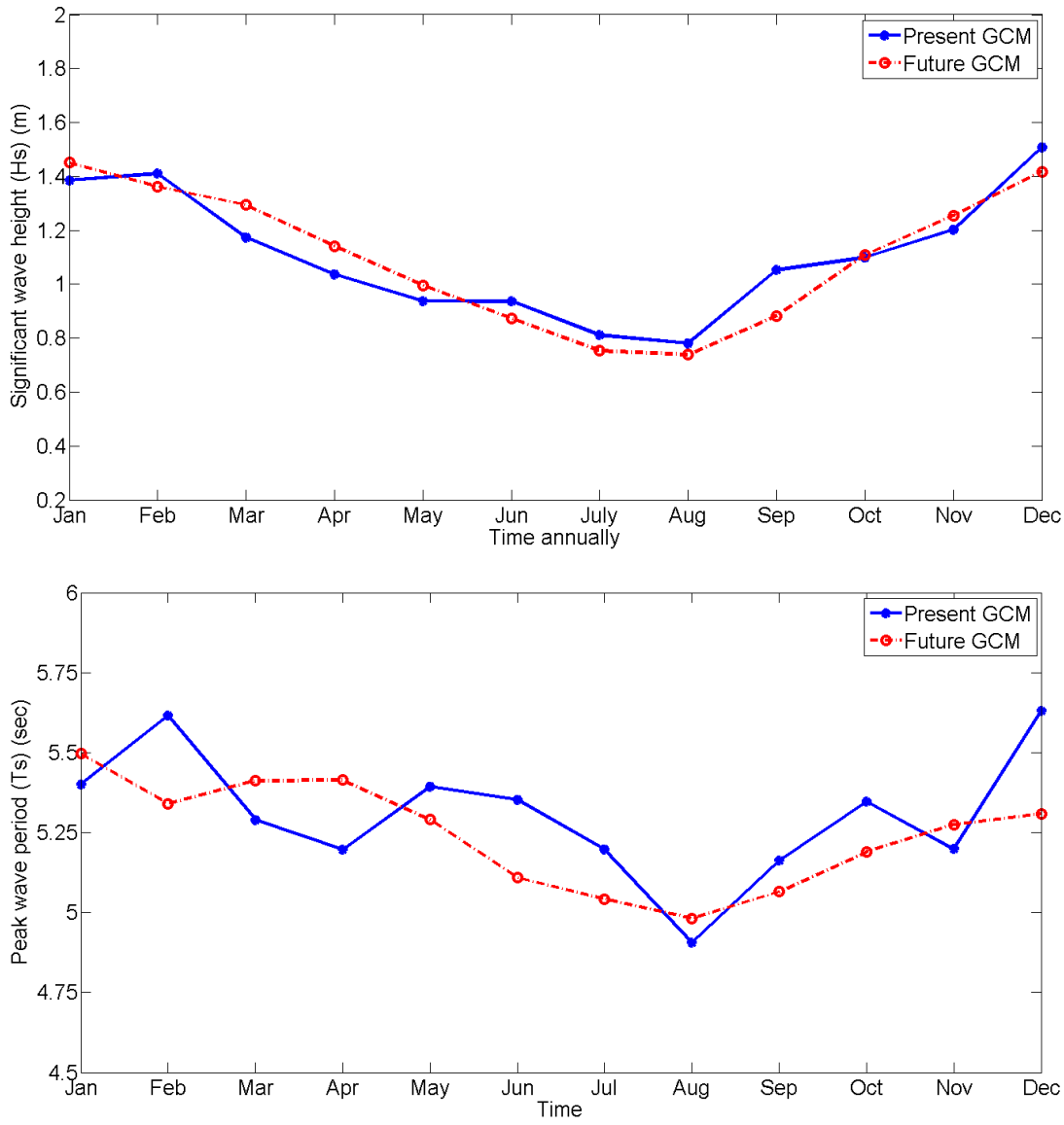

Figure 6.8 – Monthly averaged significant wave height (top) and monthly averaged peak wave period (bottom) between 'present' modelled wave data and 'future' wave data. Blue line stands for the 'present' data and red line stands for the 'future' data.

Figure 6.8 shows that 'future' monthly averaged significant wave height during the summer months are slightly smaller (maximum of 0.17m) than that of 'present' values. In contrast, they are slightly higher (maximum of 0.15m) than the 'present' values during most winter and spring months.

For the peak wave period comparison (bottom plot in Figure 6.8), the difference in peak wave periods between the modelled 'present' and 'future' data are larger than that in significant wave height. The largest difference is observed in December in which the monthly averaged peak wave period will increase by 0.3s in the future. There are 7 months experiencing a decrease on peak wave period and for the months containing an increase, the rate of increase is smaller than the decreasing rate in the decreasing months. This means the net change of the peak wave period is decreasing, as mentioned in the last section. However, all of these changes are still within the 0.5s, which is not significant and no clear trend can be seen.

Based on the above results, it is acceptable to say that the average wave conditions in the sea offshore of Deben Estuary in the end of this century will not change significantly due to the climate change according to this global projection. All the values in both 'present' and 'future' modelled data are listed in Table 6.1. It can be seen that the difference between 'present' results and 'future' results is very small.

Table 6.1 – Monthly averaged significant wave height and peak wave period in both 'present' modelled and 'future' modelled data.

		Jan	Feb	Mar	Apr	May	Jun	Jul	Aug	Sep	Oct	Nov	Dec
'present'	H_s (m)	1.39	1.30	1.25	1.11	0.99	0.93	0.80	0.79	0.99	1.06	1.20	1.49
	T_p (s)	5.28	5.38	5.38	5.26	5.28	5.28	5.16	5.05	5.19	5.22	5.25	5.51
'future'	H_s (m)	1.45	1.36	1.29	1.14	1.00	0.87	0.75	0.74	0.88	1.11	1.25	1.42
	T_p (s)	5.50	5.34	5.41	5.41	5.29	5.11	5.04	4.98	5.06	5.19	5.28	5.31

Figure 6.9 illustrates that the monthly averaged predominant wave directions of 'future' waves seems no significant changes from that in 'present' waves. However, some changes can be seen in the spread of wave approach direction.

Therefore, by considering the wave properties in both Table 6.1 and Figure 6.9, it can be concluded that the monthly averaged wave properties of both 'present' and 'future' modelled do not differ significantly.

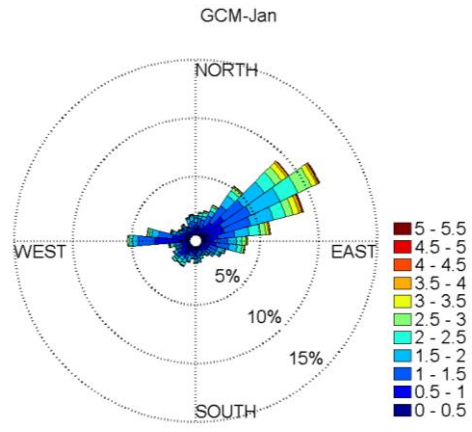
GCM-Jan
NORTH
WEST
EAST
SOUTH
5%
10%
15%
5 - 5.5
4.5 - 5
4 - 4.5
3.5 - 4
3 - 3.5
2.5 - 3
2 - 2.5
1.5 - 2
1 - 1.5
0.5 - 1
0 - 0.5

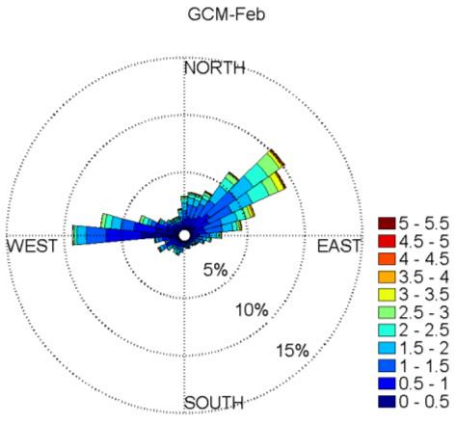
GCM-Feb
NORTH
WEST
EAST
SOUTH
5%
10%
15%
5 - 5.5
4.5 - 5
4 - 4.5
3.5 - 4
3 - 3.5
2.5 - 3
2 - 2.5
1.5 - 2
1 - 1.5
0.5 - 1
0 - 0.5

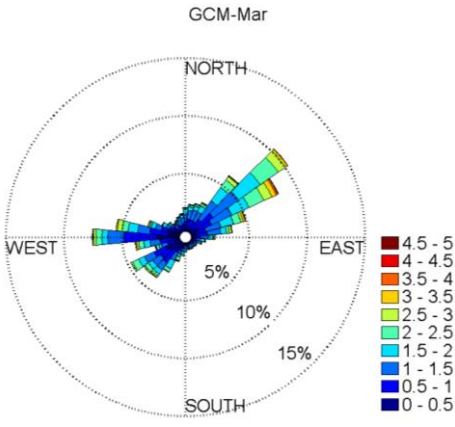
GCM-Mar
NORTH
WEST
EAST
SOUTH
5%
10%
15%
4.5 - 5
4 - 4.5
3.5 - 4
3 - 3.5
2.5 - 3
2 - 2.5
1.5 - 2
1 - 1.5
0.5 - 1
0 - 0.5

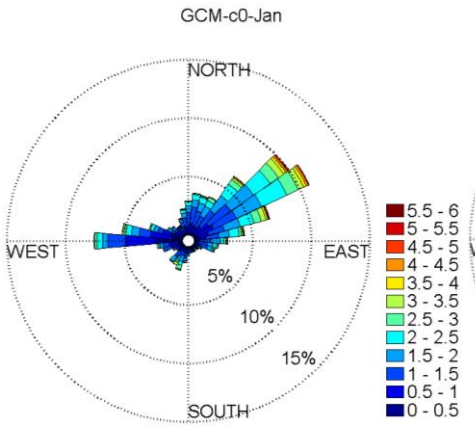
GCM-c0-Jan
NORTH
WEST
EAST
SOUTH
5%
10%
15%
5.5 - 6
5 - 5.5
4.5 - 5
4 - 4.5
3.5 - 4
3 - 3.5
2.5 - 3
2 - 2.5
1.5 - 2
1 - 1.5
0.5 - 1
0 - 0.5

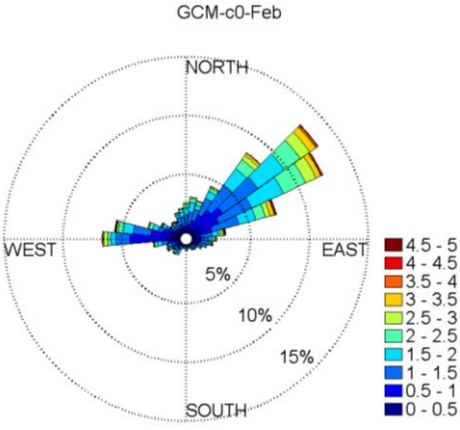
GCM-c0-Feb
NORTH
WEST
EAST
SOUTH
5%
10%
15%
4.5 - 5
4 - 4.5
3.5 - 4
3 - 3.5
2.5 - 3
2 - 2.5
1.5 - 2
1 - 1.5
0.5 - 1
0 - 0.5

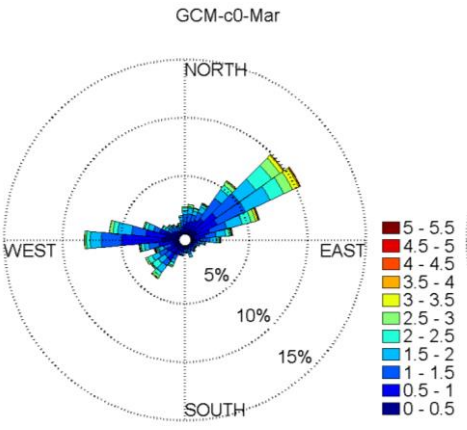
GCM-c0-Mar
NORTH
WEST
EAST
SOUTH
5%
10%
15%
5 - 5.5
4.5 - 5
4 - 4.5
3.5 - 4
3 - 3.5
2.5 - 3
2 - 2.5
1.5 - 2
1 - 1.5
0.5 - 1
0 - 0.5

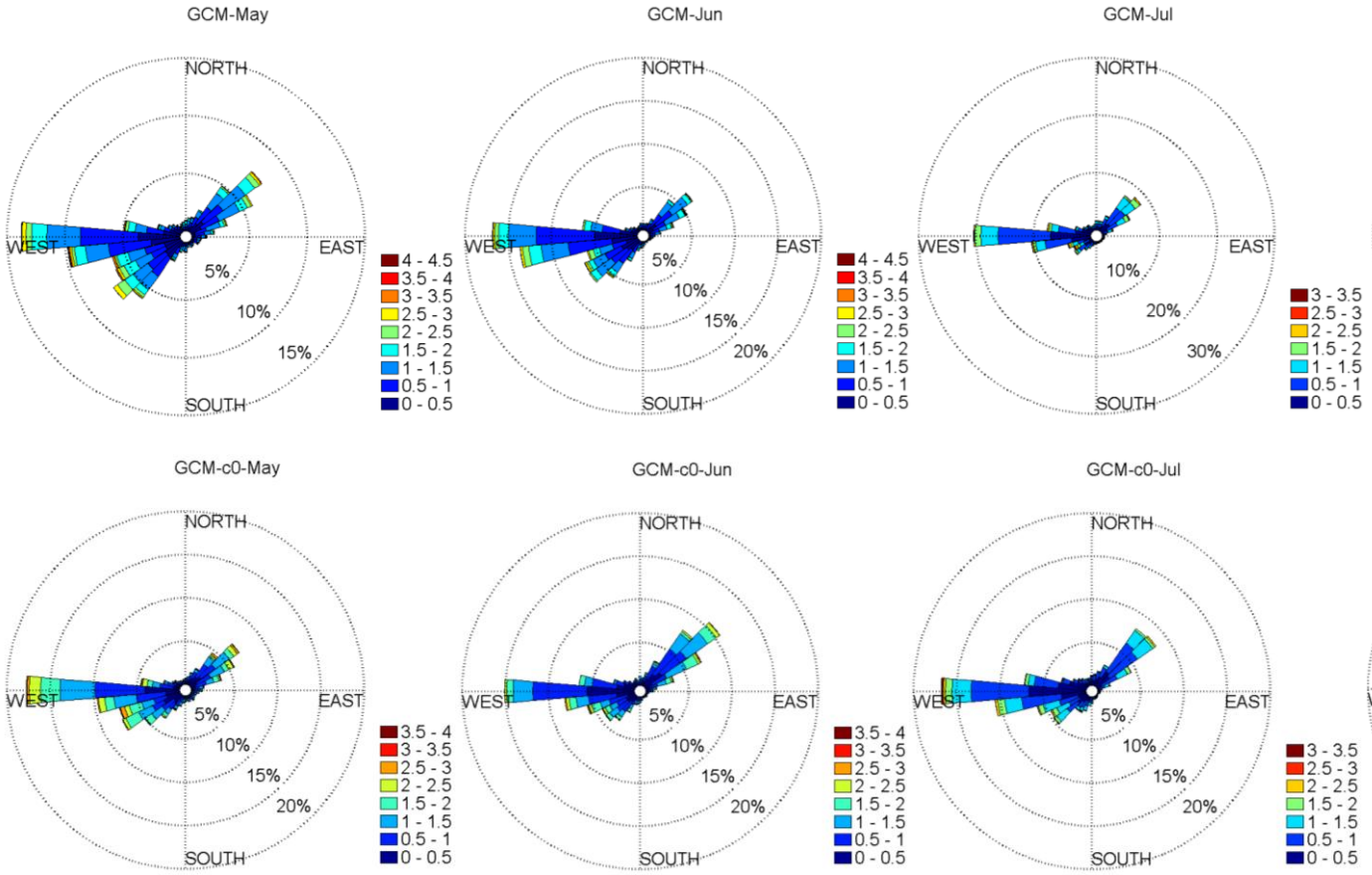
GCM-May
NORTH
WEST
EAST
SOUTH
5%
10%
15%
4 - 4.5
3.5 - 4
3 - 3.5
2.5 - 3
2 - 2.5
1.5 - 2
1 - 1.5
0.5 - 1
0 - 0.5
GCM-Jun
NORTH
WEST
EAST
SOUTH
5%
10%
15%
20%
4 - 4.5
3.5 - 4
3 - 3.5
2.5 - 3
2 - 2.5
1.5 - 2
1 - 1.5
0.5 - 1
0 - 0.5
GCM-Jul
NORTH
WEST
EAST
SOUTH
10%
20%
30%
3 - 3.5
2.5 - 3
2 - 2.5
1.5 - 2
1 - 1.5
0.5 - 1
0 - 0.5
GCM-c0-May
NORTH
WEST
EAST
SOUTH
5%
10%
15%
20%
3.5 - 4
3 - 3.5
2.5 - 3
2 - 2.5
1.5 - 2
1 - 1.5
0.5 - 1
0 - 0.5
GCM-c0-Jun
NORTH
WEST
EAST
SOUTH
5%
10%
15%
20%
3.5 - 4
3 - 3.5
2.5 - 3
2 - 2.5
1.5 - 2
1 - 1.5
0.5 - 1
0 - 0.5
GCM-c0-Jul
NORTH
WEST
EAST
SOUTH
5%
10%
15%
20%
3 - 3.5
2.5 - 3
2 - 2.5
1.5 - 2
1 - 1.5
0.5 - 1
0 - 0.5

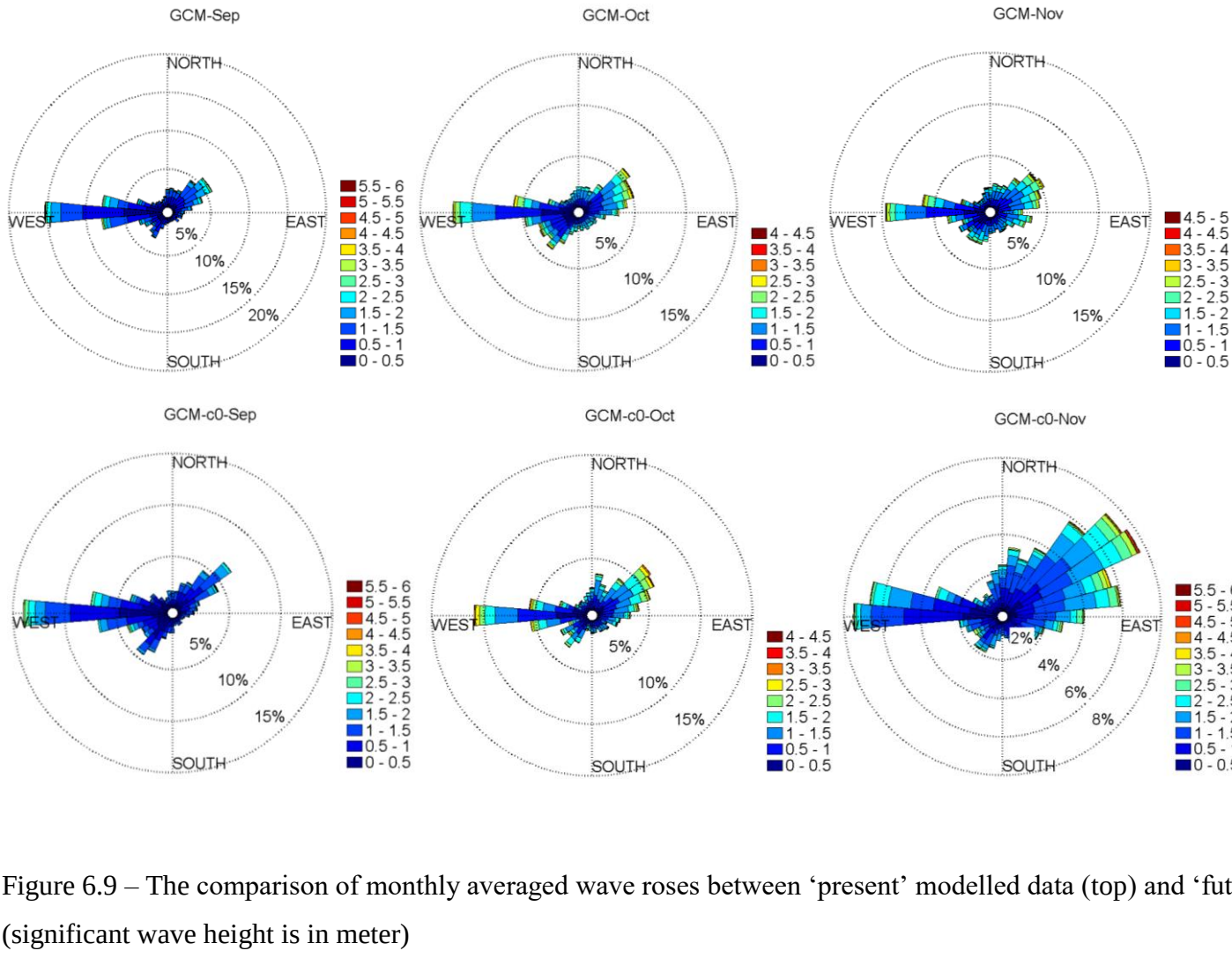

Figure 6.9 – The comparison of monthly averaged wave roses between 'present' modelled data (top) and 'fut
(significant wave height is in meter)

b) Differences in seasonally averaged wave properties between ‘present’ and ‘future’ wave conditions

For the seasonally averaged (spring-summer-autumn-winter) changes on the wave properties, the inter-seasonal variations between ‘present’ and ‘future’ modelled wave data can also be investigated. The seasonally averaged wave rose figure between ‘present’ and ‘future’ modelled data are shown in Figure 6.10. It shows that there is no obvious seasonal change to ‘present’ and ‘future’ waves. Table 6.2 also summarises the seasonally averaged ‘present’ and ‘future’ wave conditions in which no significant changes can be found.

Table 6.2 – The seasonally-averaged wave properties in both ‘present’ model and ‘future’ model

	Spring			Summer			Autumn			Winter		
	Hs (m)	Tp (s)	Main Dir (°)	Hs (m)	Tp (s)	Main Dir (°)	Hs (m)	Tp (sec)	Main Dir (°)	Hs (m)	Tp (s)	Main Dir (°)
‘present’	1.1	5.3	45.0	0.8	5.2	270.0	1.1	5.2	270.0	1.4	5.4	45.0
‘future’	1.1	5.4	45.0	0.8	5.0	270.0	1.1	5.2	270.0	1.4	5.4	45.0

Based on the above analysis, it should be noted that SLR is the most significant and important factor which governs the change in morphodynamic conditions of the Deben Estuary in future. The final selected wave conditions for ’future’ scenarios simulated in this study are shown in Table 6.3.

In summary, for the simulations that use calm weather conditions in this study, the wave data conditions in all these simulations are set to be the same. There are three options when using these outputs for simulating the morphodynamic models of the Deben Estuary: the total averaged wave input; monthly averaged wave input and seasonally averaged wave input (Table 6.3).

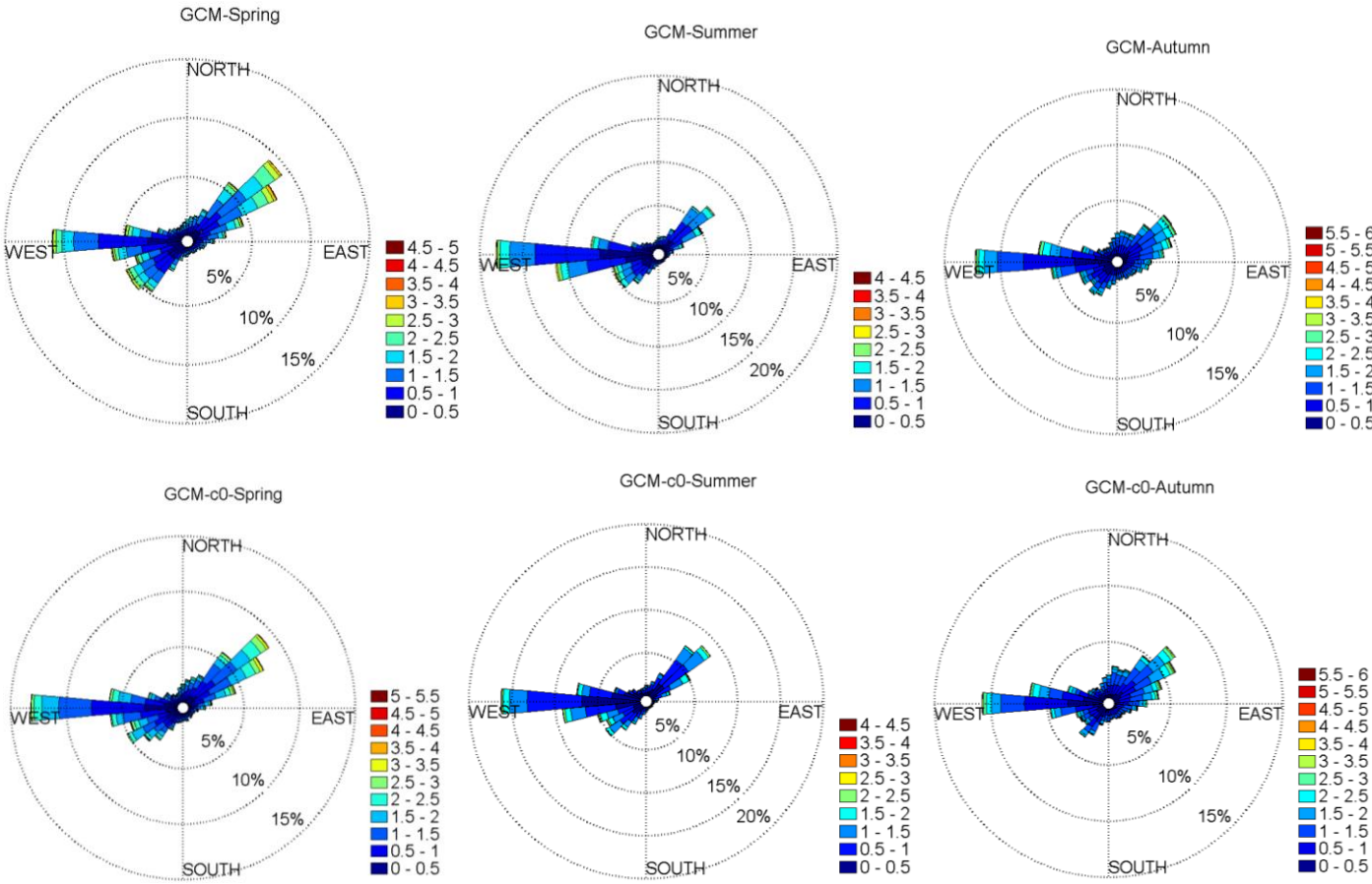

Figure 6.10 – The comparison on seasonal wave rose of ‘present’ modelled data (top) and ‘future’ modelled d
May; Summer: June--August; Autumn: September—November; Winter: December-February).

Table 6.3 shows the biggest difference between these three options is in the wave direction in which the latter two consider the wave direction variation. For the other wave properties, such as significant wave height and peak wave period, there is no great difference between these three options.

Table 6.3 – The final selected wave conditions to be used in the Deben Estuary model

		Present & Future		
		Hs(m)	Tp(s)	D(Degr)
Total averaged		1.1	5.27	50
Seasonally averaged	Spring	1.1	5.3	45
	Summer	0.8	5.2	270
	Autumn	1.1	5.2	270
	Winter	1.4	5.4	45
Monthly averaged	Jan	1.39	5.28	45
	Feb	1.3	5.38	45
	Mar	1.25	5.38	45
	Apr	1.11	5.26	45
	May	0.99	5.28	270
	Jun	0.93	5.28	270
	Jul	0.8	5.16	270
	Aug	0.79	5.05	270
	Sep	0.99	5.19	270
	Oct	1.06	5.22	270
	Nov	1.2	5.25	45
	Dec	1.49	5.51	45

6.2.3. Storm wave statistics

In addition to considering the changes of average wave properties in future, it is important to investigate the changes of storm wave conditions due to global climate change as the wave storm climate may impose notable impacts on the morphological changes in estuary.

The storm event in this study was defined as the wave height exceeding a threshold for longer than one hour and the time interval between two consecutive storm events should be larger than 24 hours (Figure 6.11). If the time interval between two storms

is less than 24hrs, it is defined to be one storm event. In this study, according to the study site, it was defined that the significant wave heights that are larger than 2.5m can be treated as the storm waves, which is similar with the threshold selection in Liverpool Bay from Channel Coastal Observatory (CCO) (Dissanayake et al., 2015).

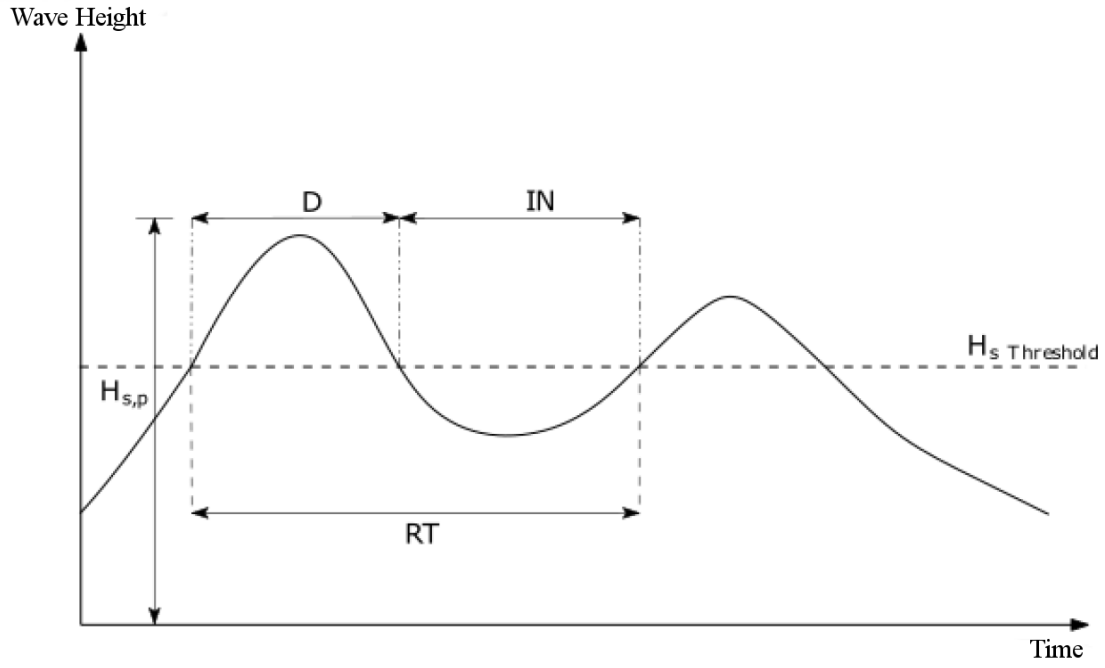

Figure 6.11 – Storm event definition

Using the above criteria, storm conditions were extracted from both 'present' and 'future' modelled wave data sets, 724 storms were found in the 'present' scenario data set (1979-2009) and 578 storms were found in the 'future' scenario dataset (2075-2099) respectively.

Based on these storm events, the peak significant wave height (H_{smax}) in every storm event was selected to make a regression to get H_{smax} return period values. Although the previous section has found that the raw H_s satisfies the Gumbel distribution, the H_{smax} of storm events fit the Generalized Pareto Distribution (GPD) much better than the Gumbel distribution. The following section will discuss the linear regression in detail by using GPD estimation method.

Return period estimation on peak wave storm heights

For a given high threshold of H_s, both 'present' and 'future' H_{smax} datasets will be fitted to converge to Generalised Pareto Distribution (GPD). In GPD approach, the distribution of excess values of *x* over threshold *u* is expressed by:

$$F_u(y) = \Pr\{x - u \le x \mid x > u\} = \frac{F(x) - F(u)}{1 - F(u)} \tag{6-3}$$

This is the probability of value of *x* exceeds *u* by an amount *y*, where *y=x-u*.

The CDF of GPD is expressed by:

$$G(x;k,\alpha,\beta) = \begin{cases} 1 - \left(1 - k\dfrac{x-\beta}{\alpha}\right)^{1/k} & k \neq 0 \\ 1 - e^{-(x-\beta)/\alpha} & k = 0 \end{cases} \tag{6-4}$$

where k is the shape parameter, β is the location parameter, α is the scale parameter.

In order to choose the threshold of the GPD distribution, which is an important practical problem, the Conditional Mean Exceedance (CME) graphs can be used. This is also known as Mean Residual Life (MRL) plot which shows the relation between the threshold values and the mean excess over threshold (Davison, 1984). The MRL plot based on the 'present' H_{smax} dataset is shown in Figure 6.12. Since there is no significant change between 'present' and 'future' H_{smax} datasets, the same threshold can be used.

It is reasonable to determine the threshold after which the two variables (threshold and mean excess) are roughly linear with each other as it is mentioned that the mean excess is a linear function of the threshold *u* (Coles, 2001). In Figure 6.12, it was found that these two variables are linear at the beginning of the plot which means the threshold of GPD distribution can be selected as 2.5m, in which the values larger than 2.5m are linear roughly to the mean excess.

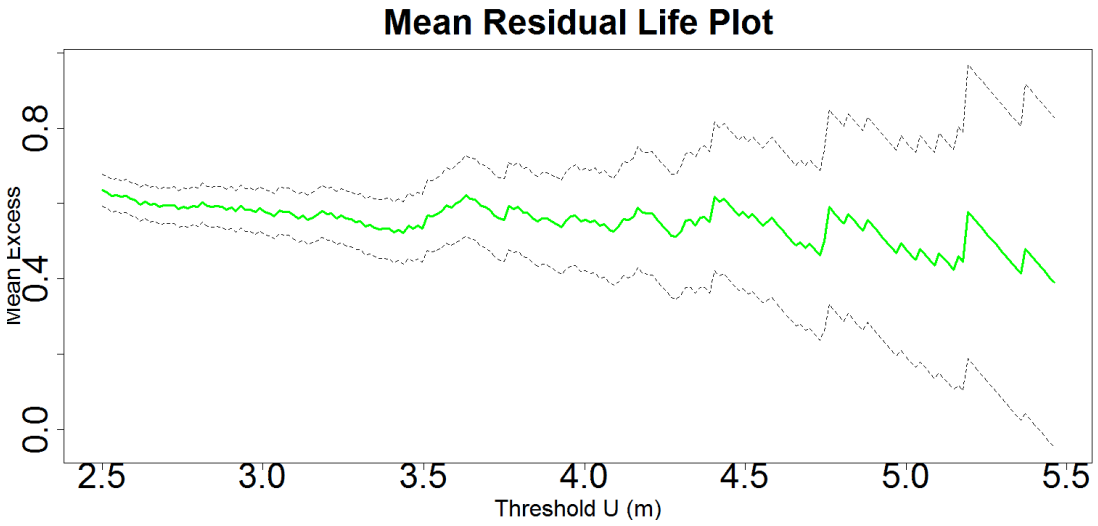

Figure 6.12 – The Mean Residual Life plot with 95% confidence interval based on 'present' H_{smax} storm events for the purpose of choosing the threshold of GPD distribution.

The return period values of different return years can be calculated by linearly regressing based on the reduced variates. The extreme return values on H_{smax} can be obtained in Table 6.4.

Table 6.4 – Different return period values on peak storm wave heights (H_{smax}) based on the GPD distributions.

	Estimation method	10-year return period H_{smax}(m)	20-year return period H_{smax}(m)	30-year return period H_{smax}(m)	50-year return period H_{smax}(m)	100-year return period H_{smax}(m)	200-year return period H_{smax}(m)
'Present'	GPD	5.51	5.80	5.96	6.16	6.42	6.66
'Future'	GPD	5.78	6.12	6.31	6.54	6.85	7.13
Increased rate	GPD	4.90%	5.52%	5.87%	6.17%	6.70%	7.06%

Table 6.4 shows clearly that the 'future' extreme wave heights will increase by approximately 5~7% from the 'present' extreme peak wave heights. Thus, the frequency of storm wave events in the future will be increased. For example, the storm wave of 1 in 100-year return period in 'present' may become 1 in 50-year return period in the 'future'. Therefore, the increase of these return period values will affect the

morphology when it coincides with SLR scenarios. In this study, the 1 in 100-year return period H_{smax}, which will increase by about 40cm (6.70%) from 'present' to 'future', will be used to investigate morphodynamic responses of the estuary during future extreme storm events. This will be discussed in Chapter 8.

6.3. Summary

Global climate change around the Deben Estuary can be indicated by the SLR and wave climate change. In this study, the following conclusions will be used.

- The assumed predicted sea level rise at the Deben Estuary will increase by approximately 0.2m, 0.5m and 0.8m under the lowest emission, medium emission and highest emission scenarios respectively.
- As for the wave climate change, the average wave condition will not change in the future. As a result, to investigate estuary morphology change during calm weather conditions in future, same wave conditions as 'present' scenario will be used with increased sea levels.
- Wave heights of extreme storm conditions will become larger in future compared to 'present' scenario. The 1 in 100-year return period significant wave height will increase by around 40cm at the offshore boundary of Deben Estuary in future, which will be used in this study to investigate the Estuary's morphodynamic response to future extreme conditions.

Chapter 7: Long-term morphodynamic change of the Deben Estuary based on different SLR scenarios

7.1. Model description

The Deben Estuary morphological change is simulated by considering three sea level rise (SLR) scenarios discussed in Chapter 6, which are low emission (LE), medium emission (ME) and high emission (HE). They are respectively associated with sea level rises of 0.2m, 0.5m and 0.8m by the end of this century. All future scenarios are based on the same reduced (averaged) wave conditions used in the 'present' climate scenario, which considers the fact that average wave conditions will not change as a result of climate change, as explained in Chapter 6.

According to the discussion in Chapter 6, three simplified input wave conditions are considered: total averaged (mean wave condition from 'present' global wave modelled data set from 1979-2009), seasonally averaged (seasonal variation) and monthly averaged (monthly variation). The wave conditions used in this study are listed in Table 6.3 in Chapter 6. All simulations represent the morphodynamic changes of the estuary during the 12-month period from September 2002 to August 2003 where the measured 2002 bathymetry of the estuary is taken as the initial bathymetry of the model.

In every future emission scenario, there are three different wave condition inputs ('total averaged' (TA), 'seasonally averaged' (SA) and 'monthly averaged' (MA)) so that the number of scenarios under every SLR emission water level would be 3. If the present scenarios were included, there would be a total number of 12 scenarios, which would confuse the discussion and over-complicate the investigation.

Therefore, to make the investigation efficient, there is no need to run all the scenarios with three different wave condition inputs if some can generate similar results. Because the wave conditions of the three options (totally averaged, seasonal averaged and monthly averaged) are similar, as shown in Table 6.3, the produced results may be similar. So, the optimisation process will be carried out first based on three present

scenarios (TA_SC0, SA_SC0 and MA_SC0 in which SC0 stands for present scenarios with no SLR).

Impacts from different average wave options to final results

In order to consider the three wave conditions (TA, SA and MA), the wave data in Table 6.3 is spread through the simulation period. For example, the TA wave data is constant during the simulation; the 4 wave heights of SA wave data are set into 4 equally distributed periods and during each period the wave condition is constant; for the MA conditions, the same process is carried out. The final estuary's morphology is determined by three different wave conditions (TA_SC0, SA_SC0 and MA_SC0) based on No SLR, as shown in Figure 7.1.

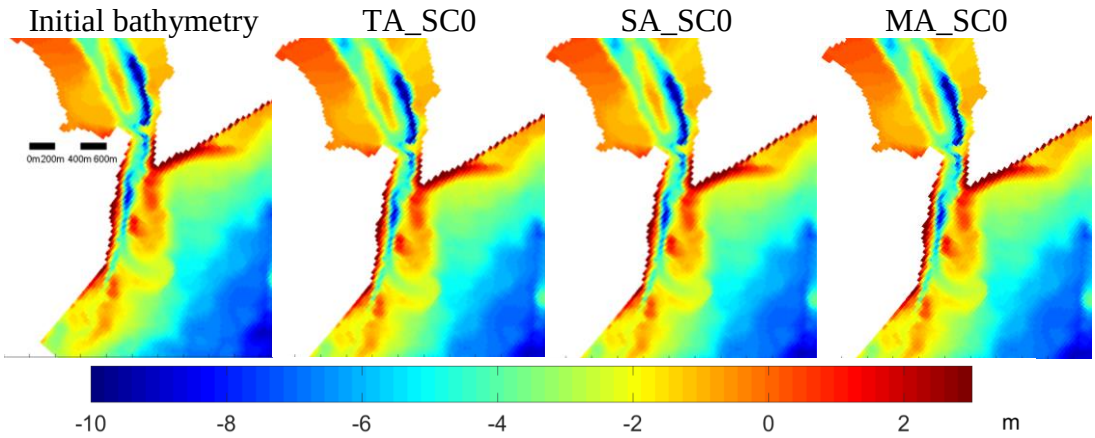

Figure 7.1 – The final bathymetries of the Deben Estuary after 1 year of morphodynamic simulation in TA_SC0, SA_SC0 and MA_SC0 scenarios. The left figure shows the initial bathymetry used in the simulations.

Very small differences were observed between the final bathymetries and determined from the above three scenarios. However, closer observation reveals some differences in the ebb delta area. The differences of bed level changes between the MA_SC0 and TA_SC0 is shown in Figure 7.2 (SA_SC0-TA_SC0 and MA_SC0-TA_SC0). The difference between SA_SC0 and TA_SC0 (Figure 7.2a) may be attributed to the fact that TA_SC0 (totally averaged wave condition) has experienced the continuous uniform significant wave height from the predominant wave direction (45^{o}N), but the SA_SC0 (seasonally averaged wave condition) has replaced the relative stronger wave impacts (1.1m offshore) with smaller significant wave height (0.8m offshore) with

non-predominant wave direction (270^{o}N), which results to smaller significant wave heights occur on the ebb jet (Figure 7.3).

The difference between MA_SC0 and TA_SC0 (Figure 7.2b) is smaller than that between SA_SC0 and TA_SC0. From the aspect of differences on wave conditions, the only discrimination between these two scenarios is that, in the MA_SC0 scenario, the small significant wave height usually occurs accompanying with non-predominant wave direction while the larger significant wave height coincides with a dominated wave direction (Table 6.3). This indicates that the change in morphology from small non-predominant waves reaching the estuary cannot compensate the impacts due to large predominant waves. The totally-averaged wave condition case (TA_SC0) overestimated the morphological changes which will generate the most serious bed level changes among these three scenarios.

(a) SA_SC0-TA_SC0 (b) MA_SC0-TA_SC0

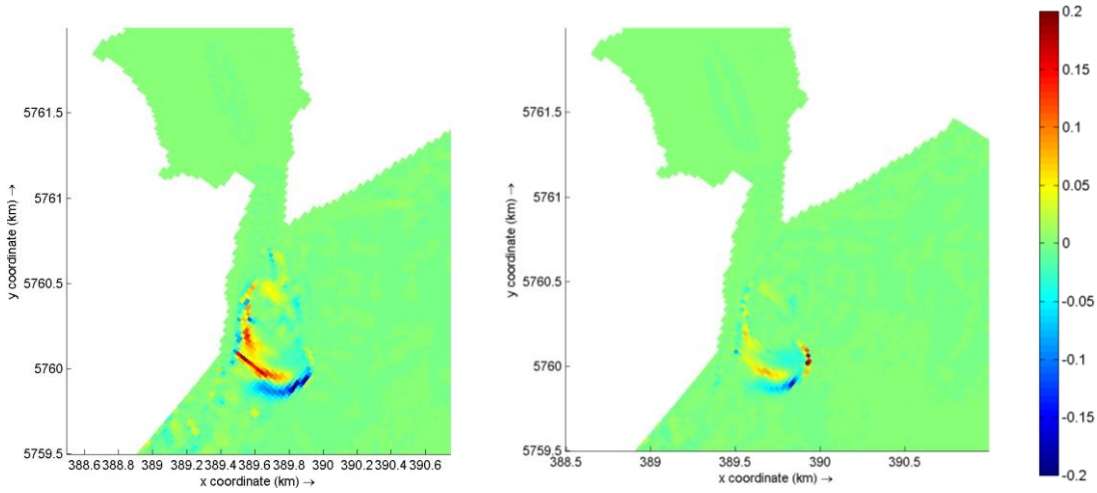

Figure 7.2 – The differences of bed level changes between seasonally averaged and totally averaged present scenarios (a: SA_SC0-TA_SC0) and the differences of bed level changes between monthly averaged and totally averaged present scenarios (b: MA_SC0-TA_SC0)

Additionally, in both the SA_SC0 and MA_SC0 scenarios, bed change around ebb jet is slightly slower than that in TA_SC0. In order to examine this, the wave conditions at the ebb jet area were investigated (Figure 7.3). The total averaged scenario provides larger wave heights in the ebb delta region than the other scenarios.

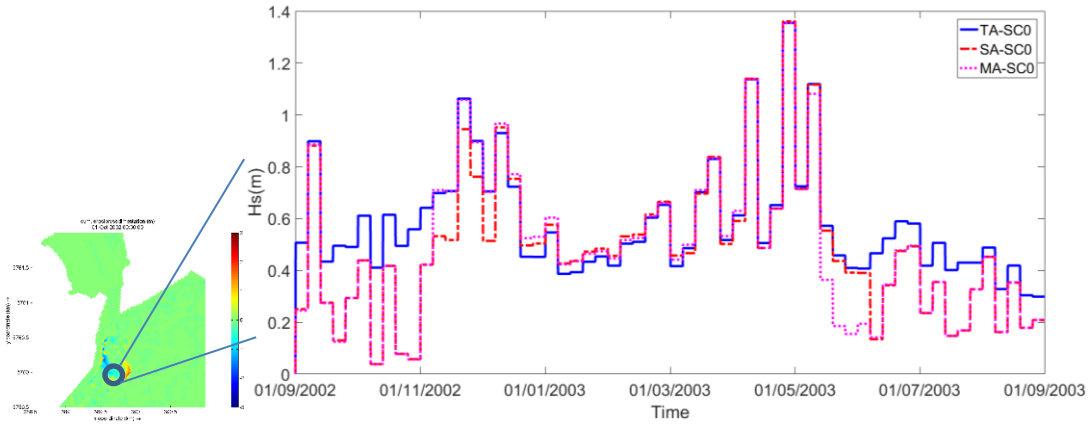

Figure 7.3 – The time series (assumed based on the Morfac values as the simulation lasted for one month) comparison on the significant wave height (H_s) at the ebb jet position (51°58'43"N, 01°23'41"E) between three options; the position is shown left.

However, the difference between morphological changes is not significant. From the visual aspect, the final bathymetries are similar among these three scenarios. A factor F was introduced for quantitative comparison of the morphological changes among these scenarios. In factor F, similarly expressed to the BSS value, the bed level in TA_SC0 were assumed to be the base model, and the values of bed level in MA_SC0 and SA_SC0 were compared to TA_SC0 scenarios, referring to initial bathymetry. It is expressed as $F=1-\langle(Z_{mol}-Z_{base})^2\rangle/\langle(Z_{ini}-Z_{base})^2\rangle$. Z_{mol} stands for the bed level of scenarios to compare (here are MA_SC0 and SA_SC0, respectively), Z_{base} stands for the bed level of base model (TA_SC0), and Z_{ini} stands for initial bathymetry.

F=0.99 is found for MA_SC0 scenario and F=0.96 for SA_SC0 scenario when compared with TA_SC0 scenario. This indicates that both the performance of MA_SC0 scenario and SA_SC0 scenario are similar with the performance of TA_SC0 scenario. Based on this outcome, it was decided that only TA scenarios will be considered when comparing 'present' and 'future' morphodynamic change of the estuary. The scenarios are listed in Table 7.1.

Table 7.1 – Morphodynamic simulation scenarios based on SLR emissions and reduced wave conditions in this chapter.

wave / wave level	Total averaged (TA)	Seasonally averaged (SA)	Monthly Averaged (MA)	Description
BA	TA_SC0	SA_SC0	MA_SC0	No sea level rise
LE	TA_SC1	/	/	LE SLR
ME	TA_SC2	/	/	ME SLR
HE	TA_SC3	/	/	HE SLR

[TA=Totally Averaged Wave Condition; BA=Basic model with Current Sea Level; LE=SLR with the Lowest Emission; ME = SLR with the Medium Emission; HE = SLR with the High Emission; SC0, SC1, SC2 and SC3 stand for present, future LE, future ME and future HE; '/' means the scenario was not carried out].

7.2. Results of TA scenarios

In this section, bathymetry changes that resulted from different SLR scenarios will be presented and discussed based on the Totally Averaged (TA) option. TA wave conditions are used in all three SLR simulations (TA_SC1, TA_SC2 and TA_SC3). All simulations used the year of 2002 bathymetry as the initial bathymetry and lasted for 1 morphodynamic year with a Morfac of 12.

7.2.1. Transient tidal flows during spring tidal cycle in future SLR scenarios

In order to understand and discuss the morphodynamic characteristics and bathymetry change of the Deben Estuary under three future SLR scenarios, the tidal flow characteristics were investigated. As the hydrodynamic effects from spring tidal cycles are the most important to the morphodynamic changes, the hydrodynamic processes during spring cycles are selected to investigate.

At the Slack spring tide Before Ebb (SBE, 09/09/2002 02:00AM), the tidal velocity is at different directions with significantly low values around the ebb delta (Figure 7.4). The tide moves from south to north. There are three obvious main differences within this system: the ebb shoal, main channel and inner estuary.

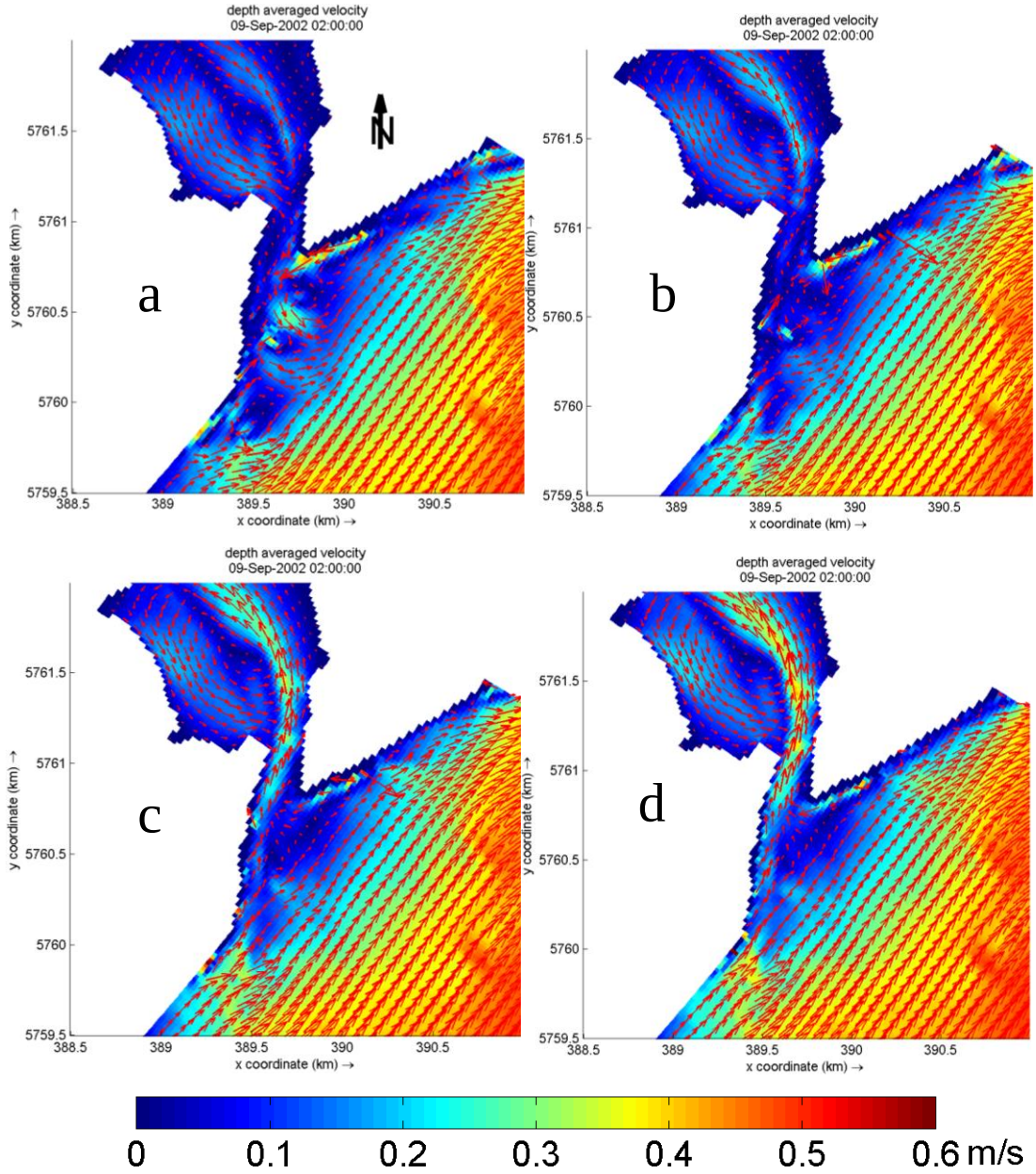

Figure 7.4 – The depth-averaged tidal current at slack water time before ebb tide (09/09/2002 02:00AM) around the Deben Estuary in present and future scenarios: a) present scenario (TA_SC0); b) TA_SC1 scenario (LE SLR); c) TA_SC2 scenario (ME SLR); d) TA_SC3 scenario (HE SLR). The colour bar indicates the current strength (m/s) and the arrow shows the current direction at every node.

In the present scenario (Figure 7.4a), the SBE seaward current on the ebb shoal reduces its average velocity to around 0.2m/s except in the middle of sand bar where the velocity reaches approximately 0.3m/s. In addition, as the current reverses at the north of ebb shoal, a small anti-clockwise circle shape current structure can be seen on the

north ebb shoal. At the downdrift side, as the tidal current that comes from southwest is divided into two directions when joining to the slack current at ebb jet, a complicated flow structure occurs at the south ebb shoal. A circular flow is also seen at the inner estuary after the current flowing through the inlet with relative high velocities at both the flood channel (north from the flood delta) and ebb channel (south from the flood delta), as shown in Figure 7.4a.

However, in the future SLR scenarios (Figure 7.4b-d), the slack water current smooths towards the northeast and the small circle-shaped current on the delta will disappear. The same trend is observed for the current at downdrift of south ebb delta, but the spatial average current speed is about 0.1m/s larger than that of the present scenario.

For the tidal current in the main channel and throat area, the strong flooding current in SLR scenarios replace the small ebb tide in present scenario, which indicates a forward shift to slack water time with the increase of sea levels (leading to tidal phase change). As a result, the current at flood dominance channel in the inner estuary (northeast of flood-delta) has increased from around 0.18m/s to 0.35m/s because of the inertia from increased flood current in the main channel.

Four hours after SBE water, the ebb tidal current has reached maximum values in the spring ebb tidal phase (09/09/2002 06:00AM). Since Deben is an ebb dominated estuary, the maximum ebb velocity at spring tide is closely linked to morphological changes. The differences between peak ebb tidal currents for the present and three SLR scenarios can be seen in Figure 7.5.

The largest flow velocity in present scenario (TA_SC0) occurs at middle channel to ebb jet region, which is around 1.8m/s. These strong velocities may increase the total sediment transport both at the downward side of the main channel and at ebb jet region. There is an expansion of flow field at the end of ebb jet region which will deposit transported sediment offshore as a result of reduced velocity after the end of channel. In the downdrift side, several small circular current structures can be seen.

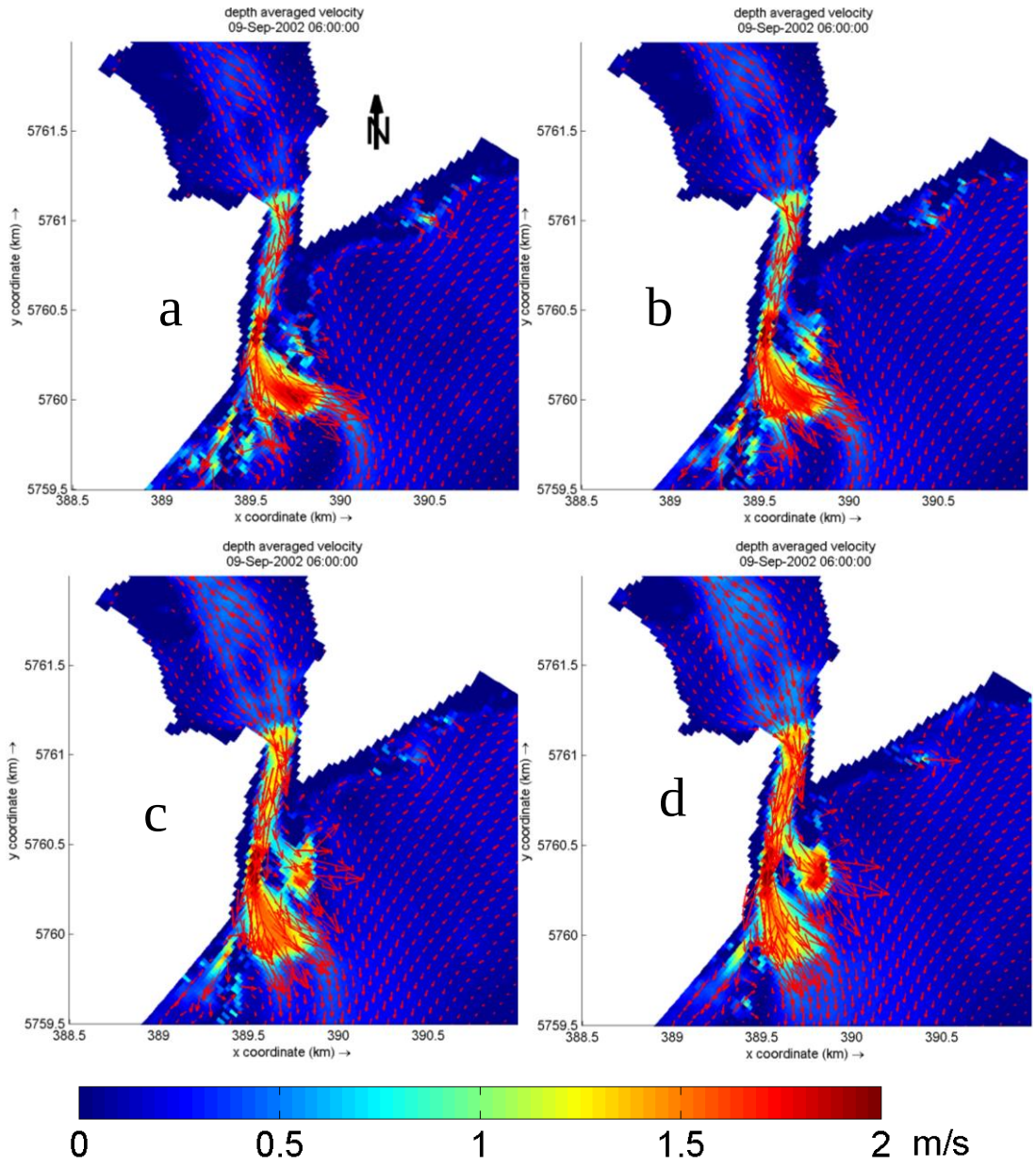

Figure 7.5 – The depth-averaged tidal current at spring ebb tide phase (09/09/2002 06:00AM) around the Deben Estuary in present and future scenarios: a) present scenario (TA_SC0); b) TA_SC1 scenario (LE SLR); c) TA_SC2 scenario (ME SLR); d) TA_SC3 scenario (HE SLR). The colour bar indicates the current strength (m/s) and the arrow shows the current direction at every node.

In the SLR scenarios, the magnitude of the original ebb jet reduced slightly, from 1.8m/s to around 1.3m/s in HE scenario. The direction also switched from east-south-east toward south (Figure 7.5). These changes will cause different morphological evolution at this area. Additionally, there is a new ebb tidal jet at the updrift side of the

main tidal jet, where the jet velocity increases from LE to HE scenarios (Figure 7.5). Even though smaller ebb jet velocities were observed in the SLR scenario, there is an overall increase in velocities at the estuary with SLR which may potentially increase sediment transport. The offshore side of this newly-formed tidal jet contains much stronger currents than that at the onshore side in all future scenarios.

The averaged velocity between the throat and the entrance of newly-formed channel will enhance, which may potentially provide more sediment for the newly-formed channel. In terms of the downdrift side, the current re-organized in the future scenarios and the velocity towards the south has been clearly observed in the HE scenario.

At the Slack water time Before Flood tide (SBF, 09/09/2002 08:00AM) a weak current still ebbs along the main channel. The velocity distributions on the ebb shoal, not including the main channel, are similar among the scenarios (Figure 7.6).

In the present scenario, the most significant current, around 0.7m/s, occurs within the main channel during the SBF water time as the estuarine geometry converged the current to the main channel (Figure 7.6a). However, after passing through the narrow channel the velocity veers towards offshore at a right angle to the coastline while decreasing its magnitude (approximately 0.55m/s), then releases from the channel to expand at ebb jet region.

When the sea level rises, the estuary's water level increases, and most of the ebb delta is submerged during low tide. Thus, the current restricted on ebb delta is released partially. The current in the main channel will decrease as most of the ebb current can retreat back to the sea in other ways before it rises up to the estuary again. Therefore, the SLR makes the currents at SBF water time gentler and more spread, which may induce sediment deposition much closer to the coastline.

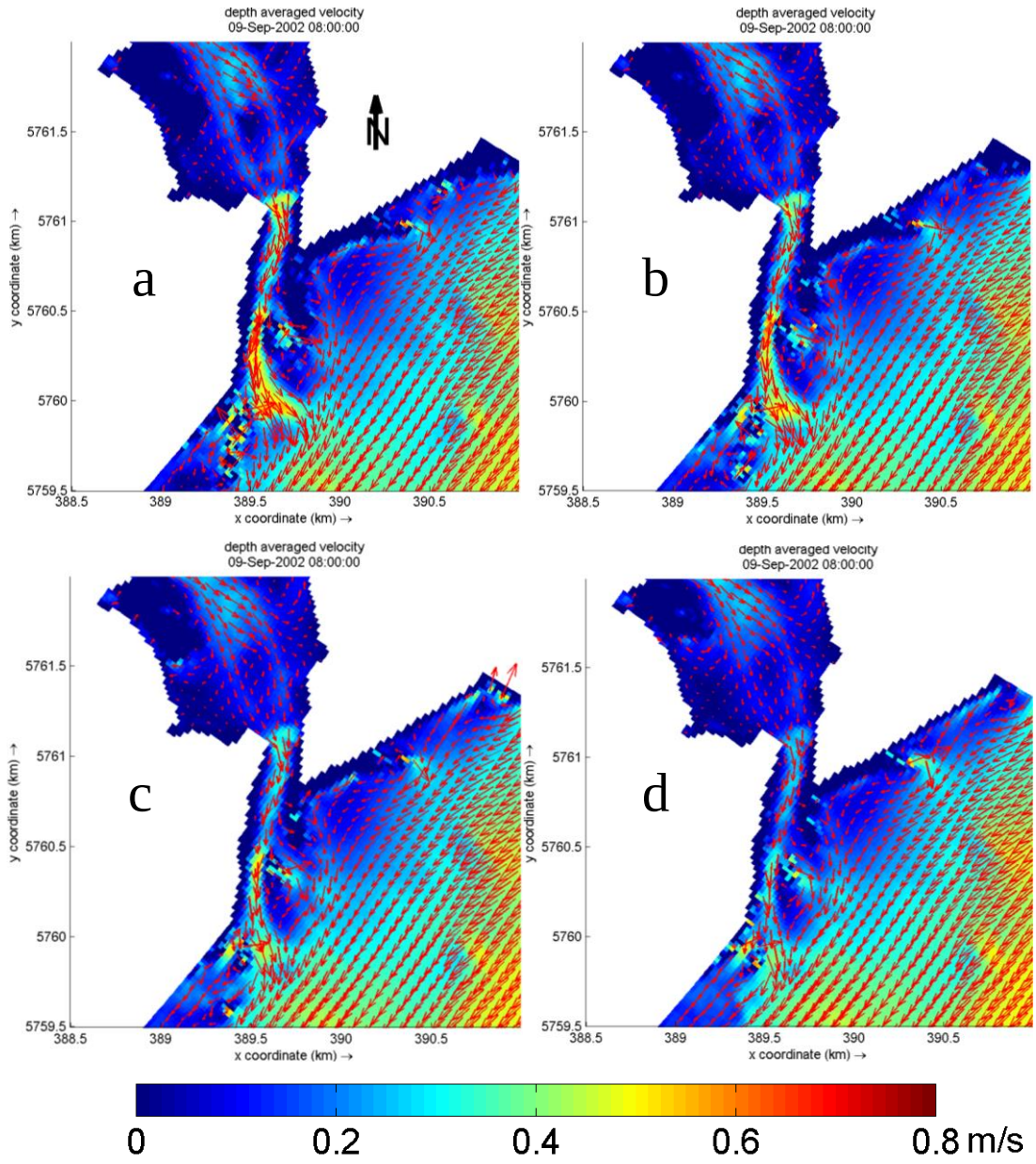

Figure 7.6 – The depth-averaged tidal current during the SBF time (09/09/2002 08:00AM) around the Deben Estuary in present and future scenarios: a) present scenario (TA_SC0); b) TA_SC1 scenario (LE SLR); c) TA_SC2 scenario (ME SLR); d) TA_SC3 scenario (HE SLR). The colour bar indicates the current strength (m/s) and the arrow shows the current direction at every node.

At the maximum flood phase (09/09/2002 12:00PM) stronger-flood currents occur in the inlet area rather in the ebb shoal area (Figure 7.7). The distributions of velocities on the ebb shoal in the future scenarios are not significantly different to the present scenario (TA_SC0). The most significant difference among SLR scenarios is that the

flood velocity magnitude at the throat of the channel has increased with the increase of SLR rate (from LE to HE). Furthermore, the velocities in the flood dominant channel at inner estuary, northeast of the flood tidal delta, have also increased.

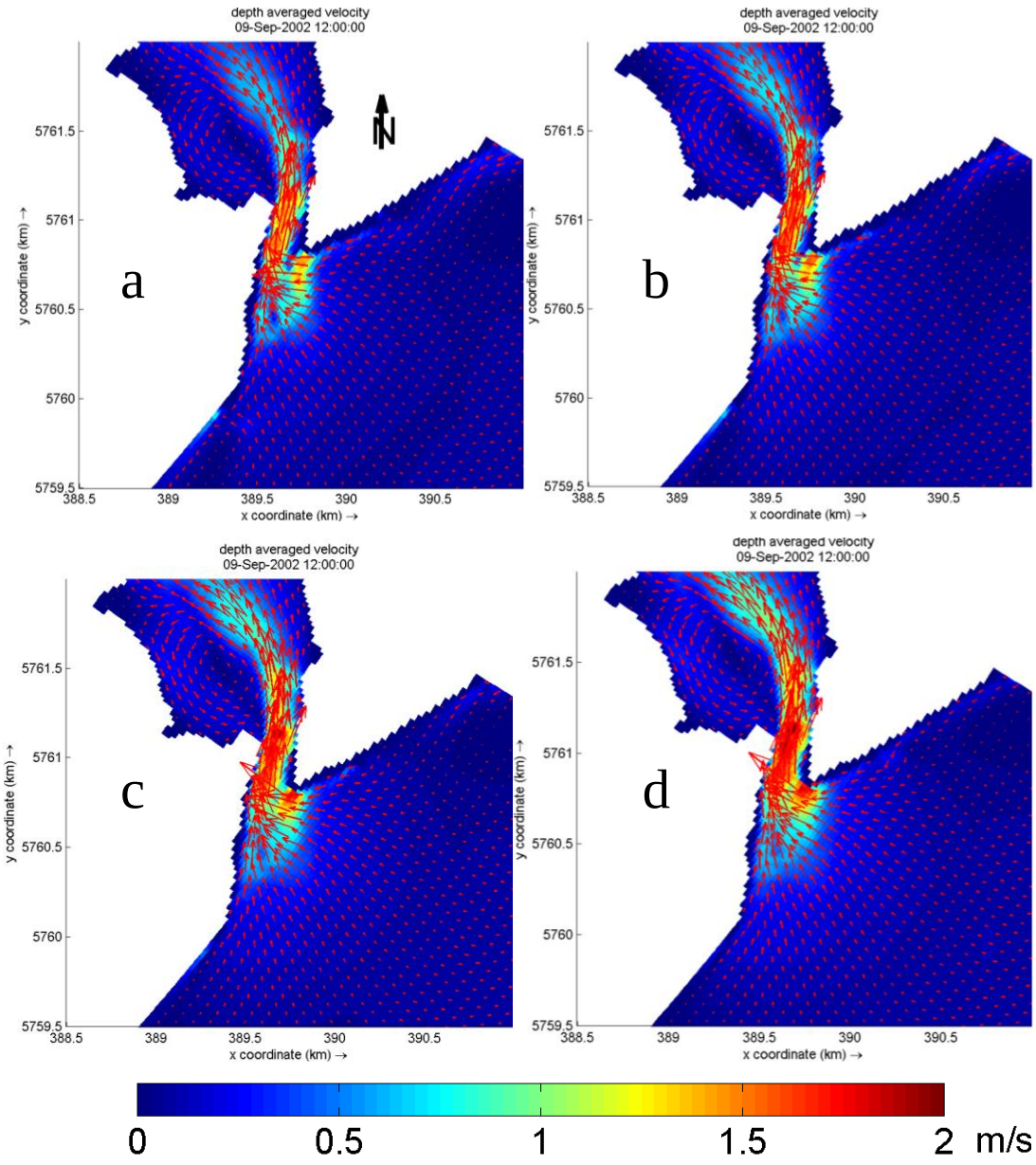

Figure 7.7 – The depth-averaged tidal current at spring flood phase (09/09/2002 12:00PM) around Deben Estuary in present scenario and future scenarios: a) present scenario (TA_SC0); b) TA_SC1 scenario (LE SLR); c) TA_SC2 scenario (ME SLR); d) TA_SC3 scenario (HE SLR). The colour bar indicates the current strength (m/s) and the arrow shows the current direction at every node.

7.2.2. Tidally-induced residual circulations

Tidally-induced residual currents (averaged the depth-averaged current over a tidal cycle) may play a significant role on sediment transport, even though the residual currents do not always indicate net bedload transport (Bastos, et al., 2003).

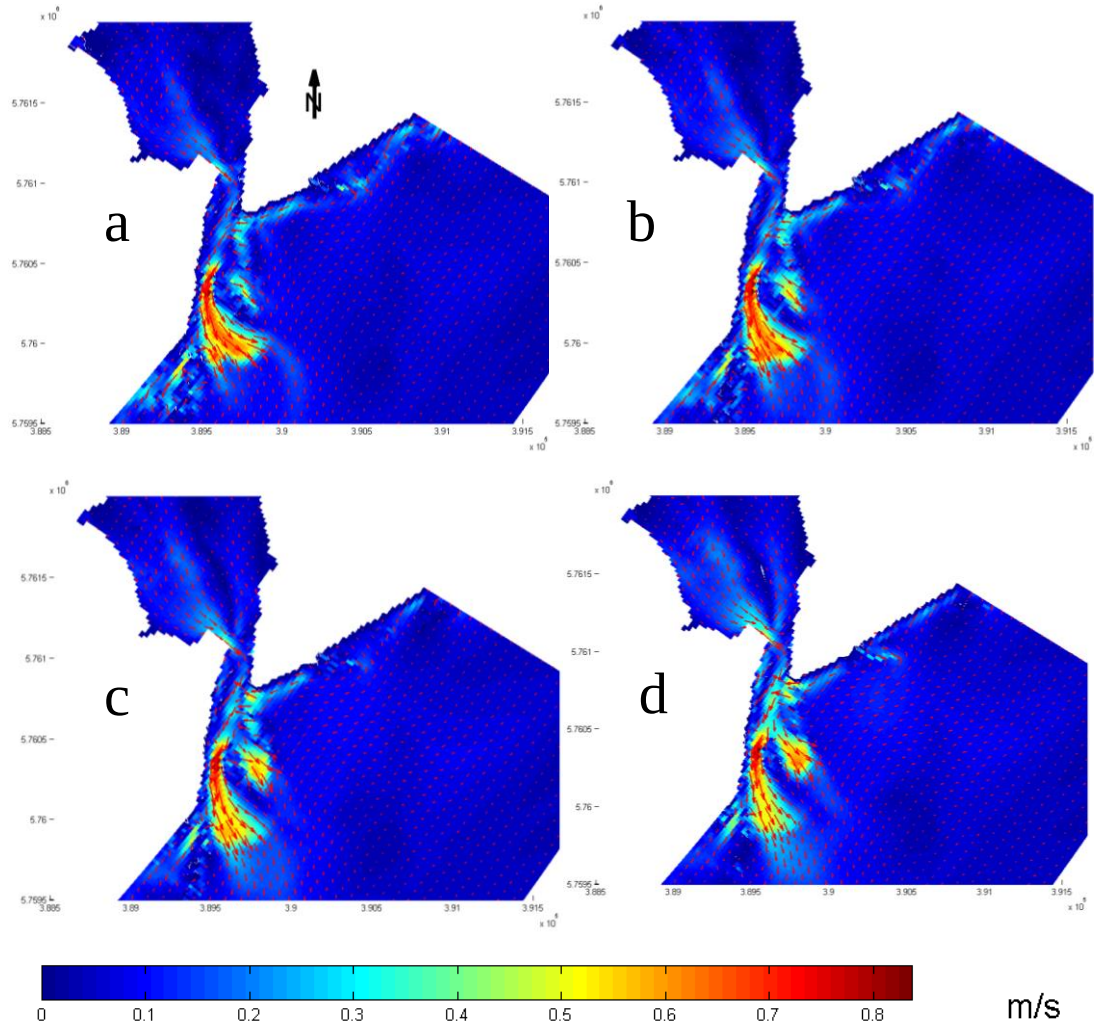

Figure 7.8 – The residual tidal flow field over a spring tide cycle around the Deben Estuary in present and three future SLR scenarios: a) present scenario (TA_SC0); b) TA_SC1 scenario (LE SLR); c) TA_SC2 scenario (ME SLR); d) TA_SC3 scenario (HE SLR). The colour bar indicates the current strength (m/s) and the arrow shows the current direction at every node.

In order to investigate the differences in morphological changes at selected SLR scenarios, it is necessary to determine whether the residual current over a spring tidal cycle coincides with sediment transport. The residual flows over a spring tidal cycle (09/09/2002 02:00AM to 12.00PM) in the present and future scenarios are presented in Figure 7.8.

Figure 7.8 shows that the residual flow show was notably different among different scenarios. In the present scenario, the residual flow at the ebb jet region (offshore directed) is the most significant. However, a shoreward-directed current can be seen in the northern part of the ebb shoal (Figure 7.8a). Additionally, a weaker seaward directed residual flow is seen in the newly formed tidal jet channel on north ebb shoal. With the help of these two opposite currents, a small circle current has been formed, probably leading to less sediment transport. Between the two main offshore current pathways (the main ebb jet and newly-formed tidal jet channel), there is a less energetic area where a tiny onshore velocity occurs.

This complicated residual current distribution between the two main currents on the ebb delta does not change significantly in future scenarios except for some switches on offshore directions and the relative magnitudes. For the residual flow at the original ebb jet, the direction shifts from east south-east to south south-east slightly after SLR occurs associated with the reduction on velocity magnitude. As the newly formed channel (produced by newly formed tidal jet) has expanded its offshore residual currents, more obvious residual circle current can be seen in Figure 7.8d between both the new channel and north tip side of ebb delta.

In the downdrift side of the ebb delta, the residual currents become smaller and well-organised in SLR scenarios. In the north of ebb delta at the throat, landward directed residual currents can be seen in the future scenarios (Figure 7.8), which may potentially increase the onshore sediment transport at the throat. For the ebb channel at the inner estuary (Southwest of flood tidal delta), the seaward current increased when joining the throat, resulting in a more dynamic throat in future scenarios. As sea level rises, the length of the flow jet through the throat to the inner estuary also increased. However, for the narrow throat, even if the instantaneous current is significant, the residual tidal current is not obvious, which implies that the net flow

through the throat will not be significantly changed by the SLR as long as the tide range is not changed in the future.

7.2.3. Residual (mean) sediment transport pattern

There are two obvious locations containing large sediment transport rates on the ebb shoal both in present and future scenarios: one is the offshore transport at the primary ebb jet and the other is the offshore transport at the position of newly-formed ebb jet channel (Figure 7.9); their distributions are similar to the residual tidal currents. The sediment transport rate will vary between present and future SLR scenarios.

In the present scenario TA_SC0 (Figure 7.9a), the sediment transport rates at the primary ebb channel are the most significant; they are much larger than that at the newly-formed channel. The maximum transport rate at primary ebb jet is around 4×10^{-6} $m^3/s/m$, roughly 3 times larger than the largest transport rate in the newly-formed channel (~1.3×10^{-6} $m^3/s/m$). Therefore, in this scenario, it seems that the most sediment is transported through the original ebb jet.

In the future scenario TA_SC1 (Figure 7.9b), the largest sediment transport rate at primary ebb jet is reduced to approximately 3×10^{-6} $m^3/s/m$ while the largest sediment transport rate at the newly-formed channel is increased slightly to 1.4×10^{-6} $m^3/s/m$ which is less than that at original ebb jet position.

In terms of the future scenario, TA_SC2 (Figure 7.9c), the largest sediment transport rates both at ebb jet and newly-formed channels are almost equivalent, approximately 2.7×10^{-6} $m^3/s/m$, after reduction on original ebb jet channel and enhancement on newly-formed channel. In this scenario, the major sediment transport pathway has shifted obviously from the original ebb jet channel towards the newly-formed channel. The other obvious difference is that the main direction of the residual sediment transport, which has changed from east south-east to south south-east; this is closely related to the residual flow change (Figure 7.8).

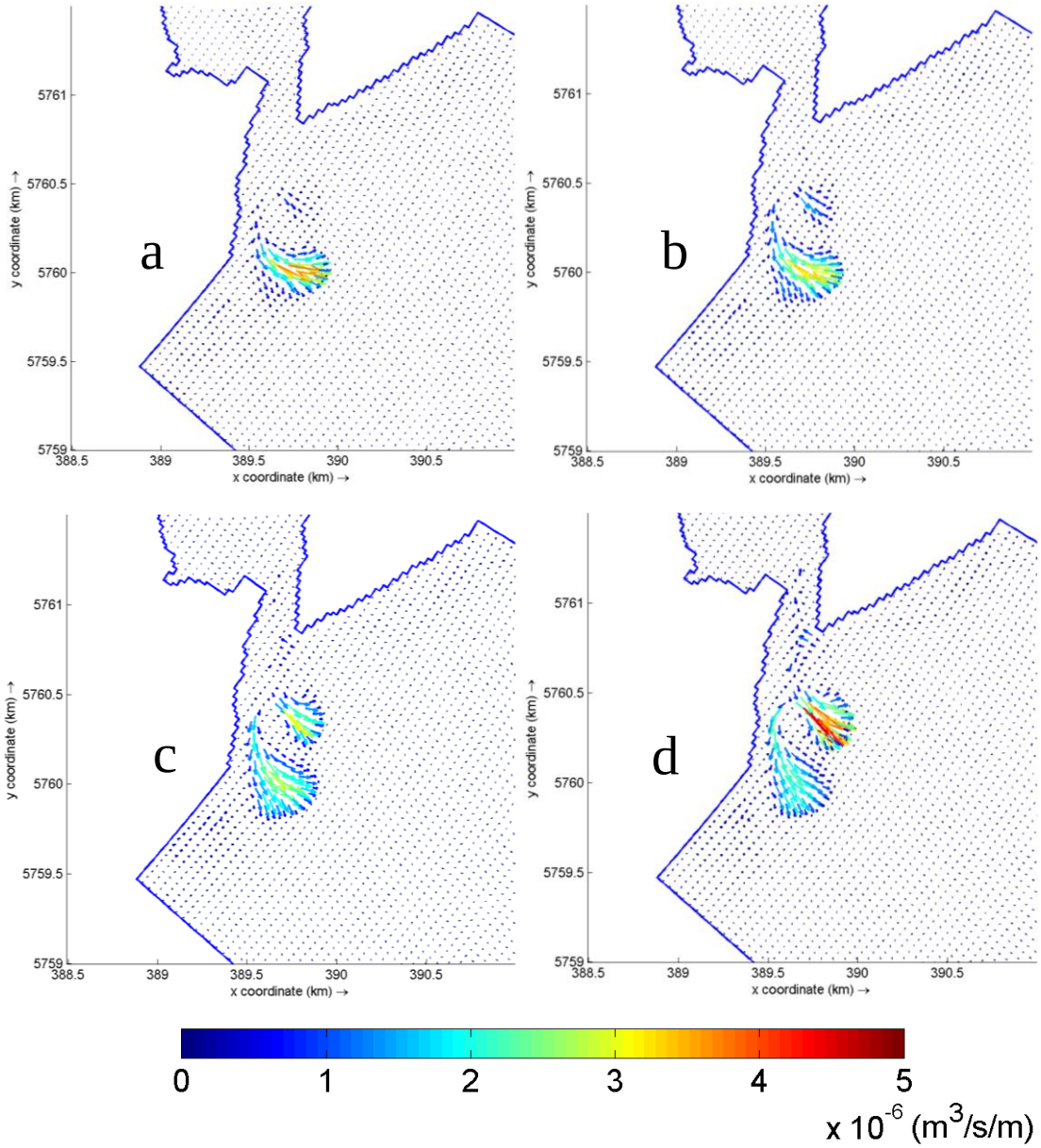

Figure 7.9 – Residual total sediment transport rate during the simulation around Deben Estuary in different scenarios: a) present scenario (TA_SC0); b) TA_SC1 scenario; c) TA_SC2 scenario; d) TA_SC3 scenario (the vector shows the transport rate per unit width at the centre of every node and the colour bar indicates the magnitude of the sediment transport rate per unit width)

For the HE SLR scenario TA_SC3, shown in Figure 7.9d, the major pathway of sediment transport has totally switched to newly-formed channel. The largest sediment transport rate at the primary ebb jet channel has reduced to less than 2×10^{-6} $m^3/s/m$ while the maximum sediment transport rate at newly-formed channel has reached 5×10^{-6} $m^3/s/m$, almost double the value of the primary ebb jet channel.

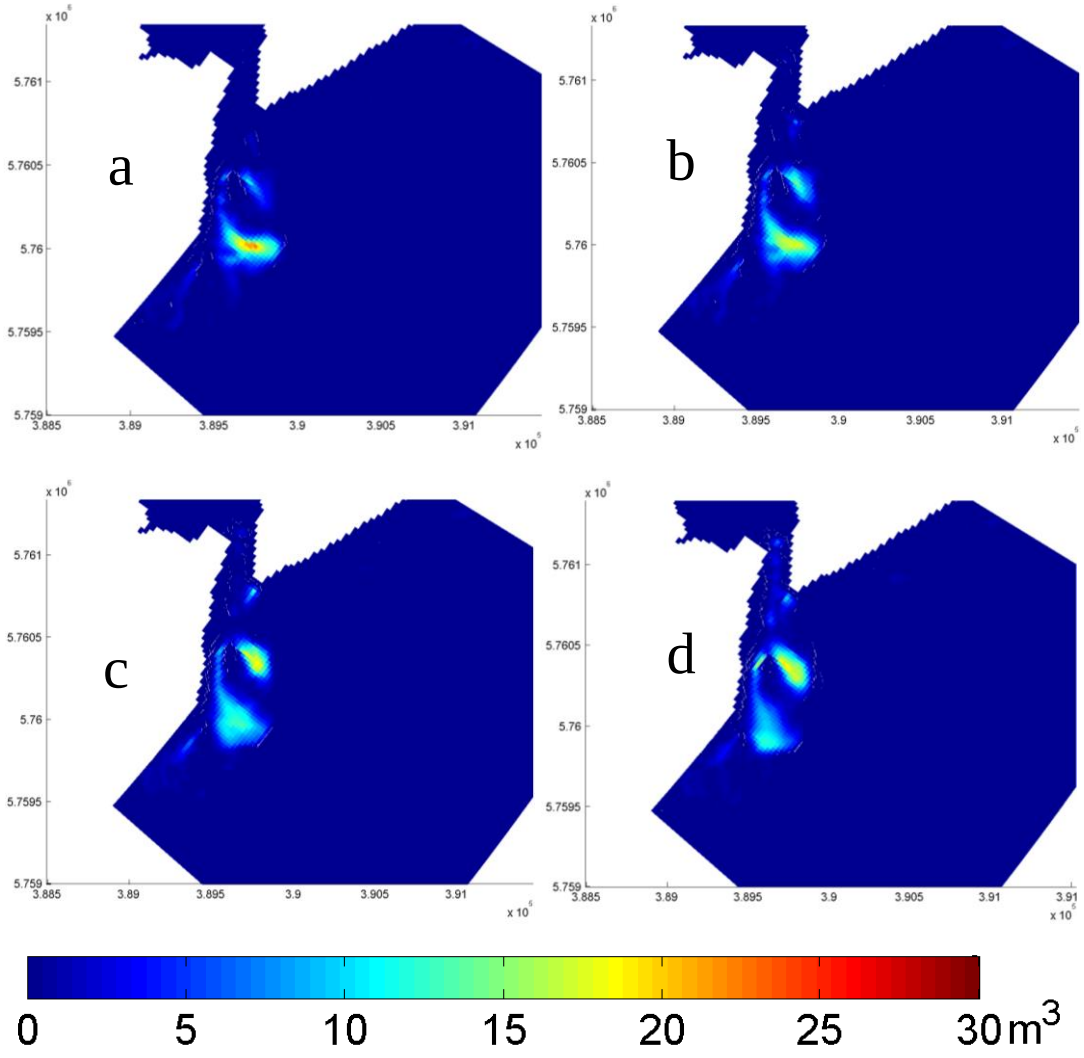

Figure 7.10 – The total sediment transport volume (m^3) around the Deben Estuary over one spring tidal cycle (from 09/09/2002 02:00AM to 09/09/2002 12:00AM) in different scenarios: a) present scenario (TA_SC0); b) TA_SC1 scenario; c) TA_SC2 scenario; d) TA_SC3 scenario. The colour bar shows the sediment transport volume in every node (one node area is $20\times25m^2$).

The total sediment transport volume over a spring cycle is shown in Figure 7.10. The total sediment transport volume at the primary ebb jet channel in the present scenario shows significant value (about $18m^3$) while there is no great sediment transport at the north ebb shoal. However, when future SLR occurs, the sediment volume that was transported at the original ebb jet channel decreases as the SLR rate increases, which is down to around $10m^3$ in the HE SLR scenario (Figure 7.10d). In the meantime, as a compromise, the sediment volume that transported in the newly-formed channel has

increased generally from LE to HE scenarios, ending with about $16m^3$ in the newly-formed channel (Figure 7.10d).

It is noted that as the SLR increases (from TA_SC1 to TA_SC3), the imported sediment transport slightly increases at the north tip of ebb delta from negligible rate ($<0.1\times10^{-6}$ $m^3/s/m$) at present scenario to slightly higher rate ($\sim1.0\times10^{-6}$ $m^3/s/m$) in the TA_SC3 scenario (Figure 7.9), which also generates a larger sediment transport volume (about $8m^3$). When this small imported sediment transport is combined with strong sediment transport rate at newly-formed channel, a small anticlockwise sediment transport circulation pattern is formed (Figure 7.9d), which coincides with the residual flow pattern that is shown in Figure 7.8 (Subsection 7.2.2). The order of this transport circulation rate is also significantly lower than that in the main pathway.

The decrease of SBE water current (Figure 7.4) makes the suspended load deposit faster at the main ebb jet position, so the large sediment transport rate area will be reduced in the future scenarios. However, the reduction of slack water current at the newly-formed channel did not generate the same results. The slack water current does not contribute much to the sediment pattern at the newly-formed channel.

However, as the order of sediment transport rate at inner estuary is minimal, it is difficult to observe any changes between present and future scenarios. Considering the relationship between sediment transport and hydrodynamics, the changes of residual tide flow (Figure 7.8) at the inner estuary are not large enough to generate significant differences on sediment transport volume (Figure 7.10).

7.2.4. Morphological changes of the estuary after one morphodynamic year simulation

The resultant cumulative erosion/accretion around the estuary system is driven by the above sediment transport pattern over the simulation period. Based on the same initial bathymetry, shown in Figure 7.11, the most significant discriminations among different SLR scenarios occur at the original ebb jet channel and newly-formed ebb jet channel north of the main jet channel (Figure 14). The detailed characteristics of

cumulative erosion/accretion and hence bed changes under these scenarios are discussed below.

TA_SC0

Before discussing the simulated results for the present scenario, the modelled results will be compared to the measured bathymetry, shown in Figure 7.12. The model based on the schematic boundary conditions is able to reproduce the primary ebb jet region which will experience a slight erosion during the simulation year (refer to the initial bathymetry in Figure 7.11). Additionally, the erosion of north ebb shoal and the small bed level changes at the south delta attached to the south bank were also reproduced by the model.

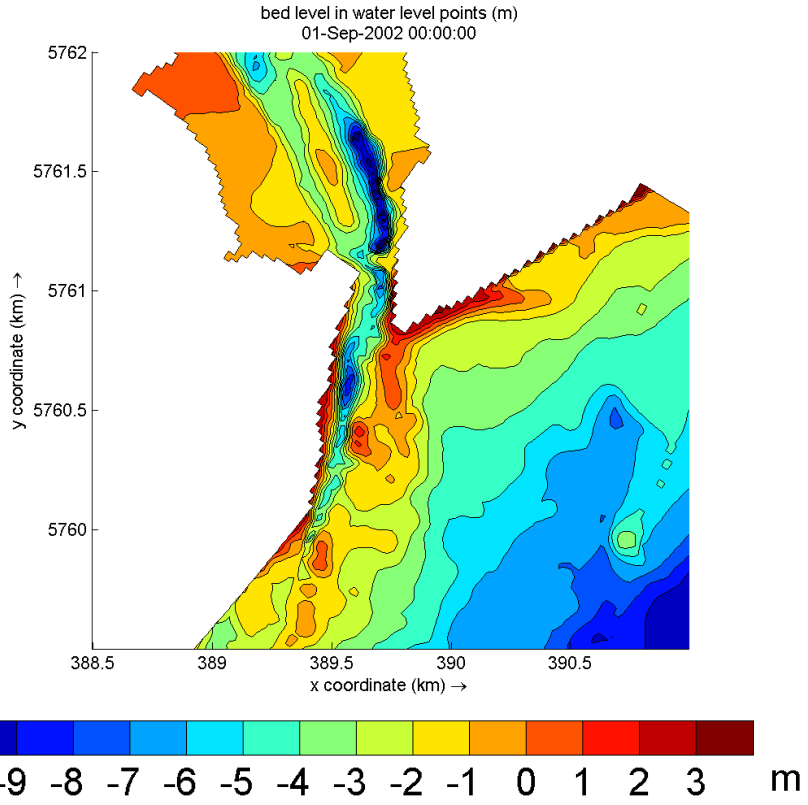

Figure 7.11 – The contour line plot of initial bathymetry in all the scenarios (2002 measured bathymetry).

In terms of the detail difference between measured and modelled bathymetry, it is shown in Figure 7.13a that there are still different between the measured bathymetry

of 2003 and the modelled results. Apart from the significant difference in the deep oceanic area, the most significant difference at the estuary is located at the deep channel. This difference may be due to the interpolation errors and miss matches when dealing with the bathymetries from different historical surveys. This is because in the aspect of physical process of model, the bed level at deep areas would not be changed easily in reality and this can be reproduced by the coastal region modelling (Figure 7.14). So any difference relating to the deep area would be due to the interpolation and measurement errors rather than the model limitations.

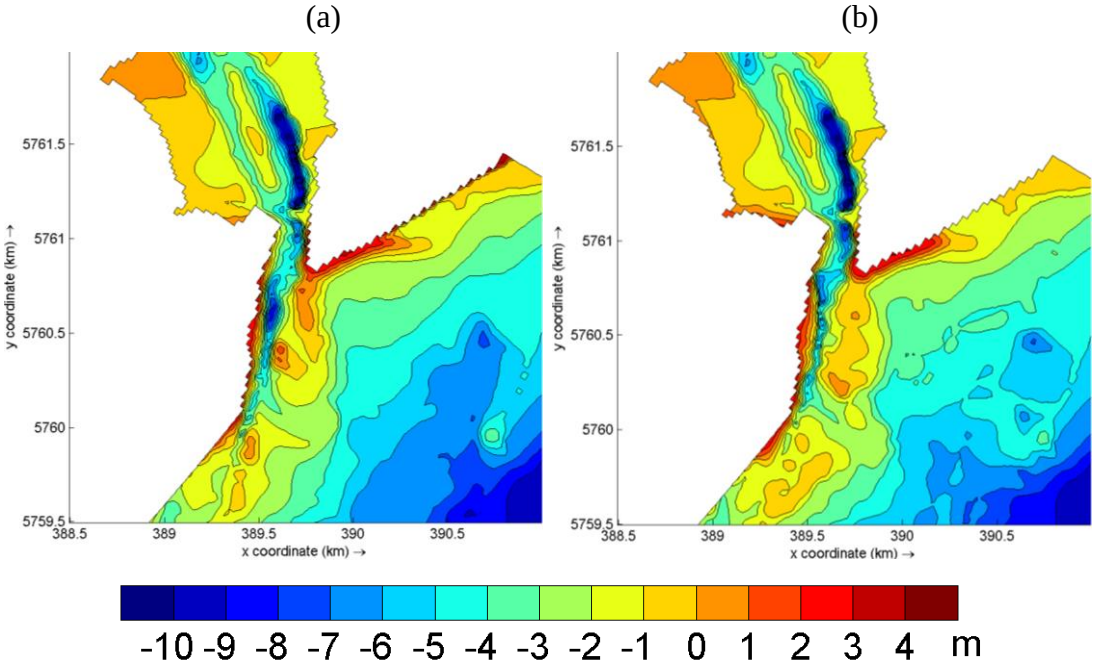

Figure 7.12 – The final modelled bathymetry in present scenario (a) and the measured bathymetry (b) at the end time of simulation (year 2003).

For the differences at the deep channel in the estuary, the model is not able to reproduce the accretion of the bed level. This is due to the schematic wave inputs instead of the real wave conditions. The model is using the average wave condition during the simulation so that some significant wave conditions may be lost such as storm waves. These differences will be increased as the simulation continuously runs. Therefore, the wave impact is one of the most important factors leading to the differences between modelled and measured bathymetries. Additionally, apart from the interpolation errors, the model limitation such as the use of Morfac also affects the accuracy. In terms of

the ebb tidal delta, the average difference between measured and modelled bathymetry is not significant which is tolerant for the morphological model. Therefore, by considering the interpolation errors, simplified boundary conditions and numerical model limitations, it is comparable on the bed level changes between modelled and measured results.

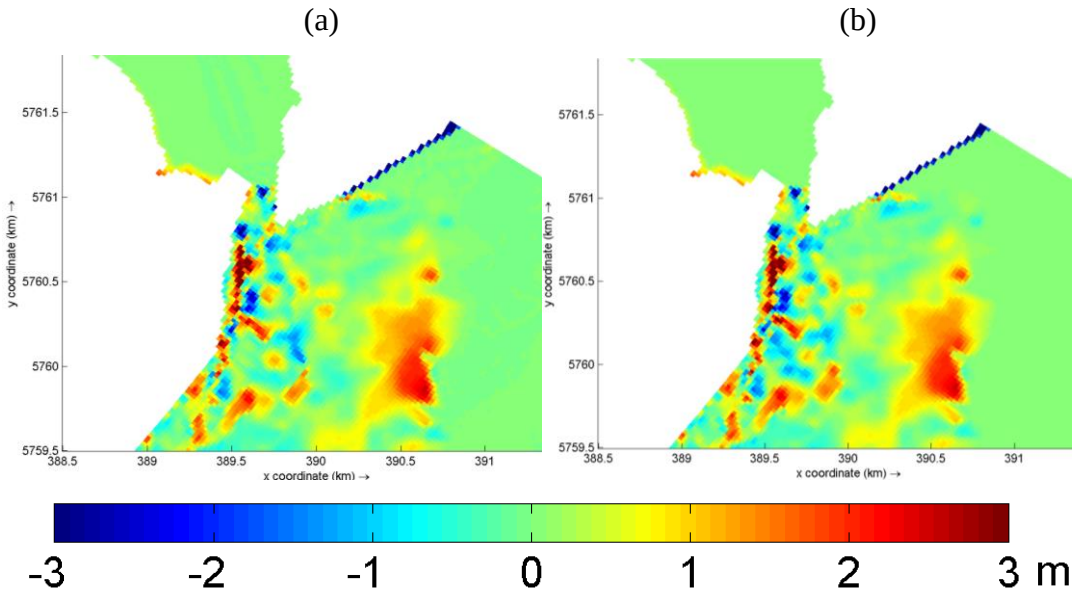

Figure 7.13 – The comparison between the measured bathymetry (2003) and the modelled final bathymetry (a) (Figure 7-12b minus Figure 7-12a) and the comparison between measured bathymetry (2003) and initial bathymetry (b) (Figure 7-12b minus Figure 7.11).

In the present modelled scenario, most erosion occurs at the middle of the ebb channel while the sediment is transported and deposited to the seaward side of the ebb jet channel resulting in accretion outside the delta (Figure 7.14a). The erosion/accretion track at the main ebb jet position indicates that the net offshore sediment transport occurs along the primary ebb jet occupying the majority morphological changes and the most serious accretion happens at approximately 600m offshore of the coastline at the end of original ebb jet channel. The maximum amount of erosion/accretion at the position of potential newly-formed channel is ±0.5m. In terms of the downdrift and throat area, no obvious erosion/accretion pattern can be observed where there are irregular bed level changes around ±0.15m.

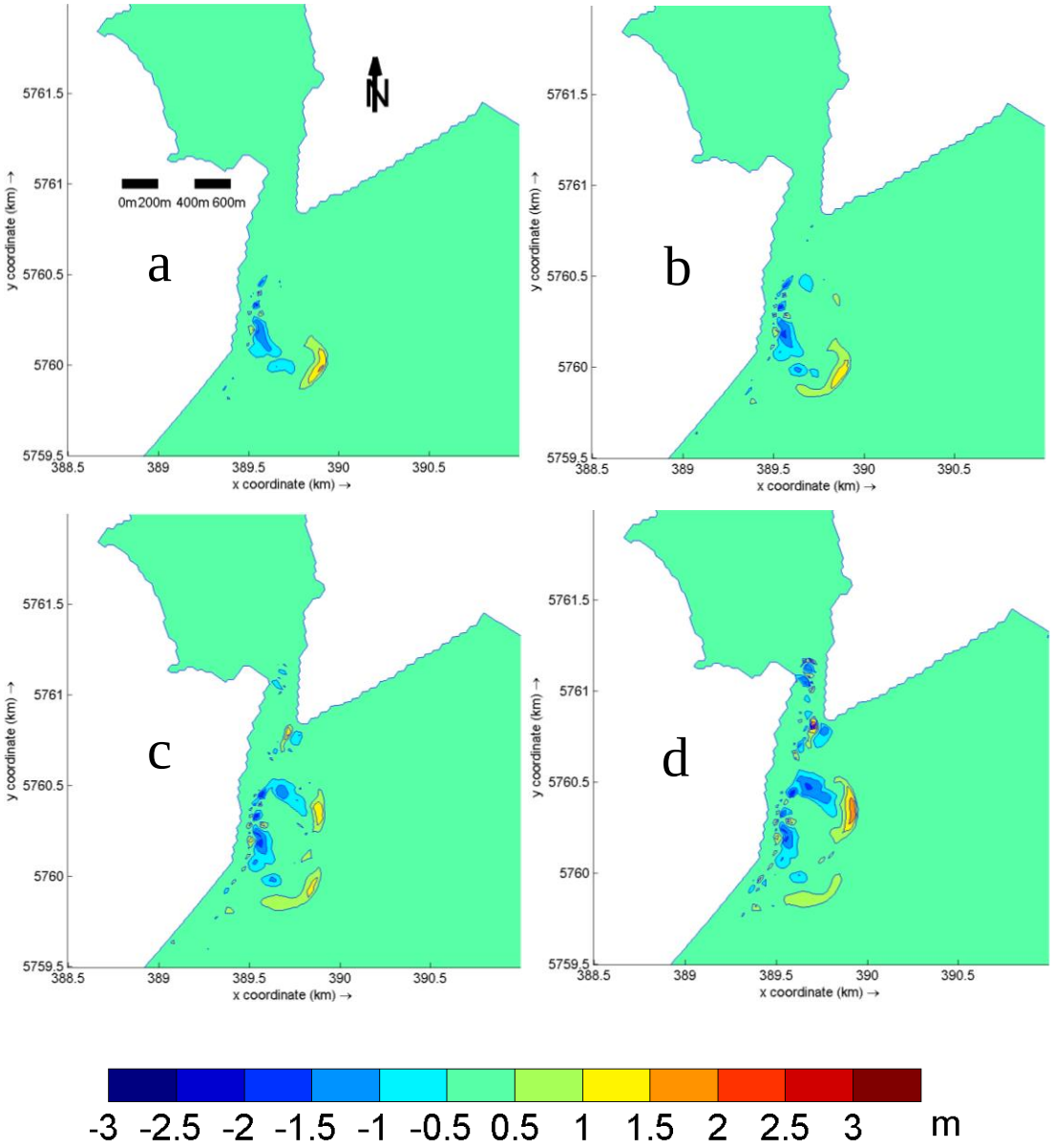

Figure 7.14 – Cumulative erosion/accretion (m) around Deben Estuary in present scenario and future scenarios at the end of the simulation: a) present scenario (TA_SC0); b) TA_SC1 scenario (LE SLR); c) TA_SC2 scenario (ME SLR); d) TA_SC3 scenario (HE SLR). The negative values mean erosion and positive values mean accretion.

TA_SC1

In the low emission scenario (TA_SC1) (Figure 7.14b), the ebb jet will experience a slight difference compared to present scenario (TA_SC0) although the most serious erosion positions will not change. The ebb jet in this scenario is not able to erode as

seriously as that in TA_SC0 scenario. The maximum offshore deposition depth is reduced from 1.8m in present scenario to about 1.4m in this scenario. Apart from the decrease on the magnitude of erosion/accretion, the length of significant bed level change (larger than 0.5m) is also shortened by approximately 30m from the present scenario due to the reduction of net sediment transport (Figure 7.9b). Therefore, in terms of original ebb jet channel, the change of morphology is gentler than that in the present scenario, as a result of the decrease of the ebb tidal flow's magnitude (Figure 7.5b).

The newly-formed channel position in this scenario has expended its path much further than that in the present scenario although it is not obvious on the ebb delta (Figure 7.14b). Compared to the present scenario, this breach has its length around 300m towards offshore (Figure 7.15) in southeast direction and its depth at the deepest point (entrance of this branch channel) is increased by approximately 1m (Figure 7.14b). At the seaward end of this newly-formed channel, some deposition has taken place: a small delta could form.

TA_SC2

For the future scenario with medium emission TA_SC2 (Figure 7.14c), the original ebb jet channel will continuously experience less erosion than that in TA_SC1 scenario while the newly-formed small channel increases its length and depth. The obvious change is that the furthest deposition site at the end of original ebb jet had moved approximately 100m landwards. The maximum accretion at the frontage of ebb jet has reduced to approximately 1m and the deposition site of the ebb jet has expanded clearly to the south. This scenario shows a clear switching on transport direction from eastwards in present scenario to southwards in this scenario as the erosion/accretion path has switched. If more sediment deposits in the ebb jet, directional change may potentially connect the north ebb delta to the downdrift beach.

The erosion/accretion pattern at newly-formed channel becomes clearer due to the increased rate of SLR. Significant erosion occurs in the channel and the maximum erosion has increased from 0.5m in TA_SC1 scenario to 1.3m in this scenario. The obvious deposition at the seaward side of this newly-formed channel (accreting about

1.3m) has also contributed to the formation of the newly-formed delta at the end of the channel.

However, the mechanism of formation of the new channel may differ from that of the original ebb jet, which may start from the offshore erosion, resulting in sediment starving at offshore side. According to the different distributions of ebb tidal current in the newly-formed channel and original ebb jet channel (Figure 7.5), the velocity magnitude at the offshore side of newly-formed channel is much larger than the nearshore side.

In this scenario, the landward sediment transport at the north tip of ebb delta is becoming more obvious. However, the residual tidal flow does not enhance the landward sediment transport as there is no significant increase on residual flow at this site within these scenarios (Figure 7.8). The most contribution is probably by the reduction of slack water velocity before spring ebb tide (Figure 7.4). The low tidal current provides sufficient time for the fine sediment transported from ebb shoal to deposit at this site, which has been mentioned by Dronkers (1986).

The erosion/accretion pattern at the middle of main channel does not change much in this scenario. The residual flow indicated that it will decrease slightly with the increase of the SLR rate (Figure 7.8); this illustrates that the residual tidal flows cannot accurately predict the erosion/accretion. Since there is coarse sediment settling within the main channel, the suspended load (which comprises most of total sediment transport) of coarse sediment is limited by the maximum current speed (Dronkers, 1986), which, in this study, is subjected to the ebb tidal currents (Figure 7.5) that do not vary at the middle of main channel among these scenarios.

TA_SC3

In the HE SLR scenario TA_SC3 (Figure 7.14d), the entire ebb delta experienced significant erosion. Although the bed changes of the original ebb jet are minimal in this scenario, the most notable observation is the increased erosion in the newly-formed channel. The maximum erosion depth in the newly-formed channel increased to around 1.5m which cut through the ebb shoal (Figure 7.15d). The eroded sediment

increased the accretion at the seaward by around 1.5m is associated with the dramatic expansion of the newly delta which will potentially connect to the deposition of south ebb jet.

In this scenario, the extent and depth of morphological change in the original ebb jet area has been reduced, which seems that the sediment will not be transported offshore further (Figure 7.9d). In addition, the direction of this shortened original ebb jet continuously shifts to south potentially connecting to downdrift coast. Because of the slowed down ebb jet, the state of original ebb jet seems much more stable. So the newly-formed channel may eventually replace the original ebb channel.

Apart from the significant changes to the ebb shoal, the throat of estuary is also going to be much more dynamic in this scenario. There is more erosion at the throat in this scenario as a result of increase on flood tide current as the SLR happens (Figure 7.7). In addition, at the north part of ebb tidal delta just beside the throat, the bed level change becomes clear in this scenario. The erosion is observed on the offshore side, with accretion on the onshore side.

The increase of the landwards current at the north tip of the ebb shoal with the increase of SLR will provide more sediment source for the main channel and then transport these extra sediments to either newly-formed channel or original ebb jet by strong ebb current in main channel. So, sediment deposited in these two places is likely to come from the north tip of the ebb delta through main channel rather than directly through ebb delta.

Similarly, with the situation in TA_SC2, when the north tip is sediment starved, the longshore feeding of sediment from updrift beaches will happen. It was reported that the delta's sediment is almost entirely derived from Orford Ness (HR Wallingford, 2002). As the starving process of sediment in ebb delta will accelerate in the future scenario, the time of longshore sediment transport along the Suffolk line will probably reduce in the future. However, this needs to be proved by a long-term analysis of longshore sediment transport by considering wave impacts.

7.2.5. Discussion on the bathymetry state changes due to SLR

After one morphodynamic year simulation, different SLR scenarios developed different morphodynamics changes (Figure 7.15). The same initial bathymetry (measured 2002) was used in all simulations (Figure 7.11).

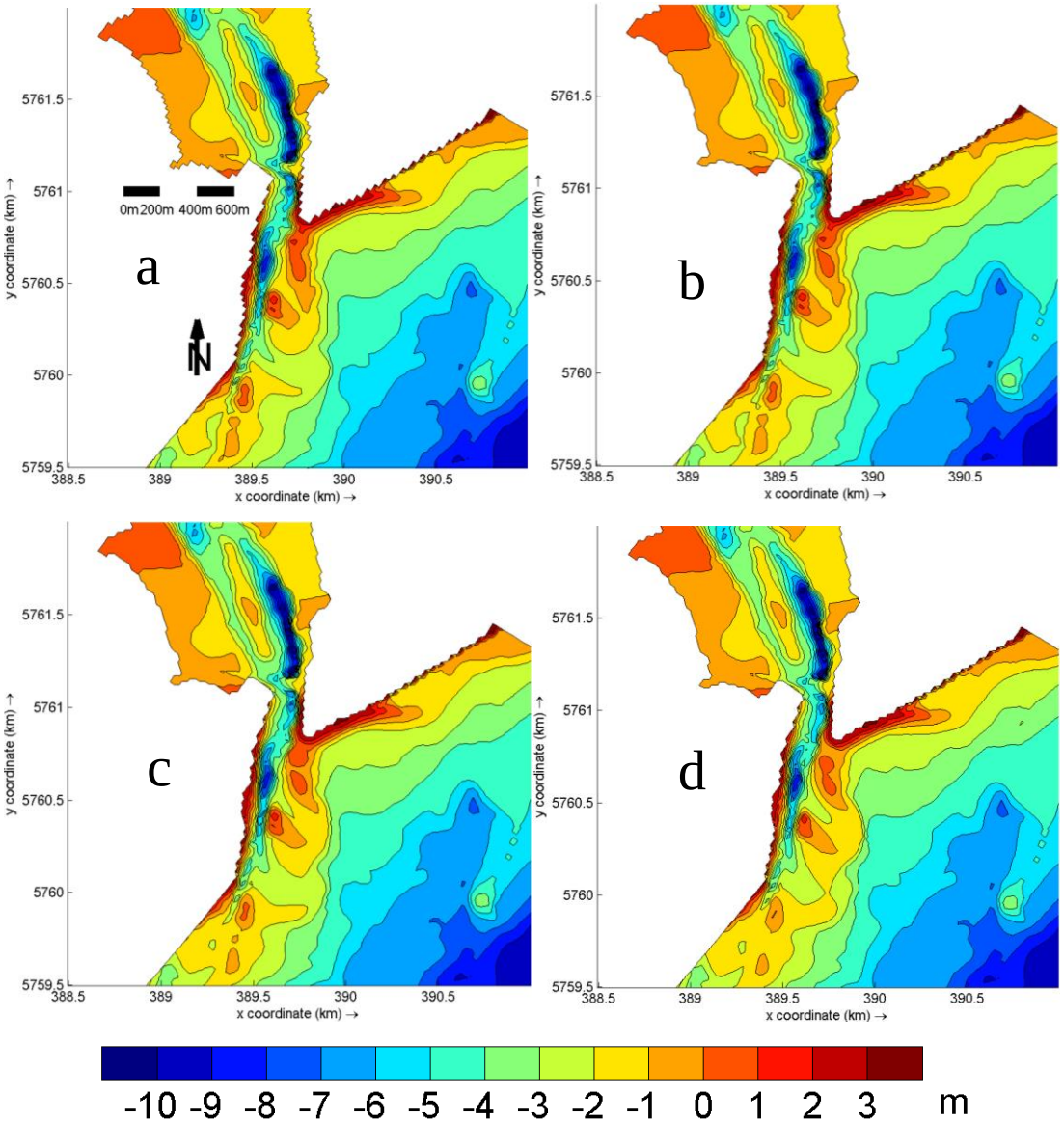

Figure 7.15 – The final bathymetries of the Deben Estuary in present scenario (a): TA_SC1 scenario (b); TA_SC2 scenario (c); TA_SC3 scenario (d).

In the present scenario (Figure 7.15a), a breach (erosion) can be found in the middle part of the north ebb shoal. The rest of the shoal is similar to the initial bathymetry. The original ebb jet region experienced slight erosions as well. All these features can be found in the measured 2003 bathymetry (Figure 7.12b) although the quantitative bed level changes are different.

With SLR, the ebb tidal delta seems to be much more vulnerable to the hydrodynamics. A small partial breach had been developed at the northern side of the ebb shoal under TA_SC1 scenario. In the TA_SC2 and TA_SC3 scenarios where sea level is higher, the developed breach becomes more pronounced (Figure 7.15b-d).

In the meantime, the original breach that was present in the initial bathymetry seems to get shallower as the sea level rises. Particularly in the HE SLR scenario, there is a connection at the original ebb jet channel between north ebb shoal and south ebb shoal. Thus, with the changes of ebb shoal, the course of the ebb channel also changes accordingly: this may change the entire outer estuary's hydrodynamic and sediment transport regime. However, the inner estuary seems to maintain stability.

In order to investigate the bed level change in detail, several cross sections are chosen (red lines in Figure 7.16). The cross section BR1 is at the primary ebb jet and cross section BR2 is located the secondary breach position. The downdrift beach is chosen as DD cross section and the throat cross section is TR in Figure 7.16. All the selected cross-sections are the limited within the first 700m from the coastline.

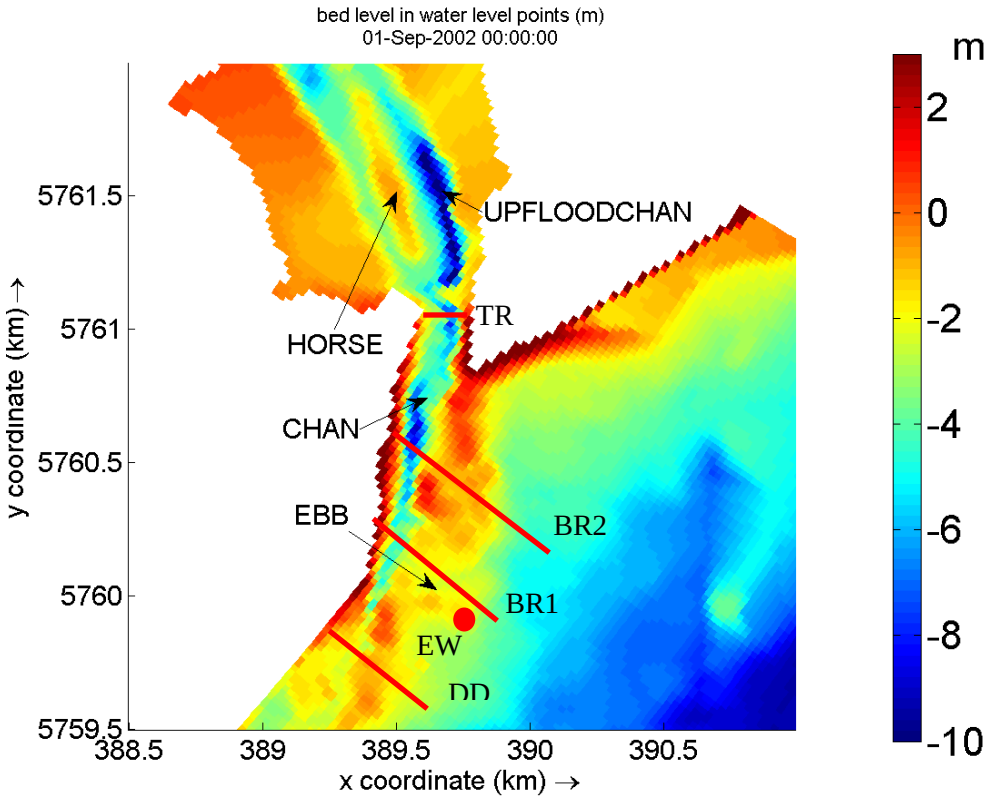

Figure 7.16 – Observation points and cross sections for the detailed investigations on the morphological changes.

The final bathymetries of these four cross sections are shown in Figure 7.17. For the throat (TR) cross section (Figure 7.17a), when the sea level rises, it will increase its depth as the increase of ebb tidal current (Figure 7.5), which seems to be because of more seaward sediment transport. As for the secondary breach section (BR2), the erosion at this profile is increasing as the sea level rises (Figure 7.17b) which results in more accreted sediment at offshore side. So, this new channel seems becomes more obvious due to the increased depth as climate change progresses.

In contrast to the increased erosion at the secondary channel, the reduction of erosion at the primary channel (BR1) can be clearly seen as the sea level rises (Figure 7.17c). In the highest emission scenario (TA_SC3), the final bed level is almost at the same level of initial bathymetry. However, it is difficult to determine the bathymetry change exactly at this site just according to this 1D figure since the ebb jet channel has switched its direction from east to south which means there is directional component parallel to the coastline in 2D figure (Figure 7.15).

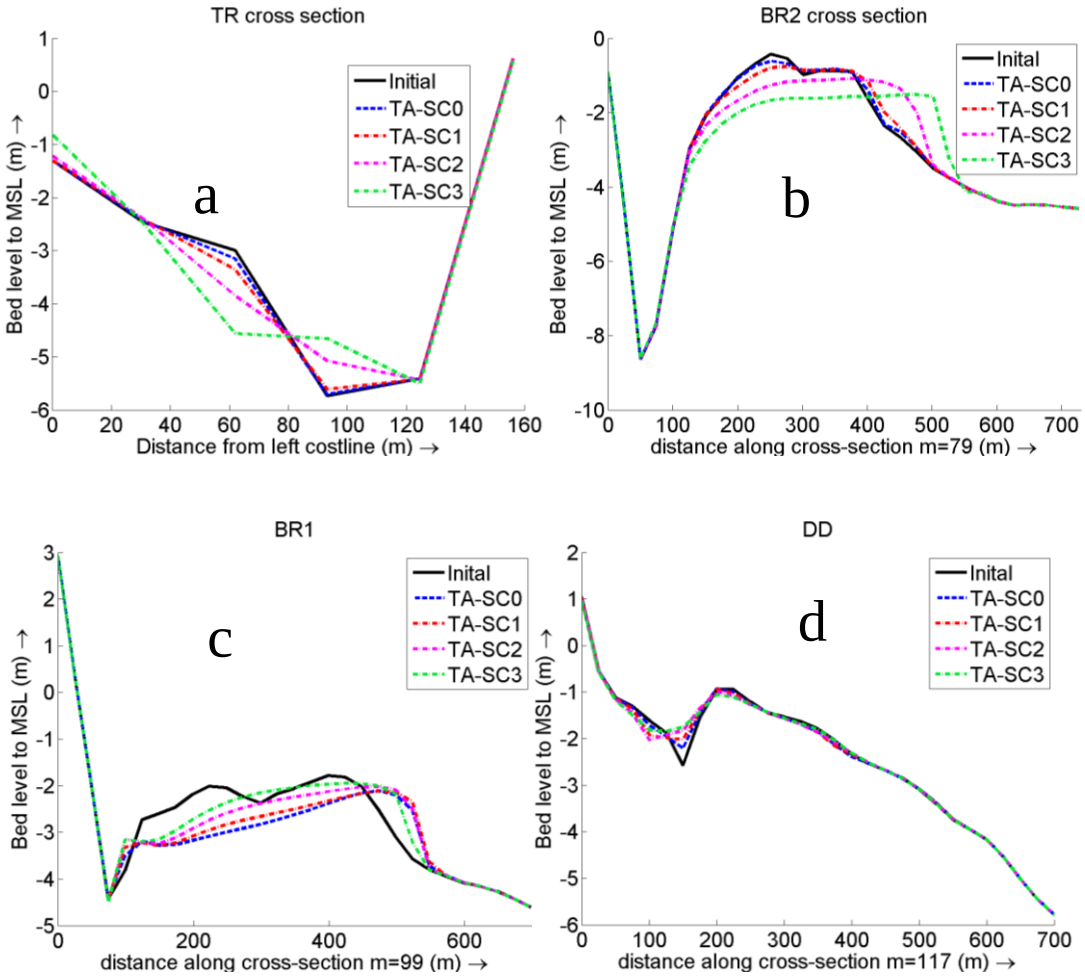

Figure 7.17 – The final bed level profiles of the selected cross sections (ref. Figure 7.16) after one morphodynamic year simulation. Note: for the last three cross profiles, the first 700m of the cross section was selected as deep area did not change on bed level.

In the downdrift beach (DD section), the deep area of the section becomes shallower with SLR, although the change rate is not obvious (Figure 7.17d). This increased accretion at the downdrift side was not obvious in 2D figure (Figure 7.15).

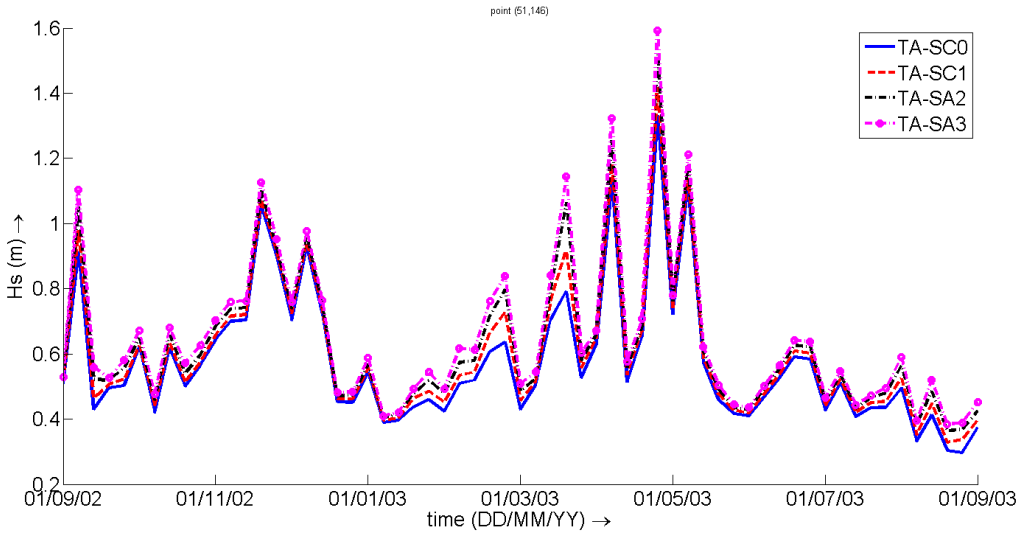

Figure 7.18 – Time series of H_s(m) at the ebb jet position (red dot shown in Figure 7.16, 51°58'46"N, 01°23'44"E) during the simulation in different scenarios.

Additionally, the significant wave height (H_s) at the ebb delta position (red dot EW in Figure 7.16) is predicted to increase slightly with SLR (Figure 7.18), although all the scenarios are based on the same simplified wave boundary condition. At this site, the mean H_s value will increase by 13% from the present scenario TA_SC0 to the high emission future scenario TA_SC3. These increased H_s will also potentially increase the sediment movement so that the ebb shoal becomes more vulnerable. Particularly when the extreme wave condition occurs, the increase rate of wave energy may be dramatically enhanced by the SLR, which will be discussed in next chapter.

7.3. Summary

This chapter presents an analysis of the morphodynamic responses of the Deben Estuary under three future sea level rise scenarios. It was found that the estuary morphology is significantly sensitive to SLR.

- The ebb shoal will become more dynamic with SLR. There will be a new secondary channel forming at the north ebb shoal while the erosion at the original ebb jet channel will be reduced as the SLR rate increases. Particularly in the high emission SLR scenario, the ebb tidal delta will be fragmented by

this newly formed small channel, making it a vulnerable morphodynamic feature.

- For the hydrodynamic regime at the Deben Estuary under the condition of SLR, the maximum spring ebb tidal current will change the ebb shoal, leading to different morphological changes. The major trend of ebb tidal current is that the velocity at the original ebb jet decreases and current at the newly-formed channel increases with the SLR. However, the spring flood tidal currents do not change significantly with sea level rise.

- Sediment transport pattern in the outer estuary changes with SLR. This is attributed to the changes in the tidal flow pattern and the residual flow pattern. The primary ebb channel shows signs of infilling, while a new channel is formed as a result of breach of the ebb shoal.

- However, the residual tidal current cannot always explain the system's morphodynamic changes. For example, the onshore sediment transport at the north tip of the ebb shoal and the middle main channel does not show a strong relationship with residual tidal current.

- For the inner estuary, there is no obvious morphodynamic change even if the SBE slack water current at inner estuary will be enhanced by SLR. The increased SBE slack water cannot change the bed level at the inner estuary.

- The original ebb jet has been shortened because of the reduction of erosion after SLR, the previous main channel may potentially be blocked while the newly-formed channel probably replaces it as a part of main channel. However, this needs to be proved by long term simulations over 3-4 years.

Chapter 8: Morphodynamic response of the Deben Estuary to extreme conditions under global climate change

Chapter 6 has discussed that the extreme wave climate at the offshore of the Deben Estuary will change due to global climate change. Therefore, regarding the impacts of climate change on estuary morphology, it is necessary to consider these extreme wave impacts on morphodynamics, in addition Sea Level Rise (SLR). As the actual future extreme storm occurrences cannot be predicted, this study considers statistically determined extreme storm conditions (the storm with 1 in 100-year return period peak wave height). The estuary's morphodynamic response to future extreme storms with 1 in 100-year return period peak wave height will be compared and contrasted to that determined from the present 1 in 100-year storm conditions.

8.1. Scenarios description

The numerical model used in this chapter is the validated coupled Flow-Wave model described in Chapter 5. The wave condition is defined at the wave domain boundary, around 45km northeast from the estuary, West Gabbard wave rider (WGW located at 51°58.96'N, 2°4.91'E).

The storm wave condition is from the 1 in 100-year return period storm wave height (1% H_{smax}) that was discussed in Chapter 6. The analysis carried out in Chapter 6 reveals that 1 in 100-year return period peak storm wave height increases from 6.42m in present scenario to 6.85m in future scenarios. In terms of the 1 in 100-year peak wave period (1% T_{smax}), it is assumed to be dependent on the 1%H_{smax} which can be expressed as: $T_{pmax} \sim 5.3 \times H_{smax}^{1/2}$. The incident wave direction is taken as the predominant wave direction determined from the global modelled waves (45°N), described in Chapter 6.

This study assumes that storms last for 48 hours, representing severe conditions according to historic storm data. A triangular storm profile is assumed as shown in Figure 8.1 to be the wave boundary conditions for the models. In this profile, the significant wave height increases linearly from threshold H_s to the 1 in 100-year return

level H_{smax}, and then decreases linearly to the threshold H_s, in which the 1 in 100-year return level is H_{smax}. To model the most extreme conditions, it is assumed that the storm peak coincides with high water spring tide. The starting time was taken as 01/09/2002, 00:00AM; simulations lasted for 3 days ending at 04/09/2002, 00:00AM (Figure 8.1).

The other potential critical scenario is when the storm peak coincides with the lowest tide: as shallow water depths at low tide may have an impact on wave breaking and morphodynamics. However, the results derived using this condition are found to be similar to the results from the former boundary condition (storm peak occurring at high tide) in terms of the cumulative morphological changes (some discussions will present in the following section). Therefore, results and discussions presented in this chapter includes simulation using only the boundary conditions shown in Figure 8.1.

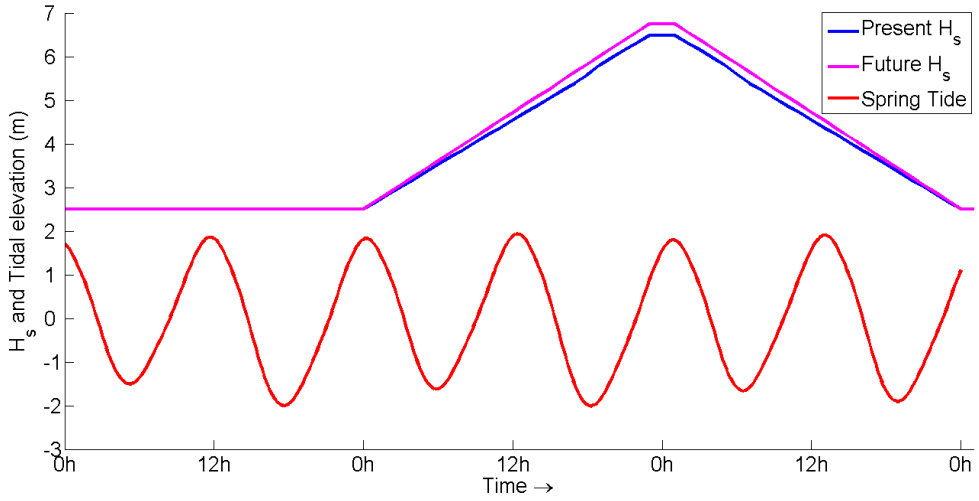

Figure 8.1—Assumed time series H_s conditions and tide conditions of the model in present and future scenarios during the 3-day simulation (from 01/09/2002 00:00AM to 04/09/2002 00:00AM) and the highest H_s value happens at 03/09/2002 00:00AM.

As discussed above, all the scenarios are categorised into ‘present’ and ‘future’ climate scenarios. The present scenarios represent current 1 in 100-year return period peak storm wave height and current sea level. For the future scenarios, wave data is based on the global climate projection whose condition is derived from the A1B scenario (Murakami et al., 2012; Shimura et al., 2015). Therefore, when considering the SLR

scenarios corresponding to a 1 in 100-year return period peak storm wave height, the medium emission SLR scenario is selected in this study because the projected future wave data is based on the medium emission SLR scenario. So, future scenarios consider both future 1 in 100-year return period peak storm wave heights and the medium emission SLR effects.

The spring tidal range of the Deben Estuary is around 3.5m. In this study, it is assumed that the tidal range will not change in the future. For tide elevation in the future scenarios, only the increased SLR is added to avoid tidal range distortion.

Historic bathymetry measurements reveal that the Deben Estuary exhibits three distinct morphological states between which the ebb tidal delta cyclically evolves (Burningham and French, 2006). These three important bathymetry states are shown in Figure 8.2. The State A is the morphology associated with the progressive extension of the updrift ebb-tidal shoal causing down-drift migration of the ebb jet and some recession of the down drift shoreline; State B contains cross-shore breakdown of the updrift shoal and downdrift shoal extension and diversion of the ebb channel; and State C has relocated the ebb jet region to a northerly position because of a permanent breach of the updrift shoal.

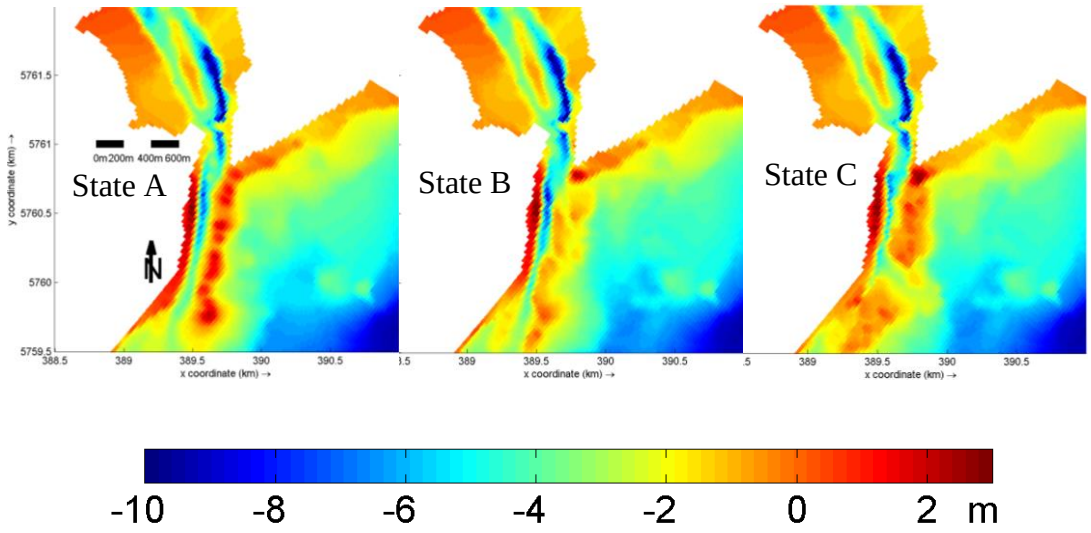

Figure 8.2 – Three representative bathymetry states that used in this study: State A; State B; State C.

In this study, the evolution of the estuary under 'present' and 'future' climate scenarios, when the estuary is in State A, B and C discussed above are simulated and discussed. This provides the opportunity to investigate how these bathymetries will respond to future wave storms and the difference in responses to climate change so that it is able to investigate the stability of ebb delta during future extreme storms. Breaching or fragmentation of the delta during a storm may significantly alter the estuary's short-term dynamics, which can have serious consequences for the entire estuary system.

All the scenarios with present and future hydrodynamic conditions will be carried out based on each initial bathymetry. The total scenarios are summarised in Table 8.1: there are 6 scenarios in this study, each containing present and future scenarios.

Table 8.1 – The total scenarios that are carried out in this study during the spring tide conditions

	State A-1% H_{smax}	State B - 1% H_{smax}	State C - 1% H_{smax}
Present	P_S_A	P_S_B	P_S_C
Future (SLR)	F_S_A	F_S_B	F_S_C

8.2. The differences of the results based on the different hydrodynamic conditions

As aforementioned, the simulated results between the conditions that the storm peak coincides with the High Spring Water Level (HSWL) and storm peak coincides with the Low Spring Water Level (LSWL) are similar. This section will briefly discuss the differences between these two cases. The latter hydrodynamic boundary conditions are shown in Figure 8.3, in which the low spring water level coincides with the storm peak. The most significant difference between Figure 8.1 and Figure 8.3 is the occurrence time of the storm peak regarding tidal variations.

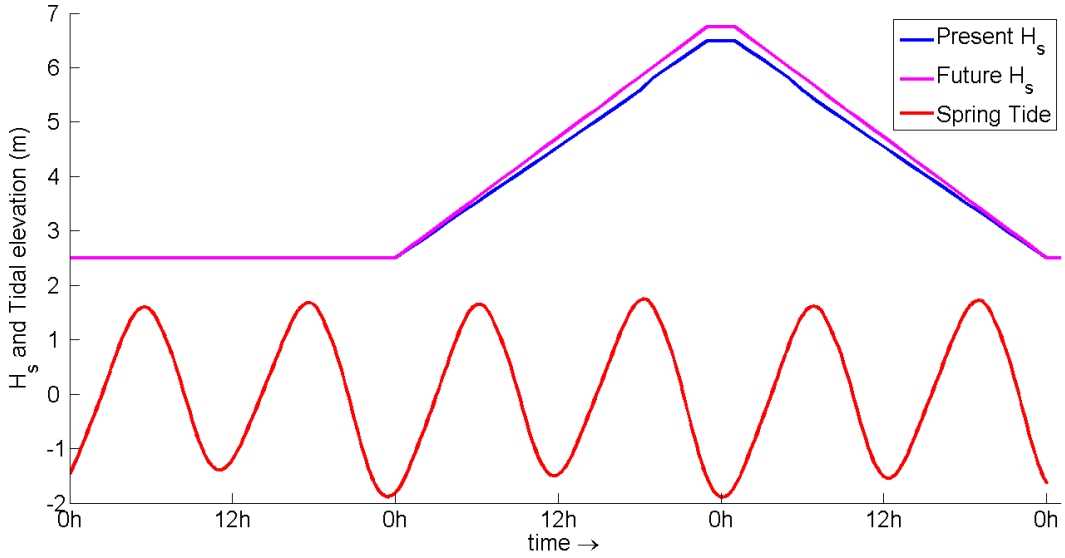

Figure 8.3 – The assumed time series H_s conditions that occur coincides with the low spring water level in present and future scenarios during the 3-day simulation (from 01/09/2002 00:00AM to 04/09/2002 00:00AM).

The most important aspect of this investigation is the morphological change due to hydrodynamic impacts. Therefore, this section is devoted to compare cumulative erosion/accretion patterns forced by the wave and hydrodynamic boundary conditions shown in Figures 8.1 and 8.3. For the sake of simplification, only 'present' results from each simulation are presented here.

The morphological changes of each state under the 'present' climate conditions based on different storm occurrence time (either storm peak storm coincides with HSWL or coincides with LSWL) are shown in Figure 8.4. It is shown that although the instantaneous hydrodynamic situation may significantly change due to the storm peak occurring at a low tide compared with high tide, because the wave effects are strongly linked to water depth, the cumulative bed level change is not significantly different between them as long as the storm duration remains the same and the tidal range does not change. In this case study, there are no obvious differences between these two cases. Therefore, the following discussions will focus only on the conditions that storm peak coincides with HSWL (Figure 8.1).

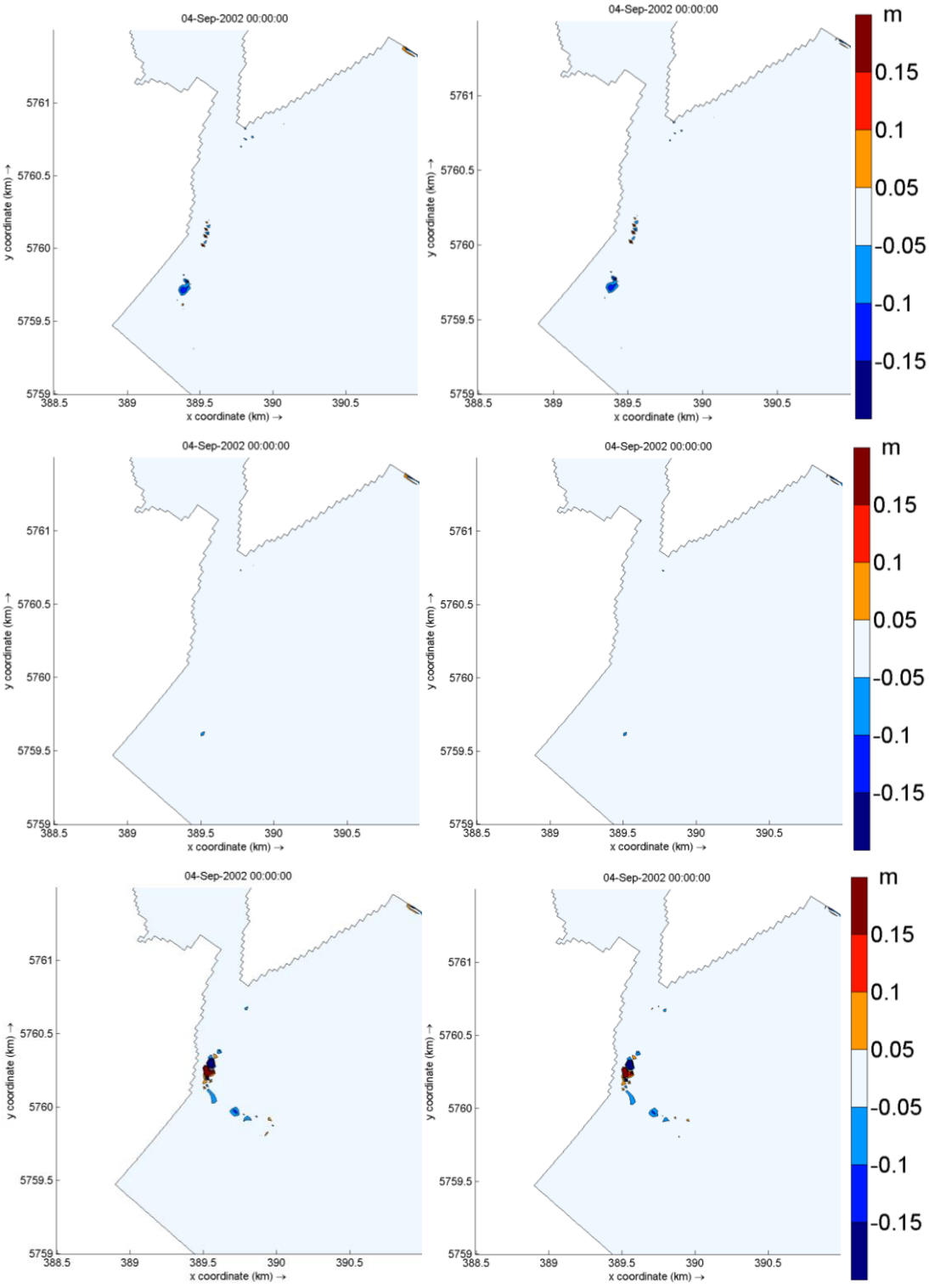

Figure 8.4 – The cumulative erosion and accretion after simulation based on the conditions in Figure 8.1 (HSWL, left figures) and the conditions in Figure 8.3 (LSWL, right figures) in each state under the present climate conditions (top: State A; middle: State B; bottom: State C).

8.3. Results in each bathymetry state under the conditions that the storm with 1 in 100-year return peak wave heights coincides with HWSL

In this section, the differences between morphodynamic change under present and future climate conditions at every estuary state will be discussed, and an inter-comparison of morphodynamics of three different estuary states will be carried out based on the assumption that the storm with 1 in 100-year return period peak wave height coincides with HWSL.

8.3.1. State A

The first selected state is State A in which initial bathymetry contains an elongated ebb shoal connected to the north bank and parallel to the south coastline. On the ebb shoal, the inter-tidal area is small, even during spring tidal cycles. In future when the SLR occurs (medium emission), the intertidal area of ebb shoal will further decrease, and the majority of the ebb shoal will be submerged. Thus, the hydrodynamic situation in this system and the morphodynamic responses will be directly changed. This will be discussed in detail in the following sections.

8.3.1.1. The tidal current change due to climate change

Since the ebb shoal evolution is closely related to the system's currents, it is vital to investigate the tidal current's changes due to the climate change. This study explores the residual tidal current after nonlinear wave-current interaction over the simulation.

The residual current distribution at the estuary is shown in Figure 8.5. The maximum residual tidal current in both present and future scenarios occurred in the main channel, and there are no significant changes between them. The most significant difference between these two scenarios is observed at the north part of the ebb shoal: the residual tidal current increases its values from average 0.2m/s in the present scenario, to around 0.3m/s in the future scenario. Additionally, residual tidal currents at the upper channel segment besides the north ebb shoal will also increase from 0.3m/s to about 0.45m/s.

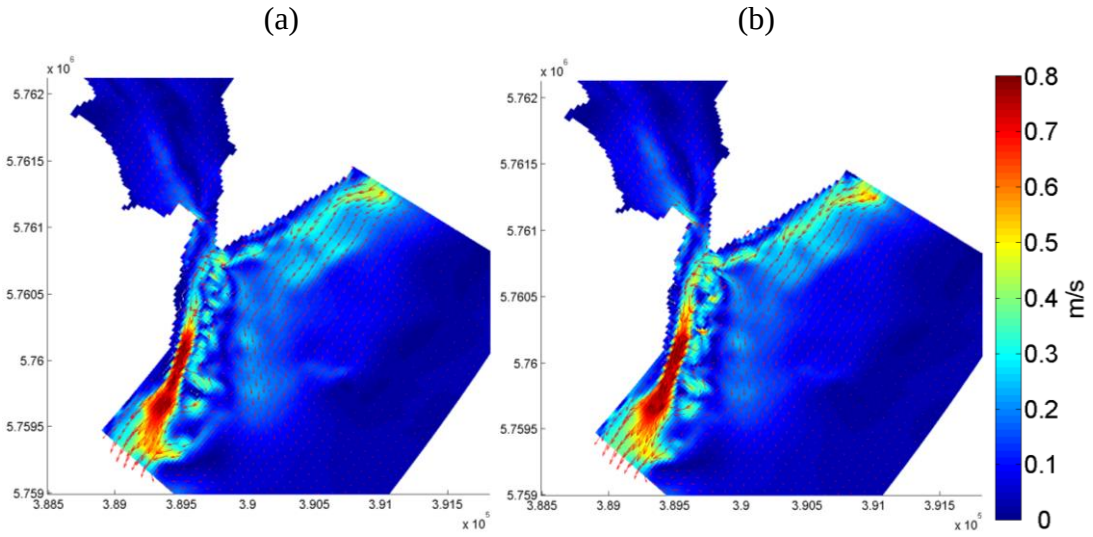

Figure 8.5 – Residual tidal current distribution in the Deben Estuary during spring tide in the present scenario (a) and the future scenario (b) in State A. The colour bar shows the magnitude of the residual current and the vector shows the direction of the residual current.

In the southern side of the estuary, there is also a slight increase of residual tidal current in the main channel, while a decrease of current in the ebb jet channel can be seen. There is also a slight change in the current's direction (Figure 8.5). These changes are not as significant as that at the north ebb shoal. Adjacent to the shoreline north of the estuary, there is a slight increase in residual current in the future climate scenario. Thus, when the estuary is under spring tide conditions, the major differences in residual currents between present and future scenarios are observed in the northern part of the estuary.

8.3.1.2. Spatial variation of peak storm wave height

When offshore storm wave conditions change due to climate change, the spatial distribution of wave conditions in shallow sea areas can change significantly because of the sea level change. Wave shoaling and depth induced wave breaking change wave height in shallow areas when water level change as a result of SLR. According to the depth limited wave breaking criteria, wave breaking point usually occurs at the place where the wave height is approximately 0.8 of water depth, the increased water depth

due to SLR makes the wave breaking point move onshore, which probably changes the morphology accordingly.

The spatial 1 in 100 H_{smax} distributions during spring tide condition in present and future scenarios are presented in Figure 8.6 in which the differences in wave height in shallow areas are clearly visible. In the present scenario, the wave energy decreases significantly when it propagates to the inlet system due to the shallow elongated ebb shoal (Figure 8.6a). However, the value of 1 in 100 H_{max} at the downdrift area is very large: it is about 1.7m under the present wave storm conditions.

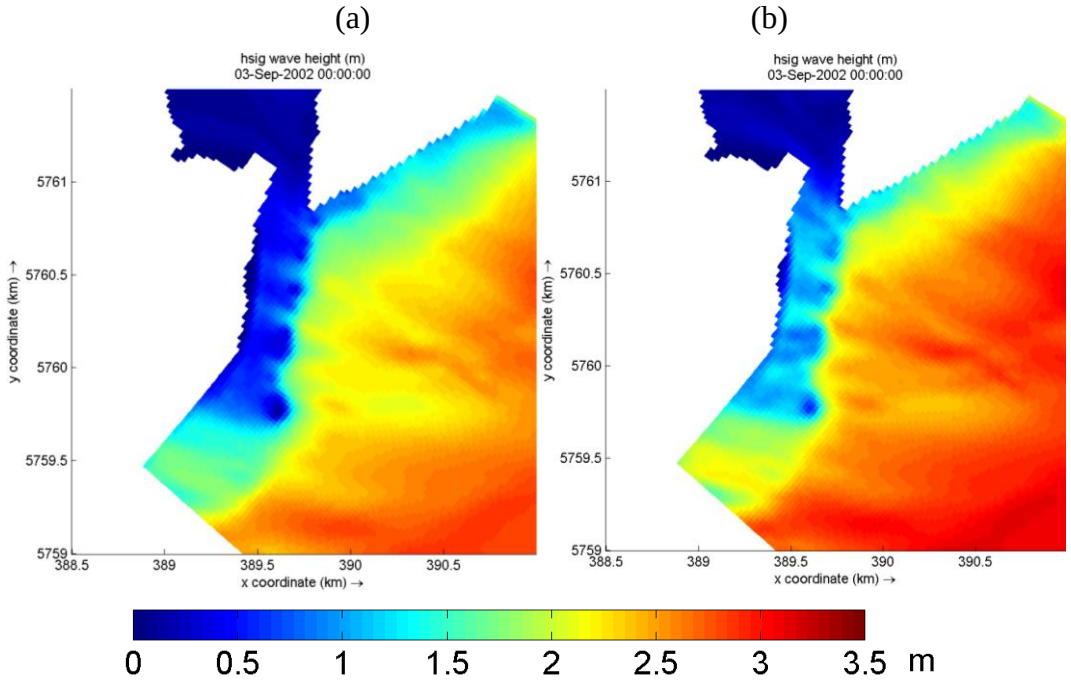

Figure 8.6 – The 1 in 100-year H_{max} distribution at the Deben Estuary at the time of peak wave storm happens (03/09/2002 00:00AM) under the spring tide conditions in present scenario (a) and future scenario (b) in State A.

In the future scenario, there is a significant increase in 1 in 100-year H_{smax} on the ebb shoal and the downdrift area (Figure 8.6b). On the ebb shoal, the peak wave height increases from 0.5m to around 1.5m; at the downdrift area it increases by about 0.6m to reach the largest wave height (approximately 2.4m) within the estuary. This increase is due to the interaction between increased MSL and wave propagation rather than due to the increase of 40cm at the boundary condition, which only increases by about

0.08m. This shows the significance of future change in extreme storm conditions due to SLR.

According to wave height variations between coastal and offshore zones in both present and future scenarios, there is a clear onshore movement of the wave height contour lines paralleling to the shoreline due to the climate change, which means the wave height will increase at the same point due to climate change.

Apart from the increase in 1 in 100-year H_{smax} at the ebb shoal area, there is a clear increase on H_{smax} at the shoreline north of the estuary, due to climate change as shown in Figure 8.6b. The H_{smax} on the far north beach has increased from 1m to 1.5m, which may potentially increase the longshore sediment transport since it has reported that the sediment source is mostly from north beaches of the estuary (HR Wallingford, 2002). However, it is noted that even if there is a great increase in wave height at the outer estuary, the wave distribution of the inner estuary (including the throat area) will not change too much due to the narrow inlet cross-section.

8.3.1.3. The residual bottom stress changes due to climate change

Since waves act as a stirring mechanism, allowing sediment to be transported even by a weak current, the wave and current motions at the seabed cannot be treated separately under the simultaneous presence of wave and current due to their strong nonlinear interaction (Grant and Madsen, 1979). Additionally, when considering the movable seabed, this process will be much more complex as the reformed bed level will change the elements' roughness to the flow. In this study, because of the short-term simulation, only wave-current interaction was considered and the alteration of roughness elements due to bed change was ignored.

As a result of wave-current interaction, the residual bottom stress during the simulation in both present and future scenarios are investigated (Figure 8.7). There is an enhancement of bottom stress in the main channel due to climate change when it is under spring tide condition, where the residual bottom stress increased from $10N/m^2$ to about $12N/m^2$.

Apart from the increase of residual bottom shear stress in main channel, there is a slight enhancement of residual bed stress at the north ebb shoal and the upper main channel besides the north ebb shoal (Figure 8.7).

In the downdrift beaches and south ebb shoal, there are no significant bed stress differences between the present and future scenarios. Therefore, in terms of the entire system under spring tide conditions, the climate change will increase the bottom stress on average at the north ebb shoal and the upper main channel but will not greatly affect the bottom stress on the downdrift beaches and south ebb shoal areas.

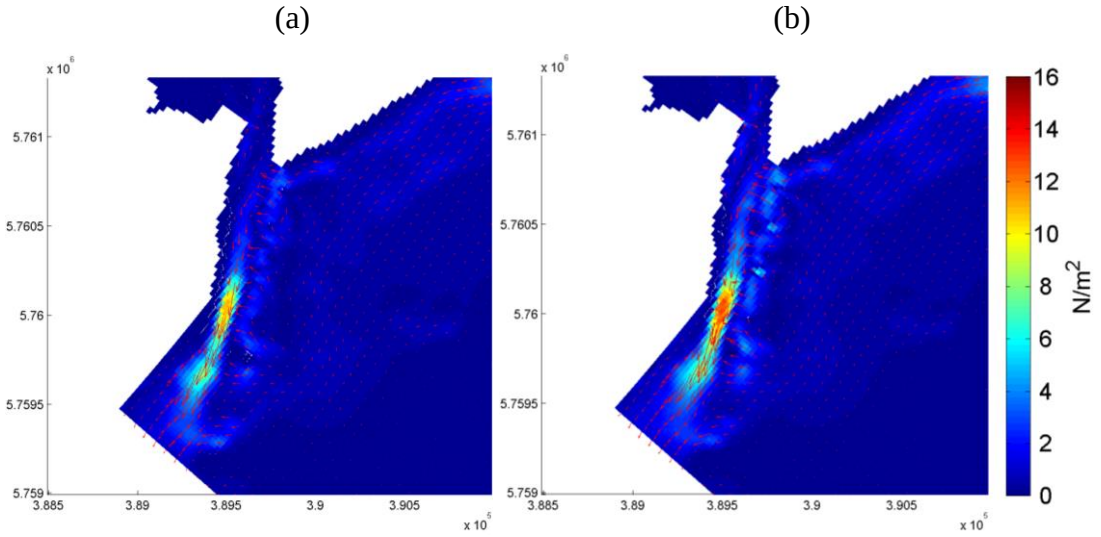

Figure 8.7 – The residual bed shear stress distribution around the Deben Estuary during the spring tidal conditions in different scenarios (a: present scenario; b: future scenario) in State A. The colour bar indicates the magnitude of the bottom stress and the vector indicates the directions of the residual bottom stress.

8.3.1.4. Morphodynamic responses to climate change

There is a significant increase in morphological changes under the future scenario than under the present scenario. This can be attributed to the combination of increased storm waves and SLR. The cumulative erosion and accretion patterns after simulations in present and future climate conditions are clearly shown in Figure 8.8.

Regarding the main channel, erosion of the south part of the channel has increased due to climate change, and has made the main channel much deeper. Apart from the

increased erosion, the south ebb jet area's erosion/sedimentation pattern has also intensified after the storm event in the future climate conditions. If the storm event occurs in the future, the reaction of the channel will become much more serious under future climate conditions. The eroded channel will allow larger tide flows, which will have some implications on the estuary behaviour.

In terms of the elongated ebb shoal attached to the north bank, the morphological change becomes clear alongside the ebb shoal particularly at the north tip of the ebb shoal where the most dynamic hydrodynamic situation occurs due to the complicated geometry. The entire ebb shoal is a shield for wave propagation under the present conditions; when the MSL has been increased, the function of shielding does not change too much on the bed level. However, when the storm event happens in the future climate conditions, with the help of direct explosion to the incident wave, the ebb shoal seems to be more dynamic (Figure 8.8).

For the aspect of adjacent beaches, although the change is not significant, the newly-formed band of erosion area almost appeared under the future storm event (Figure 8.8). The difference is not obvious compared to the estuary change (Figure 8.9).

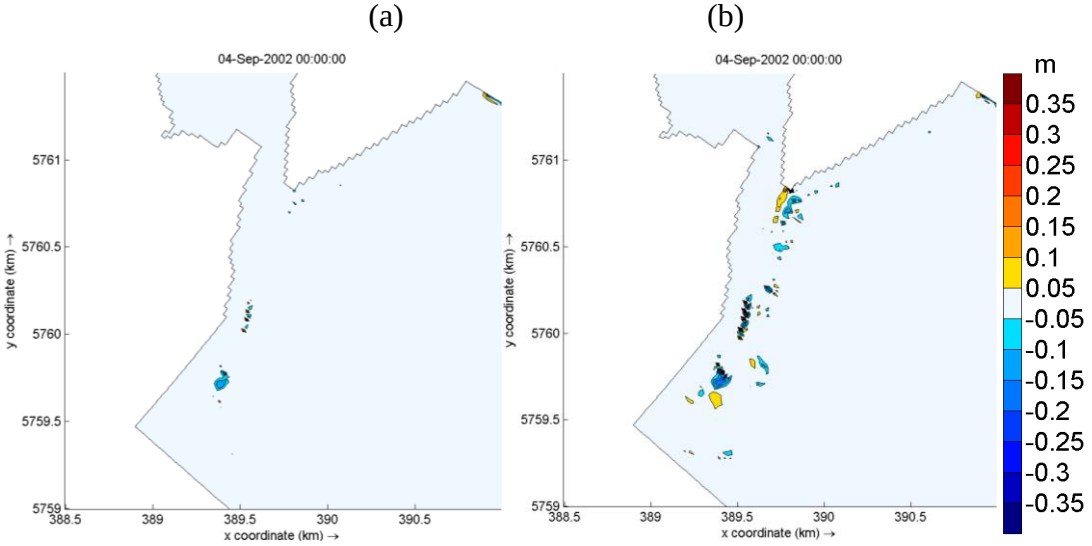

Figure 8.8 – The bed level changes is State A after simulation under the spring tide conditions in present scenario (a) and future scenario (b). Negative value means erosion and positive value means accretion.

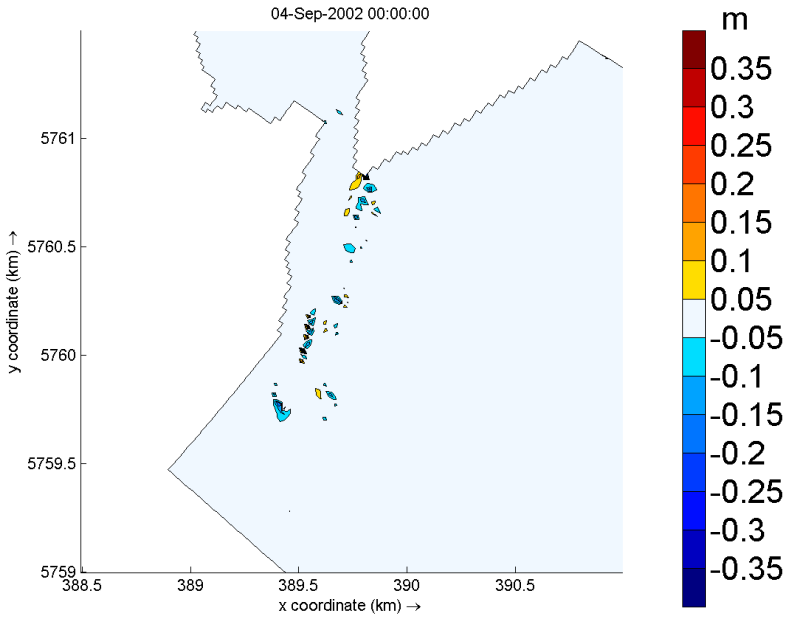

Figure 8.9 – The discrimination on bed level change between present scenario and future scenario under spring tide conditions in State A. Negative values indicate that the future bed level is lower than present bed level; positive values mean the future bed level is higher than present bed level.

For entire outer estuary, the climate change will increase its morphodynamic situation's vulnerability. The morphodynamic responses to climate change in State A will become serious alongside the outer estuary. But for the inner estuary, the morphological changes to the storm event will not differ between present and future conditions (Figure 8.9).

8.3.2. State B

Similar numerical simulations investigated the impacts of future extreme storms when the Deben Estuary is in State B (Figure 8.2). In State B, the north part of the ebb shoal was broken down into segments: there is a shallow triangular area at the south which may potentially shield wave propagation and longshore sediment transport from the north.

8.3.2.1. The residual tidal current changes due to climate change

Residual tidal currents were determined when extreme wave conditions coincided with spring tide conditions for both present and future scenarios in State B (Figure 8.10). It shows that in the present climate scenario, largest residual current occurs in the main channel with several strong flow branches at the north part of ebb shoal.

However, in the future climate scenario, the most significant residual current occurred on the ebb shoal instead of the main channel after a significant tidal current increase at the ebb shoal, and a slight reduction of the residual current in the main channel due to climate change.

The residual ebb jet current's magnitude will also clearly decrease due to climate change. Most tidal currents have switched the main pathway from south ebb jet channel to north ebb shoal under the effects of increased MSL (Figure 8.10b). As the SLR occurs, most of the northern estuary will submerge during the low tide, which releases the ebb tidal current from the constricted mouth of the main channel. Thus, the increased residual current at the north part of ebb shoal has compensated for the loss of the current in the main channel.

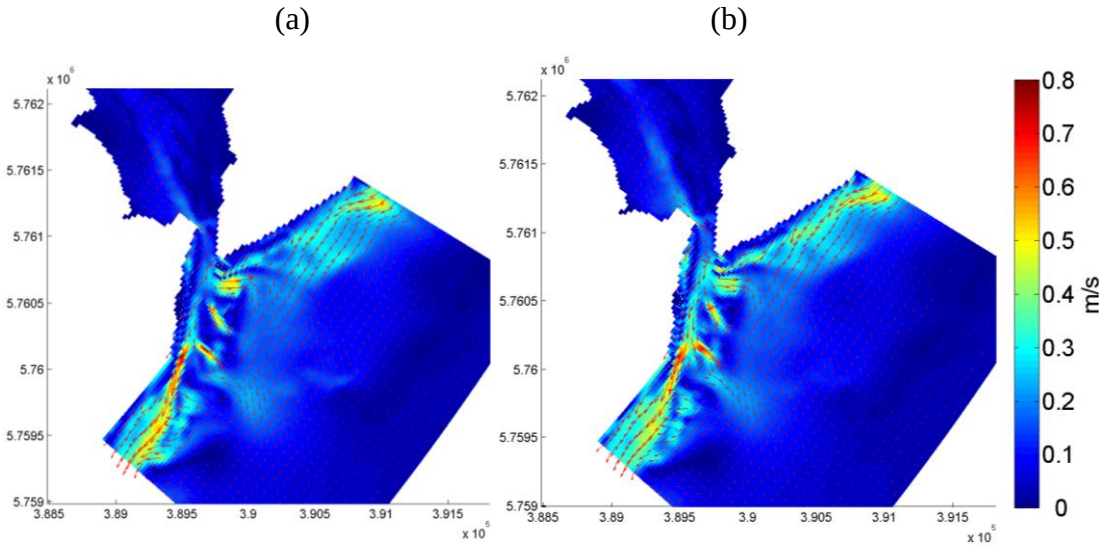

Figure 8.10 – Residual tidal current distribution in the Deben Estuary during the spring tide in the present (a) and the future scenarios (b) in State B. The colour bar shows magnitude of the residual current and the vector shows the direction of the residual current.

Under the future SLR scenario during spring tide conditions, the major increase in the residual tidal current due to climate change mostly occurs at the north ebb shoal, which has increased the strong current branches. In addition, there is only a slight increase of residual tidal current at the north adjacent beaches.

The spatial distribution of residual tidal current in this state has many similarities to that at the State A. However, the residual current in the main channel seems to be more concentrated than in State A (Figure 8.5) while the current in this state seems to be more spread as a result of shallower depths.

8.3.2.2. Spatial variation of peak storm wave height

The extreme H_{smax} around the Deben Estuary in both present and future scenarios of State B are shown in Figure 8.11, in which the changes of the H_{smax} due to the climate change is clearly seen.

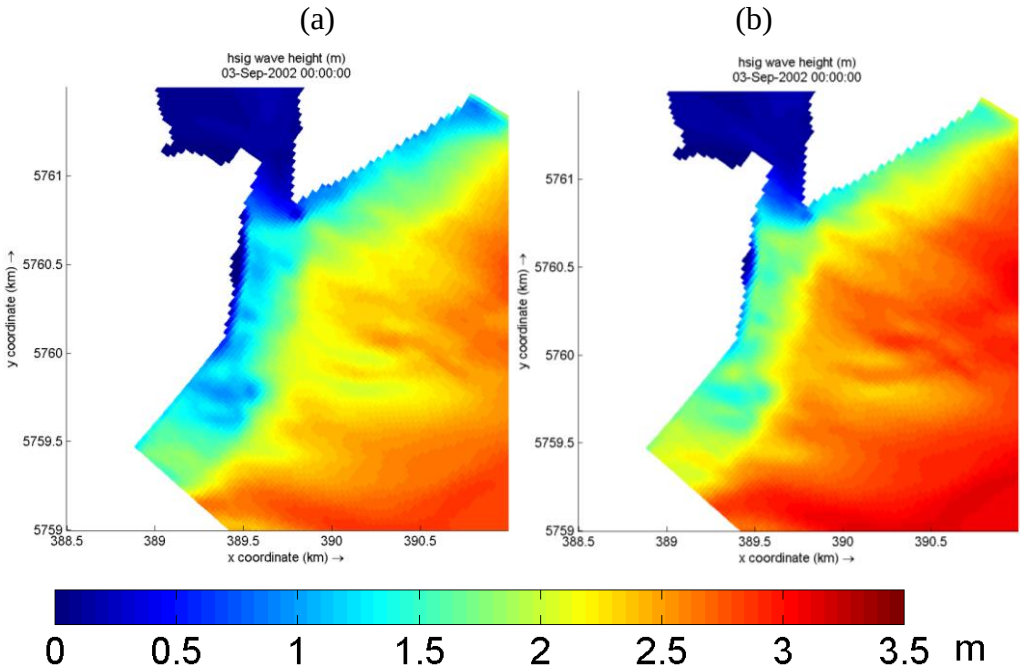

Figure 8.11 – The 1 in 100-year H_{max} distribution around the Deben Estuary under spring conditions at the time of peak wave storm happens (03/09/2002 00:00AM) in present (a) and future scenarios (b) in State B.

Figure 8.11 shows that the wave heights in shallow areas for both present and future scenarios in this state are much larger than that in State A, with the highest value reaching 1.5m on the ebb shoal. This is because in State B, water depths at ebb shoal are greater due to fragmentation. When storm waves coincide with the spring high water level, the waves can reach further onshore.

When water levels in the estuary and the surroundings increase due to SLR, wave heights at the ebb shoal during a 1 in 100-year storm increased to 2m (Figure 8.11b). This is much more significant than the situation in State A in which the maximum wave height at the ebb shoal is less than 1.5m. Therefore, the extreme wave energy in the future scenario in this state is far more significant.

In terms of spatial variation of the wave height, similarly to the situation in State A, the wave height at the down-drift beach is in general larger than that on the ebb shoal in both present and future scenarios. A comparison between present and future scenarios shows that the increase rate on the down-drift beach is similar to that on the ebb shoal: they both have increased by 0.5m. This means the spatial variation of the H_s distribution at the peak wave storm will not be modified by climate change even though the values of entire system have enhanced because the deep ebb shoal cannot efficiently shield the wave.

8.3.2.3. The residual bottom stress changes due to climate change

The spatial distribution of residual bed sheer stress under present and future climate scenarios are shown in Figure 8.12.

Figure 8.12 shows that there is no significant change between present and future scenarios. When explored in detail, both present and future scenarios contain several strips of relatively strong bottom shear stress but they are not very significant. For the north part of ebb shoal, there is a slight increase at the north tip just around the north bank where the residual stress will increase slightly.

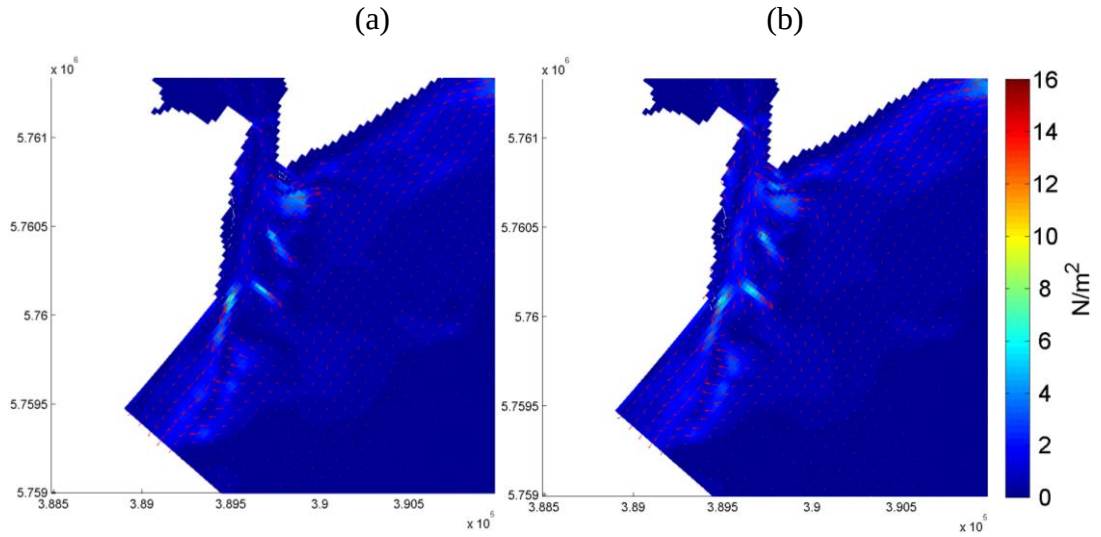

Figure 8.12 – The residual bed shear stress distribution around the Deben Estuary during the spring tidal conditions in different scenarios (a: present scenario; b: future scenario) in State B. The colour bar indicates the magnitude of the bottom stress and the vector indicates the directions of the residual bottom stress.

In addition to the small change on north ebb shoal, there is also a small increase at the upper main channel including the inlet area due to climate change. But it is also not clear enough when compared with those relative strong strips. For the entire south part of the system, there is no change due to the climate change. It seems, in this state, the residual bottom stress is not corresponding to the residual tide current very well (Figure 8.10).

8.3.2.4. Morphodynamic responses to climate change

The cumulative erosion and sedimentation patterns of State B are shown in Figure 8.13. The bed level has not changed much between present and future scenarios, at the south part of the system.

The main channel's bed level change has not increased due to climate change, since there is no big difference on residual tidal current (Figure 8.10). However, the throat of the estuary, which is also the starting point of the main channel in this system, has been clearly modified by climate change when comparing the present and future scenarios (Figure 8.13). The effect of climate change on the throat is much more significant in State B than that in State A.

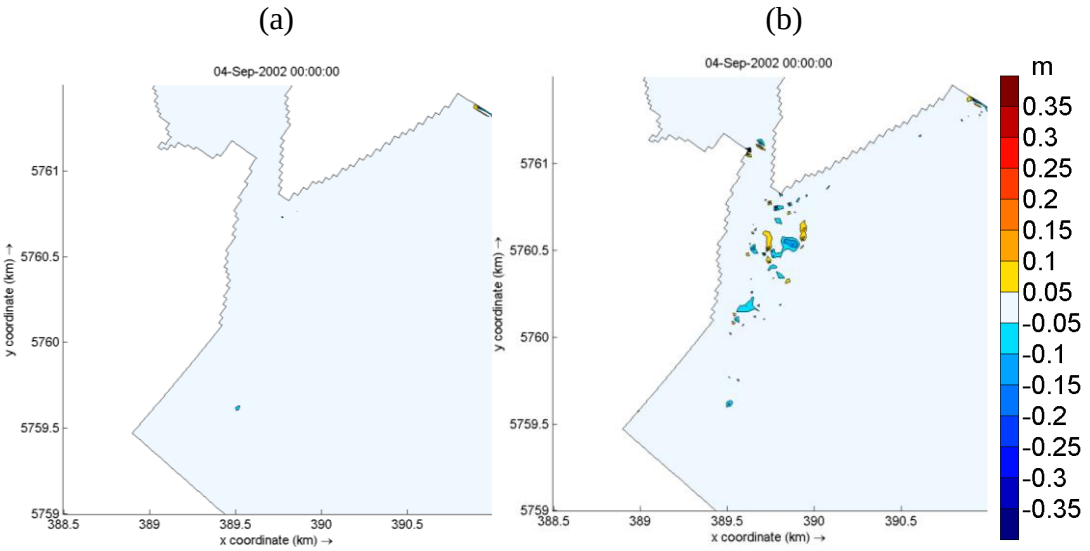

Figure 8.13 – The bed level changes in State B under the spring tidal conditions after simulation in present scenario (a) and in future scenario (b). Negative value means erosion and positive value means accretion.

The north part of the entire ebb shoal became more dynamic under the future climate conditions whereas the south part of ebb shoal will not respond much to future storm conditions. The morphodynamic response of south ebb shoal under future conditions (Figure 8.13b) is comparable to the response under the present conditions (Figure 8.13a). This indicates that the south ebb shoal of this state is not very sensitive to climate change. However, climate change may make the north part of the ebb shoal more unstable and sensitive due to the broken ebb shoal there.

For the adjacent beaches, the bed level will not experience significant changes due to climate change. Similar to State A, both the north and south adjacent beaches will be unaffected by the climate change, at least during an episodic time scale. Therefore, climate change will potentially influence the hydrodynamic distributions at the north part of the estuary due to its reorganisation of the bathymetry.

The most sensitive area of the estuary to climate change is located in the north part of ebb shoal including the inlet area. The south ebb shoal and the adjacent beaches may not be easily changed by the climate change, at least during an episodic event.

8.3.3. State C

The other main representative historical bathymetry states (State C) was also investigated by simulating the present and future scenarios. This state contains two divided fully formed ebb shoals between which the ebb jet channel crosses in the middle (Figure 8.2). Detailed discussions on the hydrodynamic and morphodynamic changes follow.

8.3.3.1. The residual tidal current changes due to climate change

Residual tidal currents occur when extreme wave conditions coincide with spring tide conditions; this was determined for both present and future scenarios when the estuary is at State C (Figure 8.14). It is shown that, the distributions of residual tidal current in the both present and future climate scenarios are similar with each other, in which the most significant residual tidal current occurs at the ebb jet region.

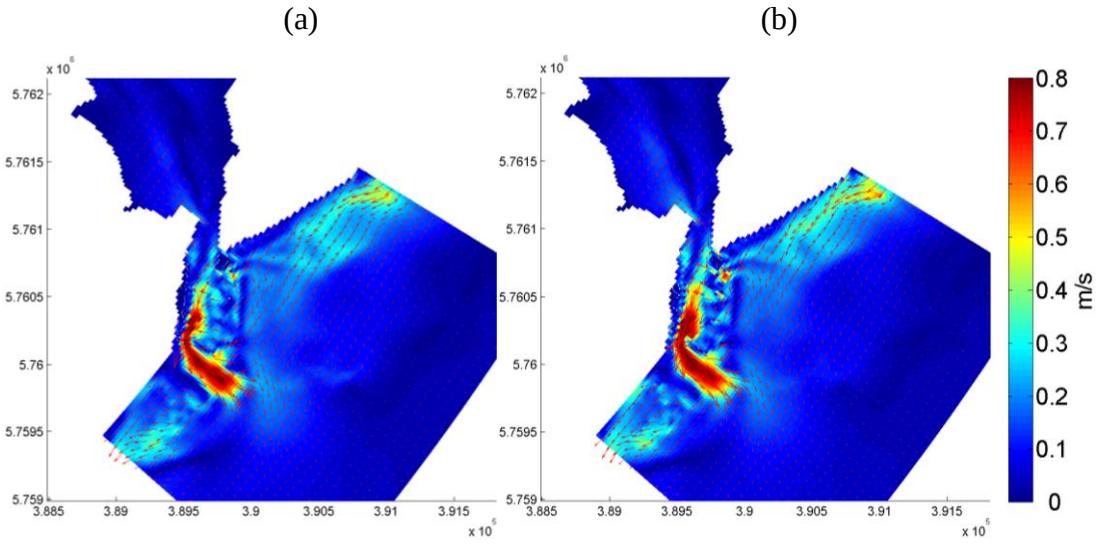

Figure 8.14 – Residual tidal current distribution in Deben Estuary in State C during spring tide condition in the present scenario (a) and the future scenario (b) in State C. The colour bar shows magnitude of the residual current and the vector shows the direction of the residual tide current.

Figure 8.14 shows that both the main channel and ebb jet region contains the most significant residual current in these two scenarios. In the present scenario, the most

dynamic hydrodynamic regime is at the ebb jet region with an expansion further to offshore side with a great inertia of the tidal current from the channel but the most dynamic regime in the main channel is a bit narrow (Figure 8.14a).

In the future scenario, the residual ebb jet current decreases slightly while the significant tidal current regime at the main channel seems to increase slightly (Figure 8.14b). The intensity of the current at the main channel will be released by the increased MSL so that the ebb jet cannot reach further offshore.

The two developed ebb shoals do not have a notable influence on the residual tidal current change due to climate change although the changes at the north ebb shoal are relatively bigger than at south ebb shoal. The current at the north tip of the north ebb shoal and the nearshore side of the south ebb shoal slightly increased (Figure 8.14). Thus, it seems that the ebb shoal is stable under climate change at spring conditions when the estuary is in State C.

8.3.3.2. Spatial variation of peak storm wave height

H_{smax} around the Deben Estuary in both present and future scenarios of State C are shown in Figure 8.15, in which the spatial distributions of the H_{smax} indicate some differences between present and future scenarios. It is shown that in both scenarios, the H_{smax} at the ebb jet region is larger than that on the ebb shoals which is mostly due to the deeper ebb jet channel preventing the wave propagation future onshore.

The wave height in the present scenario on the ebb shoal is spatially various so that the wave height gradient can be observed in this state (smaller at ebb jet and bigger at the developed ebb shoals). In the future scenario, it is increased on H_{smax} at both the ebb jet region and the developed ebb shoal areas with a similar increase rate, leading to the same spatial distribution due to climate change (Figure 8.15).

In comparison with the other two states under the spring tide conditions, the average H_{smax} on the ebb shoal in the present scenario in this state is much larger than that in State A but is slightly smaller than that in State B. Among these three states, State A

has more ability to shield the estuary's wave propagation, while State B is exposed to the wave impact more seriously. The situation will be unaffected by climate change.

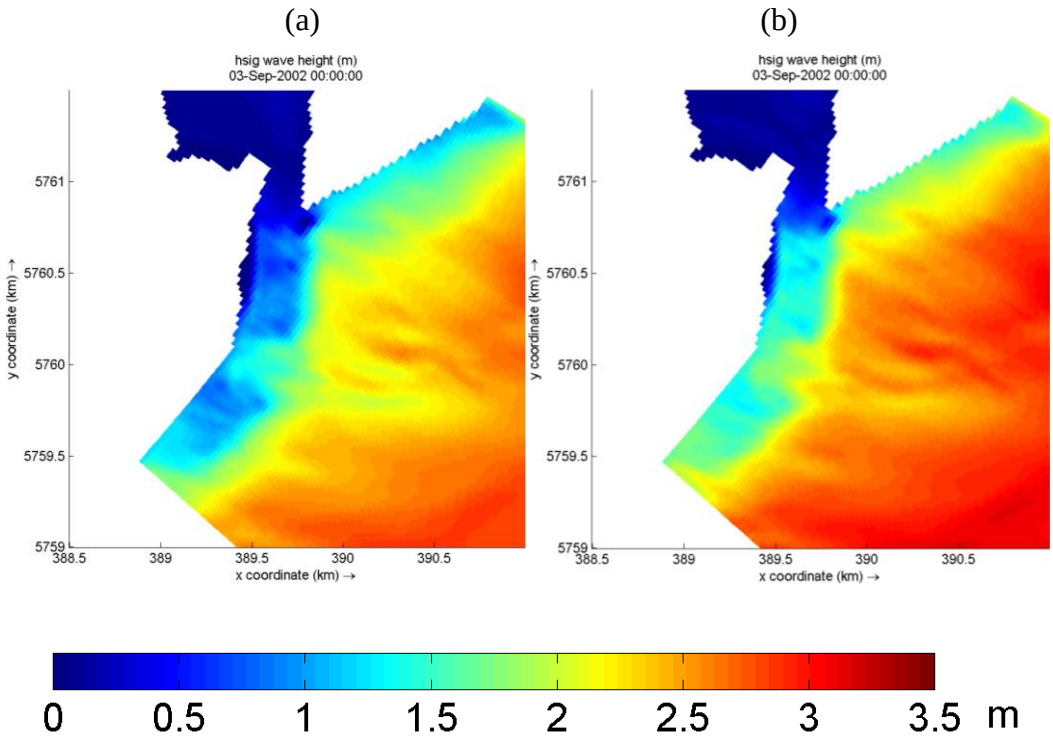

Figure 8.15 – The 1 in 100-year H_{max} distribution around the Deben Estuary in State C during spring condition at the peak wave time (03/09/2002 00:00AM) in present scenario (a) and future SLR scenario (b).

Therefore, the increased depth of water level due to SLR will only force the wave further onshore in either the ebb jet channel or on the ebb shoal but it cannot disturb the variation of spatial distribution within this system. Similar observations can be seen in the other two states.

8.3.3.3. The residual bottom stress changes due to climate change

The spatial distribution of residual bed stress under present and future climate scenarios are shown in Figure 8.16 when the estuary is in State C. Generally, there will be a slight change on the bottom stress due to climate change during the spring tidal condition at the ebb jet region.

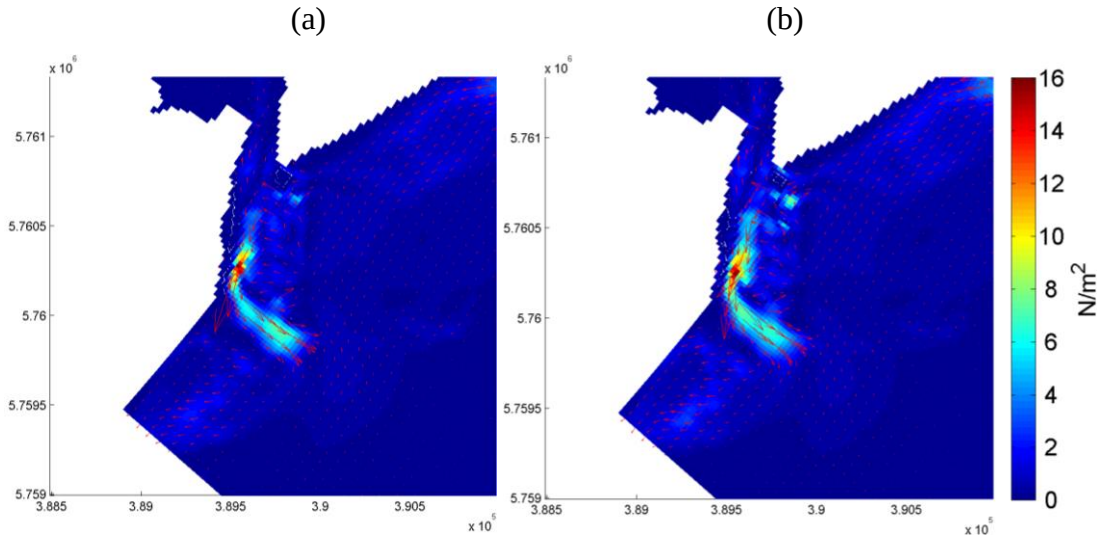

Figure 8.16 – The residual bed shear stress distribution around Deben Estuary during the spring tidal conditions in different scenarios (a: present scenario; b: future scenario) in State C. The colour bar indicates the magnitude of the bottom stress and the vector indicates the directions of the residual bottom stress.

Figure 8.16 shows an enhancement of bottom shear stress magnitude in the main channel due to climate change under the spring tide condition. The area containing significant residual stress is also expanded in the main channel due to climate change. However, the ebb jet channel will be slightly shortened due to climate change.

Apart from the increase in main channel, there is slight enhancement on the residual bed stress at the north ebb shoal and the upper main channel besides the north ebb shoal (Figure 8.16b). This corresponds to the distribution of residual tidal current shown in Figure 8.14 which also indicates the slight increase at the north ebb shoal.

In terms of south ebb shoal and north adjacent beaches, there is no great change between present scenario and future scenario, which seems to be much more stable regarding climate change impact.

Therefore, in this state, apart from the relative significant change of stress in the ebb jet channel, the stress distribution at the north ebb shoal will also experience slight changes due to climate change.

8.3.3.4. Morphodynamic responses to climate change

As the entire ebb shoal was divided by an ebb jet channel in State C, the most dynamic place under the future climate conditions is different with that in the previous two states. The bed level changes under the present climate conditions and the future climate conditions are shown in Figure 8.17. The dynamic areas in this state are much more concentrated at around the ebb jet region.

In the main channel, the bed in the middle will be severely eroded, but other part of the ebb shoal is rarely affected by the hydrodynamic changes. The most obvious dynamic place in the main channel is located at the bending point that the channel has switched its direction to the sea (eastward). As the climate change, this dynamic area has been greatly expanded (Figure 8.17b).

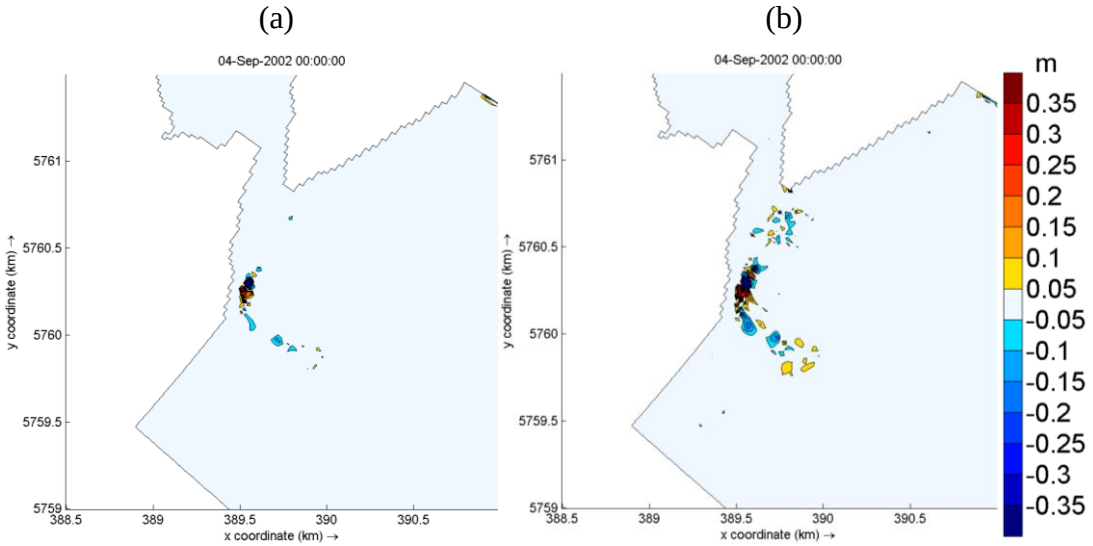

Figure 8.17 – The bed level changes in State C under the spring tide conditions after simulation in present scenario (a) and in future scenario (b). Negative values mean erosion and positive values mean accretion.

Another obvious change due to climate change is located at the ebb jet region, which crossed through the entire ebb shoal. As Figure 8.17 shows, a slight increase of the erosion due to climate change leads to more offshore sediment deposition. This process may consequently change the flows, because if the offshore delta was formed due to the increased deposition, the velocity of the ebb jet will be divided.

In terms of the two developed ebb shoals, there is rarely sediment movement in both present and future scenarios. The most significant difference is only at the north ebb shoal where the erosion/sedimentation pattern becomes clear under future climate conditions (Figure 8.17b).

In terms of the adjacent beaches and inner estuary, the morphological changes will not transform due to future climate change (Figure 8.18). All the differences are gathered at the ebb jet region including part of north ebb shoal.

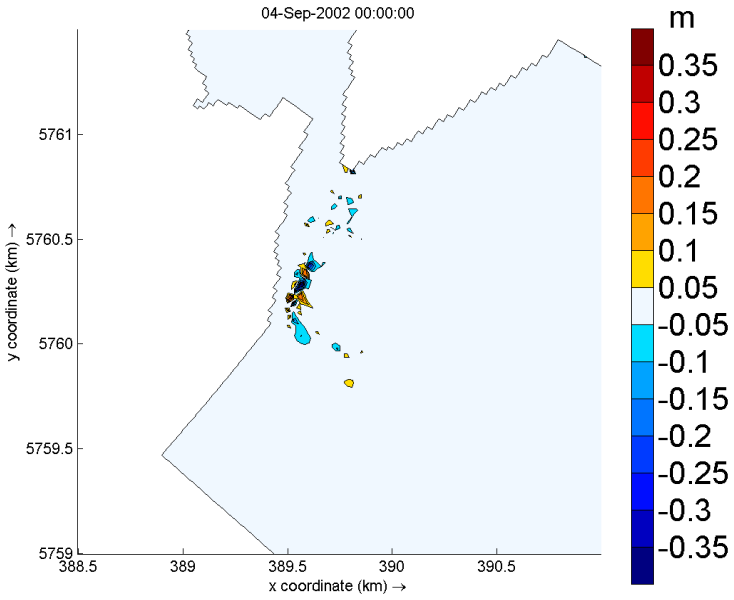

Figure 8.18 – The differences on bed level change between present scenario and future SLR scenario in State C. Negative values indicate that future bed level lower than the present bed level; positive values mean the future bed level is higher than present bed level.

Therefore, according to the discrimination, the most sensitive part in this state to climate change is located at the north of the system including the most dynamic channel system (main channel and ebb jet channel) (Figure 8.18).

8.4. The inter-comparison of the states on the morphodynamic responses to the climate change

Previous sections investigated hydrodynamic and morphodynamic responses of Deben Estuary to climate change under the spring tide conditions when the estuary will be in three different morphodynamic states. In order to establish the most vulnerable state among the them during the spring conditions under future climate change, it is necessary to interactively compare these states by considering the climate change impacts.

The differences of bed level changes between present and future scenarios in every state are shown in Figure 8.19. It has different features on morphodynamic responses to climate change among these three bathymetry states.

8.4.1. Visual comparison

All three conditions show that the north part of the outer estuary is most sensitive to climate change. Apart from some erosion and accretion occurring at the main channel in State A and State C, the most sensitive places of this system are generally located at the north ebb shoal (Figure 8.19). Therefore, if future storms coincide with spring tide at future sea levels, the inlet surroundings of the estuary may change significantly, irrespective of the state of the estuary.

The most sensitive part of the estuary to climate change in each selected state varies from state to state, as can be seen in Figure 8.19. The most sensitive area in State A spreads longshore with a thin band at the north part of ebb shoal. In addition, the main channel, including the ebb jet region which is located at the south of the system, has also changed significantly. But the throat and inner estuary are not significantly affected.

In state B, most dynamic places are concentrated within the north ebb shoal with an expansion on cross-section direction and a limited area in the middle of ebb shoal when the north ebb shoal was separated into several fragments (Figure 8.19). Unlike State

A, the throat of the estuary inlet at this state has been significantly changed but no significant changes are found in the south ebb shoal.

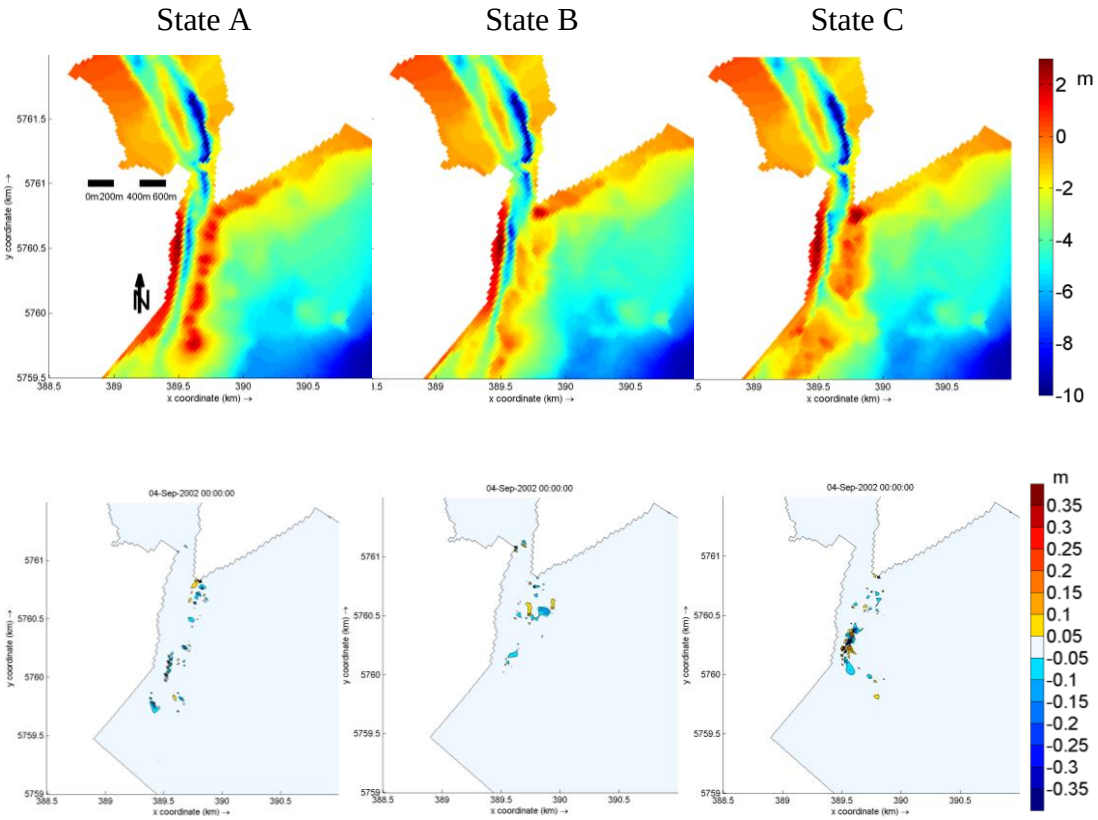

Figure 8.19 – The differences of cumulative erosion and sedimentation between present scenarios and future scenarios in three bathymetry states under spring tide conditions. Initial bathymetry (State A to State C from top left to right); Difference on final bed level between present and future scenarios in three states due to climate change (State A to State C from bottom left to right); Negative values indicate where future bed level is lower than the present bed level; positive values mean the future bed level is higher than present bed level.

In State C, the south delta attached to the south bank (south from the ebb jet region) is rarely affected by the climate change, which is similar to State B. Most differences happen at the north attached delta and at the main channel including the ebb jet region. The most sensitive location in this state is likely within the main channel where the bending direction has been formed to connect to the ebb jet region (Figure 8.19). From State A to State C, there is a trend on the sensitive area from the spreading ebb shoal to concentrating in the north part of the ebb delta (moving from south to north).

8.4.2. Quantitative bed level changes and their potential effects on hydrodynamics

Although bed level change is not significant when it is affected by only one storm, the resultant morphodynamic change will potentially change the hydrodynamic situations due to the nonlinear relationship between hydrodynamics and morphodynamics.

For State A, since the erosion along the ebb shoal will increase due to climate change, the elongated ebb shoal may increase the process of dividing into fragments with an increased cross shore current resulted from the breaking ebb shoal. The flood tidal current magnitudes at the beginning and the end of the simulation are shown in Figure 8.20. It is shown that when the ebb shoal has been eroded, the cross-shore current will increase due to the fragments. As a result, these increased currents will further enhance the erosion. Then the interaction will continue, resulting in the ebb shoal breaking. Therefore, the increase of the erosion due to climate change increases the speed of the cyclic behaviors, breaking the integrated ebb shoal.

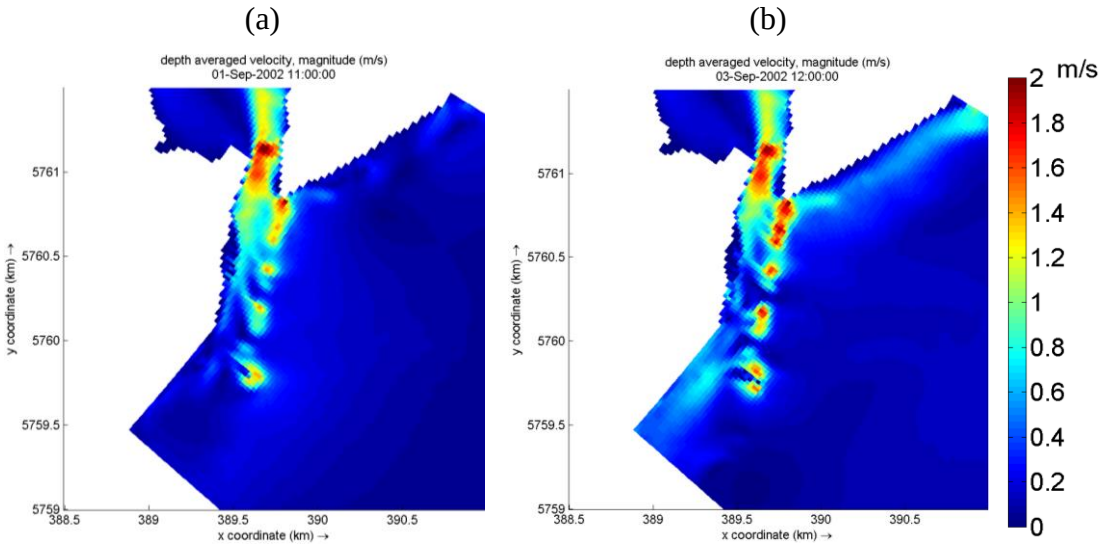

Figure 8.20 – The flood tidal current magnitudes at the beginning of the simulation (a: 01/09/2002 11:00AM) and the end of the simulation (b: 03/09/2002 12:00PM) in the future scenario for State A.

In State B, the dynamic areas are concentrated at around the north tip of ebb shoal. The existing fragment which will experience increased future dynamic morphological

changes probably efficiently re-organize the morphodynamic process so that the breaking ebb shoal is able to easily integrate together. However, this only affects the north part of the ebb shoal as the south ebb shoal will not change much in future climate conditions.

For State C, the main channel will increase its erosion which will make the bed slope more serious. But the increased sedimentation of the ebb jet region will block the primary ebb jet in future if it is continuously developed. The gradual decrease of the ebb jet current has increased the sedimentation at the ebb jet region while the increased eroded bed level at the north tip of the delta may break the developed delta into dynamic fragments, which is more significant compared to the south delta. Therefore, similarly to the situation in Chapter 7, the morphodynamics of State C may be changed in terms of ebb jet channel due to climate change.

8.5. Summary

This chapter investigated the estuary morphodynamic responses to extreme conditions in both present and future climate scenarios when the estuary is in its three representative morphodynamic states. Apart from the discussions on morphodynamic response of the estuary to both present and future climate, the difference between them are compared and contrasted in order to show how the future extreme condition will affect the estuary.

The future climate condition will not only generate different hydrodynamic changes (including wave distributions) but also generate different morphological changes. The following points have been discovered following results analysis.

- In general, the entire estuary system becomes more dynamic under future climate conditions. It is more obvious when in spring tidal conditions as the morphology is more vulnerable to high tidal energy.
- The cumulative erosion/sedimentation patterns are similar when a storm wave peaks at either high or low spring water level if the tidal range is constant.

- The wave heights in and around the estuary will increase in future climate scenarios. This is mainly due to the interaction between SLR and waves, rather than the pure increase of storm wave heights in future climate condition.
- In all three representative bathymetry states, the most sensitive areas are located at the north part of ebb shoal when the climate condition coincides with the spring tide cycles.
- For State A, apart from the north ebb shoal, the middle of the main channel and south part of delta will also experience more dynamic responses to climate change. The increased erosion due to climate change will potentially increase the speed of breaching of ebb shoal into fragments.
- For State B, only the north tip of the ebb shoal will increase its bed level change under the future climate conditions. In terms of the main channel, there are no great change under the future climate conditions. In this state, the throat is the most sensitive to the climate change.
- In State C, the most sensitive places are concentrated in the main channel where the channel bends and the ebb jet region starts. It is because this area contains dynamic tidal currents and is directly exposed to the wave incident.
- Based on the above observations, State C is the most vulnerable morphodynamic state where ebb shoal breaching can take place. The resultant bathymetry will potentially affect the hydrodynamics within the estuary due to the interaction between hydrodynamics and morphodynamics, which may have significant consequences on the future estuarine stability.

Chapter 9: Conclusions

This chapter draws conclusions from this study and presents some recommendations of future work.

9.1. Main conclusions

A hydrodynamic and morphodynamic model of the Deben Estuary in the UK was developed using Delft3D in order to investigate climate change impacts on estuary morphodynamics. The model was thoroughly calibrated and validated against measured waves, water levels and bathymetries. Since future climate change is uncertain, the study considers several possible future climate conditions.

There were two main parts of this study: the first studied the impacts of SLR on estuary morphodynamics where three future sea level scenarios were considered. Simulations were carried out to cover a period of 1 year in order to investigate morphodynamic responses of the estuary to higher future sea levels and compare these with morphodynamic change occurred during 1 year under the current conditions. The second part of the study focused on investigating the response of the estuary to extreme conditions in future climate. The analysis of forecasts of future wave conditions around the estuary showed that averaged wave conditions would not noticeably change in future whereas the extreme wave conditions such as 1 in 100 year storm waves will increase due to climate change. Therefore, current average wave conditions with future sea levels were used in this study.

Historically, the Deben Estuary has shown three distinct morphodynamic states, within which the estuary cyclically changes. In two of these historic states, the ebb shoal and the delta of the estuary, which controls wave penetration and tidal flow into the estuary show very unstable behaviour. Fragmentation or breach of the shoal may significantly affect the morphodynamics and stability of the estuary. Increased water levels and energetic wave action may enhance this process. Therefore, the second part of this study investigates how these three different morphodynamic states will respond to future rise in sea levels and increased storm activities.

The primary findings of this thesis are as follows:

1. The process-based model Delft 3D satisfactorily reproduced the hydrodynamics of the Deben Estuary. In terms of the morphodynamic prediction, although the morphological module in this package was not able to reproduce the estuarine bathymetry very accurately, the model satisfactorily predicted key morphodynamic trends of the estuary and captured its most important features. Therefore, the validated numerical model was reliable in this study.
2. In terms of future wave climate change, the average wave situations around the Deben Estuary, based on mean ensemble global wave models of CMIP3, will not noticeably change. However, extreme wave conditions will significantly increase in the future. This means that the frequency of occurrence of the storm waves will increase due to climate change, as described in Chapter 6.
3. In terms of the study of long term morphodynamic change based on different SLR scenarios, following morphodynamic responses of the selected initial bathymetry (the state of the year 2002) to climate change were observed:
    - The most notable impact of calm climate change on the estuary morphology is the formation of a new inlet at the ebb shoal.
    - The ebb tidal delta will become more dynamic with the effect of SLR. Erosion of the ebb shoal becomes larger and the new inlet formed at the ebb shoal will get wider and deeper when SLR increases from low emission to high emission scenarios.
    - The sediment transport at primary ebb jet regions will be reduced in the future and the reduction rate is increased with the increased sea level. Therefore, the original ebb channel will be shortened and narrowed. The shortest ebb jet channel is formed under the high emission scenario.
    - The inlet channel closer to the mouth of the estuary will relocate as a result of the formation of a new inlet and closure of the existing inlet in future.
    - There is not significant change in morphology in the inner estuary, even though the inlet will undergo significant changes due to climate change. This indicates the fact that the most tidal and wave energy is consumed at the estuary inlet, so creating a weak sediment transport regime in the inner estuary.

4. In terms of the short-term simulations under the combination of the one in 100-year peak storm wave conditions and the medium emission SLR condition, the morphological changes due to extreme future wave conditions vary between different representative bathymetry states. The morphodynamic responses of the estuary to the climate change were more obvious when the storm peaked at high tide.
    - The result did not show notable differences between the two cases where (i) storm peak coincides with High Spring Water Level (HSWL) and (ii) the storm peak coincides with Low Spring Water Level (LSWL). It indicates that as long as the tidal range and wave height did not change, the cumulative erosion/accretion pattern will not change irrespective where the storm peak occurs relative to the tidal level (HSWL or LSWL).
    - All estuary states are much more sensitive to the episodic events when the storm peaks at spring high tide conditions and the ebb shoal becomes more vulnerable.
    - The most sensitive area of the estuary to future storm conditions occurring at raised sea levels are located at the north part of the system including State C in which the most sensitive area is sited at the ebb jet region in the middle of the entire ebb shoal. So, it means the inlet area should be protected when the extreme conditions happen under spring tide conditions in future.
    - Among these three states, State C is the most vulnerable morphodynamic state where significant changes have taken place in the ebb shoal and the inlet of the main channel.
    - Although the least sensitive state among these three states is State B, in which the affected area is the smallest, the throat of estuary is the most vulnerable to the climate change. Therefore, in this state, the narrowest throat should be concerned in extreme weather events.
    - As the morphodynamic changes of the estuary are enhanced by the climate change, the consequent hydrodynamic situation will be changed potentially. For example, as the breaking process of ebb shoal in State A will be increased by the future storm conditions, the cross-shore flood current will increase accordingly to speed up the erosion of the ebb shoal into fragments. Consequently, the cyclical behaviour will probably increase its speed.

This study has provided a general investigation into the morphodynamic responses of the Deben Estuary to climate change, in both calm weather, and storm wave conditions. Due to the complex situation of the estuary, some future work should also be carried out to increase the knowledge of estuarine morphodynamic responses to climate change.

9.2. Future work

By considering the results obtained from this study and its limitations, the following future work is recommended:

1. The forecasts of the future climate conditions are still very uncertain. Therefore, future work should be undertaken to enhance monitoring and improve the computational modelling performance. The probabilistic numerical models can be included along with the process-based models.
2. The validation of the flow velocity was not possible due to unavailable data. Although the model incorporates the water level and waves well, it would be extremely useful to collect the velocity data around the estuary, which can be used for calibrating and validating the model more accurately.
3. The process of dealing with sand-gravel mixed estuary is still being developed. It would enhance the model's performance when the numerical model was able to take place the sand-gravel interaction procedure.
4. When considering the climate change to the estuary morphodynamic in a long-term aspect, the uncertainty of the initial bathymetry should also be considered since the Deben Estuary is an extremely dynamic estuary. The project that regarding to several simulation ensembles is one option in the future.
5. In terms of storm climate condition impacts, the scenarios considering the storm clusters will provide more information for the investigation of the estuary morphodynamic responses to the climate change. Additionally, the storm surges would probably provide a different insight of the estuarine evolution when a couple of meters would add to the water level.
6. As an integrated part of the coastline, the longshore sediment transport crossing the estuary should also be very important when considering a longer simulation

period. This is of importance for investigating the bypass sediment of the river mouth, which provides a deep insight of the specific features of an estuary. Therefore, the longshore sediment transport and the sediment exchange between estuary and adjacent beaches should be investigated in future work.

Bibliography

Al-Bakri, D., 1986. Provenance of the sediment in the Humber Estuary and the adjacent coasts, eastern England. Marine Geology, 72, 171-186.

Allen, J.R.L., 2000. Morphodynamics of Holocene salt marshes: a review sketch from the Atlantic and Southearn North Sea coasts of Europe. Quaternary Science Review, 19: 1155-1231.

Amoudry, L. O., and Souza, A. J., 2011. Deterministic coastal morphological and sediment transport modeling: a review and discussion. Review of Geophysics, 49(2010), 1–21.

Anthony, E., Levoy, F., Monfort, O., 2004. Morphodynamics of intertidal bars on a megatidal beach, Merlimont, Northern France. Marine Geology, 208, 73-100.

Aubrey, D. G., Speer, P. E., 1985. A study of Non-linear Tidal Propagation in shallow Inlet/Estuarine Systems Part I: Observations. Estuarine, Coastal and Shelf Science, 21, 185-205.

Bastos, A., Collins, M., Kenyon, N., 2003. Water and sediment movement around a coastal headland: Portland Bill, southern UK. Ocean Dynamics, 53, 309-321.

Battjes, J. and Janssen, J., 1978. Energy loss and set-up due to breaking of random waves. In Proceedings 16th International Conference Coastal Engineering, ASCE, pp. 569-587.

Baumert, H. and G. Radach, 1992. Hysteresis of turbulence kinetic energy in nonrotational tidal flows: A model study. Journal of Geophysical Research, 97 (C3), 3669-3677.

Beardall, C.H., Dryden, R.C., Holzer, T.J., 1991. The Suffolk Estuaries. Segment Publications, Colchester, pp. 77.

Beji, S., Battjes, J.A., 1993. Experimental investigation of wave propagation over a bar. Coastal Engineering, 19, 151-162.

Bindoff, N. L., Willebrand, J. W., Artale, V., Cazenave, A., et al., 2007. Observations: Oceanic Climate Change and Sea Level. In: Climate Change 2007: The Physical

Science Basis. Cambridge University Press, Cambridge, United Kingdom and New York, NY, USA.

Bijker, E., 1971. Longshore transport computation. ASCE Journal of Waterway, Port, Coastal and Ocean Engineering, 97, pp. 687-701.

Blott, S. J., Pye, K., Van der wal. D., Neal, A., 2006. Long-term morphological change and its causes in the Mersey Estuary, NW England. Geomorphology, 81, 185-206.

Booij, N., Ris, R.C., Holthuijsen, L.H., 1999. A third-generation wave model for coastal regions, Part I, Model description and validation. Journal of Geophysical Research 104 (C4): 7649–7666.

Boothroyd, J.C., 1985. Tidal inlets and tidal deltas. In: Davis Jr., R.A. (Ed.), Coastal Sedimentary Environments. Springer-Verlag, New York, pp. 445-532.

Bradley, S.L., Milne, G.A., Teferle, F.N., Bingley, R.M., Orliac, E.J., 2009. Glacial isostatic adjustment of the British Isles: new constraints from GPS measurements of crustal motion, Geophysical Journal International, 178, 14-22.

Bretschneider, C.L., 1959. Hurricane design – wave practices, Transactions of the ASCE, 124, pp. 39-62.

Brew, D. S., 1990. Sedimentary environments and Holocene evolution of the Suffolk estuaries. PhD thesis. University of East Anglia.

Brown, J.M., Souza, A.J., Wolf, J., 2010. Surge modelling in the eastern Irish Sea: present and future storm impact. Ocean Dynamics, 60, pp. 227-236.

Burningham, H. and French, J. 2006. Morphodynamic behaviour of a mixed sand–gravel ebb-tidal delta: Deben Estuary, Suffolk, UK. Marine Geology, 225, 23-44.

Capo, S., Sottolichio, A., Brenon, I., Castaing, P., Ferry, L., 2006. Morphology, hydrography and sediment dynamics in a mangrove estuary: The Konkoure Estuary, Guinea. Marine Geology, 230, 199-215.

Chen, C., Liu, H., Beardsley, R. C. 2003. An unstructured grid, finite-volume, three-dimensional, primitive equations ocean model: Application to coastal ocean and estuaries, Journal of Atmospheric and Oceanic Technology, 20, 159 – 186.

Chen, C., Huang, H., Beardsley, R. C., Liu, H., Xu, Q., Cowles G., 2007. A finite-volume numerical approach for coastal ocean circulation studies: Comparisons with finite difference models, Journal of Geophysical Research,

Chini, N., Stansby, P., Leake, J., Wolf, J., Roberts-Jones, J., Lowe, J., 2010. The impact of sea level rise and climate change on inshore wave climate: A case study for East Anglia (UK). Coastal Engineering, 57, pp. 973-984.

Christoffersen, J.B., Jonsson, I.G., 1985. Bed friction and dissipation in a combined current and wave motion. Ocean Engineering 12 _5., 387–423.

Church, J.A., Gregory, J.M., Huybrechts, P., Kuhn, M., Lambeck, K., Nhuan, M.T., Qin, D., and Woodworth, P.L., 2001. Changes in sea level. In: Houghton, J.T., Ding, Y., Griggs, D.J., Noguer, M., van der Linden, P.J., and Xiaosu, D. (eds.), Climate Change 2001. The Scientific Basis, Cambridge, UK: Cambridge University Press, pp. 639-693.

Coles, S., 2001. An introduction to statistical modeling of extreme values, Springer Series in Statistics.

Collins, J., 1972. Prediction of shallow water spectra. Journal of Geophysical Research, 77(15): 2693-2707.

Davidson, N.C. and Buck, A.L., 1997. An Inventory of UK Estuaries. Joint Nature Conservation Committee (JNCC). Vol 1-7.

Davies, A. M. and H. Gerritsen, 1994. An intercomparison of three-dimensional tidal hydrodynamic models of the Irish Sea. Tellus 46A, 200-221.

Davies, J.L., 1964. A morphogenic approach to world shorelines: Zeitschrift fur Geomorphologie, 8: 127-142.

Davison, A.C., 1984. Modelling excesses over high thresholds, with an application. In Tiago de Oliveira, J., editor, Statistical Extremes and Applications, pages 461-482. Reidel, Dordrecht.

DEFRA, 2008. Development and Demonstration of Systems-Based Estuary Simulators. R&D Technical Report FD2117/TR. London: DEFRA.

Delft3D Flow User Manual, 2014. http://oss.deltares.nl/web/delft3d/manuals.

Delf3D Wave User Manual, 2014. http://oss.deltares.nl/web/delft3d/manuals.

Deloffre, J., Verney, R., Lafite, R., Lesueur, P., Lesourd, S., Cundy, A., 2007. Sedimentation on intertidal mudflats in the lower part of macrotidal estuaries: Sedimentation rhythms and their preservation. Marine Geology, 241, 19-32.

Dennis, J., Manning, A.J., 2007. An assessment of a new settling velocity parameterisation for cohesive sediment transport modelling. Continental Shelf Research 37(13), 1835-1855.

De Vriend, H. J., Capobianco, M., Chesher,T., de Swart, H.E., et al., 1993. Approaches to long-term modelling of coastal morphology: a review. Coastal Engineering, 21, 225-269.

De Vriend, H., Ribberink, J.S., 1996. Mathematical modelling of meso-tidal barrier island coasts, Part II: process based simulation models. In: Liu, P.L.F. (Ed). Advances in Coastal and Ocean Engineering, vol. 2, pp.151-197.

De Vriend, H. J., 2003. advances in morphodynamics of tidal rivers and estuaries. International Conference on Estuaries and Coasts. Hangzhou, China.

DHI, 2009. MIKE 21 user manual, DHI water & environment, Danish Hydraulic Institute, Denmark.

Dissanayake, P. K. 2011. Modelling morphological response of large tidal inlet systems to sea level rise. Ph.D. thesis. Delft University of Technology.

Dissanayake, P., Brown, J. M., Karunarathna, H., 2014. Modelling storm-induced beach/dune evolution: Sefton coast, Liverpool Bay, UK. Marine Geology, 357, 225-242.

Dissanayake, P., Brown, J., Wisse, P. and Karunarathna, H., 2015. Comparison of storm cluster vs isolated event impacts on beach/dune morphodynamics, Estuarine, Coastal and Shelf Science, 164, pp. 301–312.

Di Silvio, G., 1989. Modelling the morphological evolution of tidal lagoons and their equilibrium configurations. XXII Congress of IAHR. IAHR, Ottawa, Canada.

Dronkers, J. 1986. Tidal asymmetry and estuarine morphology. Netherland Journal of Sea Research, 20, 117-131.

Edwards, A., Edelsten, D. J., 1977. Deep water renewal of Loch Etive: A three basin Scottish fjord. Estuarine and Coastal Marine Science, 5, 575-595.

Eldeberky, Y., Battjes, J.A., 1994. Phase lock in waves passing over a bar. Proceedings of the International Symposium: Waves – physical and numerical modelling. Vancouver, Canada, 1086-1095.

Eldeberky, Y., Battjes, J.A., 1995. Parameterization of triad interactions in wave energy models. In: Coastal Dynamics Conference, Gdansk, Poland. 140-148.

Eldeberky, Y., J. A. Battjes., 1996. Spectral modelling of wave breaking: Application to Boussinesq equations. Journal of Geophysical Research 101 (C1): 1253–1264.

Engelund, F., and Hansen, E., 1967. A monograph on sediment transport in alluvial streams, technical report, Hydraulic Laboratory, Technical University of Denmark, Copenhagen.

Finley, R. J. 1978. Ebb-tidal delta morphology and sediment supply in relation to seasonal wave energy flux, North Inlet, South Carolina. Journal of Sedimentary Petrology, 48, 227-238.

Forester, C. K., 1979. Higher order monotonic convective difference schemes. Journal of Computational Physics 23: 1–22.

Fredsoe, J., 1984. Turbulent boundary layer in wave-current interaction. ASCE Journal of Hydraulic Engineering. 110, pp.1103-1120.

Fredsoe, J., Deigaard, R., 1992. Mechanics of coastal sediment transport, Singapore, World Scientific.

French, J., Reeve, D., Owen, M., 2002. Estuaries Research Programme Phase 2 Research Plan. Report.

Friedrichs, C. T., and Aubrey, D. G., 1988. Non-linear tidal distortion is shallow well-mixed estuaries: a synthesis. Estuarine, Coastal and Shelf Science, 27, 521-545.

Funnell, B. M., 1996. Plio-pleistocene palaeogeography of the southern North Sea basin (3.75-0.60 Ma). Quaternary Science Reviews, 15, pp. 391-405.

Galland, J.C., Goutal, N., Hervouet, J.M., 1991. TELEMAC: A new numerical model for solving shallow water equations. Advances in Water Resources, 14 (3), 138-148.

Gaudiano, D.J., Kana, T.W, 2001. Shoal bypassing in mixed energy inlets: geomorphic variables and empirical predictions for nine South Carolina inlets. Journal Coastal Research. 17(2), pp.280-291.

Gornitz, V., Couch, S., and Hartig, E. K., 2002. Impacts of sea level rise in the New York City metropolitan area. Global and Planetary Change, 32(1), 61–88.

Grant, W.D., Madsen, O.S., 1979. Combined wave and current interaction with a rough bottom. Journal of Geophysical Research, 84 (C4), 1797–1808.

Gumbel, E. J., 1941. The return period of flood flows. The Annals of Mathematical Statistics, 12(2), 163-190.

Guthrie, G., Cottle, R., 2002. Suffolk coast and estuaries coastal habitat management plan. Posford Haskoning Ltd: Report to English Nature/Environment Agency. 209 pp.

Hansen, D. V. and Rattray, M. Jr. 1996. New dimensions in estuary classification. Limnology and Oceanography, 11, 319-326.

Hasselmann, K., Barnett, T.P., et al., 1973. Measurements of wind-wave growth and swell decay during the Joint North Sea Wave Project (JONSWAP). Hamburg.

Hasselmann, S., K. Hasselmann, J. Allender and T. Barnett, 1985. Computations and parameterizations of the nonlinear energy transfer in a gravity wave spectrum. Part II: Parameterizations of the nonlinear transfer for application in wave models. Journal of Physical Oceanography 15 (11): 1378–1391.

Hayes, M. O., 1979. Barrier island morphology as a function of wave and tide regime, in Leatherman, S. P. ed., Barrier islands from the Gulf of St. Lawrence to the Gulf of Mexico: Academic Press, New York, NY, pp 1-29.

Hersi, O.S., Dix, G.R., 1999. Blackriveran (lower Mohawkian, Upper Ordovician) lithostratigraphy, rhythmicity, and paleogeography: Ottawa Embayment, eastern Ontario, Canada. Canadian Journal of Earth Science, 36(12): 2033-2050.

Hibma, A., de Vriend, H.J., Stive, M.J.F., 2003. Numerical modelling of shoal pattern formation in well-mixed elongated estuaries. Estuarine, Coastal and Shelf Science, 57, 981-991.

Hick, D.M., Hume, T.M., 1996. Morphology and size of ebb tidal deltas at natural inlets on open-sea and pocket-bay coasts, North Island, New Zealand. Journal of Coastal Research. 12(1), 47-63.

Holgate, S.J., 2007. On the decadal rates of sea level change during the twentieth century. Geophysical Research Letter, 34(1), L01602.

Holthuijsen. L., N. Booij and T. Herbers, 1989. A prediction model for stationary, short-crested waves in shallow water with ambient currents. Coastal Engineering, 13, pp. 23–54.

Holthuijsen, L., N. Booij and R. Ris, 1993. A spectral wave model for the coastal zone. In Proceedings of 2nd International Symposium on Ocean Wave Measurement and Analysis, New Orleans, pages 630–641.

Houghton, G.T., Ding, Y., Griggs, D.J., Noguer, M., Van der Linden, P.J., Dai, X., Maskell, K., Johnson, C.A., 2001. Climate Change Scientific Basis, Contribution of Working Group 1 to the third Assessment report of the Intergovernmental Panel of Climate Change (IPCC), Cambridge University Press, UK, pp.74-77.

HR Wallingford, 2002. Southern North Sea Sediment Transport Study (phase 2). HR Wallingford Report EX, pp.4526.

Hulme,M., Jenkins,G.J., Lu,X., Turnpenny,J.R., Mitchell,T.D., Jones,R.G., Lowe,J., Murphy,J.M., Hassell,D., Boorman,P., McDonald,R. and Hill,S., 2002. Climate Change Scenarios for the United Kingdom: The UKCIP02 Scientific Report, Tyndall Centre for Climate Change Research, School of Environmental Sciences, University of East Anglia, Norwich, UK. 120pp.

Hume, T.M. and Herdendorf, C.E., 1988. A geomorphic classification of estuaries and its application to coastal resource management – A New Zealand example. Journal of Ocean and Shoreline Management 11, 249-274.

Hume, T.M., Herdendorf, C.E., 1992. Factors controlling tidal inlet characteristics on low drift coasts. Journal of Coastal Research. 8(2), 355-375.

Huthnance, J.M., Karunarathna, H., Lane, A., Manning, A.J., Norton, P.,Reeve, D.E., Spearman, J., Soulsby, R.L., Townend, I.H., Wolf, J. and Wright, A, 2008. Development of Estuary Morphological Models. R&D Technical Report FD2107/TR, Joint Defra/Environment Agency Flood and Coastal Erosion Risk Management R&D Programme.

Hydrographic Office, 2002. Admiralty tide tables: United Kingdom and Ireland (including European channel ports). Hydrographer of the Navy, pp.440.

Janssen, P. A. E. M. 1991. Quasi-linear theory of wind-wave generation applied to wave forecasting. Journal of Physical Oceanography, 21, 1631-1642.

Jenkins, G.J., Perry, M.C., Prior, M.J., 2008. The climate of the United Kingdom and recent trends. Met Office Hadley Centre, Exeter, UK.

Karunarathna, H. and Reeve, D.E., 2008. A Boolean approach to prediction of long-term evolution of estuary morphology. Journal of Coastal Research, 24(2B), 51-61.

Karunarathna, H., Reeve, D. E., Spivack, M., 2008. Long-term morphodynamic evolution of estuaries: An inverse problem. Estuarine, Coastal and Shelf Science, 77 (3), 385-395.

Karunarathna, H., Horrillo-Caraballo, J.M., Burningham, H., Pan, S., and Reeve, D.E., 2016. Two-dimensional reduced-physics model to describe historic morphodynamic behaviour of an estuary inlet, Marine Geology, 382, pp. 200-209.

Kendall, A. C. and Glegg, N. M., 2000. Pleistocene decalcification of Late Pliocene Red Crag shelly sands from Walton-on-the-Naze, England. Sedimentology, 47, pp. 1199-1209.

Komen, G. J., Hasselmann, K., 1984. On the existence of a fully developed wind-sea spectrum. Journal of Physical Oceanagraphy, 14, 1271-1285.

Lanzoni, S. and Seminara, G., 2002. Long-term evolution and morphodynamic equilibrium of tidal channels. Journal of Geophysical research, 107(C1), pp 11100-11113.

Leendertse, J. J., Liu, S.-K., 1973. A three-dimensional model for estuaries and coastal seas. Volume i, Principle of Computation, The Rand Corporation, R-1417-OWRR.

Lesser, G.R., Roelvink, J.A., van Kester, J.A.T.M., Stelling, G.S., 2004. Development and validation of a three-dimensional morphological model. Coastal Engineering, 51, pp. 883-915.

Lousters, T., Gerritsen, F., 1994. The Riddle of the sands; A tidal system's answer to a rising sea level, Report 94.040, RIKZ, The Hague.

Lowe, J. A., Gregory, J. M., Flather, R. A., 2001. Changes in the occurrence of storm surges around the United Kingdom under a future climate scenario using a dynamic storm surge model driven by Hadley Centre climate models. Climate Dynamics, 18(3–4), 179–188.

Madsen, O., Poon, Y.K., Graber, H.C., 1988. Spectral wave attenuation by bottom friction: Theory. In Proceedings 21th international Conference Coastal Engineering. ASCE, pp: 492-504.

Mastenbroek, C., Burgers, G., Janssen, P., 1993. The Dynamic Coupling of a Wave Model and a Storm Surge Model though the Atmospheric Boundary Layer. Journal of Physical Oceanography, 23, 1856-1866.

Meehl, G.A., Curt, C., et al., 2007. The WCRP CMIP3 multimodel dataset: A new era in climate change research. Bulletin of the American Meteorological Society, 88(9), 1383-1394.

Meyer-Peter, E., and Muller, R., 1948. Formulas for bedload transport, paper presented at 2nd Meeting of International Association for Hydraulic Research, Stockholm.

Mori, N., Shinura, T., Yasuda, T., Mase H., 2013. Multi-model climate projections of ocean surface variables under different climate scenarios--Future change of waves, sea level and wind. Ocean Engineering, 71, 122-129.

Mori, N., Yasuda, T., Mase, H., Tom, T. and Oku, Y., 2010. Projection of Extreme Wave Climate Change under Global Warming. Hydrological Research Letters, 4, 15-19.

Murphy, A.H., Epstein, E.S., 1989. Skill scores and correlation coefficients in model verification. Monthly Weather Review, 117, 572–581.

Nicholls, R.J., P.P.Wong, V.R. Burkett, J.O. Codignotto, J.E. Hay, R.F. McLean, S. Ragoonaden and C.D.Woodroffe, 2007: Coastal systems and low-lying areas. Climate Change 2007: Impacts, Adaptation and Vulnerability. Contribution ofWorking Group II to the Fourth Assessment Report of the Intergovernmental Panel on Climate Change, M.L. Parry, O.F. Canziani, J.P. Palutikof, P.J. van der Linden and C.E. Hanson, Eds., Cambridge University Press, Cambridge, UK, 315-356.

Niedoroda, A.W., Reed, C.W., Stive, M., Cowell, P., 2001. Numerical simulation of coastal-tract morphodynamics. Coastal Dynamics 2001: ASCE 4th Conference on Coastal Dynamics, 403-412.

O'Brien, M.P., 1969. Equilibrium flow areas of inlets on sandy coasts. In: Journal of Waterways and Harbors Division, Proceedings of the American Society of Civil Engineers. ASCE, 43-52.

Pedrozo-Acuna, A., Simmonds, D.J., Otta, A.K., Chadwick, A.J., 2006. On the cross-shore profile change of gravel beaches. Coastal Engineering, 53, 335-347.

Perillo, G. M. E. 1995. Geomorphology and Sedimentology of Estuaries, Amsterdam.

Pierson, W.J.Jr., Moskowitz, L., 1964. A proposed sepctral form for fully developed wind seas based on the similarity theory of S. A. Kitaigorodskii. Journal of Geophysical Research, 69(24), 5181-5190.

Posford Duvivier, 1999. Suffolk Estuarine Strategies: Deben Estuary. Strategy Report: Phase 2 volume 1 Main Report. Peterborough: Environment Agency: Anglian Region, pp. 5-20.

Prandle, D., 2003. Relationships between Tidal Dynamics and Bathymetry in Strongly Convergent Estuaries. Journal of Physical Oceanography, 33, 2738-2750.

Ranasinghe, R., Swinkels, C, Luijendijk, A., et al. 2011. Morphodynamic upscaling with the MORFAC approach: Dependencies and sensitivities. Coastal Engineering, 58, 806-811.

Reeve, D. E. and Karunarathna, H., 2009. On the prediction of long-term morphodynamic response of estuarine systems to sea level rise and human interference. Continental Shelf Research, 29 (7), 938-950.

Reeve, D. E., Chadwick, A., Fleming, C., 2012. Coastal Engineering: Processes, theory and design practice. CRC press (2nd Ed.), pp. 112-122.

Ren, M. and Shi, Y.L., 1986. Sediment discharge of the Yellow River (China) and its effect on the sedimentation of the Bohai and the Yellow Sea. Continental Shelf Research, 6(6): 785-810.

Rodi, W., 1984. Turbulence models and their application in hydraulics, State-of-the-art paper sur l'etat de connaissance. IAHR-Section on Fundamentals of Division Ⅱ: Experimental and Mathematical Fluid Dynamics, The Netherlands.

Roelvink, J. A. and Walstra, D. J. R., 2004. Keeping it simple by using complex models. In Proceeding of the 6th International Conference on Hydro-Science and Engineering. Advance in Hydro-Science and Engineering, vol. page 12. Brisbane, Australia.

Roelvink, D., Reniers, A., van Dongeren, A., et al., 2009. Modelling storm impacts on beaches, dunes and barrier islands. coastal Engineering, 56, 1133-1152.

Roelvink, D. and Reniers, A., 2012. A guide to modeling coastal morphology, Singapore.

Ruessink, B.G., Walstra, D.J.R., Southgate, H.N., 2003. Calibration and verification of a parametric wave model on barred beaches. Coastal Engineering, 48, 139–149.

Ruggiero, P., Walstra, D.J.R., Gelfenbaum, G., Van Ormondt, M., 2009. Seasonal-scale nearshore morphological evolution: Field observations and numerical modelling. Coastal Engineering, 56, 1153–1172.

Schuttelaars, H. M., de Swart, H. E., 2000. Mutiple morphodynamic equilibria in tidal embayments. Journal of Geophysical research, 105, 24105-24118.

Sha, L. P. and Van den Berg, J. H., 1993. Variation in ebb-tidal delta geometry along the coast of the Netherlands and the German Bight. Journal of Coastal Research, 9(3), pp. 730-746.

Shennan, I., and Woodworth, P.L., 1992. A comparison of late Holocene and twentieth-century sea-level trends from the UK and North Sea region. Geophysical Journal International, 109, 96-105.

Shimura, T., Mori, N., Mase, H., 2015. Future Projection of Ocean Wave Climate: Analysis of SST Impacts on Wave Climate Changes in the Western North Pacific. Journal of Climate, 28, 3171-3190.

Smith, S.D. and Banke, E.g., 1975. Variation of the sea surface drag coefficient with wind speed. Quarterly Journal of the Royal Meteorological Society, 101, 665-673.

Soulsby, R., 1997. Dynamics of marine sands, a manual for practical applications. Thomas Telford, London.

Speer, P. E., Aubrey, D. G., 1985. A study of Non-linear Tidal Propagation in shallow Inlet/Estuarine Systems Part II: Theory. Estuarine, Coastal and Shelf Science, 21, 207-224.

Spencer, T., Brooks, S.M., Evans, B.R., Tempest, J.A., Moller, I., 2015. Southern North Sea storm surge event of 5 December 2013: Water levels, waves and coastal impacts. Earth-Science Reviews, 146, 120-145.

Stelling, G.S., 1984. On the construction of computational methods for shallow water flow problem. Rijkswaterstaat Communications vol. 35. Government Printing Office, The Hague, The Netherlands.

Stelling, G. S. and Leendertse, J. J., 1992. Approximation of Convective Processes by Cyclic AOI methods. In M. L. Spaulding, K. Bedford and A. Blumberg, eds., Estuarine and coastal modeling, Proceedings of 2nd Conference on Estuarine and Coastal Modelling, ASCE, pages 771–782. Tampa.

Stelling, G. S. and van Kester, J. A. T. M., 1994. On the approximation of horizontal gradients in sigma co-ordinates for bathymetry with steep bottom slopes. International Journal Numerical Methods in Fluids 18: 915–955.

Stigebrandt, A., 1981. A mechanism governing the estuarine circulation in deep, strongly stratified fjords. estuarine, Coastal and Shelf Science, 13, 197-211.

Stive, M. J. F., 1987. A model for cross-shore sediment transport. In: ENGINEERS, A. S. O. C., ed. 20th International Coastal Engineering Conference, 1986 New York. 1550-1564.

Stive, M.J.F., Wang, Z.B., Capobianco, M., Ruol, P., Buijsman, M., 1998. Morphodynamics of a tidal lagoon and the adjacent coast. In Dronkers and Scheffers, editors, Physical of Estuaries and Coastal Seas, Rotterdam, Balkema. 397-407

Sutherland, J., Peet, A.H., Soulsby, R.L., 2004. Evaluating the performance of morphological models. Coastal Engineering, 51, 917-939.

SWAN user manual – complete input and usage of the SWAN package, 2017. Delft University of Technology, Environmental Fluid Mechanics Section, available from *http://www.swan.tudelft.nl* (Version 41.20)

Taylor, J.A., Murdock, A.P., Pontee, N.I., 2004. A macroscale analysis of coastal steepening around the coast of England and Wales. The Geographical Journal, 170 (3), pp. 179-188.

Thomas, C. G., Spearman, J.R., Turnbull, M.J., 2002. Historical morphological change in the Mersey Estuary. Continental Shelf Research, 22, 1775-1794.

Townend, I. H., Wang, Z.B., Rees, J. G., 2007. Millennial to annual volume changes in the Humber Estuary. In: Proceedings of The Royal Society, 837-854.

Uittenbogaard, R. E., van Kester, J. A. T. M. and Stelling, G. S., 1992. Implementation of three turbulence models in 3D-TRISULA for rectangular grids. Tech Rep. Z81, WL Delft Hydraulics, Delft, The Netherlands.

Valle-Levinson, A. 2010. Definition and classification of estuaries. In: VALLE-LEVINSON, A. (ed.) Contemporary issues in estuarine physics. London: Cambridge University Press.

Van der wal, D., Pye, K., Neal, A., 2002. Long-term morphological change in the Ribble Estuary, northwest England. Marine Geology, 189, 249-266.

Van der Wal, D., Pye, K., 2004. Patterns, rates and possible causes of saltmarsh erosion in the Greater Thames area (UK). Geomorphology 61, 373–391.

Van Goor, M.A., Stive, M.J.F., Wang, Z.B., and Zitman, T.J., 2001. Influence of relative sea level rise on coastal inlets and tidal basins. Coastal Dynamics 2001: ASCE 4th Conference on Coastal Dynamics, Lund, Sweden, ASCE, 242-251.

Van Leer, B., 1974. Towards the ultimate conservative difference scheme II. Monotonicity and conservation combined in a second order scheme. Journal of Computational Physics 32: 101–136.

Van Rijn, L.C., 1993. Principle of Sediment Transport in Rivers, Estuaries and Coastal Seas. Aqua Publications, Amsterdam.

Van Rijn, L.C., 2001. Approximation Formulae for Sand Transport by Currents and Waves and Implementation in DELFT-MOR. WL Delft Hydraulics Report vol. Z054.20, Delft Hydraulics. The Netherlands.

Van Rijn, L.C., Walstra, D. J. R., Grasmeijer, B., Sutherland, J., Pan, S., Sierra, J.P., 2003. The predictability of cross-shore bed evolution of sandy beaches at the time scale of storms and seasons using process-based profile models. Coastal engineering, 47, 295-327.

Vega-Leinert, A.C., and Nicholls, R.J., 2008. Potential implications of sea-level rise for Great Briton. Journal of Coastal Research, 24(2), 342-357.

Verboom, G.K., Slob, A., 1984. Weakly-reflective boundary conditions for two-dimensional shallow water flow problems. Advances in Water Resources, 7(4), 192-197.

Villaret, C., 2004. SISYPHE release 5.4: User's manual, Rep. P75G17, Lab. Natl. Hydraul. et Environ., Electr. de Fr., Chatou, France.

WAFO – A MATLAB toolbox for analysis of random waves and loads, Lund University, Sweden, homepage http://www.maths.lth.se/matstat/wafo/, 2000.

Walkden, M., Rossington, K., et al., 2009. Characterisation and prediction of large scale, long-term change of coastal geomorphological behaviours: Proof of concept

modelling. Joint Defra/Environment Agency Flood and Coastal Erosion Risk Management R&D Programme. Bristol.

Walton, T.L. and Adams, W.D., 1976. Capacity of inlet outer bars to store sand, In: Proc. 15th Coastal Engineering Conference, Honolulu, ASCE, New York, Vol. II, 1919-1937.

Weibull, W., 1951. A Statistical Distribution Function of Wide Applicability. Journal of Applied Mechanics, 18, 293-297.

Willebrand, J., 1975. Energy transport in a nonlinear and inhomogeneous random gravity wave field. Journal of Fluid Mechenism, 70, 113-126.

Whitham, G., 1974. Linear and nonlinear waves. Wiley, New York.

Wolf, J., Prandle, D., 1999. Some observations of wave-current interaction. Coastal Engineering 37, 471–485.

Woth, K., Weisse, R., Von Storch, H., 2006. Climate change and North Sea storm surge extremes: An ensemble study of storm surge extremes expected in a changed climate projected by four different regional climate models. Ocean Dynamics, 56(1), 3–15.